PHOTOIONIZATION DYNAMICS AND ION STATE DISTRIBUTIONS IN SINGLE-PHOTON AND RESONANCE ENHANCED MULTIPHOTON IONIZATION OF MOLECULES

Thesis by

Matthew Braunstein

In Partial Fulfillment of the Requirements

for the Degree of

Doctor of Philosophy

California Institute of Technology

Pasadena, California

1991

(Submitted July 9, 1990)

Acknowledgments

I would like to thank my thesis advisor Vincent McKoy for wise advice and patience during the course of this work. I am also indebted to Jochen Schirmer, Carl Winstead, Sham Dixit, and especially Jeff Stephens for their time and energy in teaching me about molecular physics, and instilling in me by their examples what it means to be a good scientist and researcher.

Although my work at Caltech has been solely concerned with theoretical ideas and methods, most of the studies presented in this thesis were done in collaboration with experimentalists. These include Erwin Poliakoff, Lorraine Kelly, Trish Ferrett, Mike White, William Chupka, C. A. de Lange and Josef Feldhaus. Working with these fine scientists has greatly enriched my graduate education and the quality of this thesis.

Finally I would like to thank my wife Waverly for her excellent proofreading and most of all for providing support, friendship, and humor through some difficult times.

Abstract

This thesis presents results of theoretical studies of single-photon ionization and resonance enhanced multiphoton ionization (REMPI) of several small molecules. These studies parallel several recent experiments which use tunable sources of radiation to photoionize molecules and measure the resulting electronic, vibrational, and rotational population of ions via photoelectron spectroscopy. The objective of this thesis is to examine the underlying dynamics between the ion and the ejected electron and to understand how these interactions affect photoion state distributions. In particular, this work focuses on the presence and influence of localized quasi-bound states of the photoelectron called "shape resonances" which significantly influence these ion distributions. A key feature of these studies is the use of accurate Hartree-Fock photoelectron wave functions determined from the Schwinger variational method. This method provides a photoelectron wave function determined in the static-exchange and non-central field of the molecular ion. Use of such photoelectron wave functions is crucial in an accurate determination of transition moments and ion state populations.

The first part of the thesis examines shape resonances in the photoionization of O_2. Studies reported here include investigations of branching ratios of electronic multiplet states in the $3\sigma_g$ and $1\pi_u$ photoionization of O_2 and a comparison of photoionization of the singlet states, a $^1\Delta_g$ and d $^1\Pi_g$ $(3s\sigma_g 1\pi_g)$, with that of the ground state of O_2. These studies show that the electronic exchange interaction between the ion core and the photoelectron in shape resonant energy regions profoundly affects the electronic state distributions of the molecular ion. We also report vibrational branching ratios in the single-photon ionization of O_2, and in REMPI of O_2 via the C $^3\Pi_g$ Rydberg state. In these studies, we find that a shape

resonance causes a dependence of the electronic transition moment on the molecular geometry leading to non-Franck-Condon ion vibrational distributions and a dependence of the rotational branch intensity on the ion vibrational state.

The second part of this thesis examines shape resonances in other molecules, focusing on the more general aspects of the photoionization dynamics. Here we present studies of the vibrational state distributions in the 7σ photoionization of the polyatomic N_2O, where a shape resonance causes non-Franck-Condon vibrational state distributions, the degree of which depends on the nuclear displacements involved and whether the shape resonance is localized on a particular bond. We also study the photoionization dynamics of the valence shell of Cl_2, where a shape resonance is also seen. In contrast to what has been seen in other molecules, this shape resonance is not oriented along the molecular axis, but perpendicular to it. The shape resonance therefore is less sensitive to vibrational motion and does not influence vibrational distributions. Finally, we present studies of the K-shell ionization of CO. Studies in this energy region have assumed a new importance with the development of tunable X-ray synchrotron sources. Here, electronic relaxation in the production of a K-shell hole is seen to significantly influence the photoionization cross section in shape resonant energy regions. The mathematical framework is given to separate and analyze the effects of electronic relaxation in the photoionization cross section and calculate K-shell satellite spectra from first principles.

The results of examination of all these photoionization processes are discussed in the context of recent experiments.

Table of Contents

I. Introduction

This thesis presents results of theoretical studies of the photoionization of molecules, emphasizing the underlying dynamics of the photoelectron-ion interactions and how this affects ionic state distributions. These studies were largely motivated by the need to understand recent experiments which use tunable sources of radiation in the ultraviolet to soft X-ray range, such as pulsed dye-lasers[1] and synchrotrons,[2] to ionize small molecules and measure the cross section for the product ions as a function of incident energy. These experiments are highly molecule- and state-specific, and can measure cross sections, both integral and differential, for ionization of specific electronic, vibrational, and rotational levels of the neutral molecule leading to specific rovibronic levels of the ion. Understanding the photoionization process and resulting ion distributions in these experiments is important in modeling chemical reactions which occur in the atmosphere[3] and in plasmas,[4] in probing the orientation of adsorbates on surfaces,[5] in state-selection and state-specific production of ions,[6] and as a probe of electronically excited states.[7]

The photoionization cross section of molecules can depend on the energy of the incident radiation in a complex way, exhibiting structure which reflects the underlying dynamics between the ejected electron and the molecular ion field. In particular, this thesis focuses on the presence and influence of localized, quasi-bound states of the photoelectron called "shape resonances," which are caused by the trapping of the ejected electron by the centrifugal barrier of the molecular ion field. These resonances are usually observed as distinct enhancements in the photoionization cross section of two to ten electron volts in width and have been observed in a wide variety of molecules.[2] Shape resonances also strongly influence photoelectron angular distributions.

This thesis consists of two main parts. The first part (chapters 1-9) investigates shape resonances in the photoionization of O_2. These investigations of O_2 are presented in order of increasing resolution of the product ions, from electronic to vibrational to rotational, and reflect the increasingly rich dynamical information obtained in these studies. In open-shell molecules such as O_2, where photoionization of a molecular orbital can lead to ions with different spin couplings, shape resonances may lead to electronic branching ratios which differ significantly from those expected on the basis of the spin multiplicities of the final state ions. For example, $3\sigma_g$ photoionization of O_2 ($X\ ^3\Sigma_g^-$) leads to quartet and doublet ions which are expected to occur in the statistical ratio given by the spin degeneracy of these states (2S+1): two quartet ions for every doublet ion formed. Deviations from this statistical ratio can occur in the energy region of a shape resonance. This is due to the localized nature of shape resonances and their resulting sensitivity to details of the inner region of the molecular ion potential field, in this case the differing exchange potentials of the different multiplet ions. Evaluation of the transition moments to specific ion multiplets requires an accurate potential which incorporates the proper exchange interactions. A key feature of the present studies is the use of accurate static-exchange Hartree-Fock photoelectron wave functions determined with the iterative Schwinger variational method.[8,9] We examine multiplet-specific effects in the electronic branching ratios in the photoionization of the $3\sigma_g$ (chapter 1) and $1\pi_u$ (chapter 2) orbitals of O_2. We compare our results with recent experiments and note significant differences with previous calculations which did not explicitly take into account such differences in the multiplet potentials. We also show how multiplet-specific effects can be important in excited state ionization of O_2 in the context of a recent resonance enhanced multiphoton ionization (REMPI) experiment via the d $^1\Pi_g$ state (chapter 3) and a single-photon experiment from the first electronically excited state, a $^1\Delta_g$, of O_2 (chapter 4).

In chapter 5, we again look at $3\sigma_g$ photoionization of O_2, but here the multiplet ions are *vibrationally* resolved. Because of their localized nature, these shape resonances are quite sensitive to details of the molecular ion potential and, hence, to molecular geometry. This sensitivity of shape resonances to nuclear geometry induces a dependence of the electronic transition moment on the internuclear distance. In shape-resonant energy regions, the factorization of the nuclear and electronic coordinates in the evaluation of the transition amplitude assumed in the Franck-Condon approximation can hence become a poor approximation. The presence of a shape resonance in the $3\sigma_g$ photoionization of O_2 therefore causes large deviations from predictions based on the Franck-Condon principle for the branching ratios of ion vibrational states and the associated angular distributions of photoelectrons. In this thesis, we examine such shape resonant deviations from Franck-Condon behavior by explicitly evaluating the internuclear distance dependence of the electronic transition moments by *ab initio* methods. Results of these calculations are presented in chapters 6-8 for $1\pi_g$ photoionization of O_2 and are discussed in the context of recent experiments. This work on O_2 demonstrates for the first time how shape resonances, known to affect ground state photoionization processes, can significantly influence the vibrational distribution of ions in photoionization from an excited state.

Chapter 9 presents studies on the single-photon ionization of O_2 with *rotational* resolution of the ions. Here the internuclear distance dependence of the shape resonance causes a dependence of the rotational branch intensity on the ion vibrational level. Analysis of the relative spectral intensities reveal highly detailed information on the angular momentum composition of the shape resonance and how it changes with vibrational excitation of the ion. These results provide a useful analysis of recent state-of-the-art high-resolution experiments and are the first to examine a shape resonance in the context of rotationally resolved transitions.

The second part of this thesis (chapters 10-13) investigates other molecules, focusing on ways shape resonances may affect the grosser features of photoionization spectra. Chapters 10 and 11 are studies of shape resonances in the photoionization of N_2O. This work represents the first quantitative study concerning localization of shape resonances about a particular bond in a polyatomic molecule and how this may selectively affect ion vibrational distributions associated with various vibrational modes of the molecule.

In chapter 12, we present results for photoionization of the valence orbitals of Cl_2. Although a shape resonance is found here, it is insensitive to internuclear distance, in marked contrast to behavior observed in the vicinity of shape resonances in other diatomics. Unlike the shape resonances found in O_2 and N_2O, which are polarized along the molecular axis, the shape resonance in Cl_2 has a polarization perpendicular to the molecular axis and is therefore less sensitive to changes in the internuclear geometry. This study was motivated by recent studies of REMPI of Cl_2 which showed non-Franck-Condon ion vibrational distributions. This work rules out a shape resonant mechanism as the origin of these non-Franck-Condon effects and gives an initial examination of the rich and unusual behavior of shape resonances which can be expected for heavier systems.

Finally, in chapter 13, we will explore the influence of shape resonances in K-shell photoionization of CO. In contrast to ionization of valence shell electrons discussed in the previous chapters, ejection of a K-shell electron leads to major restructuring of the ionic core. The position and width of the shape resonance are seen to be extremely sensitive to this restructuring, particularly the screening of the K-shell hole which accompanies the relaxation of the valence electrons. Since the final state "relaxed" ion orbitals are different from those of the initial neutral molecule, this restructuring of the ionic wave function introduces severe complications in the derivation of the Hartree-Fock equations for the photoelectron wave

function and in the evaluation of the photoionization transition moment. The mathematical framework is given for separating and analyzing the effects of electronic relaxation in these photoionization cross sections and for obtaining K-shell satellite spectra from first principles. This work parallels recent experimental advances in the use of tunable X-ray radiation and photoelectron spectroscopy which are generating much new data for K-shell photoionization processes.[10]

In the following section we present in detail the illustrative example of (2+1) REMPI of O_2 via the C $^3\Pi_g$ state, discussed in chapters 7 and 8. Here we will show the general theoretical framework used in the evaluation of the photoionization cross section and the experimental motivation behind the present work. We will also discuss more completely the physical origin of shape resonances and how they affect ion state distributions, the main theme of this thesis. This example of REMPI of O_2 provides a good background for the other chapters in this thesis.

II. REMPI of molecular oxygen via the C $^3\Pi_g$ state

Photoionization of molecular oxygen plays an extremely important role in the chemistry of the atmosphere.[11] Because it is an open shell system, with an electron configuration $1\sigma_g^2\ 1\sigma_u^2\ 2\sigma_g^2\ 2\sigma_u^2\ 3\sigma_g^2\ 1\pi_u^4\ 1\pi_{gx}\ 1\pi_{gy}$, valence excitations can produce a wide variety of states[12] which makes the spectrum of this molecule particularly complicated and difficult to assign.[13] In fact, the first detailed characterization of states involving excitation of the outermost ($1\pi_g$) electron to a Rydberg orbital to produce the C $^3\Pi_g$ state ($1\pi_g 3s\sigma_g$) was obtained only in 1985.[14] In this (2+1) REMPI experiment,[14] pulsed dye-laser radiation was used to excite molecular oxygen from its ground state (2-photon absorption) to the C $^3\Pi_g$ excited state and a third photon of the same color (1-photon ionization) ionized the excited state before it could decay. This excitation scheme is shown in figure 1. Because of the narrow bandwidth of the laser radiation, REMPI is highly state-selective and the

radiation frequency can be tuned so that a specific vibrational level of the C $^3\Pi_g$ excited state can be accessed and ionized when the two-photon laser wavelength is exactly in resonance with it. Because dipole selection rules forbid g $\longrightarrow$ g transitions for absorption of a single photon, this state had only been observed in electron impact experiments[15] before the advent of REMPI techniques.

The C $^3\Pi_g$ $(1\pi_g 3s\sigma_g)$ state is the first member of a Rydberg series which has the general electron configuration (core)$1\pi_g n\ell$, where n is the principal quantum number and ℓ indicates the orbital angular momentum. The members of this Rydberg series have excitation energies which follow the Rydberg formula, E_{exc} = I.P. - $R/(n-\delta)^2$. Here δ = 1.103, I.P. = 12.01 eV, and R is the Rydberg constant. The value of δ measures the relative penetration of the Rydberg electron into the molecular ion core. For example, the "s" Rydberg states are the most penetrating due to the absence of an angular momentum barrier and have a higher value of δ than "p" Rydbergs. Calculations show that this orbital has about 95% s-character and 5% d-character.

Since the Rydberg electron is essentially non-bonding, the equilibrium geometry and spectroscopic constants are nearly the same for the the C $^3\Pi_g$ state and X $^2\Pi_g$ ion; and the potential energy curves for these states are nearly parallel (see Fig. 1). The Franck-Condon principle predicts that the intensities of the ion vibrational states formed are proportional to the Franck-Condon factors, that is, the square of the overlap of the vibrational wave functions of the initial Rydberg and final ion states. Since the potential energy curves for these sates are nearly parallel, this suggests that *the vibrational quantum number should be conserved in the ionization step.* The Franck-Condon factors for the ionizing transition are shown in Table I, and indicate that this conservation of vibrational qunatum number should be quite strong, better than 98% in all cases. Thus (n+1) REMPI via molecular Rydberg states would appear to be an ideal method for production of vibrationally

state-selected ions. In fact, REMPI has been used to produce state-selected ions, with greater than 80% state selection in a large number of cases. The ability to produce ions in a specific quantum state is extremely useful in the detailed study of reaction dynamics.[6,7]

Vibrational state selection of ions was the experimental motivation behind the (2+1) REMPI experiments by Katsumata *et al.*[16] and Miller *et al.*[17] which went beyond previous experiments, which had only detected the total mass ion spectrum,[14] and kinetic-energy analyzed the photoelectrons by time of flight, to obtain the ion vibrational state distribution for excitation through a particular vibrational level of the C $^3\Pi_g$ state:

$$O_2(v_0) \xrightarrow{2h\nu} C\ ^3\Pi_g(v') \xrightarrow{h\nu} O_2^+\ X\ ^2\Pi_g(v^+).$$

The distribution of ions from the experiment of Miller *et al.*[17] is shown in Fig. 2. Each frame corresponds to the resulting ion distributions, v^+, for excitation through a particular vibrational level, v', of the C $^3\Pi_g$ state. Clearly, intense off-diagonal transitions, $\Delta v = v^+ - v' \neq 0$, are observed for ionization through the $v' = 1$-3 levels of the C $^3\Pi_g$ state which are thousands of times larger than those predicted from the Franck-Condon factors shown in Table I. The Franck-Condon intensities for the off-diagonal vibrational levels, $\Delta v \neq 0$, would be too small to be visible on the scale of these figures. The observed ion state distributions therefore strongly deviate from predictions based on the Franck-Condon principle. In fact, for v'=2 nearly 40% of the ions are redistributed from the $v^+ = 2$ level of the ion to other vibrational levels.

Figure 2 also shows the vibrational ion distribution for photoelectron detection parallel and perpendicular to the polarization of the laser for excitation through the $v' = 2$ level of the C $^3\Pi_g$ state.[16] This vibrational state dependence of the photoelectron angular distributions further reflects non-Franck-Condon behavior.

Clearly, something is happening in the photoionization step which is making the Franck-Condon factorization of the electronic and vibrational factors in the transition moment quite inaccurate. The theoretical motivation behind chapters 6-8 was to try to understand the mechanism which produces these non-Franck-Condon effects, and severely hindered ion state-selection. Although these experiments are molecule specific, the origins of these non-Franck-Condon effects can be found in many molecular systems and the mechanism is quite general.

III. The physical origin of shape resonances and their effects on ion state distributions in REMPI of O_2

To put the underlying dynamical processes in some context, we briefly examine photoexcitation and ionization of the simplest of cases, the 1s $\longrightarrow$ np, . . ., ϵp transition in the hydrogen atom. Figure 3 shows the oscillator strength of the hydrogen atom in the discrete and adjoining continuum. The boxes in the discrete spectrum represent transitions to states with n=2,3, . . normalized so that the width is dE/dn and the height is f (dn/dE).[18] As the excitation energy becomes greater, and the final state wave function becomes more diffuse, the overlap between it and the 1s orbital becomes less and the oscillator strength monotonically decreases through the discrete and into the ionization continuum, joining smoothly at the ionization threshold. Figure 3 also shows results from calculations of single-photon ionization of the ground state of O_2 which accesses the same photoionization continuum as the (2+1) REMPI experiments discussed previously. The profile of this oscillator strength distribution is very non-hydrogenic, with an enhancement around the ionization threshold region.

In most situations, the ion potential in which the outgoing electron moves is more complex than in the hydrogenic 1s $\longrightarrow$ ϵp case. An example of such a more complex effective potential in which the photoelectron moves is shown in Fig. 4

for photoionization of the 3p orbital of argon. The effective potential is formed from a combination of the electrostatic potential (nuclear attraction and electron-electron repulsion) between the ion core and the photoelectron which is mostly attractive and accounts for the deep inner well, shown as V_c, and the centrifugal potential which is purely repulsive and behaves as $\ell(\ell + 1)/2r^2$. This effective potential has three distinct regions, a deep inner well, a barrier, and a shallow outer well. The deep inner well corresponds to the part of the potential which supports bound localized electrons. At very large distances, the molecular ion 1/r Coulomb attraction dominates and leads to the shallow outer well supporting diffuse Rydberg states. However, at distances at the "edges" of the atom, the centrifugal force overcomes the attractive electrostatic force and a barrier forms. The height and "shape" of the barrier may give rise to a quasi-discrete state of the photoelectron at certain energies, E_r, above the ionization potential which is trapped behind the barrier. These trapped states are also called "shape resonances" because they arise from the special shape of the effective potential in which the photoelectron moves. It should be noted that these states would occur in the same energy region accessed by the REMPI experiments on O_2, within a few electron volts of the ionization threshold.

In shape resonant energy regions, the wave function of the photoelectron, being trapped by the barrier, becomes quite localized in character. This is shown schematically in Fig. 5, where at the shape resonant energy, $E=E_r$, the amplitude of the photoeletron wave function behind the barrier (near the ion core) becomes much greater. Because of the relatively compact valence-like nature of shape resonances, there is a greater overlap between the initial and final state wave functions, so the transition matrix element can become large and the cross section enhanced in these regions. The cross section for 3p ionization of argon is shown in the top of Fig. 5 and indicates an enhancement in the cross section around threshold

which reflects the localized character of the photoelectron wave function and its greater overlap with the target 3p orbital.[19] These quasi-discrete states or shape resonances thus have a profound effect on the photoionization cross section.

Since shape resonances are quite localized in nature, the position and width of shape resonances depend critically on the interplay of different parts of the molecular ion potential, namely the electrostatic and the centrifugal parts. In particular, how the ion potential changes when the nuclei of a molecule move can influence the energy position and width of shape resonances. The pioneering work of Dehmer, Dill, and Wallace[20] first brought this to light in examining the energy dependence of the ion vibrational distributions in the photoionization of the $3\sigma_g$ orbital of N_2. The sensitivity of shape resonances to the position of the nuclei in molecules induces a *dependence of the electronic transition moment on the internuclear distance.* A strong internuclear distance dependence of the electronic transition moment makes the Franck-Condon approximation no longer valid. With initial and final state wave functions written as products of vibrational and electronic wave functions (Born-Oppenheimer approximation), the Franck-Condon approximation gives the intensity of a transition between vibrational levels as being proportional to the square of the overlap between the initial and final vibrational wave functions:

$$\begin{aligned} I_{if} &\propto |\langle \chi_i(R)\psi_i(r;R)|\vec{\mu}|\chi_f(R)\psi_f(r;R)\rangle|^2 \\ &\simeq |\langle \psi_i|\vec{\mu}|\psi_f\rangle|^2 |\langle \chi_i|\chi_f\rangle|^2 = M(R_e)|\langle \chi_i|\chi_f\rangle|^2, \end{aligned} \tag{1}$$

where $\psi_i(r;R)$ and $\psi_f(r;R)$ are the initial and final electronic wave functions, respectively, $\chi_i(R)$ and $\chi_f(R)$ are initial and final vibrational wave functions, respectively, and $\vec{\mu}$ is the dipole operator. The electronic transition moment at R_e, $M(R_e)$, results from integration of $\psi_i\vec{\mu}\psi_f$ over the electronic coordinates at R_e. The number, $|\langle \chi_i|\chi_f\rangle|^2$, is the Franck-Condon factor. It is quite clear from Fig. 3

and the enhancement of the cross section near threshold, that the photoelectron continuum of O_2 is shape resonant. This will induce a dependence of the electronic transition moment on the internuclear distance due to the localized nature of the photoelectron wave function and therefore produce ion vibrational distributions quite different from those given by the Franck-Condon approximation.

Fig. 6 shows the photoionization cross section for $3s\sigma_g \longrightarrow k\sigma_u$ channel, the same ionizing transition as in the REMPI experiments on O_2 described above, at various internuclear distances. At R=2.088 a.u., the $k\sigma_u$ shape resonance is clearly seen as a large enhancement in the photoionization cross section. As the internuclear distance is decreased, the shape resonant maximum moves to higher energy. This strong sensitivity of the electronic transition moment to the internuclear distance due to the shape resonance is similar to that observed in the $3\sigma_g$ single-photon ionization of N_2 out of the ground electronic state.[20] The present work on O_2 establishes for the first time shape resonances in excited state photoionization, and suggests that this phenomenon will be equally prevalent in REMPI processes as it has been in single-photon ionization. This dependence of the electronic transition amplitude on the internuclear distance induces strong non-Franck-Condon effects in the ion vibrational state distributions. This is seen in Fig. 7, which shows calculated branching ratios for excitation through the $v' = 1$-3 levels of the C $^3\Pi_g$ state compared with peak intensities obtained from the measured photoelectron spectra.[17] In these calculations, we have included full R-dependence of the electronic transition amplitude. The calculations predict pronounced non-Franck-Condon distributions for all v' levels. Recall that the vibrational wave functions for the C $^3\Pi_g$ and X $^2\Pi_g$ states are nearly identical, and the branching ratios, $\Delta v = v^+ - v' \neq 0$, of Franck-Condon factors are negligible when plotted on the scale of Fig. 7 (see Table I). For the $v' = 2$ and 3 levels, the $\Delta v < 0$ branching

ratios are in satisfactory agreement with experiment, while those for $\Delta v > 0$ appear to show systematic deviation. Our results for the $v' = 1$ level account for some of the observed $\Delta v \neq 0$ intensity, although there is substantial disagreement. Accurate bound state calculations predict three dissociative states, A $^3\Sigma_u^+$, B $^3\Sigma_u^-$, and C $^3\Delta_u$, arising from terms of $1\pi_u^3\ 1\pi_g^3$ electronic configuration which intersect the ion curve.[12] These states, which arise from a $\pi_u \longrightarrow \pi_g$ valence excitation, open up an indirect autoionizing channel which could significantly affect the ion state vibrational distributions. In addition, these states could also dissociate giving neutral oxygen atoms. A full theoretical treatment requires consideration of the competing processes of direct ionization, autoionization, and dissociation and the interference among these channels.

In figure 8, results for photoelectron angular distributions are compared with experiment through the $v' = 3$ level of the C $^3\Pi_g$ state.[21] In these plots, the laser propagation direction is into the paper, while the angle between the polarization vector of the light (vertical direction) and the photoelectron detector is denoted by θ. For example, for the diagonal transition ($v^+ = 3$), most of the photoelectron flux is along the electric field polarization direction. The most prominent observation in both theoretical and experimental results is the difference in angular distributions between diagonal, $\Delta v = 0$, and off-diagonal, $\Delta v \neq 0$, transitions. This indicates that the electronic transition moment is quite sensitive to the nuclear motion and hence non-Franck-Condon. The differences in photoelectron angular distributions between diagonal and off-diagonal transitions occur because the non-resonant $k\pi_u$ channel contributes to the diagonal transition but is extremely small for the off-diagonal transition. Being nonresonant, the $k\pi_u$ channel follows the Franck-Condon approximation. The integrals of the off-diagonal vibrational overlaps are almost zero, greatly reducing the contribution of this channel to the off-diagonal intensity. The shape resonant $k\sigma_u$ channel, being sensitive to internuclear distance

and hence non-Franck-Condon, is present in both diagonal *and* off-diagonal transitions. Therefore different partial waves will contribute to diagonal transitions, namely $k\sigma_u$ and $k\pi_u$ channels, versus off-diagonal transitions which will be mostly $k\sigma_u$. Hence the diagonal and off-diagonal photoelectron angular distributions are different due to the shape resonance and its sensitivity to internuclear distance.

In this illustrative example of REMPI of O_2 (discussed also in chapters 7 and 8 of this thesis), we have shown how a shape resonance can profoundly affect ion state distributions, creating large deviations from Franck-Condon expectations, and in this case significantly hindering ion-state selection. The remaining chapters of this thesis concern how shape resonances, and particularly the localized character of the photoelectron wave functions, can affect ion state distributions in other photoionization processes and in other molecular systems. It should be stressed that the phenomenon studied here can be expected to be quite widespread in molecular systems and will be the focus of attention as experimental techniques improve and more systems and more details of the photoelectron spectrum are addressed.

As a final part of the introduction I will explain in more detail how we evaluate the transition amplitude, emphasizing the treatment of the photoelectron wave function, an accurate determination of which is crucial in evaluating and understanding molecular photoionization cross sections and photoelectron angular distributions.

IV. Theoretical Framework

Typical photoionization experiments are done in the gas-phase with linearly polarized light. It is also assumed that the wavelength of the incident radiation is such that the dipole approximation applies ($\lambda \gg 1\text{Å} \cong 12$ keV). We then apply

Fermi's Golden Rule[19] to obtain an expression for the (vibrationally and rotationally unresolved) photoionization cross section (in a.u.):

$$\sigma = \frac{4\pi^2 E}{3c} |\langle \Psi_f | \vec{\mu} | \Psi_i \rangle|^2 . \tag{2}$$

Here Ψ_i represents an antisymmetrized product of orbitals of the neutral molecule, generally a single configuration which is also called the Self-Consistent-Field (SCF) or Hartree-Fock (HF) wave function. The wave function Ψ_i is calculated at the equilibrium geometry of the initial state neutral molecule and within the Born-Oppenheimer approximation. The constant c is the speed of light and E is the energy of the incident radiation. The dipole operator, $\vec{\mu} = -e\vec{r}$, represents the coupling of the electric field of the incident photons with each of the charged particles of the target molecule. The final state wave function Ψ_f is an antisymmetrized product of orbitals of the molecular ion and a photoelectron orbital with energy $(E - I.P.)$, where $I.P.$ is the ionization potential of the target molecule. In studies where the molecular orbital being ionized is in the valence shell, the molecular ion orbitals are taken to be the same as those of the neutral molecule. This is called the frozen-core Hartree-Fock (FCHF) approximation. This considerably simplifies the evaluation of Eq. (2), so that the transition amplitude, according to the Slater-Condon rules, involves only the orbital being photoionized and the photoelectron orbital multiplied by a factor which allows for the fact that the final state is not in general a single Slater determinant.[22] For ionization of inner-shell electrons, where there is a large restructuring of the electrons in the final state ion due to the inner-shell hole, the molecular orbitals of the final state ion are used. This leads to several complications in the evaluation of Eq. (2), discussed in chapter 13, due to non-orthogonality of the initial state and final state.

If vibrationally-resolved cross sections are required, $\Psi_i(r;R)$ and $\Psi_f(r;R)$ are multiplied by the appropriate vibrational wave functions, $\chi_i(R)$ and $\chi_f(R)$. The electronic transition moment is then calculated over the range of vibrational motion and the resulting electronic transition moment as a function of R is then integrated over the vibrational coordinates. Expressions for the *rotationally* resolved cross section require inclusion of the rotational wave functions of the neutral molecule and the ion and can become quite complicated, requiring explicit coupling of several angular momenta.[23]

Along with the total cross section, one can also measure the cross section for photoionization at a particular angle, θ, with respect to the incident light polarization. This angular distribution of photoelectrons provides another window on the photoelectron-molecular ion interaction. It has been shown[24] that the differential angular cross section per solid angle for single photon ionization only depends on the angle between the light polarization and the direction of the ejected electron and has a particularly simple form,

$$\frac{d\sigma}{d\Omega} = \frac{\sigma}{4\pi}(1 + \beta P_2(cos\theta)), \tag{3}$$

where σ is the total angle integrated cross section, P_2 is a Legendre polynomial, $P_2 = \frac{1}{4}(1+3\cos 2\theta)$, and β is defined in terms of the ratios of transition amplitudes and allows the various partial waves of the transition amplitude to interfere.[8] For example, for photoionization of the hydrogen atom, where only s→p transitions take place and there is only one angular momentum component in the final state, $\beta = 2$, and the photoelectron angular distribution takes on a $\cos^2\theta$ dependence. The photoelectron flux is therefore peaked around the direction of polarization of the photon beam. For molecular targets there are in general many possible final

angular momentum states, each of which is energy dependent, so the angular distribution of photoelectrons is significantly more complex, but nevertheless contains rich information on the photoionization process. Photoionization processes involving absorption of more than one photon include higher order Legendre polynomials in the expression for the photoelectron angular distribution.[23]

Calculation of the initial state Hartree-Fock wave function is straightforward and with widely available computer programs has become routine.[25] However, in the case of molecular photoionization, calculation of the photoelectron orbital in the final state wave function presents several difficulties. The photoelectron orbital, $\phi_{\vec{k}}$, must satisfy the one electron Schrödinger equation (in a.u.)

$$[-1/2\nabla^2 + V_{N-1} - k^2/2]\phi_{\vec{k}}(\vec{r}) = 0, \tag{4}$$

where V_{N-1} is the molecular ion potential and is non-local and nonspherical, and $\phi_{\vec{k}}$ must satisfy appropriate physical boundary conditions. The fact that V_{N-1} is nonspherical means that $\phi_{\vec{k}}$ is not an eigenfunction of angular momentum and there is a coupling of partial waves by the molecular potential, which can be especially important near the ion core. The anisotropic and non-local character of the molecular ion potential therefore makes Eq. (4) particularly difficult to solve.

To address and attack these two problems of non-locality and the anisotropic molecular potential encountered in problems of molecular photoionization, we recast the differential equation, Eq. (4), into an integral form, i.e., the Lippmann-Schwinger equation,[8,9]

$$\phi_{\vec{k}}(\vec{r}) = \phi^c_{\vec{k}} + G_c^{(-)} V \phi_{\vec{k}}, \tag{5}$$

where $\phi_{\vec{k}}^{c}$ is the Coulomb scattering wave function which is analytically known, V is the molecular ion potential, V_{N-1}, with the Coulomb potential removed, i.e.,

$$V = V_{N-1} + \frac{1}{r}, \tag{6}$$

and $G_c^{(-)}$ is the Coulomb Green's function with incoming wave boundary conditions. If one considers a partial wave expansion in angular momentum eigenfunctions,

$$\phi_{\vec{k}}(\vec{r}) = (\frac{2}{\pi})^{1/2} \sum_{\ell m} i^{\ell} \phi_{k\ell m}(\vec{r}) Y_{\ell m}^{*}(\hat{k}), \tag{7}$$

where $\phi_{k\ell m}$ has an implicit sum over spherical harmonics in coordinate space, substitution into Eq. (5) shows that *each* $\phi_{k\ell m}$ satisfies its own Lippmann-Schwinger equation

$$\phi_{k\ell m}(\vec{r}) = \phi_{k\ell m}^{c} + G_c^{(-)} V \phi_{k\ell m}. \tag{8}$$

To address the non-locality of the molecular potential we introduce an approximate expression by assuming a separable approximation for the potential V of Eq. (6) of the form,

$$V(\mathbf{r},\mathbf{r}') \cong V^{S}(\mathbf{r},\mathbf{r}') = \sum_{i,j} \langle \mathbf{r}|V|\alpha_i\rangle [V^{-1}]_{i,j} \langle \alpha_j|V|\mathbf{r}\,'\rangle, \tag{9}$$

where the matrix V^{-1} is the inverse of the matrix with elements $V_{ij} = \langle \alpha_i|V|\alpha_j\rangle$ and the α's are discrete basis functions such as Cartesian or spherical Gaussian functions which are known to be effective in representing the multicenter nature of molecular ion potentials.[25] With this approximation to V substituted into Eq.

(8), the partial wave solution to the integral equation, after some algebra, can be written as

$$\phi^{(0)}_{k\ell m}(\vec{r}) = \phi^{c}_{k\ell m}(\vec{r}) + \sum_{ij} \langle \vec{r}|G_c^{(-)}V|\alpha_i\rangle [D^{-1}]_{ij} \langle \alpha_j|V|\phi^{c}_{k\ell m}\rangle, \tag{10}$$

where

$$D_{ij} = \langle \alpha_i|V - VG_c^{(-)}V|\alpha_j\rangle. \tag{11}$$

With adequate basis sets, α's, these approximate solutions $\phi^{(0)}_{k\ell m}$, which satisfy scattering boundary conditions, can provide quantitatively reliable cross sections. Starting with these solutions, $\phi^{(0)}_{k\ell m}$, converged solutions of Eq. (8) can be obtained through an iterative procedure.[8,9] We are thus able to obtain an accurate description of the photoelectron wave functions which are then used to evaluate the electronic transition moments and photoionization cross sections.

Table I. Calculated Franck-Condon factors for the transitions

$O_2\ C\ ^3\Pi_g(v') \rightarrow\ O_2^+\ \ X\ ^2\Pi_g(v^+)$.[a]

v'	v^+	$\lvert \langle v^+ \mid v' \rangle \rvert^2$
0	0	0.999845
1	0	0.416395×10^{-4}
1	1	0.999381
1	2	0.132412×10^{-3}
2	0	0.109287×10^{-3}
2	1	0.106457×10^{-3}
2	2	0.995847
2	3	0.322933×10^{-2}
3	0	0.163960×10^{-5}
3	1	0.421358×10^{-3}
3	2	0.284685×10^{-2}
3	3	0.983515
3	4	0.123974×10^{-1}
3	5	0.699919×10^{-3}

[a] See chapter 8 for details on the molecular potentials used to construct this table.

References

[1] R. N. Compton and J. C. Miller, in *Laser Applications in Physical Chemistry*, edited by D. K. Evans (Dekkar, New York, 1988), Sec. 4.

[2] J. L. Dehmer, A. C. Parr, and S. H. Southworth, in *Handbook on Synchrotron Radiation*, edited by G. V. Marr (North Holland, Amsterdam, 1986), Vol II.

[3] D. M. Hunten and M. B. McElroy, J. Geophysical Research, **73**, 2421 (1968).

[4] See, for example, *Principles of Laser Plasmas*, edited by G. Bekefi (John Wiley and Sons, New York, 1976).

[5] R. L. Dubs, S. N. Dixit, and V. McKoy, Phys. Rev. Lett. **54**, 1249 (1985).

[6] J. P. Reilly, Israel Journal of Chemistry, **24**, 266 (1984). See also, J. S. Morrison, W. E. Conway, and R. N. Zare, Chem. Phys. Lett. **113**, 435 (1985), for an excellent example of the use of REMPI for ion state selection in the study of molecular reaction dynamics.

[7] K. Kimura, "Photoelectron Spectroscopy of Excited States," in *Photodissociation and Photoionization* (John Wiley and Sons, New York, 1985), p.161.

[8] R. R. Lucchese, G. Raseev, and V. McKoy, Phys. Rev. A. **25**, 2572 (1982).

[9] R. R. Lucchese, K. Takatsuka, and V. McKoy, Phys. Rep. **131**, 147 (1986).

[10] A. Reimer, J. Schirmer, J. Feldhaus, A. M. Bradshaw, U. Becker, H. G. Kerkhoff, B. Langer, D. Szostak, R. Wehlitz, and W. Braun, Phys. Rev.

Lett. **57**, 1707 (1986).

[11] R. E. Huffman, D. E. Paulson, J. C. Larrabee, and R. B. Cairns, J. Geophysical Research **76**, 1028 (1971).

[12] R. P. Saxon and B. Liu, J. Chem. Phys. **67**, 5432 (1977).

[13] P. M. Dehmer and W. A. Chupka, J. Chem. Phys. **62**, 4525 (1975).

[14] A. Sur, C. V. Ramana, and S. D. Colson, J. Chem. Phys. **83**, 904 (1985).

[15] D. C. Cartwright, W. J. Hunt, W. Williams, S. Trajmar, and W. A. Goddard, III, Phys. Rev. A **8**, 2436 (1973).

[16] S. Katsumata, Y. Achiba, and K. Kimura, J. Electron Spectrosc. Relat. Phenom. **17**, 229 (1979).

[17] P. J. Miller, L. Li, W. A. Chupka, and S. D. Colson, J. Chem. Phys. **89**, 3921 (1988).

[18] U. Fano and J. W. Cooper, Rev. Mod. Phys. **40**, 441 (1968).

[19] A. F. Starace, in *Handbuch der Physik*, edited by M. Mehlhorn (Springer, Berlin, 1982) Vol. 31.

[20] J. L. Dehmer, D. Dill, and S. Wallace, Phys. Rev. Lett. **43**, 1005 (1979); R. Stockbauer, B. E. Cole, D. L. Ederer, J. B. West, A. C. Parr, and J. L. Dehmer, *ibid* **43**, 757 (1979); J. B. West, A. C. Parr, B. E. Cole, D. L. Ederer, R. Stockbauer, and J. L. Dehmer, J. Phys. B **13**, 1105 (1980).

[21] P. J. Miller, W. A. Chupka, J. Winniczek, and M. G. White, J. Chem. Phys. **89**, 4058 (1988).

[22] A. Szabo and N. S. Ostlund, in *Modern Quantum Chemistry: Introduction to Advanced Electronic Structure Theory* (Macmillan, New York, 1982), p. 70.

[23] S. N. Dixit and V. McKoy, J. Chem. Phys. **82**, 3546 (1985).

[24] C. N. Yang, Phys. Rev. **74**, 764 (1948).

[25] See, for example, *Methods of Electronic Structure Theory*, Vol. III, edited by Henry F. Schaefer III (Plenum Press, New York, 1977).

Figure Captions

Fig. 1: Resonance enhanced multiphoton ionization (REMPI) scheme showing the (2+1) transition from the ground state of O_2 to O_2^+ via the C $^3\Pi_g$ Rydberg state. Note that the ion and the C $^3\Pi_g$ potential energy curves are nearly parallel.

Fig. 2: top: Photoelectron spectrum of Ref. 17 for (2+1) REMPI of O_2 via the C $^3\Pi_g$ state. Each frame corresponds to excitation through a different vibrational level of the C $^3\Pi_g$ state. bottom: Photoelectron spectrum of Ref. 16 for (2+1) REMPI of O_2 via the v'=2 level of the C $^3\Pi_g$ state detected at angles parallel and perpendicular to the laser polarization direction.

Fig. 3: top right: Oscillator strength distribution for the 1s $\longrightarrow$ p transition in hydrogen atom from Ref. 18. The ionization potential is set to the zero of energy. bottom: Oscillator strength distribution in the discrete and continuous spectra for the $1\pi_g \longrightarrow \sigma_u$ transition in O_2 at R_e. The energy scale is relative to the ionization threshold at 12.07 eV.

Fig. 4: Coulombic (V_c), Centrifugal ($V_{centrifugal} = \frac{\ell(\ell+1)}{2r^2}$) and $V_{eff} = V_c + V_{centrifugal}$ potentials for the ϵd photoelectron in the 3p photoexcitation of Ar. Note the barrier in the effective potential, V_{eff}, at ~2 - 3 a.u.

Fig. 5: Schematic diagram of the effective potential, V_{eff}, and the photoelectron wave function below, on, and above the shape resonance energy, E_r, from Ref.

2. Note the localization of the photoelectron wave function behind the potential barrier at $E=E_r$. Also shown is the photoionization cross section for 3p photoionization of argon including experimental results and results from various levels of theory, from Ref. 19. Note the enhancement in the cross section around the shape resonant energy region near threshold.

Fig. 6: Calculated (velocity form) photoionization cross sections for the $3s\sigma_g \longrightarrow k\sigma_u$ transition of the C $^3\Pi_g$ state of O_2 at various internuclear distances.

Fig. 7: Calculated vibrational branching ratios for O_2 C $^3\Pi_g$ (v' = 1-3) photoionization compared to the measurements of Ref. 17. The theoretical results are normalized to the experimental results by dividing by the $\Delta v = 0$ peak.

Fig. 8: Calculated (dash curve) velocity form photoelectron angular distributions for the $v' = 3$ level of the C $^3\Pi_g$ state of O_2 along with the measurements of Ref. 21 (solid curve).

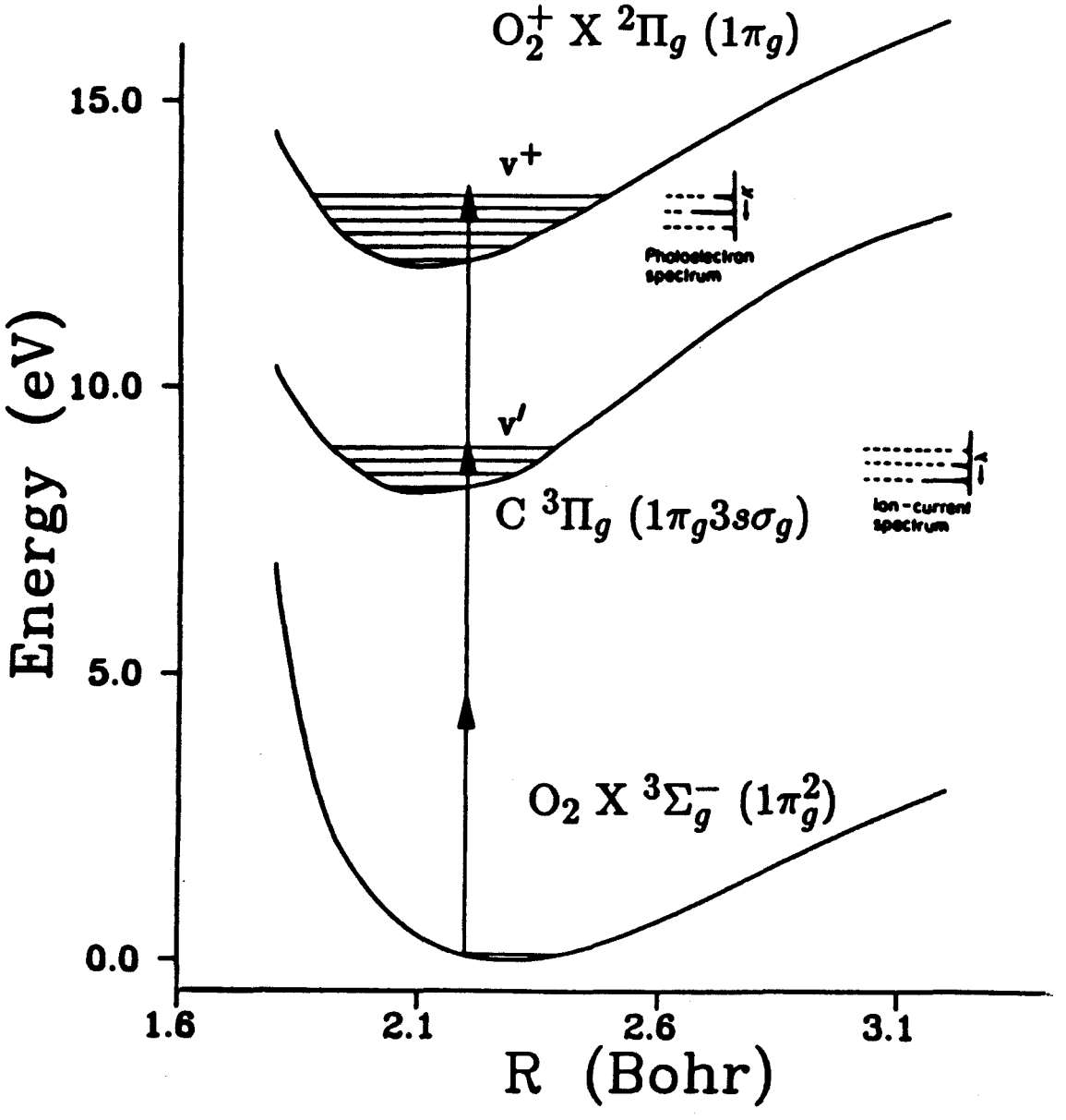
O_2^+ X $^2\Pi_g$ $(1\pi_g)$
15.0
v^+
Photoelectron spectrum
10.0
v'
C $^3\Pi_g$ $(1\pi_g 3s\sigma_g)$
Ion-current spectrum
5.0
O_2 X $^3\Sigma_g^-$ $(1\pi_g^2)$
0.0
Energy (eV)
1.6
2.1
2.6
3.1
R (Bohr)

Figure 1

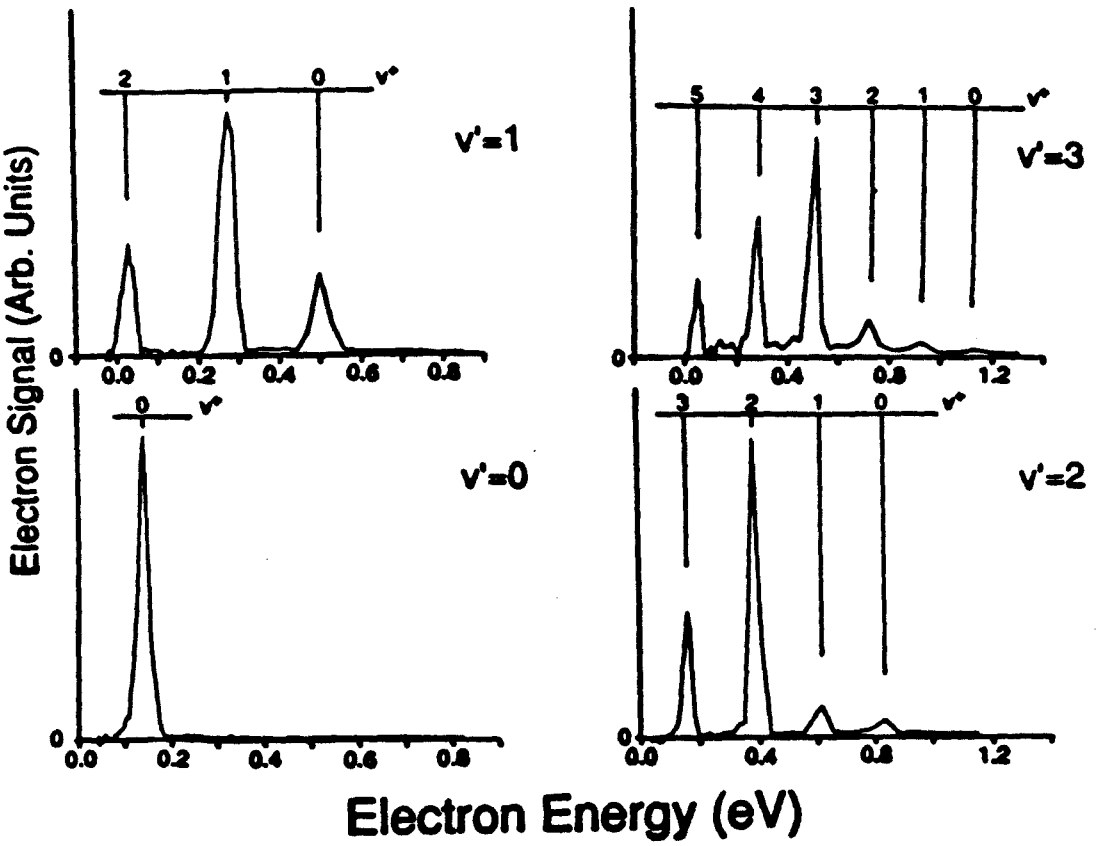
Electron Signal (Arb. Units)
v'=1
v'=3
v'=0
v'=2
Electron Energy (eV)

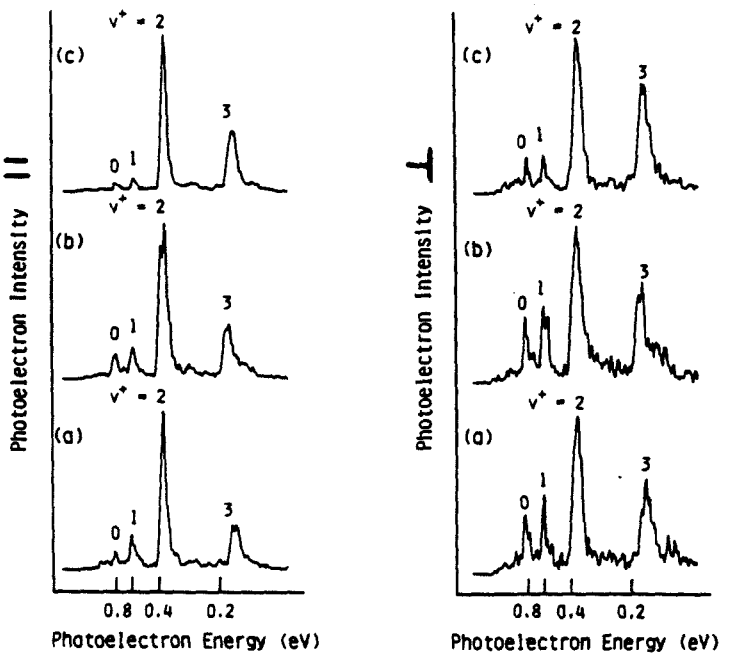
Photoelectron Intensity
Photoelectron Energy (eV)
Photoelectron Intensity
Photoelectron Energy (eV)

Figure 2

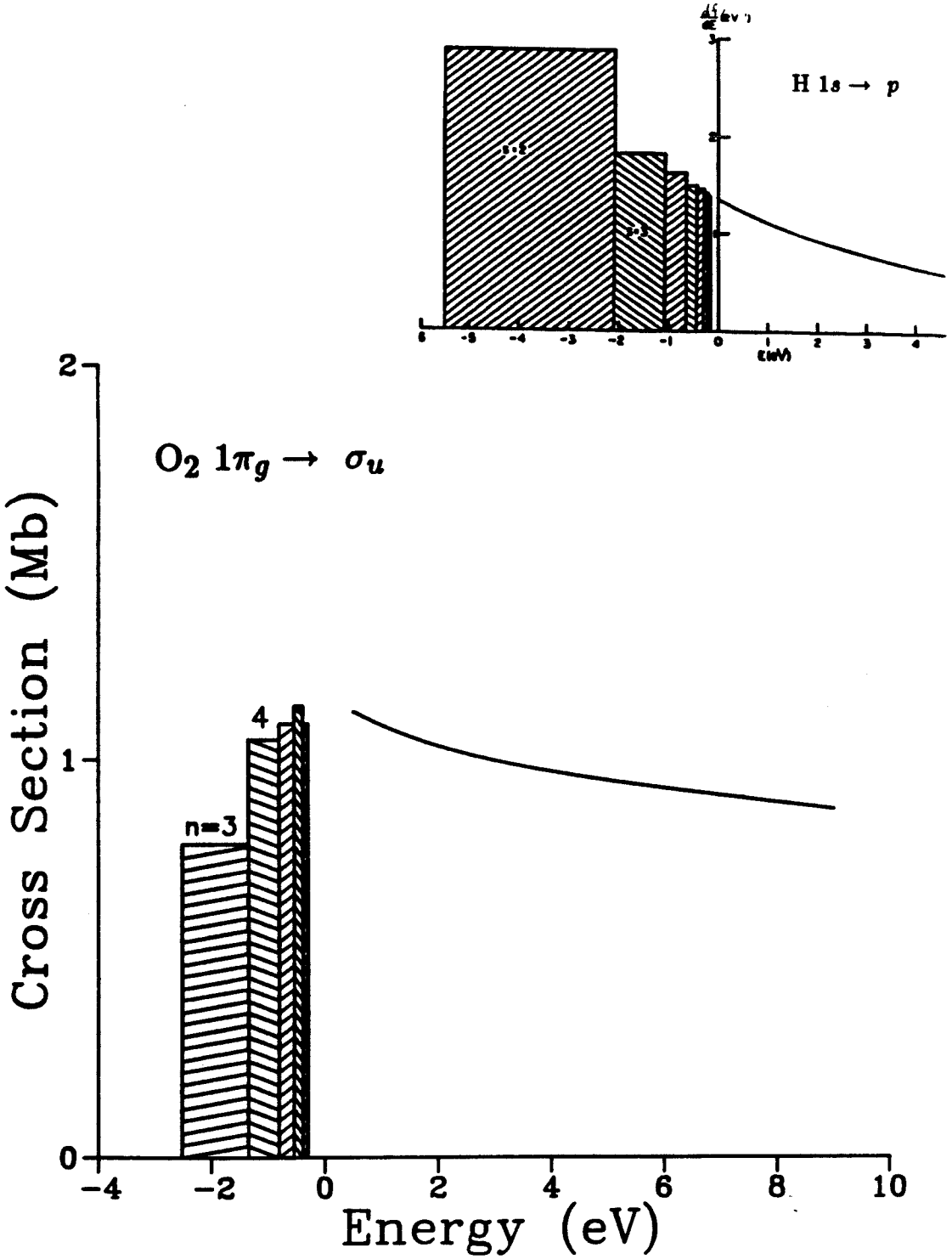

Figure 3

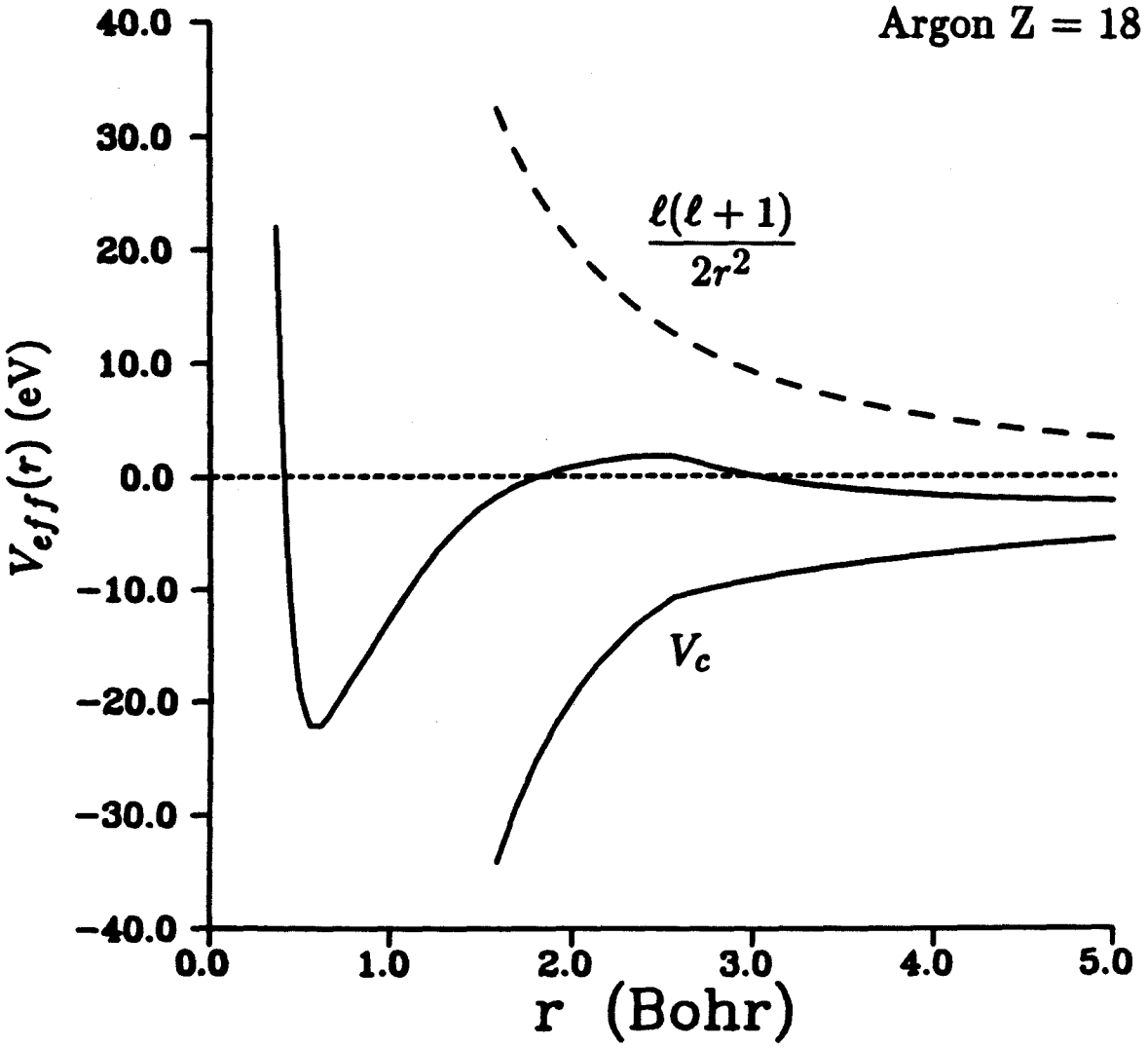
Argon Z = 18
40.0
30.0
20.0
10.0
0.0
−10.0
−20.0
−30.0
−40.0
$V_{eff}(r)$ (eV)
$\frac{\ell(\ell+1)}{2r^2}$
V_c
0.0
1.0
2.0
3.0
4.0
5.0
r (Bohr)

Figure 4

Figure 5

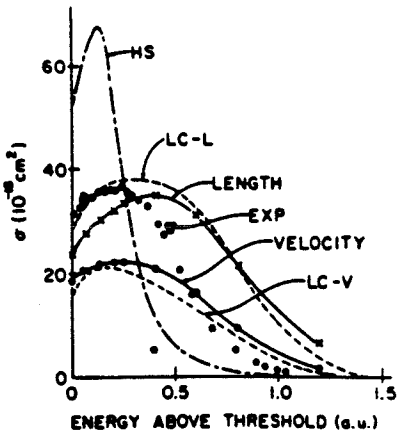

Argon $1s^2 2s^2 2p^6 3s^2 3p^6$

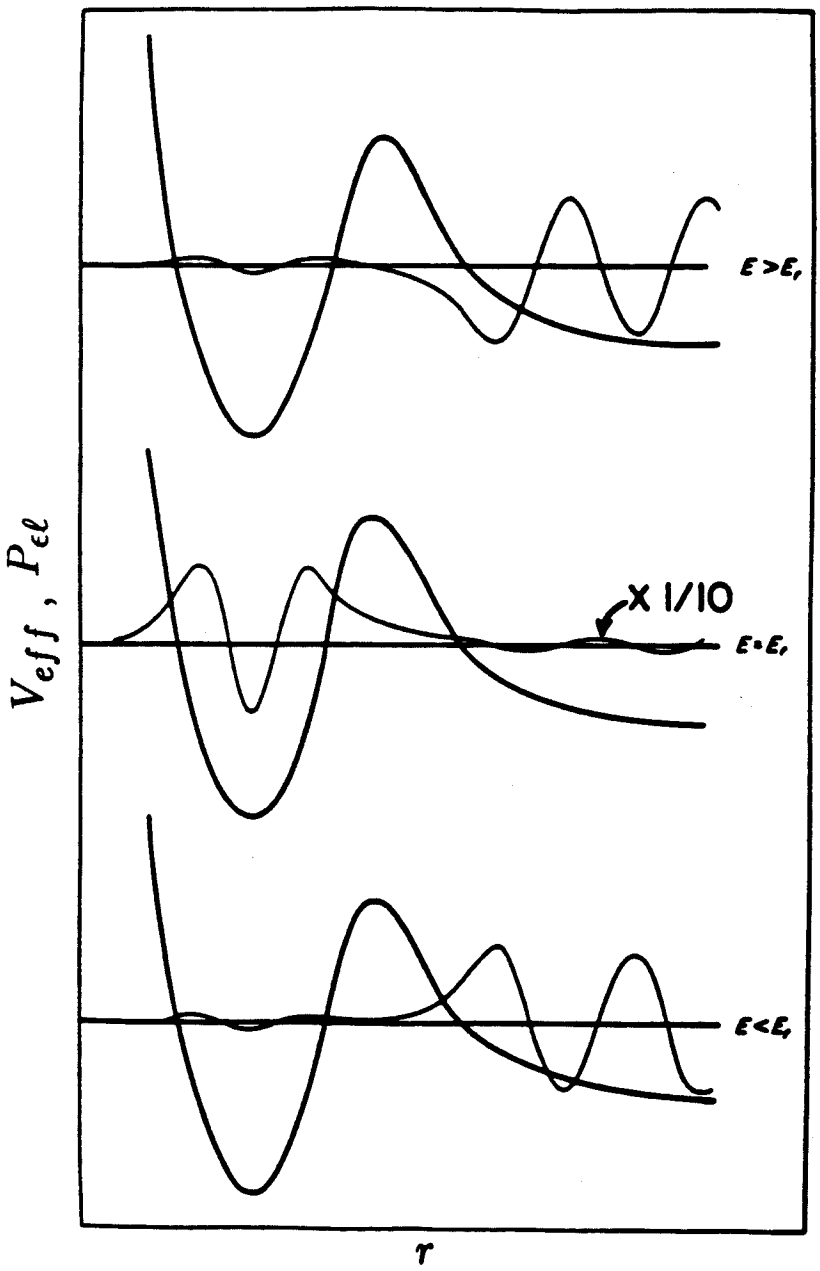

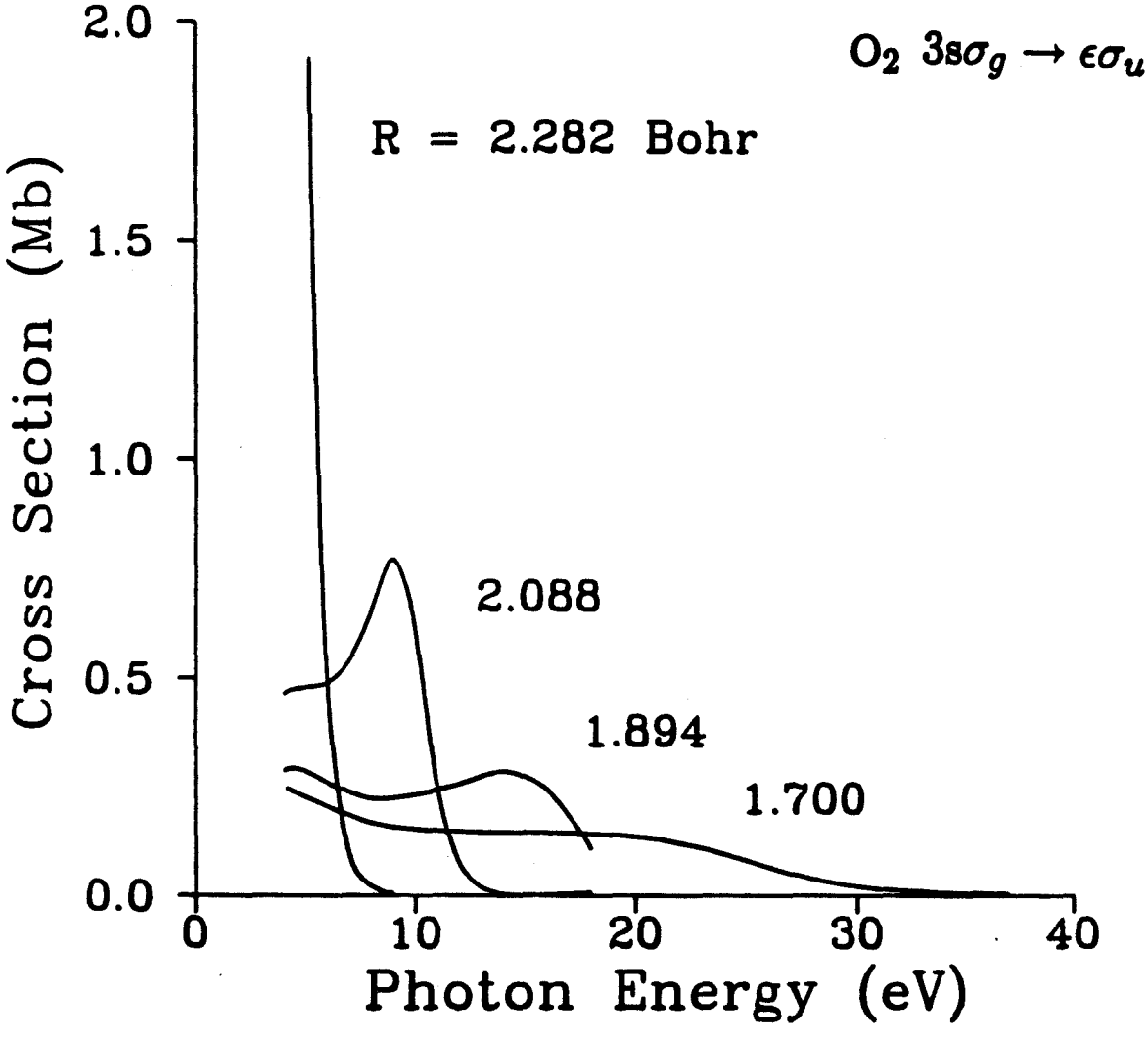
O_2 $3s\sigma_g \rightarrow \epsilon\sigma_u$
R = 2.282 Bohr
2.088
1.894
1.700
Cross Section (Mb)
2.0
1.5
1.0
0.5
0.0
0
10
20
30
40
Photon Energy (eV)

Figure 6

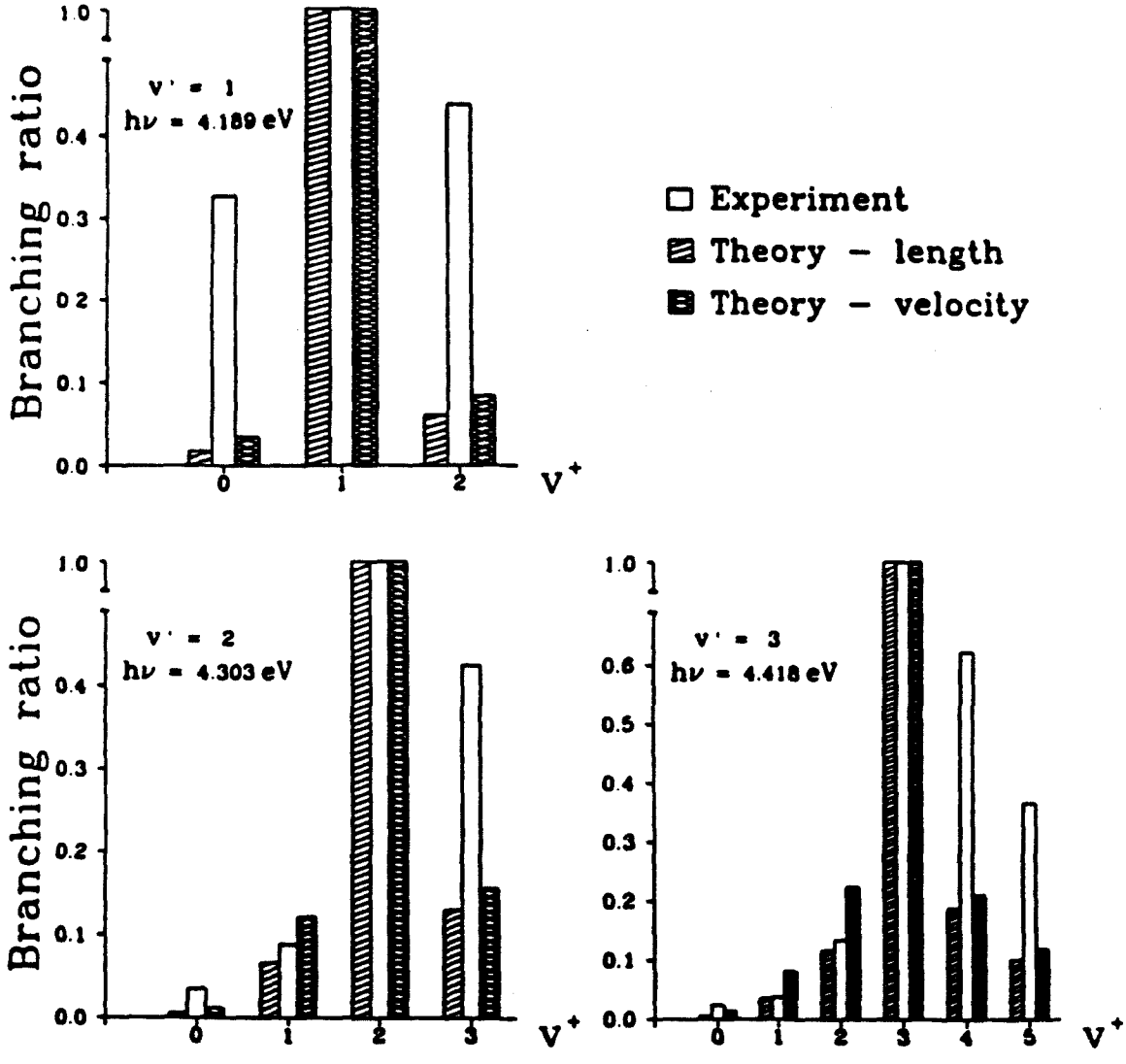
Branching ratio
v' = 1
hν = 4.189 eV
v' = 2
hν = 4.303 eV
v' = 3
hν = 4.418 eV
V+
Experiment
Theory – length
Theory – velocity

Figure 7

$v' = 3 \rightarrow v^+ = 3$

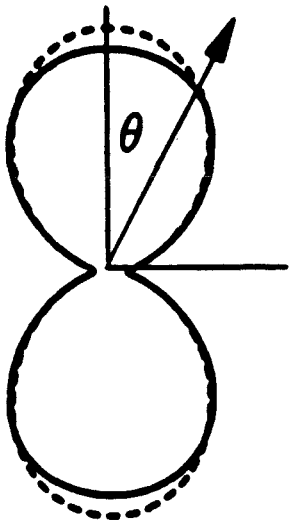

$v' = 3 \rightarrow v^+ = 2$

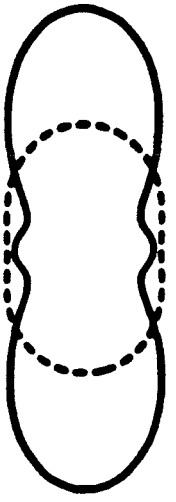

$v' = 3 \rightarrow v^+ = 4$

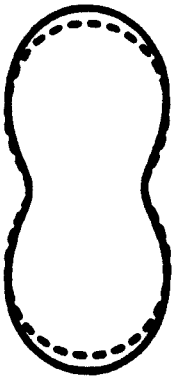

$v' = 3 \rightarrow v^+ = 1$

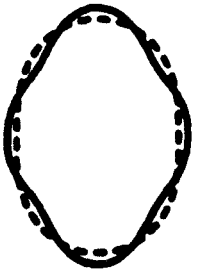

$v' = 3 \rightarrow v^+ = 5$

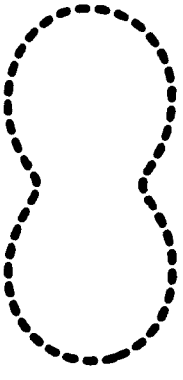

$v' = 3 \rightarrow v^+ = 0$

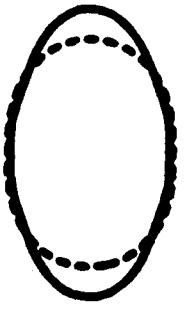

Figure 8

Chapter 1

Multiplet-specific shape resonant features in $3\sigma_g$ photoionization of O_2

(The text of this chapter appeared in: M. Braunstein, V. McKoy, and M. E. Smith, J. Chem. Phys. **90**, 3931 (1989).)

Multiplet-specific shape resonant features in $3\sigma_g$ photoionization of O_2

M. Braunstein and V. McKoy
A. A. Noyes Laboratory of Chemical Physics, California Institute of Technology, Pasadena, California 91125

Maile E. Smith
Institute for Defense Analysis, Alexandria, Virginia 22311

(Received 5 December 1988; accepted 21 December 1988)

We report multiplet-specific photoionization cross sections and photoelectron angular distributions for the $3\sigma_g$ orbital of O_2 leading to the $b\,^4\Sigma_g^-$ and $B\,^2\Sigma_g^-$ ion states obtained using Hartree–Fock photoelectron orbitals. These cross sections show significant nonstatistical behavior at low photoelectron energies which arises from the sensitivity of the $k\sigma_u$ shape resonance to the exchange potentials of these two molecular ions. Specifically, the oscillator strength associated with the shape resonance in the $B\,^2\Sigma_g^-$ cross section is shifted to lower energy compared to that of the $b\,^4\Sigma_g^-$ cross section. This shift gives rise to a quartet to doublet cross section ratio of more than 15:1 near threshold. These effects are difficult to assess in the measured cross sections due to the presence of strong autoionization features. Significant multiplet dependence is also seen in the calculated photoelectron angular distributions.

INTRODUCTION

Recent (2 + 1) resonant-enhanced multiphoton ionization (REMPI) studies via the $C\,^3\Pi_g(3s\sigma_g 1\pi_g)$ and $d\,^1\Pi_g(3s\sigma_g 1\pi_g)$ states of O_2 have shown significant differences in the photoelectron spectra for these two multiplets.[1,2] Strong multiplet-specific effects have also been observed in the 5σ photoionization of NO, where a difference of as much as 3 eV is seen in the positions of the shape resonance in the cross sections for the $A\,^1\Pi(5\sigma^{-1})$ and $b\,^3\Pi(5\sigma^{-1})$ ions.[3,4] These effects arise from differences in the exchange potentials experienced by the photoelectron associated with these multiplets. Such differences can be especially important in shape resonant regions due to the localized nature of the photoelectron wave function. With further development and application of REMPI techniques coupled with high resolution photoelectron spectroscopy,[5] such effects will become increasingly important in our understanding of molecular photoionization dynamics.

Studies of $3\sigma_g$ photoionization of O_2 by Winstead *et al.*[6] using an L^2 Feshbach–Fano formulation of Stieltjes moment theory and multiplet-specific potentials have shown significant nonstatistical behavior in the $b\,^4\Sigma_g^-$ and $B\,^2\Sigma_g^-$ cross sections at energies around the well known $k\sigma_u$ shape resonance.[7–13] Due to strong autoionizing features,[14] these differences are difficult to assess in the experimental photoelectron spectrum. However, recent high-resolution studies[14,15] clearly show multiplet-specific differences in these $3\sigma_g$ cross sections. To further examine these multiplet-specific effects, we have studied the photoionization cross sections and photoelectron angular distributions for the $3\sigma_g$ level of O_2 using Hartree–Fock photoelectron orbitals obtained with the iterative Schwinger method.[16] Our results for these cross sections agree well with those of Winstead *et al.*[6] and, furthermore, show large differences in the multiplet-specific photoelectron angular distributions.

An outline of the paper is as follows. In the next section we discuss the static-exchange potentials used in these multiplet-specific calculations and give a brief description of our method for obtaining the photoelectron orbitals. In the remaining sections we present the results of our studies of the $3\sigma_g$ level of O_2 along with a comparison of these results with experimental data.

THEORY

Multiplet-specific wave functions and potentials

Photoionization of the $3\sigma_g$ orbital of O_2 leads to the $b\,^4\Sigma_g^-$ and $B\,^2\Sigma_g^-$ ion states with experimental ionization potentials 18.17 and 20.29 eV respectively. The dipole-allowed final-state wave functions for photoionization leading to the $b\,^4\Sigma_g^-$ ion are

$$\Psi(^3\Sigma_u^-) = \frac{1}{\sqrt{12}}\big[3|(\text{core})3\sigma_g\,\overline{k\sigma_u}\,1\pi_g^+\,1\pi_g^-| - |(\text{core})\,\overline{3\sigma_g}k\sigma_u\,1\pi_g^+\,1\pi_g^-| - |(\text{core})3\sigma_g k\sigma_u\,\overline{1\pi_g^+}\,1\pi_g^-| - |(\text{core})3\sigma_g k\sigma_u\,1\pi_g^+\,\overline{1\pi_g^-}|\big], \tag{1a}$$

$$\Psi(^3\Pi_u) = \frac{1}{\sqrt{12}}\big[3|(\text{core})3\sigma_g\,\overline{k\pi_u^+}\,1\pi_g^+\,1\pi_g^-| - |(\text{core})\,\overline{3\sigma_g}k\pi_u^+\,1\pi_g^+\,1\pi_g^-| - |(\text{core})3\sigma_g k\pi_u^+\,\overline{1\pi_g^+}\,1\pi_g^-| - |(\text{core})3\sigma_g k\pi_u^+\,1\pi_g^+\,\overline{1\pi_g^-}|\big], \tag{1b}$$

where $(\text{core}) = 1\sigma_g^2 1\sigma_u^2 2\sigma_g^2 2\sigma_u^2 1\pi_u^4$. For photoionization leading to the $B\,^2\Sigma_g^-$ ion, the dipole-allowed final-state wave functions are

$$\Psi(^3\Sigma_u^-) = \frac{1}{\sqrt{6}}\left[2|(\text{core})\ \overline{3\sigma_g}\, k\sigma_u\, 1\pi_g^+\, 1\pi_g^-| - |(\text{core})3\sigma_g\, k\sigma_u\ \overline{1\pi_g^+}\, 1\pi_g^-| \right.$$
$$\left. - |(\text{core})3\sigma_g\, k\sigma_u\, 1\pi_g^+\ \overline{1\pi_g^-}|\right], \tag{2a}$$

$$\Psi(^3\Pi_u) = \frac{1}{\sqrt{6}}\left[2|(\text{core})\ \overline{3\sigma_g}\, k\pi_u^+\, 1\pi_g^+\, 1\pi_g^-| - |(\text{core})3\sigma_g\, k\pi_u^+\ \overline{1\pi_g^+}\, 1\pi_g^-| \right.$$
$$\left. - |(\text{core})3\sigma_g\, k\pi_u^+\, 1\pi_g^+\ \overline{1\pi_g^-}|\right]. \tag{2b}$$

With these wave functions, the static-exchange one-electron equations for the photoelectron orbital ϕ_k can be obtained from the variational expression, $\langle \delta\Psi|H - E|\Psi\rangle = 0$, where H is the fixed-nuclei Hamiltonian and E is the total energy. They are of the form

$$P\left[f + \sum_{\text{core}}(2J_i - K_i) + \sum_{\text{open}}(a_n J_n + b_n K_n) - \epsilon\right]P|\phi_k\rangle = 0, \tag{3}$$

where J_i and K_i are the Coulomb and exchange operators, respectively, P is a projection operator which enforces orthogonality of the continuum orbital to the occupied orbitals,[17] the one-electron operator f is given by

$$f = -1/2\nabla_i^2 - \sum_\alpha \frac{Z_\alpha}{r_{i\alpha}}, \tag{4}$$

Z_α is the nuclear charge, and ϵ is the photoelectron kinetic energy. The coefficients a_n and b_n of Eq. (3) determined using the multiplet-specific wave functions of Eqs. (1) and (2) are given in Table I.

Calculations

The photoelectron orbitals of the static-exchange equations of Eq. (3) were obtained using the iterative Schwinger variational method, discussed extensively elsewhere.[16,17] To solve the Lippmann–Schwinger equations for the continuum orbital associated with the nonlocal molecular ion potential of Eq. (3), the scattering potential is approximated by a separable form,

$$U(\mathbf{r},\mathbf{r}') \cong U^S(\mathbf{r},\mathbf{r}') = \sum_{ij}\langle \mathbf{r}|U|\alpha_i\rangle (U^{-1})_{ij}\langle \alpha_j|U|\mathbf{r}'\rangle, \tag{5}$$

where the matrix U^{-1} is the inverse of the matrix with elements $U_{ij} = \langle \alpha_i|U|\alpha_j\rangle$ and the α_i's are discrete basis functions (see Table II). To ensure convergence of the photoionization cross sections, we use photoelectron orbitals obtained after one step in our iterative procedure.[16,17]

For the ground state of O_2, we used the [3s2p1d] Cartesian Gaussian basis set of Dunning *et al.*[18] Calculations with this basis at the equilibrium geometry of $R(0-0) = 2.282$ a.u. give an SCF energy of $-149.635\ 14$ a.u.

TABLE I. Coefficients of the static-exchange potentials of Eq. (3).

		a_n/b_n		
Ion	Channel[a]	$3\sigma_g$	$1\pi_g^+$	$1\pi_g^-$
$b\,^4\Sigma_g^-$	$^3\Sigma_u^-(k\sigma_u)$	1/1	1/1	1/1
	$^2\Pi_u(k\pi_u)$	1/1	1/1	1/1
$B\,^2\Sigma_g^-$	$^3\Sigma_u^-(k\sigma_u)$	1/−1	1/−1	1/−1
	$^3\Pi_u(k\pi_u)$	1/−1	1/−1	1/−1

[a] Channel symmetry designation of the ion plus photoelectron system.

All matrix elements and functions arising in the solution of the Lippmann–Schwinger equations associated with Eq. (3) were evaluated via single-center expansions about the molecular center. The partial wave expansion of the photoelectron orbital, i.e.,

$$\phi_k^{(-)} = \left(\frac{2}{\pi}\right)^{1/2}\sum_{l=0}^{l_p}\sum_{m=-l}^{+l} i^l \phi_{klm}^{(-)}(\mathbf{r})\, Y_{lm}^*(\Omega_{\hat{k}}), \tag{6}$$

was truncated at $l_p = 7$. The other partial wave expansion parameters were chosen as follows[17]:

(i) maximum partial wave in the expansion of the occupied orbitals in the direct potential = 30,

(ii) maximum partial wave in the expansion of the occupied orbitals in the exchange potential = $20(1\sigma_g)$, $20(1\sigma_u)$, $10(2\sigma_g)$, $10(2\sigma_u)$, $10(3\sigma_g)$, $10(1\pi_u)$, $10(1\pi_g)$,

TABLE II. Scattering basis sets used in Eq. (5).

Continuum symmetry	Type of Gaussian function[a]	Exponents
σ_u	Cartesian s	16.0,8.0,4.0,2.0,1.0,0.5
	z	1.0,0.5
	Spherical $l=1$	4.0,2.0,1.0,0.5
	$l=3$	4.0,2.0,1.0,0.5
	$l=5$	1.0,0.5
π_u	Cartesian x	8.0,4.0,2.0,1.0,0.5
	Spherical xz	0.5
	$l=1$	1.0
	$l=3$	1.0

[a] Cartesian functions are centered at the nuclei and the spherical functions at the molecular center. For details of the forms of these functions and their use see Ref. 17.

(iii) maximum partial wave in the expansion of $1/r_{12}$ in the direct and exchange terms = 60 and 30, respectively,

(iv) all other partial wave expansions were truncated at $l = 30$.

Based on earlier convergence studies,[17] this choice of expansion parameters should provide photoionization cross sections within a few percent of the converged values. The associated radial integrals were obtained with a Simpson's rule quadrature. The grid contained 800 points and extended out to 64.0 a.u. with a step size of 0.01 a.u. from the origin to 2.0 a.u. Beyond 2.0 a.u. the largest step size was 0.16 a.u.

RESULTS AND DISCUSSION

Figure 1 shows the calculated eigenphase sums for the $k\sigma_u$ continuum for the two ion cores. These multiplet-specific eigenphase sums are quite different. The $b\,^4\Sigma_g^-$ eigenphase sum illustrates shape resonance behavior with a rapid increase starting at threshold. The $B\,^2\Sigma_g^-$ eigenphase sum also shows shape resonant behavior, but this behavior suggests that the discrete oscillator strength distribution below this threshold must be perturbed. Studies by Morin *et al.*[14] show significant Rydberg–valence mixing for the low members of the $np\sigma_u$ series leading to the $B\,^2\Sigma_g^-$ ion. To examine this effect on the discrete spectrum we have calculated the oscillator strengths for the first four members of this Rydberg series. The oscillator strength f_n is given by

$$f_n = 4/9E\,|\langle\phi(3\sigma_g)|z|n\sigma_u\rangle|^2. \qquad (7)$$

The factor of 4/9 is due to the multiplicity of the final state ion and E is the excitation energy in a.u. The $np\sigma_u$ orbitals were obtained using the improved virtual orbital (IVO) approximation[19] with our SCF basis augmented by a set of p functions with exponents of 0.1, 0.05, 0.025, 0.001 25, and 0.000 625 at the molecular center. Figure 2 shows the resulting oscillator strength in histogram form for the $n\sigma_u$ Rydberg series of the $B\,^2\Sigma_g^-$ ion and the adjoining $k\sigma_u$ continuum cross section. The height and width of each step in the histogram are $f_n\,(dn/dE)$ and dE/dn, respectively.[20] These results show that the σ_u spectral distribution for the $B\,^2\Sigma_g^-$ state is strongly perturbed below threshold. Our calculated discrete spectrum agrees qualitatively with the results of Winstead *et al.*[6] obtained with a more extensive basis set.

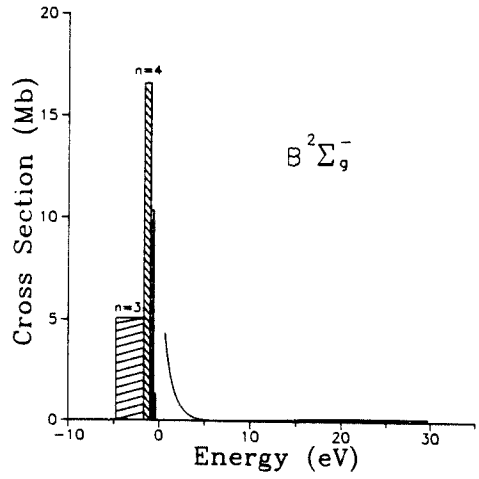

FIG. 2. Oscillator strength distribution in the discrete and continuous spectra for the $3\sigma_g \rightarrow \sigma_u$ transition. The energy scale is relative to the ionization threshold of 20.29 eV.

In Fig. 3 we show our calculated $3\sigma_g$ photoionization cross sections along with those of Winstead *et al.*[6] leading to the $b\,^4\Sigma_g^-$ (IP = 18.17 eV) and $B\,^2\Sigma_g^-$ (IP = 20.29 eV) ions. The behavior near threshold in the cross sections for

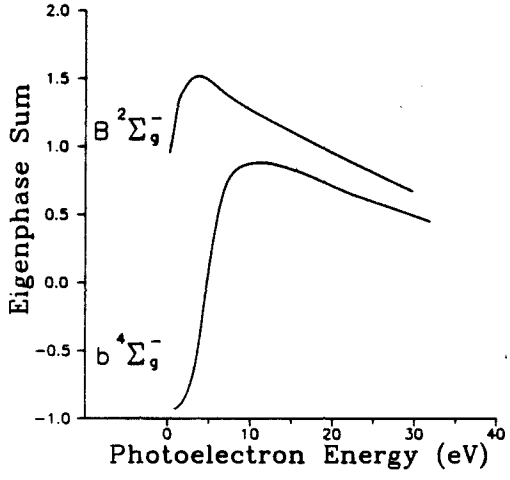

FIG. 1. Multiplet-specific eigenphase sums for the resonant $3\sigma_g \rightarrow k\sigma_u$ channel leading to the $b\,^4\Sigma_g^-$ $(3\sigma_g^{-1})$ and $B\,^2\Sigma_g^-$ $(3\sigma_g^{-1})$ ion states of O_2^+.

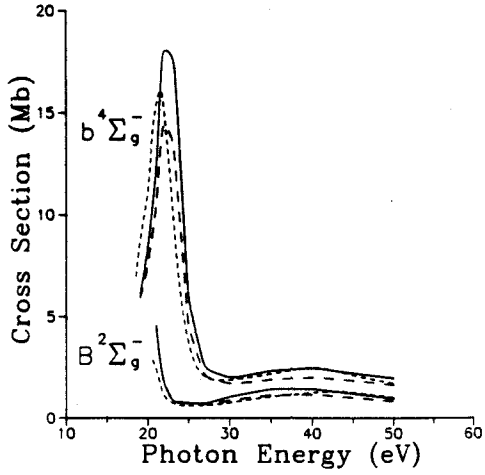

FIG. 3. Multiplet-specific cross sections for the $b\,^4\Sigma_g^-$ and $B\,^2\Sigma_g^-$ states of O_2^+:—and – –, present results in the dipole length and velocity forms, respectively; - - - Feshbach–Fano Stieltjes moment theory multiplet-specific results of Ref. 6.

each ion is due to the σ_u shape resonance seen in the associated eigenphase sums in Fig. 1. The weak maximum at higher energy in these cross sections arises from the energy dependence of the nonresonant $k\pi_u$ channel. These results show significant nonstatistical behavior near threshold, with the resonance maximum for the $b\,^4\Sigma_g^-$ state at a photoelectron energy of about 4 eV and the oscillator strength for the $B\,^2\Sigma_g^-$ cross section significantly shifted toward threshold. This behavior in the oscillator strength leads to a ratio of the quartet to doublet photoionization cross sections of over 15:1 just below 25 eV photon energy as shown in Fig. 4. These large deviations from statistical behavior are obviously not seen in studies with a multiplet-averaged potential which give a resonance position of ~3.5 eV above threshold for both ions.[7-10] At higher energies our results are in good agreement with these studies[7-10] and show the expected 2:1 statistical ratio.

In Fig. 5 we compare our calculated $b\,^4\Sigma_g^-$ and $B\,^2\Sigma_g^-$ cross sections with the experimental data of Gustaffson.[13] At low photoelectron energy, the experimental cross sections are dominated by an autoionizing window resonance at ~21 eV involving Rydberg states leading to the $c\,^4\Sigma_u^-$ ion (IP = 24.5 eV)[13] and the $k\sigma_u$ shape resonant background. Higher resolution work shows this autoionizing structure at low energy in more detail,[14,15] as well as additional structure in the $b\,^4\Sigma_g^-$ cross section arising from Rydberg levels leading to the $B\,^2\Sigma_g^-$ ion.[14] In fact, a window resonance appears at nearly the same energy as the peak of the shape resonance in our calculated $b\,^4\Sigma_g^-$ cross section[14] and in the region of rapid increase in our calculated $B\,^2\Sigma_g^-$ cross section.[14,15] Although this autoionizing structure hinders a simple "assignment" of the shape resonance feature in the two multiplet cross sections, these high resolution studies show relatively broad shape resonance features at significantly different photoelectron energies for the two ions. The high resolution

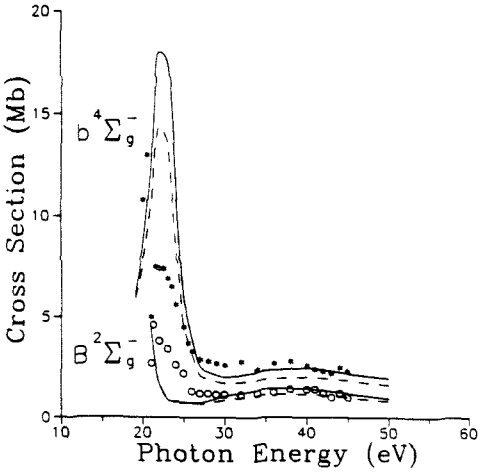

FIG. 5. Photoionization cross sections for the $b\,^4\Sigma_g^-$ and $B\,^2\Sigma_g^-$ states of O_2^+: — and – –, present results in the dipole length and velocity forms, respectively; •, experimental results of Ref. 13 for the $b\,^4\Sigma_g^-$ state; O, experimental results of Ref. 13 for the $B\,^2\Sigma_g^-$ state.

study of Morin *et al.*[14] shows a maximum in the cross section at 21.5 eV photon energy or about 3.5 eV kinetic energy for the $b\,^4\Sigma_g^-$ ion. The $B\,^2\Sigma_g^-$ cross section peaks at about 1 eV above threshold.[14,15] This can be seen more clearly in Fig. 6 which shows the $B\,^2\Sigma_g^-$ cross section on an expanded energy scale near threshold. Assignment of this maximum is hindered by the difficulty of obtaining accurate measurements at very low photoelectron energies.[15] Clearly, however, there is no shape resonant maximum in the $B\,^2\Sigma_g^-$ cross sections at 23 eV photon energy, as seen in previous theoretical studies using multiplet-averaged potentials.[7-10]

Figure 7 shows our calculated photoelectron asymme-

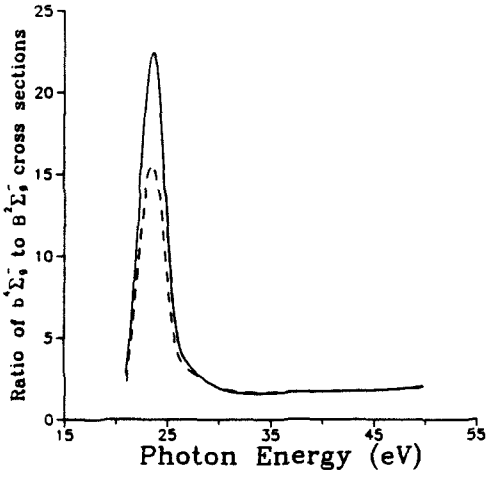

FIG. 4. Ratio of the calculated $b\,^4\Sigma_g^-$ cross section to the $B\,^2\Sigma_g^-$ cross section: — and – –, present results in the dipole length and velocity forms, respectively.

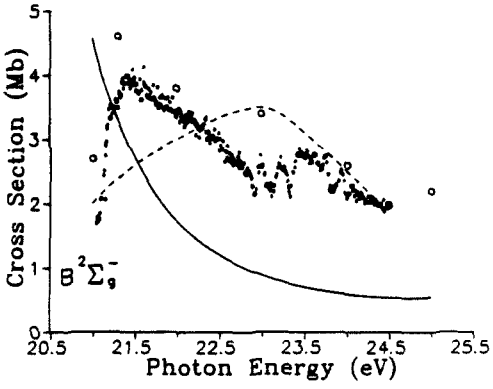

FIG. 6. Photoionization cross sections for the $B\,^2\Sigma_g^-$ state of O_2^+ near threshold: —, present results (length); - - -, calculated static-exchange vibrationally averaged results of Ref. 9 using a multiplet-averaged potential; O, experimental results of Ref. 13. The dots are the experimental total cross sections from Fig. 2 of Ref. 14. The structure at ~23 eV arises from autoionization as discussed in Refs. 14 and 15.

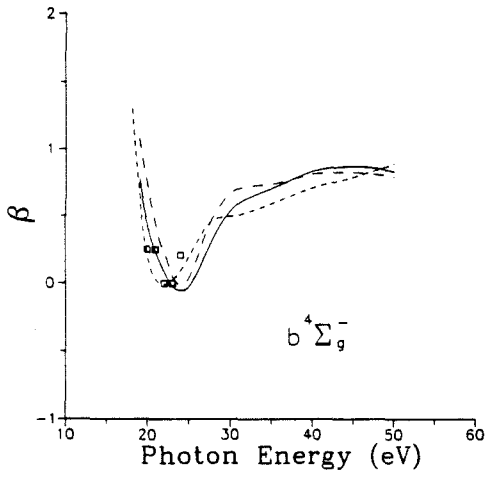

FIG. 7. Photoelectron asymmetry parameters for the $b\,^4\Sigma_g^-$ state of O_2^+: — and – –, present results in the dipole length and velocity forms, respectively; - - -, MSM calculations of Ref. 10 using a multiplet-averaged potential; □, experimental results of Ref. 21.

try parameters for the $b\,^4\Sigma_g^-$ state along with the data of Holmes *et al.*[21] and the multiple scattering model (MSM) calculations of Dittman *et al.*[10] using a multiplet-averaged potential. Both calculations are in good agreement with experiment and show a dip in the asymmetry parameter at roughly the resonance position of Fig. 3. In Fig. 8 we compare our calculated photoelectron asymmetry parameters for the $B\,^2\Sigma_g^-$ state with the results of MSM calculations of Dittman *et al.*[10] With the multiplet-averaged potential used in the MSM calculations the $B\,^2\Sigma_g^-$ asymmetry parameter is similar to that of the $b\,^4\Sigma_g^-$ state. The large differences between our results and the multiplet-averaged calculations of Dittman *et al.*[10] arise primarily from our use of a multiplet-specific potential and the resulting shift in the oscillator strength as discussed above. In Fig. 9 we show our calculated photoelectron asymmetry parameters for the $b\,^4\Sigma_g^-$ and $B\,^2\Sigma_g^-$ states to more clearly illustrate the large predicted multiplet-specific differences in β. Katsumata *et al.*[22] have reported values of 0.58 ± 0.06 and 1.05 ± 0.06 for β for the $b\,^4\Sigma_g^-$ ($v^+ = 0$) and $B\,^2\Sigma_g^-$ ($v^+ = 1$) ions respectively at the He I line (21.2 eV). Although these measurements cannot be directly compared to the present vibrationally unresolved results, they do show the same large qualitative differences between the quartet and doublet asymmetry parameters as seen in the present work. Continuum source measurements could provide considerable insight into the multiplet-specific behavior of these photoelectron angular distributions.

CONCLUSIONS

We have calculated photoionization cross sections and photoelectron angular distributions for the $3\sigma_g$ level of O_2 using Hartree–Fock photoelectron orbitals obtained with multiplet-specific potentials. These cross sections for the $b\,^4\Sigma_g^-$ and $B\,^2\Sigma_g^-$ ions show highly nonstatistical behavior arising from the sensitivity of the $k\sigma_u$ shape resonance to the exchange components of the different ion potentials seen by the photoelectron. Specifically, the oscillator strength associated with the σ_u shape resonance for the $B\,^2\Sigma_g^-$ ion is shifted to lower energy compared to that of the $b\,^4\Sigma_g^-$ cross section which peaks at ~4 eV above threshold. Our calculated cross sections agree well with the multiplet-specific Feshbach–Fano Stieltjes moment theory results of Winstead *et al.*[6] Previous theoretical studies using a multiplet-averaged potential could not distinguish such differences between the doublet and quartet photoelectron orbitals and

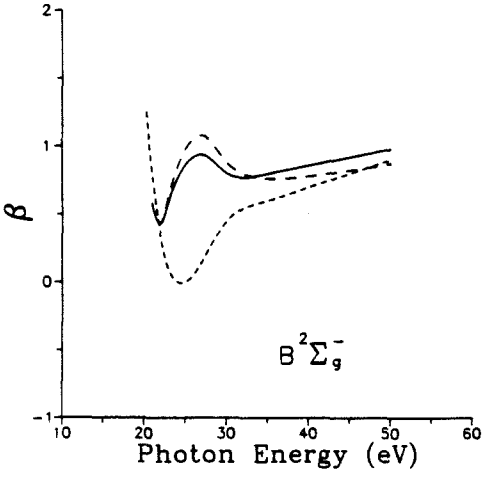

FIG. 8. Photoelectron asymmetry parameters for the $B\,^2\Sigma_g^-$ state of O_2^+: — and – –, present results in the dipole length and velocity forms, respectively; - - -, MSM calculations of Ref. 10 using a multiplet-averaged potential.

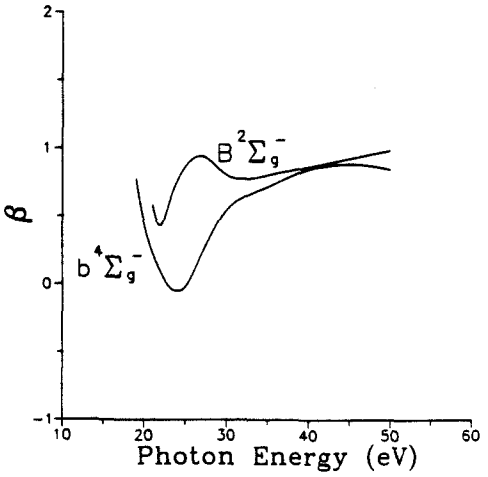

FIG. 9. Multiplet-specific photoelectron asymmetry parameters (length) for the $b\,^4\Sigma_g^-$ and $B\,^2\Sigma_g^-$ states of O_2^+.

hence led to a resonance peak at ~3.5 eV photoelectron kinetic energy for both ions.[7-10] Although autoionization structure complicates the photoelectron spectrum at low energy, high resolution experimental results do show that the σ_u shape resonance for the $B\,^2\Sigma_g^-$ ion appears much closer to threshold than that for the $b\,^4\Sigma_g^-$ ion.[14,15] These multiplet-specific effects are also seen in the photoelectron angular distributions where our results show substantial differences from the multiplet-averaged results of Dittman *et al.*[10] for the $B\,^2\Sigma_g^-$ ion in the shape resonance region. Continuum source measurements of the photoelectron angular distributions for the $B\,^2\Sigma_g^-$ ion would provide insight into such multiplet-specific effects. Above the shape resonance region our results agree well with previous calculations[7-10] as well as experimental results[11-13] and show the expected 2:1 statistical ratio.

ACKNOWLEDGMENTS

This work is supported by the National Science Foundation under Grant No. CHE8521391. The authors acknowledge use of the resources of the San Diego SuperComputer. The authors also thank Dr. C. L. Winstead for bringing the Feshbach–Fano Stieltjes moment theory results of his Ph.D. thesis to our attention.

[1]P. J. Miller and W. A. Chupka (private communication).
[2]J. A. Stephens, M. Braunstein, and V. McKoy (to be published).
[3]M. E. Smith, V. McKoy, and R. R. Lucchese, J. Chem. Phys. **82**, 4147 (1985).
[4]M. R. Hermann, C. W. Bauschlicher, Jr., W. M. Huo, S. R. Langhoff, and P. W. Langhoff, Chem. Phys. **109**, 1 (1986).
[5]P. M. Dehmer, J. L. Dehmer, and S. T. Pratt, Comments At. Mol. Phys. **19**, 205 (1987).
[6]C. L. Winstead *et al.* (to be published); see also C. L. Winstead, Ph.D. thesis, Indiana University, 1987.
[7]P. W. Langhoff, A. Gerwer, C. Asaro, and B. V. McKoy, Int. J. Quantum Chem. Symp. **13**, 645 (1979).
[8]A. Gerwer, C. Asaro, B. V. McKoy, and P. W. Langhoff, J. Chem. Phys. **72**, 713 (1980).
[9]G. Raseev, H. Lefebvre-Brion, H. Le Rouzo, and L. A. Roche, J. Chem. Phys. **74**, 6686 (1981).
[10]P. M. Dittman, D. Dill, and J. L. Dehmer, J. Chem. Phys. **76**, 5703 (1982).
[11]C. E. Brion, K. H. Tan, M. J. van der Wiel, and Ph. E. van der Leeuw, J. Electron Spectrosc. Relat. Phenom. **17**, 101 (1979).
[12]J. A. R. Samson, J. L. Gardner, and G. N. Haddad, J. Electron Spectrosc. Relat. Phenom. **12**, 281 (1977).
[13]T. Gustaffson, Chem. Phys. Lett. **75**, 505 (1980).
[14]P. Morin, I. Nenner, M. Y. Adams, M. J. Hubin-Franskin, J. Delwiche, H. Lefebvre-Brion, and A. Giusti-Suzor, Chem. Phys. Lett. **92**, 609 (1982).
[15]M. Ukai, A. Kimura, S. Arai, P. Lablanquie, K. Ito, and A. Yagishita, Chem. Phys. Lett. **135**, 51 (1987).
[16]R. R. Lucchese, K. Takatsuka, and V. McKoy, Phys. Rep. **131**, 147 (1986).
[17]R. R. Lucchese, G. Raseev, and V. McKoy, Phys. Rev. A **25**, 2572 (1982).
[18]T. H. Dunning and P. J. Hay, in *Modern Theoretical Chemistry*, edited by H. F. Schaefer III (Plenum, New York, 1976), Vol. 3, Chap. 1.
[19]W. J. Hunt and W. A. Goddard III, Chem. Phys. Lett. **3**, 414 (1969).
[20]U. Fano and J. W. Cooper, Rev. Mod. Phys. **40**, 441 (1968).
[21]R. M. Holmes and G. V. Marr, J. Phys. B **13**, 945 (1980).
[22]S. Katsumata, Y. Achiba, and K. Kimura, J. Electron Spectrosc. Relat. Phenom. **17**, 229 (1979).

Chapter 2

Photoionization of the $1\pi_u$ orbital of O_2

Photoionization of the $1\pi_u$ orbital of O_2

M. Braunstein and V. McKoy

Arthur Amos Noyes Laboratory of Chemical Physics

California Institute of Technology

Pasadena, California 91125

M. E. Smith

Institute for Defense Analysis

Alexandria, Virginia 22311

Abstract

We report multiplet-specific cross sections and photoelectron angular distributions for photoionization of the $1\pi_u$ orbital of O_2 leading to the a $^4\Pi_u$, A $^2\Pi_u$ and III $^2\Pi_u$ ions using Hartree-Fock photoelectron orbitals. Unlike $3\sigma_g$ photoionization of O_2 which also leads to quartet and doublet ions, the $1\pi_u$ cross sections show mainly statistical behavior. This reflects the fact that the photoelectron continuum is non-resonant and largely insensitive to differences in the exchange potentials between the doublet and quartet ions. The well-known mixed nature of the doublet states is accounted for by weighting the doublet transition moments by the contribution of the ground state parentage ion to the final mixed ion state. Comparison with experimental data for the a $^4\Pi_u$ ion is made. Although experimental data on the doublet states are fragmentary, comparison with the present results is encouraging.

I. Introduction

Recent studies of 5σ photoionization of NO leading to the b $^3\Pi$ and A $^1\Pi$ ions[1-3] and $3\sigma_g$ photoionization of O_2 leading to the b $^4\Sigma_g^-$ and B $^2\Sigma_g^-$ ions[4-6] have shown that multiplet photoionization cross sections can deviate substantially from the expected statistical ratio. These mulitplet-specific effects arise from differences in the exchange potentials of the final ion states and are especially important in shape-resonant regions due to the localized nature of the photoelectron wave function. Previous studies have suggested shape-resonant behavior in the $1\pi_u$ photoionization of O_2,[7,8] which leads to doublet and quartet ions. To further examine such behavior in producing non-statistical effects, we have calculated mulitplet-specific photoionization cross sections and photoelectron angular distributions for the $1\pi_u$ orbital of O_2 leading to the a $^4\Pi_u$, A $^2\Pi_u$ and III $^2\Pi_u$ ions. We use the notation[9] III $^2\Pi_u$ to refer to the diffuse band seen at ~24 eV in the photoelectron spectrum and previously assigned $^2\Pi_u$.[10-12]

It is well-known that the doublet ions are heavily mixed states and can be described by a basis of three principal $^2\Pi_u$ configurations.[9,13-15] In the notation of Ref. 14,

$$|^2\Pi_{ui}(\mathrm{A}\ ^2\Pi_u, \mathrm{II}\ ^2\Pi_u, \mathrm{III}\ ^2\Pi_u)\rangle = c_{1i}|^2\Pi_u(1)\rangle + c_{2i}|^2\Pi_u(2)\rangle + c_{3i}|^2\Pi_u(3)\rangle, \quad (1)$$

where $^2\Pi_u(1)$, $^2\Pi_u(2)$, and $^2\Pi_u(3)$ correspond to ion states of $^1\Sigma_g^+$, $^3\Sigma_g^-$, and $^1\Delta_g$ parentages, respectively. Only final-state configurations built on the $^2\Pi_u(2)$ ion, which is of $^3\Sigma_g^-$ (ground state) parentage, are dipole-allowed. In the present work, the transition moments for photoionization leading to the A $^2\Pi_u$ and III $^2\Pi_u$ states are calculated with the potential corresponding to the ground state parentage ion, $^2\Pi_u(2)$. The transition moments are then weighted by c_{2i}, the contribution of

the ground state parentage ion to the final mixed ion state, as determined from a configuration-interaction calculation. The theoretically predicted II $^2\Pi_u$ ion (I.P. ~20 eV),[9,13-15] has essentially zero contribution from the basis configuration of $^3\Sigma_g^-$ parentage, $^2\Pi_u(2)$, and has not been observed experimentally.

An outline of the paper is as follows. In the next section we discuss the static-exchange potentials used in these multiplet-specific calculations and give a brief description of our method for obtaining the photoelectron orbitals. In Section III we present the results of our studies along with a comparison to experimental data.

II. Method and Calculations

Photoionization of the $1\pi_u$ orbital of O_2 leads to two ion states with ground state ($^3\Sigma_g^-$) parentage: the a $^4\Pi_u$ and $^2\Pi_u(2)$ states. The dipole-allowed final state wave functions for photoionization leading to the a $^4\Pi_u$ ion are

$$\Psi(^3\Pi_u) = \frac{1}{\sqrt{12}}\{3|1\pi_u^+\,\overline{1\pi_u}^+\,1\pi_u^-\,\overline{k\sigma_g}\,1\pi_g^+\,1\pi_g^-| - |1\pi_u^+\,\overline{1\pi_u}^+\,\overline{1\pi_u}^-\,k\sigma_g\,1\pi_g^+\,1\pi_g^-|$$

$$-|1\pi_u^+\,\overline{1\pi_u}^+\,1\pi_u^-\,k\sigma_g\,\overline{1\pi_g}^+\,1\pi_g^-| - |1\pi_u^+\,\overline{1\pi_u}^+\,1\pi_u^-\,k\sigma_g\,1\pi_g^+\,\overline{1\pi_g}^-|\}, \qquad (2a)$$

$$\Psi(^3\Sigma_u^-) = \frac{1}{\sqrt{24}}\{3|1\pi_u^+\,\overline{1\pi_u}^+\,\pi_u^-\,\overline{k\pi_g}^-\,1\pi_g^+\,1\pi_g^-| - |1\pi_u^+\,\overline{1\pi_u}^+\,\overline{1\pi_u}^-\,k\pi_g^-\,1\pi_g^+\,1\pi_g^-|$$

$$-|1\pi_u^+\,\overline{1\pi_u}^+\,1\pi_u^-\,k\pi_g^-\,\overline{1\pi_g}^+\,1\pi_g^-| - |1\pi_u^+\,\overline{1\pi_u}^+\,1\pi_u^-\,k\pi_g^-\,1\pi_g^+\,\overline{1\pi_g}^-|$$

$$+3|1\pi_u^-\,\overline{1\pi_u}^-\,1\pi_u^+\,\overline{k\pi_g}^+\,1\pi_g^+\,1\pi_g^-| - |1\pi_u^-\,\overline{1\pi_u}^-\,\overline{1\pi_u}^+\,k\pi_g^+\,1\pi_g^+\,1\pi_g^-|$$

$$-|1\pi_u^-\,\overline{1\pi_u}^-\,1\pi_u^+\,k\pi_g^+\,\overline{1\pi_g}^+\,1\pi_g^-| - |1\pi_u^-\,\overline{1\pi_u}^-\,1\pi_u^+\,k\pi_g^+\,1\pi_g^+\,\overline{1\pi_g}^-|\}, \qquad (2b)$$

$$\Psi(^3\Pi_u) = \frac{1}{\sqrt{12}}\{3|1\pi_u^- \overline{1\pi_u^-}\, 1\pi_u^+ \overline{k\delta_g^+}\, 1\pi_g^+ 1\pi_g^-| - |1\pi_u^- \overline{1\pi_u^-}\, \overline{1\pi_u^+}\, k\delta_g^+ 1\pi_g^+ 1\pi_g^-|$$

$$-|1\pi_u^- \overline{1\pi_u^-}\, 1\pi_u^+ k\delta_g^+ \overline{1\pi_g^+}\, 1\pi_g^-| - |1\pi_u^- \overline{1\pi_u^-}\, 1\pi_u^+ k\delta_g^+ 1\pi_g^+ \overline{1\pi_g^-}|\}, \qquad (2c)$$

where we include implicitly the closed-shell core. For photoionization leading to the $^2\Pi_u(2)$ ion, the dipole-allowed final state wave functions are

$$\Psi(^3\Pi_u) = \frac{1}{\sqrt{6}}\{2|1\pi_u^+ \overline{1\pi_u^+}\, \overline{1\pi_u^-}\, k\sigma_g 1\pi_g^+ 1\pi_g^-| - |1\pi_u^+ \overline{1\pi_u^+}\, 1\pi_u^-\, k\sigma_g 1\pi_g^+ \overline{1\pi_g^-}|$$

$$-|1\pi_u^+ \overline{1\pi_u^+}\, 1\pi_u^-\, k\sigma_g \overline{1\pi_g^+}\, 1\pi_g^-|\}, \qquad (3a)$$

$$\Psi(^3\Sigma_u^-) = \frac{1}{\sqrt{12}}\{2|1\pi_u^+ \overline{1\pi_u^+}\, \overline{1\pi_u^-}\, k\pi_g^- 1\pi_g^+ 1\pi_g^-| - |1\pi_u^+ \overline{1\pi_u^+}\, 1\pi_u^-\, k\pi_g^- 1\pi_g^+ \overline{1\pi_g^-}|$$

$$-|1\pi_u^+ \overline{1\pi_u^+}\, 1\pi_u^-\, k\pi_g^- \overline{1\pi_g^+}\, 1\pi_g^-| + 2|1\pi_u^- \overline{1\pi_u^-}\, \overline{1\pi_u^+}\, k\pi_g^+ 1\pi_g^+ 1\pi_g^-|$$

$$-|1\pi_u^- \overline{1\pi_u^-}\, 1\pi_u^+ k\pi_g^+ 1\pi_g^+ \overline{1\pi_g^-}| - |1\pi_u^- \overline{1\pi_u^-}\, 1\pi_u^+ k\pi_g^+ \overline{1\pi_g^+}\, 1\pi_g^-|\}, \qquad (3b)$$

$$\Psi(^3\Pi_u) = \frac{1}{\sqrt{6}}\{2|1\pi_u^- \overline{1\pi_u^-}\, \overline{1\pi_u^+}\, k\delta_g^+ 1\pi_g^+ 1\pi_g^-| - |1\pi_u^- \overline{1\pi_u}\, 1\pi_u^+ k\delta_g^+ 1\pi_g^+ \overline{1\pi_g^-}|$$

$$-|1\pi_u^- \overline{1\pi_u^-}\, 1\pi_u^+ k\delta_g^+ \overline{1\pi_g^+}\, 1\pi_g^-|\}. \qquad (3c)$$

With these wave functions, the static exchange one-electron equations for the photoelectron orbital, $\phi_{\mathbf{k}}$, can be obtained from the variational expression, $\langle \delta\Psi | H -$

$E|\Psi\rangle = 0$, where H is the fixed-nuclei Hamiltonian and E is the total energy. These equations have the form

$$P[f + \sum_{core}(2J_i - K_i) + \sum_{open}(a_n J_n + b_n K_n) + \alpha S''_{1\pi_u} + \beta S'_{1\pi_u} - \epsilon]P \mid \phi_k >= 0, \quad (4)$$

where J_i and K_i are Coulomb and exchange operators respectively and P is a projection operator which enforces orthogonality of the continuum orbital to the occupied orbitals.[16] The photoelectron kinetic energy is given by $\epsilon = 1/2\ k^2$. The operators S'' and S' are given by

$$S''_{1\pi_u}\phi_+(\mathbf{r}_1) = \phi_-(\mathbf{r}_1)\int d^3\mathbf{r}_2[\pi_-(\mathbf{r}_2)]^*\frac{1}{r_{12}}\pi_+(\mathbf{r}_2) \quad (5a)$$

and

$$S'_{1\pi_u}\phi_+(\mathbf{r}_1) = \pi_+(\mathbf{r}_1)\int d^3\mathbf{r}_2[\pi_-(\mathbf{r}_2)]^*\frac{1}{r_{12}}\phi_-(\mathbf{r}_2). \quad (5b)$$

The one-electron operator, f, in Eq. (3) is

$$f = -\frac{1}{2}\nabla_i^2 - \sum_\alpha \frac{Z_\alpha}{r_{i\alpha}}, \quad (6)$$

where Z_α is the nuclear charge of center α. Using the wave functions given in Eqs. (2) and (3), the coefficients a_n, b_n, α, and β in Eq. (4) are given in Table I.

The photoelectron orbitals of the the static-exchange equations, Eq. (3), were obtained using the iterative Schwinger variational method, discussed extensively elsewhere.[16,17] To solve the Lippmann-Schwinger equations for the continuum orbital associated with the non-local molecular ion potential, the scattering potential is approximated by a separable form

$$U(\mathbf{r},\mathbf{r}') \cong U^S(\mathbf{r},\mathbf{r}') = \sum_{ij} \langle \mathbf{r} \mid U \mid \alpha_i \rangle (U^{-1})_{ij} \langle \alpha_j \mid U \mid \mathbf{r}' \rangle, \tag{7}$$

where the matrix U^{-1} is the inverse of the matrix with elements $U_{ij} = \langle \alpha \mid U \mid \alpha_j \rangle$ and the α_i's are discrete basis functions (see Table II).

The initial state wave function, partial wave expansions and radial grids employed are identical to those discussed in Ref. 5. To ensure convergence, we use photoelectron orbitals obtained after one step in our iterative procedure.[16,17]

III. Results and Discussion

Figure 1 shows cross sections for photoionization of the $1\pi_u$ orbital of O_2 leading to the a $^4\Pi_u$ and $^2\Pi_u(2)$ ions. The photon energy scale assumes an ionization potential of 16.1 eV.[10] The a $^4\Pi_u$ and $^2\Pi_u(2)$ cross sections show mainly statistical behavior, with deviations from the 2 : 1 statistical ratio of 15% at most. This insensitivity to differences in the exchange potential of the multiplet ions is in marked contrast to the shape-resonant photoionization of the $3\sigma_g$ orbital of O_2.[4-6]

The partial channel cross sections and eigenphase sums for a $^4\Pi_u$ photoionization are shown in Fig. 2. The $^2\Pi_u(2)$ results are quite similar and are not shown. The total cross section is dominated by the $k\delta_g$ partial channel which has a maximum around ~20 eV photon energy. This structure as well as the cross sections of the other partial channels are non-resonant, as shown by examination of the associated eigenphase sums. The non-resonant nature of the photoelectron continuum leads to the statistical behavior seen in the a $^4\Pi_u$ and $^2\Pi_u(2)$ cross sections.

Figure 3 shows our calculated photoionization cross sections for the a $^4\Pi_u$ ion along with the experimental data of Samson *et al.*[12] and Gustafsson.[18] These experimental data also include a weak contribution from the A $^2\Pi_u$ ion, on the

order of 15% of the a $^4\Pi_u$ cross section.[10] Because we have neglected configuration interaction in the final state, which would include small admixtures of configurations not dipole-allowed from the ground state,[9] our calculated result actually overestimates the pure a $^4\Pi_u$ cross section and accounts for some of the A $^2\Pi_u$ cross section in the experiment. At low energy, the experimental data suggests sharp structure which indicates the possible role of autoionizing resonances. The photoionization efficiency spectrum of Dehmer and Chupka,[19] as well as work by others,[20] have identified several Rydberg series in this energy range leading to higher excited states of O_2^+ which warrant further study in the present context. The present results, however, agree well with the experimental data above these Rydberg states, showing a gradual decline from a maximum at ~20 eV photon energy.

Figure 4 shows our calculated results for the A $^2\Pi_u$ (I. P. = 17.0 eV[10]) and III $^2\Pi_u$ ions (I.P. = 24.0 eV[10]), along with the experimental data of Samson *et al.*[12] and Tabche-Fouhaile *et al.*[21] The calculated A $^2\Pi_u$ and III $^2\Pi_u$ cross sections are obtained by weighting the transition moments for final configurations derived from the $^2\Pi_u(2)$ ion by 0.5719 and 0.6699, respectively. These weights are determined from the minimal basis configuration interaction calculation of Honjou *et al.*[9] and correspond to the contribution of the dipole-allowed $^2\Pi_u(2)$ configuration to the observed mixed doublet ion states. The data of Tabche-Fouhaile *et al.*[21] actually extends from threshold to ~23 eV photon energy and includes rich structure near threshold, which has also been examined in the polarized fluorescence experiments of Keller *et al.*[22] and the multichannel quantum defect theory (MQDT) calculations of Lefebvre-Brion.[23] We show the data of Tabche-Fouhaile *et al.*[21] at energies just above this structure and at 22.5 eV where we have normalized their relative measurements to our calculated length-form result. Between these points, the experimental data show a general monotonic increase with increasing energy. The

data of Samson *et al.*[12] for the $^2\Pi_u$ state, which we assign as III $^2\Pi_u$, also show the same energy dependence as the present results, although we appear to overestimate the cross section slightly at low energy. Samson *et al.*[12] also report a point at 23.1 eV of 0.1 Mb (not shown), which accesses only a small part of the broad III $^2\Pi_u$ vibrational envelope.[10,11] In contrast to the a $^4\Pi_u$ state, the present length and velocity results are quite different, which we believe results from not solving the static-exchange equations for the fully mixed doublet states. Such a problem goes beyond the frozen-core Hartree-Fock (FCHF) model and requires solution of considerably more complicated static-exchange equations for the photoelectron continuum orbital than those given in Section II.[16] However, the present theoretical treatment seems to at least qualitatively reproduce the available experimental data. More experimental data are needed to fully assess the accuracy of the present results.

Figure 5 shows our calculated photoelectron angular distributions along with the multiple-scattering-model (MSM) calculations of Dittman *et al.*[24] and the experimental data of Holmes *et al.*[25] and Katsumata *et al.*[26] for the $v^+=4$ state. Because of the non-resonant nature of the photoelectron continuum, the experimental data for $v^+=4$ should be directly comparable to the present vibrationally-unresolved results. At low energy, the present results agree well with those of experiment, showing a steep increase in β from $\sim$-0.5. This behavior closely resembles 2p photoionization of atomic oxygen.[27] The present results indicate that the experimental "jump" at 24 eV photon energy could be the result of autoionization, possibly from Rydberg series leading to the c $^4\Sigma_u^-$ ion. Further experimental studies are needed to explore these features.

The calculated photoelectron asymmetry parameters for the A $^2\Pi_u$ and III $^2\Pi_u$ ions are essentially identical to those of the a $^4\Pi_u$ ion as a function of photoelectron

kinetic energy and are not shown. The weighting factors introduced in the calculation of the doublet cross sections have no effect on the asymmetry parameters, as the transition moments appearing in the expression for β occur as a ratio, and the weighting factors cancel.

Acknowledgments

This work was supported by grants from the National Science Foundation (CHE-8521391). We also acknowledge use of resources of the San Diego SuperComputer Center, which is supported by the National Science Foundation. One of us (M. B.) wishes to acknowledge a Department of Education Fellowship.

TABLE I. Coefficients of the static-exchange potential of Eq. (4).

		a_n/b_n				α/β
Ion	Channel[a]	$1\pi_u^+$	$1\pi_u^-$	$1\pi_g^+$	$1\pi_g^-$	
a $^4\Pi_u$	$^3\Pi_u(k\sigma_g)$	2/-1	$1/\frac{1}{3}$	$1/\frac{1}{3}$	$1/\frac{1}{3}$	0/0
	$^3\Sigma_u^-(k\pi_g)$	2/-1	$1/\frac{1}{3}$	$1/\frac{1}{3}$	$1/\frac{1}{3}$	$-1/\frac{4}{3}$
	$^3\Pi_u(k\delta_g)$	2/-1	$1/\frac{1}{3}$	$1/\frac{1}{3}$	$1/\frac{1}{3}$	0/0
$^2\Pi_u(2)$	$^3\Pi_u(k\sigma_g)$	2/-1	$1/-\frac{1}{3}$	$1/-\frac{5}{6}$	$1/-\frac{5}{6}$	0/0
	$^3\Sigma_u^-(k\pi_g)$	2/-1	$1/-\frac{1}{3}$	$1/-\frac{5}{6}$	$1/-\frac{5}{6}$	$-1/\frac{2}{3}$
	$^3\Pi_u(k\delta_g)$	2/-1	$1/-\frac{1}{3}$	$1/-\frac{5}{6}$	$1/-\frac{5}{6}$	0/0

[a] Channel symmetry designation of the ion plus photoelectron system.

TABLE II. Basis sets used in separable potential, Eq. (7).

Photoionization symmetry	Type of Gaussian function[a]		Exponents
σ_g	Cartesian	s	16.0,8.0,4.0,2.0,1.0,0.5
		z	1.0,0.5
	Spherical	$\ell = 0$	2.0,1.0,0.5
		$\ell = 2$	2.0,1.0,0.5
π_g	Cartesian	x	8.0,4.0,2.0,1.0,0.5
		xz	0.5
	Spherical	$\ell = 2$	1.0
		$\ell = 4$	1.0
δ_g	Cartesian	xy	8.0,4.0,2.0,1.0,0.5,0.25
	Spherical	$\ell = 2$	2.0,1.0,0.5
		$\ell = 4$	2.0,1.0,0.5

[a] Cartesian functions are centered at the nuclei and the spherical functions at the molecular center. For details of the forms of these functions and their use, see Refs. 16 and 17.

References

[1] M. E. Smith, V. McKoy, and R. R. Lucchese, J. Chem. Phys. **82**, 4147 (1985).

[2] M. R. Hermann, C. W. Bauschlicher, Jr., W. M. Huo, S. R. Langhoff, and P. W. Langhoff, Chem. Phys. **109**, 1 (1986).

[3] M. R. Hermann, S. R. Langhoff, T. J. Gil, and P. W. Langhoff, Chem. Phys. Lett. **125**, 336 (1986).

[4] C. L. Winstead *et al.*, see also C. L. Winstead, Ph.D. thesis, Indiana University, 1987.

[5] M. Braunstein, V. McKoy, and M. E. Smith, J. Chem. Phys. **90**, 3931 (1989).

[6] M. Braunstein and V. McKoy, J. Chem. Phys. (to be published).

[7] P. W. Langhoff, A. Gerwer, C. Asaro, and B. V. McKoy, Int. J. Quantum Chem. Symp. **13**, 645 (1979).

[8] A. Gerwer, C. Asaro, B. V. McKoy, and P. W. Langhoff, J. Chem. Phys. **72**, 713 (1980).

[9] N. Honjou, K. Tanaka, K. Ohno, and H. Taketa, Mol. Phys. **35**, 1569 (1978).

[10] O. Edqvist, E. Lindholm, L. E. Selin and L. Åsbrink, Physica Scripta **1** 25 (1970).

[11] J. L. Gardner and J. A. R. Samson, J. Chem. Phys. **62**, 4460 (1975).

[12] J. A. R. Samson, J. L. Gardner, and G. N. Haddad, J. Electron Spectrosc. Relat. Phenom. **12**, 281 (1977).

[13] R. N. Dixon and S. E. Hull, Chem. Phys. Lett. **3**, 367 (1969).

[14] H. Lefebvre-Brion and R. W. Field, *Perturbations in the Spectra of Diatomic Molecules* (Academic Press, Orlando, 1986), pp. 58-65.

[15] N. H. F. Beebe, E. W. Thulstrup, and A. Andersen, J. Chem. Phys. **64**, 2080 (1976).

[16] R. R. Lucchese, G. Raseev, and V. McKoy, Phys. Rev. A. **25**, 2572 (1982).

[17] R. R. Lucchese, K. Takatsuka, and V. McKoy, Phys. Rep. **131**, 147 (1986).

[18] T. Gustafsson, Chem. Phys. Lett. **75**, 505 (1980).

[19] P. M. Dehmer and W. A. Chupka, J. Chem. Phys. **62**, 4525 (1975).

[20] See, for example, P. Krupenie, J. Phys. Chem. Ref. Data **1**, 423 (1972).

[21] A. Tabche-Fouhaile, I. Nenner, P.-M. Guyon, and J. Delwiche, J. Chem. Phys. **75**, 1129 (1981).

[22] J. W. Keller, W. T. Hill III, D. L. Ederer, T. J. Gil, and P. W. Langhoff, J. Chem. Phys. **87**, 3299 (1987).

[23] H. Lefebvre-Brion, J. Chem. Phys. **89**, 2691 (1988).

[24] P. M. Dittman, D. Dill, and J. L. Dehmer, J. Chem. Phys. **76**, 5703 (1982).

[25] R. M. Holmes and G. V. Marr, J. Phys. B **13**, 945 (1980).

[26] S. Katsumata, Y. Achiba, and K. Kimura, J. Electron Spectrosc. Relat. Phenom. **17**, 229 (1979).

[27] A. F. Starace, S. T. Manson, and D. J. Kennedy, Phys. Rev. A **9**, 2453 (1974).

Figure Captions

Fig. 1: Cross sections for photoionization of the $1\pi_u$ orbital of O_2 leading to the ground state parentage ions, a $^4\Pi_u$ and $^2\Pi_u(2)$: —, present length results; - - - present velocity results. The observed doublet ion states are actually heavily mixed, as discussed in the text.

Fig. 2: Partial photoionization cross sections (length) and eigenphase sums for the the a $^4\Pi_u$ state of O_2^+.

Fig. 3: Photoionization cross sections for the a $^4\Pi_u$ states of O_2^+: —, present length results; - - -, present velocity results; ×, experimental results of Ref. 18; ○, experimental results of Ref. 12. Note that the experimental results contain a small contribution (~15%) from the A $^2\Pi_u$ ion.

Fig. 4: Photoionization cross sections for the A $^2\Pi_u$ and III $^2\Pi_u$ states of O_2^+: —, present length results; - - -, present velocity results; △, experimental results of Ref. 21 for the A $^2\Pi_u$ state; □, experimental results of Ref. 12 for the $^2\Pi_u$ state, here assigned III $^2\Pi_u$. Note that the data of Ref. 21 have been normalized to the present results at 22.5 eV.

Fig. 5: Photoelectron asymmetry parameters for the a $^4\Pi_u$ state of O_2^+: —, present length results; - - -, present velocity results; - - -, Multiple-Scattering (MSM) results of Ref. 24; ■, experimental results of Ref. 25, ●, experimental results of

Ref. 26 for the $v^+ = 4$ state. The experimental results of Ref. 25 contain a small contribution from the A $^2\Pi_u$ state.

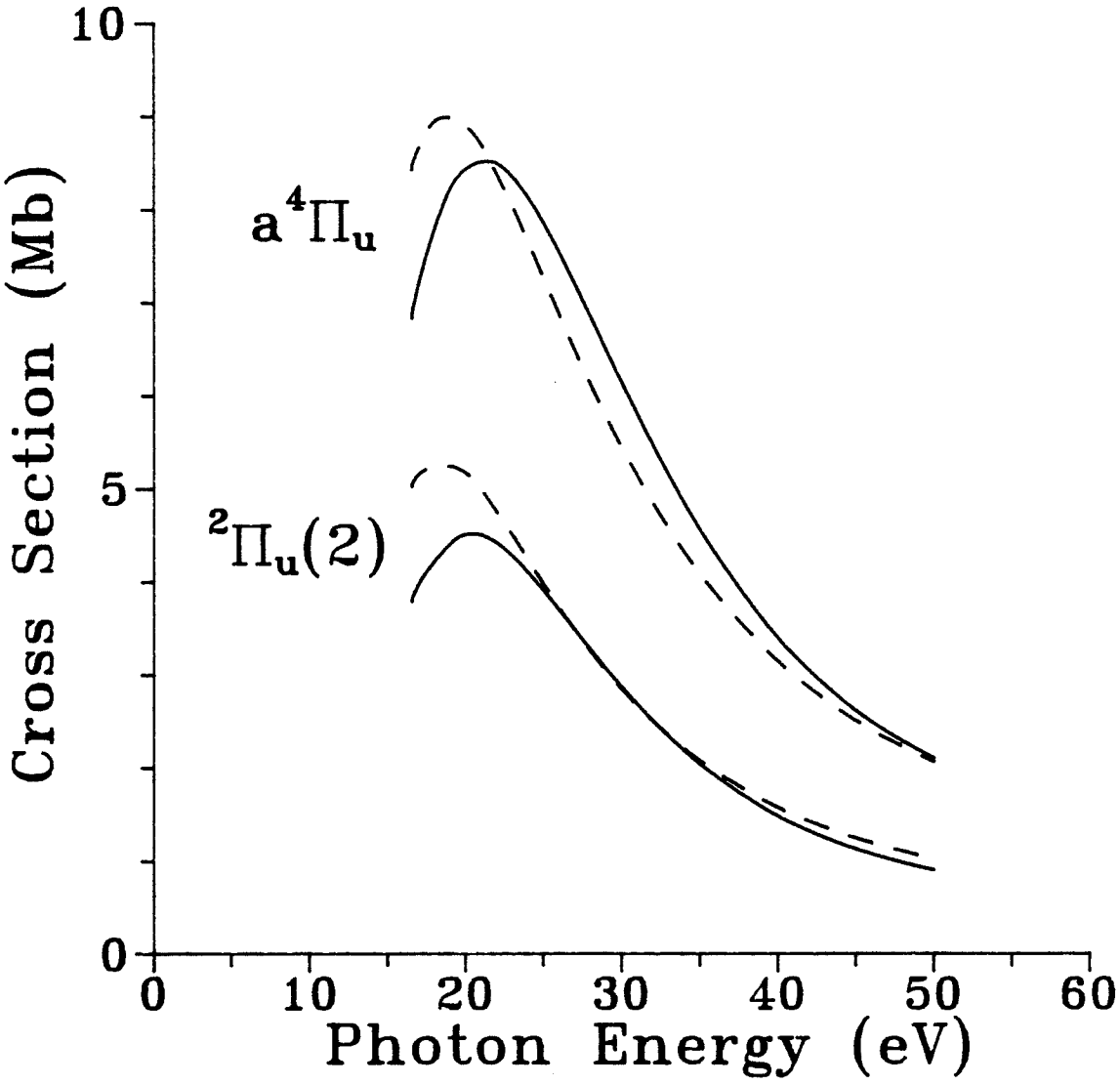
10
5
0
Cross Section (Mb)
$a^4\Pi_u$
$^2\Pi_u(2)$
0
10
20
30
40
50
60
Photon Energy (eV)

Figure 1

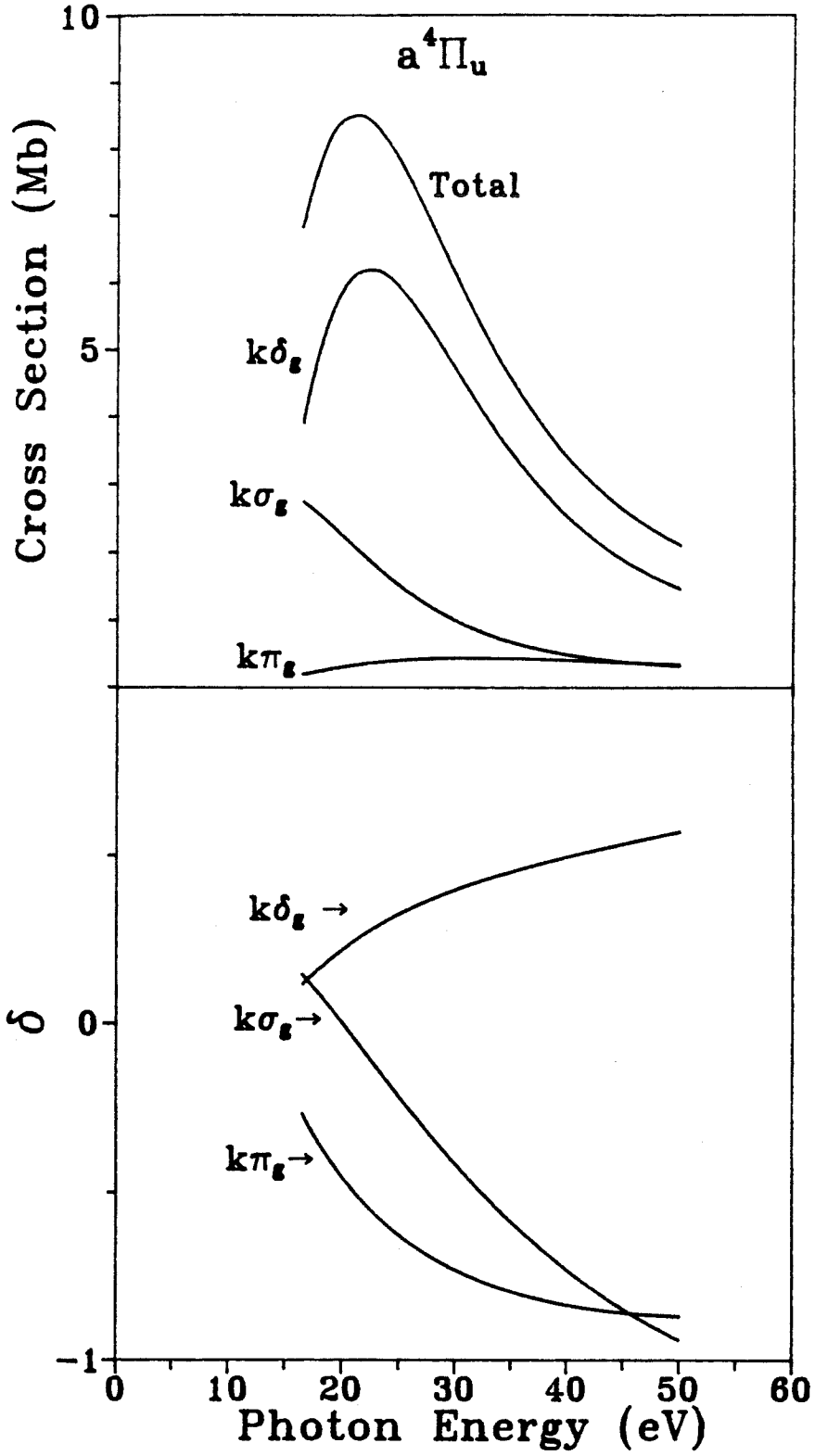
a $^4\Pi_u$
Total
$k\delta_g$
$k\sigma_g$
$k\pi_g$
Cross Section (Mb)
10
5
$k\delta_g \rightarrow$
$k\sigma_g \rightarrow$
$k\pi_g \rightarrow$
δ
0
−1
0
10
20
30
40
50
60
Photon Energy (eV)

Figure 2

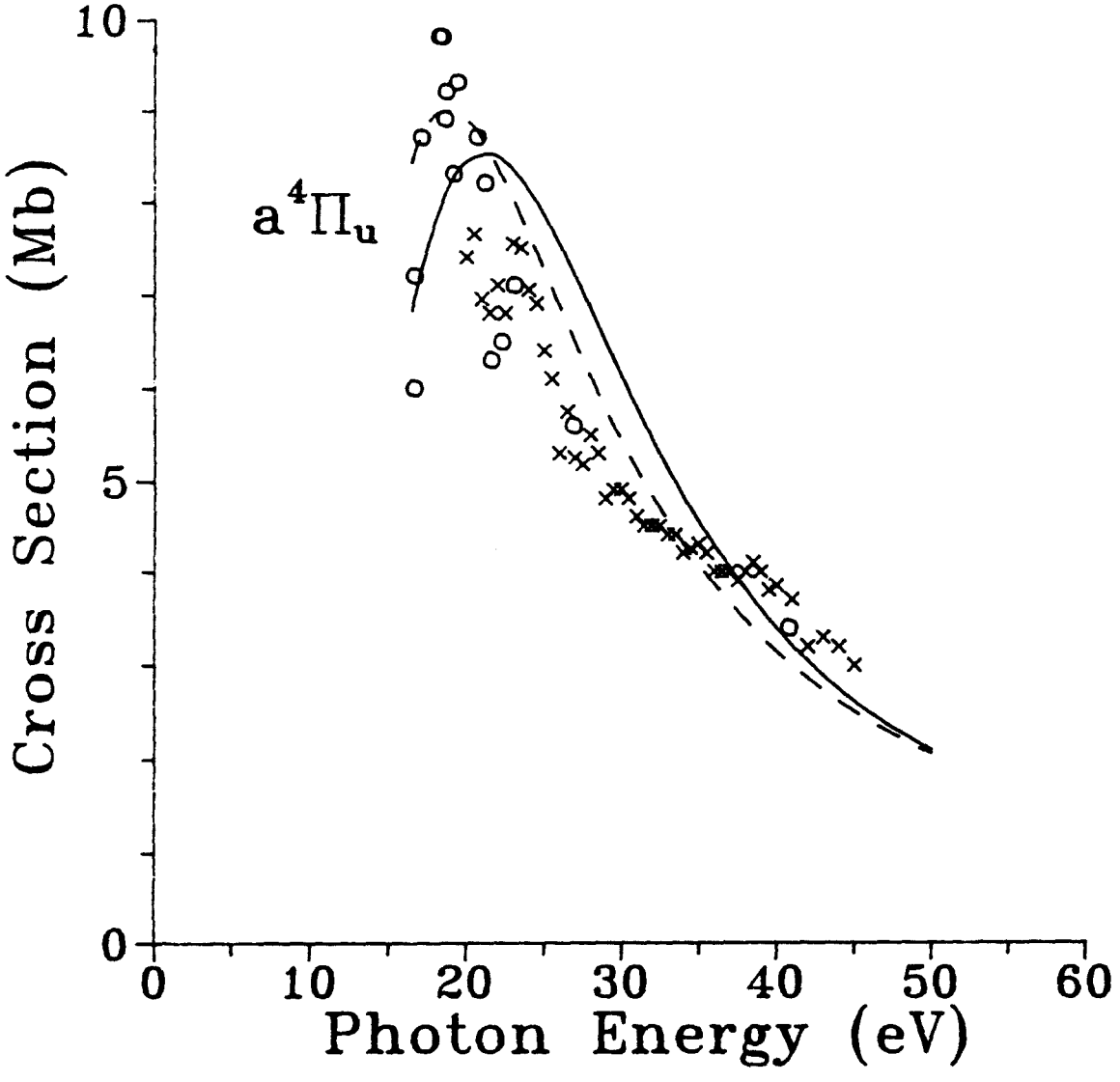
10
5
0
Cross Section (Mb)
$a^4\Pi_u$
0
10
20
30
40
50
60
Photon Energy (eV)

Figure 3

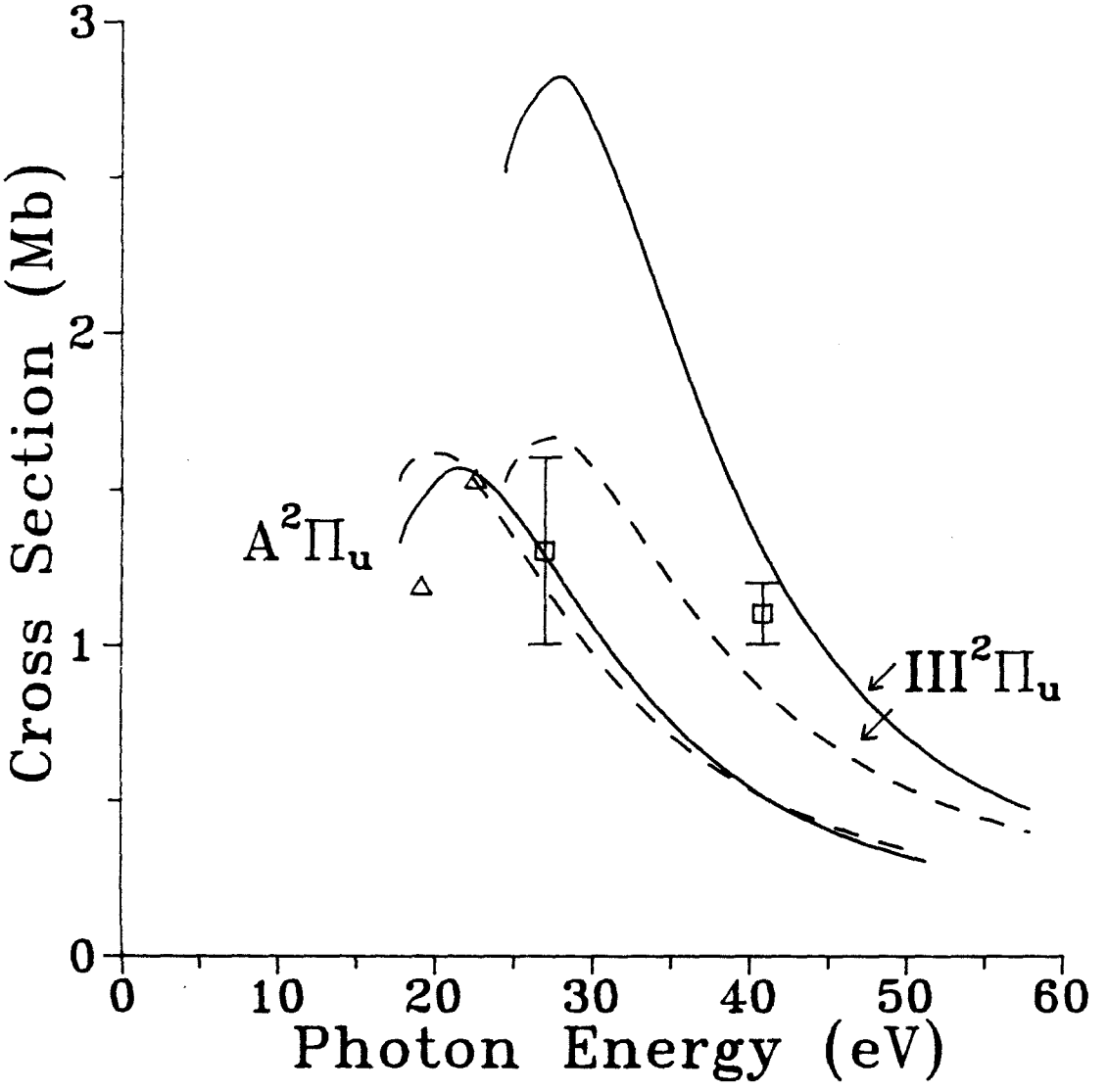
Cross Section (Mb)
3
2
1
0
0
10
20
30
40
50
60
Photon Energy (eV)
$A^2\Pi_u$
$III^2\Pi_u$

Figure 4

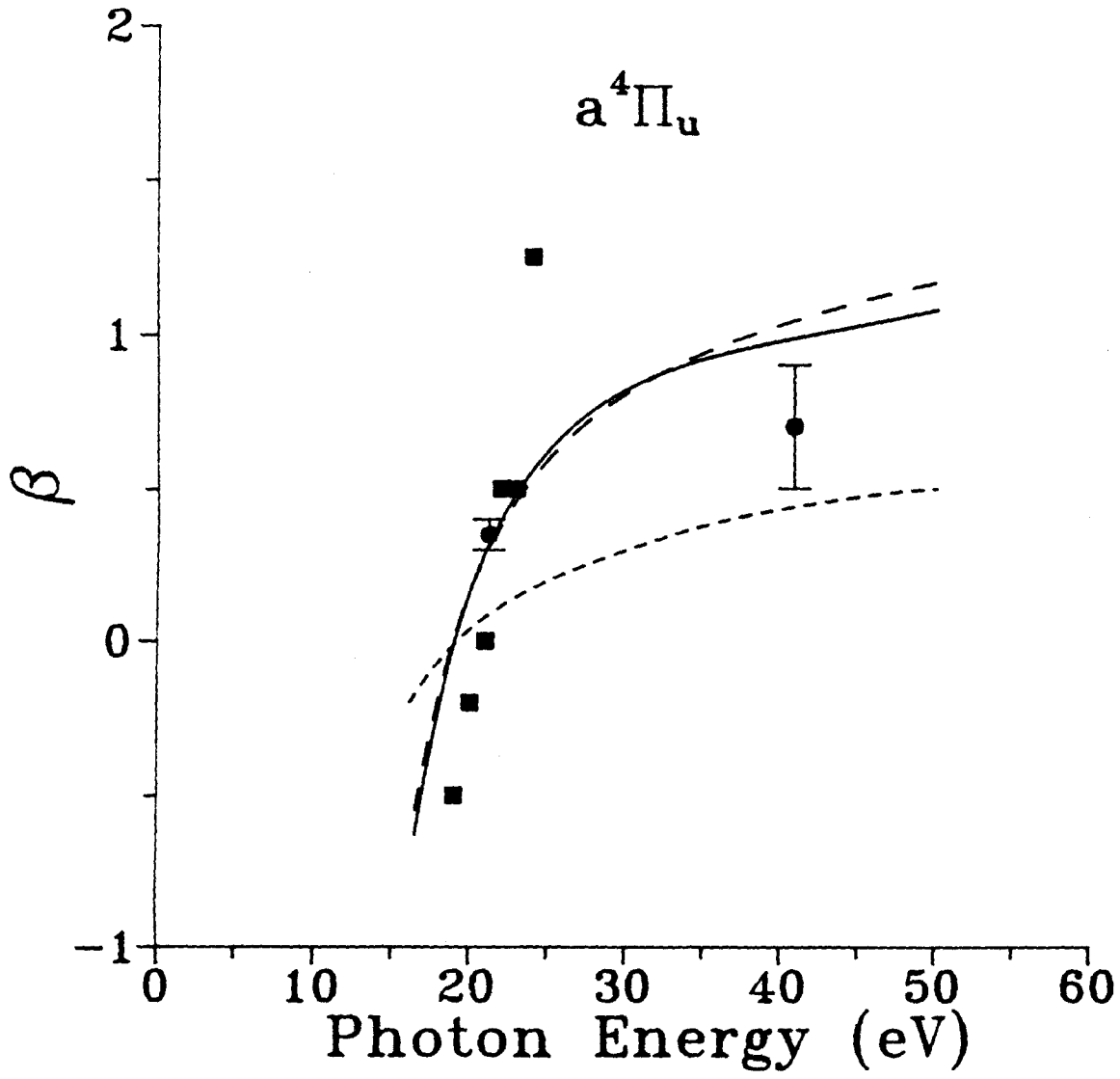

Figure 5

Chapter 3

Multiplet-specific shape resonance and autoionization effects in (2+1) resonance enhanced multiphoton ionization of O_2 via the d $^1\Pi_g$ state

(The text of this chapter appeared in: J. A. Stephens, M. Braunstein, and V. McKoy, J. Chem. Phys. **92** 5319 (1990).)

Multiplet-specific shape resonance and autoionization effects in (2+1) resonance enhanced multiphoton ionization of O_2 via the $d\,^1\Pi_g$ state

J. A. Stephens, M. Braunstein, and V. McKoy
Arthur Amos Noyes Laboratory of Chemical Physics,[a] *California Institute of Technology, Pasadena, California 91125*

(Received 9 August 1989; accepted 26 January 1990)

In this paper we discuss the single-photon ionization dynamics of the $d\,^1\Pi_g$ Rydberg state of O_2. Comparision is made with vibrationally resolved measurements of photoelectron spectra which employ (2 + 1) resonance enhanced multiphoton ionization (REMPI) through the $d\,^1\Pi_g$ state. A σ_u shape resonance near the ionization threshold leads to non-Franck–Condon vibrational branching ratios and a substantial dependence of photoelectron angular distributions on the vibrational state of the $X\,^2\Pi_g$ ion. Significant differences exist between our one-electron predictions and experiment. These are mainly attributed to electronic autoionization of repulsive $^1\Sigma_u^-$, $^1\Sigma_u^+$, and $^1\Delta_u$ states associated with the $1\pi_u^3 1\pi_g^3$ configuration. A proposed singlet "K" $^1\Pi_u$ Rydberg state converging to the $A\,^2\Pi_u$ ion probably also contributes to autoionization in the $d\,^1\Pi_g$ state spectrum. We also show that autoionizing H and $J\,^3\Pi_u$ Rydberg states of O_2 converging to the $a\,^4\Pi_u$ and $A\,^2\Pi_u$ ionic thresholds, respectively, may play a previously unsuspected role in the $C\,^3\Pi_g$ state one-color REMPI spectra. We discuss multiplet-specific (spin-dependent) effects via comparision of these results with recent experimental and theoretical studies of O_2 $C\,^3\Pi_g$ photoionization.

I. INTRODUCTION

The photoionization dynamics of the $C\,^3\Pi_g$ ($1\pi_g 3s\sigma_g$) Rydberg state of O_2 have recently been studied experimentally and theoretically by (2 + 1) resonance enhanced multiphoton ionization spectroscopy (REMPI).[1-5] These studies have shown that a σ_u shape resonance leads to strong non-Franck–Condon ionic vibrational distributions and photoelectron angular distributions. Presently there is significant interest in using REMPI to prepare molecular ions in vibrationally (and rotationally) state-selected states. Since the shape resonance in O_2 was shown to effectively inhibit efficient vibrational state-specific production of ions via the $C\,^3\Pi_g$ state, additional experimental studies have probed the higher-lying "4s–3d" Rydberg states.[6,7] Due to the symmetry of the excited orbital, some of these levels may not access the σ_u ionization continuum, thus permitting O_2^+ state preparation to better than ~80% for several vibrational levels.

In this paper, we present studies of photoionization dynamics of the $d\,^1\Pi_g$ ($1\pi_g 3s\sigma_g$) Rydberg state of O_2, the singlet analog of the $C\,^3\Pi_g$ state. The $d\,^1\Pi_g$ state of O_2 has been detected, and partially characterized, by several electron impact and REMPI studies.[8-13] The singlet coupling of the $3s\sigma_g$ Rydberg electron to the $X\,^2\Pi_g$ ion core results in a small, positive energy shift of the potential energy curve, relative to the triplet state (~0.1 eV). In contrast, the σ_u shape resonance with its localized character, as well as the energetically accessible valence autoionizing states, exhibit large (~1–3 eV) energy shifts relative to their triplet analogs. Due to these considerations, the REMPI photoelectron dynamics may significantly depend on which spin state of the neutral Rydberg level is accessed in the two-photon absorption step. In particular, the photoelectron spectra observed by Miller *et al.*[14] for the $d\,^1\Pi_g$ Rydberg state display greater non-Franck–Condon behavior than that observed for the $C\,^3\Pi_g$ spectra. As discussed below, we attribute this mainly to autoionization of repulsive valence states and Rydberg states converging to excited states of the ion and not to the σ_u shape resonance. Such multiplet-specific shape resonance and autoionization effects are generally energy dependent. They could be further probed to great advantage via two-color REMPI experiments.

Although we believe that autoionization is the major source of disagreement between present theory and available experiments, another class of electronic interactions relevant to excited-state photoionization dynamics are avoided crossings between the resonantly prepared Rydberg state and repulsive valence states of the same electronic symmetry. Van der Zande *et al.*[15,16] have recently studied the $C\,^3\Pi_g$ and $d\,^1\Pi_g$ Rydberg states of O_2 using charge-exchange translational spectroscopy. Specifically they investigated and deduced details of the Rydberg-valence interactions and associated predissociation processes. These interactions may influence ion vibrational distributions through electronic correlations and perturbations of vibrational levels of the neutral Rydberg in the vicinity of the curve crossing.

In Sec. II we give a brief discussion of numerical details of the calculations. In Sec. III we present vibrational branching ratios and discuss the shape-resonance and electron correlation effects relevant to ionic vibrational distributions for photoionization of the $d\,^1\Pi_g$ Rydberg state. A qualitative discussion of the correlation effects in terms of Franck–Condon factors, survival factors, and SCF calculations is given. Rigorous incorporation of these states in the photoionization calculations remains a major goal of our studies. Also presented in Sec. III are two-color (energy-dependent)

[a] Contribution No. 8015.

branching ratios and vibrationally resolved photoelectron angular distributions. Section IV gives a brief conclusion.

II. CALCULATIONAL DETAILS

In the frozen-core Hartree–Fock approximation there are four dipole-allowed channels for ionization of the $d\,^1\Pi_g$ state corresponding to photoionization of the singly occupied $3s\sigma_g$ Rydberg orbital. The electronic continuum wave functions are

$$\Psi(^1\Pi_u) = \frac{1}{\sqrt{2}}\{|[\text{core}]1\pi_g^+\,\overline{k\sigma_u}| - |[\text{core}]\,\overline{1\pi_g}^+ k\sigma_u|\}, \tag{1a}$$

$$\Psi(^1\Sigma_u^+) = \tfrac{1}{2}\{|[\text{core}]1\pi_g^+\,\overline{k\pi_u}^-| + |[\text{core}]1\pi_g^-\,\overline{k\pi_u}^+| - |[\text{core}]\,\overline{1\pi_g}^+ k\pi_u^-| - |[\text{core}]\,\overline{1\pi_g}^- k\pi_u^+|\}, \tag{1b}$$

$$\Psi(^1\Sigma_u^-) = \tfrac{1}{2}\{|[\text{core}]1\pi_g^+\,\overline{k\pi_u}^-| - |[\text{core}]1\pi_g^-\,\overline{k\pi_u}^+| - |[\text{core}]\,\overline{1\pi_g}^+ k\pi_u^+| + |[\text{core}]\,\overline{1\pi_g}^- k\pi_u^-|\}, \tag{1c}$$

$$\Psi(^1\Delta_u) = \frac{1}{\sqrt{2}}\{|[\text{core}]1\pi_g^+\,\overline{k\pi_u}^+| - |[\text{core}]\,\overline{1\pi_g}^+ k\pi_u^+|\}, \tag{1d}$$

where $[\text{core}] = 1\sigma_g^2 1\sigma_u^2 2\sigma_g^2 2\sigma_u^2 3\sigma_g^2 1\pi_u^4$. The associated one-particle Schrödinger equations for the continuum orbitals can be derived straightforwardly[17,18] and have been presented in detail in Eq. (2) of Ref. 5 for the case of triplet coupling. The singlet-coupled equations can be obtained simply by changing the signs preceeding the exchange operators for the $1\pi_g$ electron, and the nonlocal S' terms.

The Gaussian basis sets, internuclear distances, partial-wave expansions, and radial grids used to evaluate the R-dependent transition moments for the $k\sigma_u$ and $k\pi_u$ channels are identical to those for the $C\,^3\Pi_g$ calculations.[3,5] The initial state $d\,^1\Pi_g$ SCF wave functions were calculated using a $(9s5p2d/4s3p2d)$ Gaussian basis set with diffuse functions on the center of mass with exponents identical to those in Ref. 5. The total SCF energy of the $d\,^1\Pi_g$ state at $R = 2.282a_0$ with this basis is $-149.285\,87$ a.u., resulting in an energy splitting of 0.073 eV compared to the $C\,^3\Pi_g$

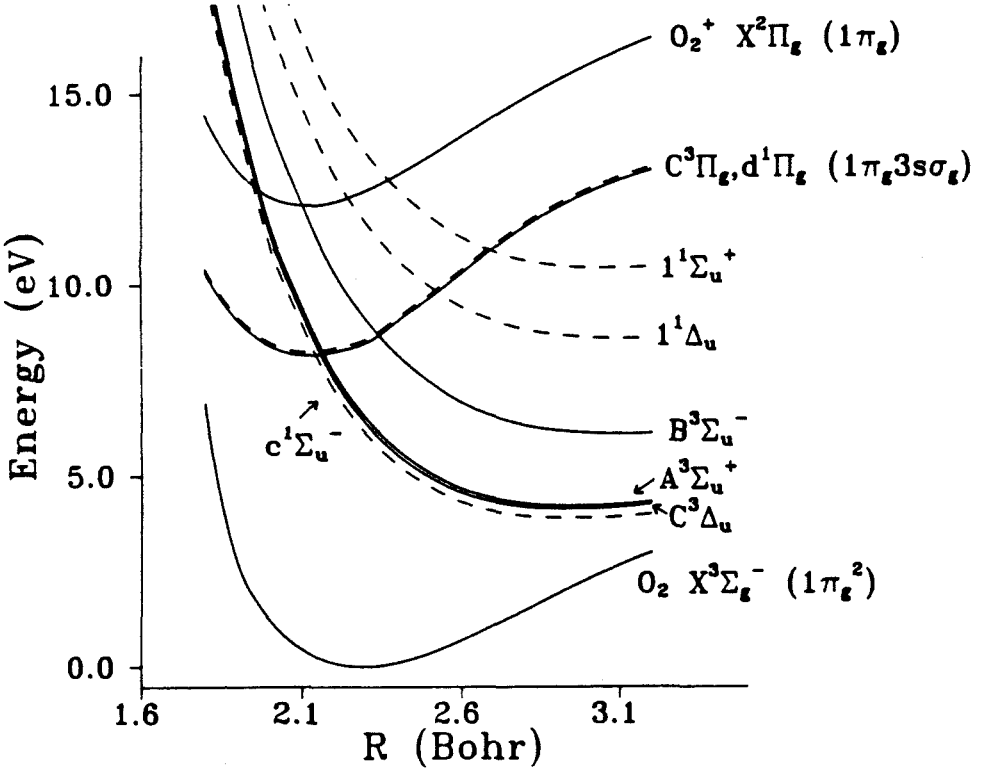

FIG. 1. O_2 potential energy curves for the ground state, the first ionic state, and singlet and triplet valence states deriving from the electronic configuration $1\pi_u^3 1\pi_g^1$. The potential curves are taken from Refs. 29 and 30.

state. The $d\ ^1\Pi_g$ state vibrational wave functions and those for the $X\ ^2\Pi_g$ ion were calculated using the RKR potentials discussed in Refs. 3 and 5. For later discussion, in Fig. 1 we summarize potential energy curves for the O_2 neutral and ionic ground states and several singlet and triplet Rydberg and repulsive valence states relevant to this discussion.

III. DISCUSSION OF RESULTS

A. Shape resonance effects

In Fig. 2 we show the calculated photoionization cross section for the singlet and triplet-coupled $3s\sigma_g \rightarrow k\sigma_u$ channel at the internuclear distance $R = 2.088\ a_0$. The σ_u shape resonance in the singlet-coupled channel is shifted ~ 2.5 eV higher in kinetic energy than the triplet-coupled channel, similar to singlet–triplet energy shifts typically observed for excited valence states. This shift is due to the greater (repulsive) exchange interaction of the ionized electron with the ion core in the singlet-coupled final state. In Fig. 2 the large difference between the length and velocity cross sections at low energy is due to our neglect of electron correlations beyond the Hartree–Fock level in the $^{1,3}\Pi_u$ ionization channels. These differences largely cancel upon forming the vibrational branching ratios (see Fig. 3). Residual discrepancies with experiment are attributed mainly to autoionization of repulsive valence states (discussed below).

For ground state photoionization of O_2, the σ_u shape resonance has been discussed by Raseev *et al.*[19] for the $3\sigma_g$ level, and by Gerwer *et al.*,[20] Dittman *et al.*,[21] and Braunstein and McKoy[22,23] for both the $3\sigma_g$ and $1\pi_g$ levels. Particularly for the $3\sigma_g$ level, it was shown[23] that it is essential to include multiplet-specific aspects of this problem to account for observed one-electron features of the photoionization spectra. In these ground and the present excited-state studies, the R dependence of the transition moment induced by the shape resonance results in non-Franck–Condon effects observable in both vibrational branching ratios and photoelectron angular distributions.[24–26]

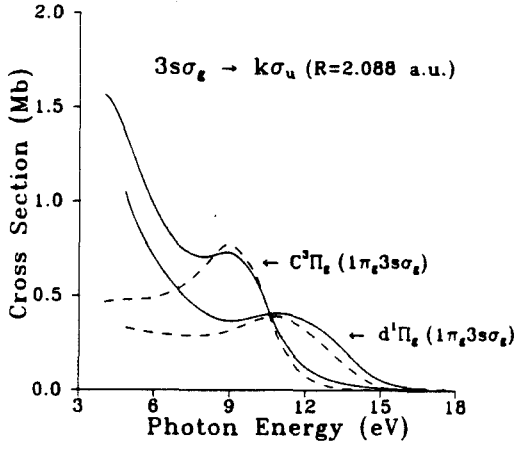

FIG. 2. Calculated photoionization cross sections for the $3s\sigma_g \rightarrow k\sigma_u$ channel of the $O_2\ d\ ^1\Pi_g$ and $C\ ^3\Pi_g$ states. Solid curves: length form; dash curve: velocity form.

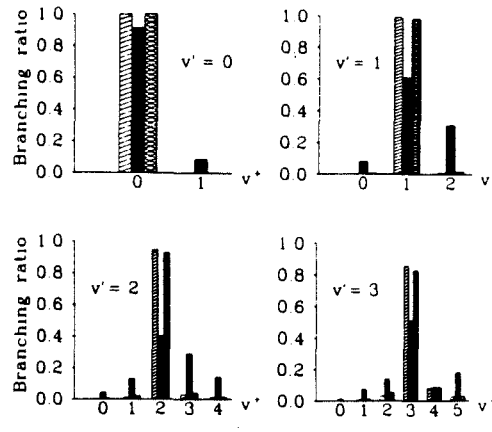

FIG. 3. Calculated vibrational branching ratios for photoionization of the $v' = 0$–3 levels of the $O_2\ d\ ^1\Pi_g$ state. Length form (crossed bar); velocity form (crosshatched bar). The calculations are compared with the measurements of Miller *et al.* (Ref. 14, solid bar).

For the present REMPI studies, the shift of the resonance to higher kinetic energy will result in some decrease in the calculated non-Franck–Condon effect, but not as much as Fig. 2 may suggest. Note that the shift in the σ_u resonance position is much larger than the difference in ionization thresholds (3.84 and 3.93 eV for the $v' = 0$ levels, respectively). The photoelectron energies for the $d\ ^1\Pi_g$ and $C\ ^3\Pi_g$ $(2+1)$ spectra range from ~ 0.2–1.3 eV, which is a small portion of the abcissa scale in Fig. 2. The σ_u cross section still depends strongly on R, causing only a weak detuning effect when compared against the triplet results.[3,5] Branching ratios and angular distributions which illustrate the energy dependence over a broad energy range are discussed below.

TABLE I. Summary of vibrationally resolved cross sections and branching ratios.

		σ_{v',v^+} (Mb)		$\sigma_{v',v^+}/\Sigma_{v^+}\sigma_{v',v^+}$		$\sigma_{v',v^+}/\Sigma_{v^+}\sigma_{v',v^+}$
		Length (Theory)	Velocity (Theory)	Length (Theory)	Velocity (Theory)	
v'	v^+					(Experiment[a])
0	0	2.8373	0.9946	0.9985	0.9969	0.91
0	1	0.0042	0.0031	0.0015	0.0031	0.089
1	0	0.0050	0.0045	0.0016	0.0042	0.079
1	1	3.0365	1.0489	0.9882	0.9804	0.61
1	2	0.0313	0.0165	0.0102	0.0154	0.31
2	0	0.0073	0.0030	0.0022	0.0025	0.043
2	1	0.0350	0.0241	0.0107	0.0203	0.13
2	2	3.1049	1.1031	0.9450	0.9267	0.40
2	3	0.0971	0.0449	0.0295	0.0377	0.29
2	4	0.0415	0.0152	0.0126	0.0128	0.14
3	0	0.0014	0.0001	0.0004	0.0001	0.012
3	1	0.0216	0.0135	0.0063	0.0103	0.072
3	2	0.1080	0.0694	0.0315	0.0529	0.14
3	3	2.9231	1.0805	0.8535	0.8235	0.51
3	4	0.2802	0.1123	0.0818	0.0856	0.087
3	5	0.0905	0.0363	0.0264	0.0277	0.18

[a] From Ref. 14.

B. Branching ratios and correlation effects

Figure 3 shows our calculated vibrational branching ratios compared with the photoelectron intensities measured by Miller *et al.*[14] for the $v' = 0$–3 levels of the $d\,^1\Pi_g$ state. Table I gives a summary of the calculated and measured branching ratios. These distributions have been normalized so that the sum over v^+ for each intermediate level equals unity. Inclusion of the R dependence of the transition moment arising from the shape resonance accounts for some of the observed $\Delta v \neq 0$ intensity, e.g., the $v^+ = 3$–5 states accessed via the $v' = 2$ and 3 intermediate states. The Franck–Condon approximation predicts essentially zero intensity for these off-diagonal transitions. However, major discrepancies between theory and experiment are more apparent for the singlet spectra than for the triplet.[2,3,5] We attribute these discrepancies mainly to autoionizing repulsive valence states and Rydberg states converging to excited ionic states. Perturbations of the resonant intermediate levels by repulsive valence states cannot be ignored; however, as discussed below, we expect this interaction to be of lesser consequence in the present REMPI problem.

1. Autoionization of repulsive valence states

Prior studies[2-5] of the photoionization of the O_2 $C\,^3\Pi_g$ Rydberg state have suggested the importance of autoionizing $^3\Delta_u$, $^3\Sigma_u^+$, and $^3\Sigma_u^-$ valence states derived from the $1\pi_u^3 1\pi_g^3$ electronic configuration. These repulsive states intersect the lower portion and rise above the potential energy curve of the $X\,^2\Pi_g$ ion, and may thus autoionize into the $^3\Delta_u$, $^3\Sigma_u^+$, and $^3\Sigma_u^-$ channels deriving from $3s\sigma_g \rightarrow k\pi_u$ ionization. To qualitatively discuss the importance of autoionization of these repulsive states, we introduce dimensionless autoionization probabilities $\zeta_{v^+}^2$ and the "survival factor" S ($S \leq 1$). The survival factor is the ratio between the dissociative recombination cross section and the capture cross section for a positive ion plus electron. Its departure from unity indicates the importance of autoionization compared with dissociation.[27] Following Giusti,[27] we define the quantities

$$\zeta_{v^+} = \pi \langle \chi_{v^+} | V(R) | \chi_d \rangle, \tag{2a}$$

$$V(R) = \langle \Phi_k | H | \Phi_d \rangle, \tag{2b}$$

$$S = \left[1 + \sum_{v^+} \zeta_{v^+}^2 \right]^{-2}, \tag{2c}$$

where χ_{v^+} and χ_d are vibrational wave functions of the ion and neutral dissociating state Φ_d, respectively, and H is the fixed-nuclei electronic Hamiltonian. Here Φ_k is the continuum wave function for $3s\sigma_g \rightarrow k\pi_u$ photoionization. We made Franck–Condon approximations to these quantities, i.e., $\zeta_{v^+} = \pi V(\bar{R}) \langle \chi_{v^+} | \chi_d \rangle$, where $\bar{R}$ is the centroid[28] $\bar{R} = \langle \chi_{v^+} | R | \chi_d \rangle / \langle \chi_{v^+} | \chi_d \rangle$. The differential Franck–Condon factors $\langle \chi_{v^+} | \chi_d \rangle$ were calculated using the $X\,^2\Pi_g$ curve of Krupenie[29] and the valence $^{1,3}\Sigma_u^-$, $^{1,3}\Sigma_u^+$, and $^{1,3}\Delta_u$ potential energy curves of Saxon and Liu[30] (shown in Fig. 1). The widths for the $^3\Sigma_u^-$, $^1\Delta_u$, and $^1\Sigma_u^+$ states calculated by Guberman[31] were employed, and we have assumed the triplet and singlet widths for states of the same spatial symmetry to be identical. The R-centroid procedure was employed only for the $^{1,3}\Sigma_u^-$ valence states, since widths for the other symmetries are essentially R independent.[31] In Tables II and III we give our calculated $\zeta_{v^+}^2$ matrix elements and survival factors for singlet and triplet valence states.

TABLE II. Autoionization probabilities and survival factors for singlet valence states.

v'[a]	v^+	$c\,^1\Sigma_u^-$	$1\,^1\Sigma_u^+$	$1\,^1\Delta_u$
0	0	5.0×10^{-1}	1.1×10^{-4}	6.7×10^{-2}
	1	3.3×10^{-2}	2.1×10^{-3}	0.21
		0.93[b]	1.0	0.61
1	0	2.8×10^{-3}	5.8×10^{-4}	0.11
	1	2.1×10^{-2}	8.3×10^{-3}	0.21
	2	6.7×10^{-2}	4.6×10^{-2}	2.6×10^{-2}
		0.84	0.90	0.55
2	0	1.5×10^{-3}	2.4×10^{-3}	0.16
	1	1.2×10^{-2}	2.5×10^{-2}	0.17
	2	4.5×10^{-2}	9.5×10^{-2}	2.1×10^{-1}
	3	9.5×10^{-2}	0.15	0.12
	4	0.12	6.8×10^{-2}	1.7×10^{-1}
		0.62	0.56	0.47
3	0	8.2×10^{-4}	6.9×10^{-2}	0.21
	1	7.4×10^{-3}	5.3×10^{-2}	9.5×10^{-2}
	2	3.0×10^{-2}	0.14	4.5×10^{-2}
	3	7.1×10^{-2}	0.11	8.4×10^{-2}
	4	0.11	2.7×10^{-3}	2.7×10^{-2}
	5	0.10	6.2×10^{-2}	6.5×10^{-2}
		0.57	0.48	0.43

[a] The single photon energy used in the (2 + 1) REMPI experiments of Ref. 14 for the $v' = 0$–3 levels are 4.118, 4.230, 4.349, and 4.450 eV, respectively. The continuum vibrational energies for each repulsive state were obtained from the relation $E_c = 3\hbar\omega - [E(\infty) - \frac{1}{2}\hbar\omega_e]$, where $E(\infty)$ is the asymptotic energy with respect to the minimum of the $X\,^3\Sigma_g^-$ potential curve (Ref. 29), and ω_e is the ground-state vibrational frequency.
[b] Survival factors (see explanation in text).

Focusing on the $v' = 0$ level in Fig. 3, most of the observed intensity is concentrated in the $\Delta v = 0$ peak. The $\sim 10\%$ intensity in the $v^+ = 1$ peak likely derives from

TABLE III. Autoionization probabilities and survival factors for triplet valence states.

v'[a]	v^+	$B\,^3\Sigma_u^-$	$A\,^3\Sigma_u^+$	$C\,^3\Delta_u$
1	0	0.27	3.5×10^{-3}	3.9×10^{-3}
	1	0.20	2.0×10^{-2}	2.4×10^{-2}
	2	3.6×10^{-3}	4.8×10^{-2}	6.4×10^{-2}
		0.46[b]	0.87	0.84
2	0	0.20	2.0×10^{-3}	2.2×10^{-3}
	1	0.24	1.3×10^{-2}	1.5×10^{-2}
	2	1.4×10^{-2}	3.7×10^{-2}	4.7×10^{-2}
	3	9.6×10^{-2}	5.5×10^{-2}	7.9×10^{-2}
		0.42	0.82	0.77
3	0	0.14	1.2×10^{-3}	1.2×10^{-3}
	1	0.24	8.4×10^{-3}	9.6×10^{-3}
	2	6.8×10^{-2}	2.7×10^{-2}	3.3×10^{-2}
	3	2.5×10^{-2}	4.8×10^{-2}	6.6×10^{-2}
	4	0.14	4.9×10^{-2}	7.7×10^{-2}
	5	4.5×10^{-2}	2.3×10^{-2}	4.8×10^{-2}
		0.36	0.75	0.66

[a] The single-photon energy used in the (2 + 1) REMPI experiments of Ref. 2 for the $v' = 1$–3 levels are 4.192, 4.306, and 4.418 eV, respectively.
[b] Survival factors (see explanation in text).

autoionization of the $^1\Delta_u$ valence state since its survival factor (Table II) deviates considerably from unity. Autoionization of the $^1\Delta_u$ state should remain prevalent for the $v' = 1$ intermediate state.

Comparison with theory suggests that the $v' = 2$ off-diagonal transitions have little contribution from direct ionization. At this level of excitation, the survival factor is about equal for all autoionizing states. Interestingly, there appears to be an effective partitioning of autoionization strength according to whether $\Delta v < 0$ or $\Delta v > 0$. Particularly for $\Delta v < 0$ autoionization of the $^1\Delta_u$ state is strongest, while for $\Delta v > 0$, $^1\Sigma_u^-$ and $^1\Sigma_u^+$ autoionization dominates.

For the $v' = 3$ level again each symmetry makes a substantial contribution to autoionization. In Fig. 3 the apparent agreement between theory and experiment for the $v^+ = 4$ ionic level may be fortuitous since a theoretical treatment incorporating these autoionizing states will redistribute the photoelectron intensity. The increase of the parameter $\zeta^2_{v^+}$ for the $v^+ = 5$ ionic level relative to $v^+ = 4$ for $^1\Sigma_u^+$ and $^1\Delta_u$ symmetries may qualitatively account for the observed increase in photoelectron intensity.

It is interesting to compare the survival factors of the singlet autoionizing valence states with their triplet counterparts of Table III. With the exception of the $^3\Sigma_u^-$ state, autoionization of the singlet states appears more significant than in the triplet case. This circumstance supports the apparent poor level of agreement between present theory and experiment for the $d\,^1\Pi_g$ state. The large shift of the singlet valence states (compared to the triplets) results in overall more favorable Franck–Condon overlaps between the repulsive and ion potential curves.

The above qualitative analysis in terms of survival factors neglects interference with direct ionization. In fact, full theoretical consideration requires simultaneous treatment of the competing processes of direct ionization, autoionization, and dissociation. Such calculations have recently been achieved in REMPI studies[32,33] of the $C\,^1\Pi_u$ state of H_2. MQDT studies[34,35] of H_2 and NO have earlier considered a unified treatment of these competing processes in single-photon absorption. We are currently attempting to include these interactions in further studies of O_2.

2. Autoionization of Rydberg states converging to the $a\,^4\Pi_u$ and $A\,^2\Pi_u$ ionic states

Autoionizing states converging to the $a\,^4\Pi_u$ and $A\,^2\Pi_u$ states of O_2^+ have been investigated by many workers since the early work of Price and Collins,[36] and have recently been discussed and reviewed by Wu.[37] A high-resolution synchrotron study of autoionizing states converging to the $a\,^4\Pi_u$ ion has recently been reported,[38] as well as studies which prepare these states by charge-exchange translational spectroscopy.[39] The earlier discussions[1-5] of the $C\,^3\Pi_g$ REMPI-PES spectra neglected the possible role of these states. Their singlet analogs may influence the $d\,^1\Pi_g$ REMPI spectra as well. In Fig. 4 we show the relevant potential energy curves, and discuss qualitatively in the following section the role of these states in the $C\,^3\Pi_g$ and $d\,^1\Pi_g$ (2 + 1) REMPI problems.

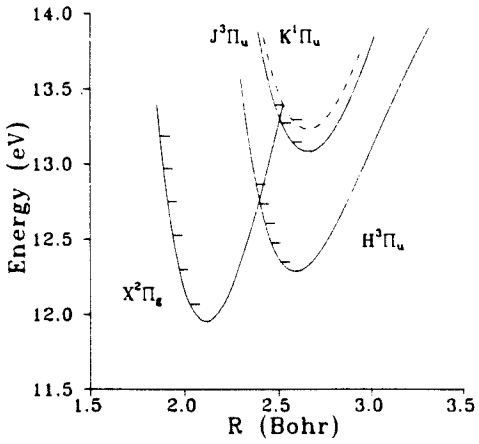

FIG. 4. Potential energy curves for the first ionic state, the $H\,^3\Pi_u$ ($1\pi_u^1 1\pi_g^2 3s\sigma_g$) Rydberg state converging to the $a\,^4\Pi_u$ ionic state (IP = 16.10 eV), and the $J\,^3\Pi_u$ and $K\,^1\Pi_u$ Rydberg states which converge to the $A\,^2\Pi_u$ ionic state (IP = 17.05 eV). The potentials for the H and J states are Morse curves constructed from constants given in Refs. 37 and 40. The K state (dashed curve) is shifted upward from the J state by 0.15 eV, as discussed in the text.

a. $^3\Pi_u$ *autoionizing states.* For triplet states, Nishitani *et al.*[40] have unambiguously assigned the vibrational progression in the 900–1010 Å region as all belonging to a single $H\,^3\Pi_u$ ($1\pi_u^1 1\pi_g^2 3s\sigma_g$) Rydberg state converging to the $a\,^4\Pi_u$ ion. This state is energetically accessible in the $v' = 1$–3 levels of the $C\,^3\Pi_g$ one-color REMPI studies. Due to the large displacement of the potential curves, Franck–Condon factors become appreciable mainly for higher vibrational levels of the $X\,^2\Pi_g$ ion. Calculated Franck–Condon factors between the $H\,^3\Pi_u$ state and the $X\,^2\Pi_g$ ion are given in Table IV, which agree with the corresponding distributions plotted in Fig. 5 of Ref. 40. For one-color (2 + 1) REMPI via the $v' = 1,2$ levels of the $C\,^3\Pi_g$ state, the total photon energy nearly coincides with the $v = 2 (T_0 = 12.61$ eV) and $v = 5 (T_0 = 12.98$ eV) levels of the $H\,^3\Pi_u$ state, respectively. Qualitatively, as follows from the theoretical analysis of

TABLE IV. Calculated Franck–Condon factors for the transitions O_2 $H\,^3\Pi_u(v) \rightarrow O_2^+$ $X\,^2\Pi_g(v^+)$.[a]

	$v = 0$	1	2	3	4	5	6
$v^+ = 0$	0.0000	0.0002	0.0007	0.0019	0.0043	0.0080	0.0132
1	0.0003	0.0021	0.0069	0.0156	0.0280	0.0419	0.0543
2	0.0024	0.0117	0.0297	0.0520	0.0698	0.0755	0.0672
3	0.0104	0.0385	0.0716	0.0871	0.0746	0.0441	0.0149
4	0.0317	0.0825	0.0997	0.0672	0.0211	0.0002	0.0102
5	0.0718	0.1170	0.0715	0.0106	0.0046	0.0336	0.0477

[a] Franck–Condon factors were obtained using a Morse potential with spectroscopic constants from Ref. 40 for the O_2 $H\,^3\Pi_u$ state, and with the RKR potential of Ref. 29 for the O_2^+ $X\,^2\Pi_g$ state.

Smith[41] and Mies,[42] we would expect autoionization to be favored in the $\Delta v > 0$ transitions, i.e., the $v^+ = 2$ and 3 levels. These states could influence the vibrational distribution for the $v' = 3$ level of the $C\,^3\Pi_g$ state as well. Note that, although the Franck–Condon factors in Table IV are small, autoionization of the $H\,^3\Pi_u$ state is prominent in single-photon ionization spectra leading to the $X\,^2\Pi_g$ ion.[38,44]

The $J\,^3\Pi_u(1\pi_u^3 1\pi_g^2 3s\sigma_g)$ state, which is the first member of a Rydberg series converging to the $A\,^2\Pi_u$ ion,[37,40] lies 0.8 eV above the $H\,^3\Pi_u$ state and is energetically accessible in the $v' = 3$ REMPI spectra of the $C\,^3\Pi_g$ state. The total photon energy for $v' = 3$ (13.254 eV) lies slightly below the $v = 1$ level ($T_0 = 13.27$ eV) of the $J\,^3\Pi_u$ state. This level would preferentially autoionize into the $v^+ = 3$–5 levels of the ion, as qualitatively indicated by examining the $v = 1$ Franck–Condon distribution in Table IV, which should be nearly identical for the $J\,^3\Pi_u$ and $H\,^3\Pi_u$ states.

b. $^1\Pi_u$ *autoionizing states.* Singlet Rydberg states with the $1\pi_u^3 1\pi_g^2 3s\sigma_g$ configuration, which have not yet been observed, are likely relevant to one-color REMPI of the $d\,^1\Pi_g$ state. Such a singlet Rydberg state with the above configuration, which we denote $K\,^1\Pi_u$, may only be associated with the $A\,^2\Pi_u$ ion core, i.e., the singlet analog of the $J\,^3\Pi_u$ state (see Fig. 4). The predicted term value of $T_0 = 13.30$ eV (derived below) makes this state energetically accessible for the $v' = 3$ REMPI spectra of the $d\,^1\Pi_g$ state (Fig. 3). In particular, the total photon energy for the $v' = 3$ $d\,^1\Pi_g$ state REMPI spectra (13.380 eV) nearly coincides with the $v = 0$ level of the $K\,^1\Pi_u$ state. Therefore, from Table IV (which should remain essentially valid for the $K\,^1\Pi_u$ state) we expect preferential autoionization into $v^+ = 3$–5 levels of the ion.

c. SCF calculations. To support the above qualitative discussion and previous assignments of the H and $J\,^3\Pi_u$ states,[37,40] we have performed single-configuration SCF calculations on the J, H, and the $K\,^1\Pi_u$ state of O_2. The open-shell wave functions for these states have the form

$$\Psi(H\,^3\Pi_u) = \frac{1}{\sqrt{12}}\{3|1\pi_u^+\,\overline{1\pi}_u^+\,1\pi_u^-\,\overline{3s\sigma}_g\,1\pi_g^+\,1\pi_g^-| - |1\pi_u^+\,\overline{1\pi}_u^+\,\overline{1\pi}_u^-\,3s\sigma_g\,1\pi_g^+\,1\pi_g^-| - |1\pi_u^+\,\overline{1\pi}_u^+\,1\pi_u^-\,3s\sigma_g\,\overline{1\pi}_g^+\,1\pi_g^-| - |1\pi_u^+\,\overline{1\pi}_u^+\,1\pi_u^-\,3s\sigma_g\,1\pi_g^+\,\overline{1\pi}_g^-|\}, \quad (3a)$$

$$\Psi(J\,^3\Pi_u) = \frac{1}{\sqrt{6}}\{2|1\pi_u^+\,\overline{1\pi}_u^+\,\overline{1\pi}_u^-\,3s\sigma_g\,1\pi_g^+\,1\pi_g^-| - |1\pi_u^+\,\overline{1\pi}_u^+\,1\pi_u^-\,3s\sigma_g\,1\pi_g^+\,\overline{1\pi}_g^-| - |1\pi_u^+\,\overline{1\pi}_u^+\,1\pi_u^-\,3s\sigma_g\,\overline{1\pi}_g^+\,1\pi_g^-|\}, \quad (3b)$$

$$\Psi(K\,^1\Pi_u) = \frac{1}{\sqrt{12}}\{2|1\pi_u^+\,\overline{1\pi}_u^+\,1\pi_u^-\,3s\sigma_g\,\overline{1\pi}_g^+\,\overline{1\pi}_g^-| - |1\pi_u^+\,\overline{1\pi}_u^+\,\overline{1\pi}_u^-\,3s\sigma_g\,1\pi_g^+\,\overline{1\pi}_g^-| - |1\pi_u^+\,\overline{1\pi}_u^+\,\overline{1\pi}_u^-\,3s\sigma_g\,\overline{1\pi}_g^+\,1\pi_g^-| + 2|1\pi_u^+\,\overline{1\pi}_u^+\,\overline{1\pi}_u^-\,\overline{3s\sigma}_g\,1\pi_g^+\,1\pi_g^-| - |1\pi_u^+\,\overline{1\pi}_u^+\,1\pi_u^-\,\overline{3s\sigma}_g\,1\pi_g^+\,\overline{1\pi}_g^-| - |1\pi_u^+\,\overline{1\pi}_u^+\,1\pi_u^-\,\overline{3s\sigma}_g\,\overline{1\pi}_g^+\,1\pi_g^-|\}. \quad (3c)$$

With a basis identical to that of the $C\,^3\Pi_g$ and $d\,^1\Pi_g$ state SCF calculations, we find total energies of $-149.240\,43$, $-148.875\,84$, and $-148.870\,34$ a.u., at $R = 2.282\,a_0$, respectively, for these states. For the $H\,^3\Pi_u$ state, we calculate the $3s\sigma_g$ orbital eigenvalue to be -3.52 eV. Using the experimental ionization potential of 16.10 eV,[37,40] we calculate a term value and quantum defect of $T_0 = 12.58$ eV and $\delta = 1.034$, which compare reasonably well with the experimental values[40] of 12.35 eV and 1.095, respectively. The $J\,^3\Pi_u$ and $K\,^1\Pi_u$ states each consist of a mixture between three components, corresponding to the three parentages $^3\Sigma_g^-$, $^1\Delta_g$ and $^1\Sigma_g^+$ associated with the $^2\Pi_u(1\pi_u^3 1\pi_g^2)$ states of the ion core.[45,46] Instead of solving a three term secular problem, we invoke a simplification by initially calculating the $J\,^3\Pi_u$ and $K\,^1\Pi_u$ SCF states corresponding to pure $^3\Sigma_g^-$ parentage. The wave functions given in Eqs. (3b) and (3c) above assume this single parentage. We then calculated an empirically corrected term value for the $J\,^3\Pi_u$ state by employing the $3s\sigma_g$ orbital eigenvalue, -3.67 eV, and the observed $A\,^2\Pi_u$ ionization potential, 17.05 eV.[37,40] For the $J\,^3\Pi_u$ state our calculation gives $T_0 = 13.38$ eV and $\delta = 1.075$, compared to the experimental values[40] of 13.15 eV and 1.133, respectively. Using the singlet–triplet splitting obtained by subtracting total $J\,^3\Pi_u$ and $K\,^1\Pi_u$ SCF energies (0.15 eV), and the *experimental* term value of the $J\,^3\Pi_u$ state, the predicted term value of the $K\,^1\Pi_u$ state is $T_0 = 13.30$ eV, with a singlet quantum defect of $\delta = 1.095$.

The $^{1,3}\Pi_u$ Rydberg states may be incorporated into *ab initio* photoionization calculations using the Smith–Mies–Fano[41–43] procedure or an appropriate MQDT treatment. However since the $^{1,3}\Pi_u$ ionization channels contain the σ_u shape resonance, the associated non-Franck–Condon effect must be incorporated explicitly, as done here at the one-electron level for direct photoionization.

3. Initial-state perturbations

Another mechanism leading to non-Franck–Condon effects in vibrational distributions is perturbation of the initial Rydberg state by the valence–Rydberg interaction, i.e., an avoided crossing. The $C\,^3\Pi_g$ and $d\,^1\Pi_g$ Rydberg states of O_2 are intersected by $1\,^3\Pi_g$ and $1\,^1\Pi_g$ valence potential energy curves, which are derived from the electronic configuration $3\sigma_g 1\pi_g^3$. Cartwright *et al.*[8] first postulated the weak electronic interaction leading to the interpretation of two crossing diabatic states near the minimum of the $C\,^3\Pi_g$ Rydberg potential curve. For the $d\,^1\Pi_g$ state, Van der Zande *et al.*[16] have recently deduced the coupling matrix element H_{el} of 55 meV from their kinetic-energy-release spectra, and accounted for the decrease in rotational constant $B_{v'}$ going from $v' = 0$–3, and its return to that of the ion for $v' > 3$. To estimate the effect of this perturbation on the $d\,^1\Pi_g$ REMPI spectra, we calculated the $v' = 0$–3 vibrational wave functions for the lower adiabatic potential ($v' = 1,4,8,12$ for the double well[16]) without nonadiabatic coupling, and directly incorporated them in the calculation of the vibrational

branching ratios. Since a dipole transition between the $3\sigma_g 1\pi_g^2$ state and the $3s\sigma_g \rightarrow k\pi_u$ continuum is very weak, and nonadiabatic corrections to the vibrational wave functions are small,[16] we expect this procedure to be a good approximation. We found almost negligible changes in the branching ratios, due to the preservation of nodal structure of the vibrational wave functions in the inner region of the double-well potential curve. This further indicates that the (final-state) autoionization effects discussed above are likely dominant. For situations where there is a strong avoided crossing, e.g., the $B\,^3\Sigma_u^- - E\,^3\Sigma_u^-$ system of O_2, one must solve the coupled Schrödinger equations for a full treatment.[47,48]

C. Photoelectron angular distributions

Figure 5 shows calculated vibrationally resolved photoelectron angular distributions for the $v' = 0$ and 1 levels of the $d\,^1\Pi_g$ Rydberg state. In these figures we have plotted the angular distribution

$$\frac{d\sigma}{d\Omega} \propto 1 + \beta P_2(\cos\theta), \tag{4}$$

where β is the asymmetry parameter for an unaligned molecular target, θ is the angle between the direction of the light polarization and the photoelectron momentum, and P_2 is a Legendre polynomial. The numerical values of the β parameters and those for other v' levels are given in Table V. No experimental values are available for the $d\,^1\Pi_g$ state, although a comparision between theory and experimental results for the $C\,^3\Pi_g$ state has been made, with satisfying results.[4,5] Note that we have neglected any effects due to state alignment arising from the two-photon excitation. This will be of interest in future experimental studies of specific rotational branches.

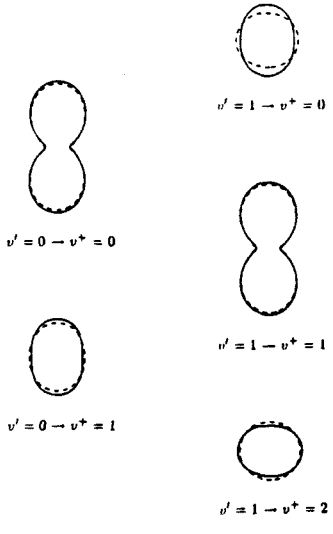

FIG. 5. Calculated photoelectron angular distributions for the $v' = 0$ and 1 levels of the O_2 $d\,^1\Pi_g$ state. Solid curve: length form; dash curve: velocity form. In this figure $\theta = 0$ is vertical.

TABLE V. Summary of calculated vibrationally resolved asymmetry parameters.

v'	v^+	$\beta_{v'v^+}$	
		Length	Velocity
0	0	1.213	1.126
0	1	0.282	0.143
1	0	0.202	−0.086
1	1	1.227	1.162
1	2	−0.150	−0.027
2	0	0.572	0.591
2	1	−0.181	−0.110
2	2	1.232	1.201
2	3	0.013	−0.092
2	4	0.790	0.660
3	0	0.121	0.128
3	1	0.448	0.445
3	2	0.002	0.086
3	3	1.240	1.278
3	4	0.335	0.098
3	5	0.683	0.583

The difference between $\Delta v = 0$ and $\Delta v \neq 0$ distributions is very large, due to the non-Franck–Condon effect associated with the σ_u resonance. This is similar to that discussed for the $C\,^3\Pi_g$ state.[5] However, there is also considerable difference between the $\Delta v \neq 0$ angular distributions for the singlet state compared to the triplet. For example, for the $v' = 1 \rightarrow v^+ = 2$ transition, the calculated[5] (velocity form) β for the triplet state is 0.55, and $\beta = -0.027$ for the singlet (Table V), at nearly the same total photon energy of ~12.5 eV.

It would be interesting to experimentally measure these photoelectron angular distributions to confirm this large multiplet-specific effect, which is not too apparent when comparing the singlet and triplet branching ratios. Additionally, it would be useful to measure changes in the higher-order terms in the REMPI angular distributions and compare them with their triplet counterparts[4,5] so as to ascertain the role of spin coupling in the alignment induced by the two-photon absorption step.

D. Energy-dependent branching ratios and angular distributions

(2 + 1′) two-color REMPI studies of the $d\,^1\Pi_g$ state may provide useful insight into the role of autoionization on these ion vibrational distributions. To illustrate what the present one-electron theory predicts for the energy dependence of such distributions, Fig. 6 shows calculated vibrationally resolved branching ratios and photoelectron angular distributions for photoionization of the $v' = 3$ level over a range of photon energies. For the branching ratios, all curves begin at 4.32 eV photon energy above the $v' = 3$ level of the $d\,^1\Pi_g$ state and the $v^+ = 0$–5 channels are hence energeti-

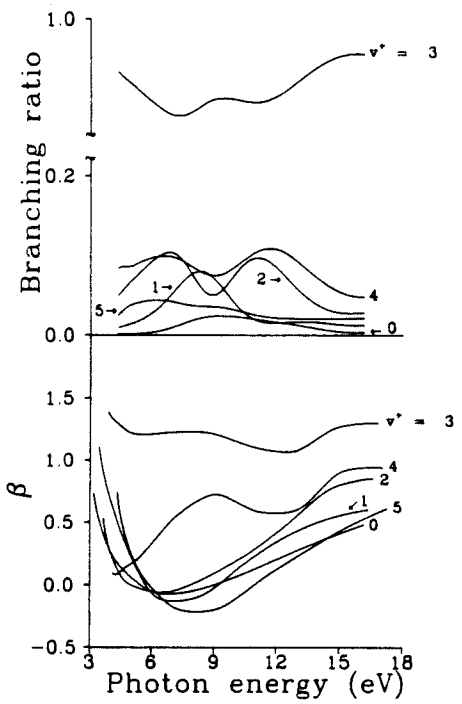

FIG. 6. Calculated energy-dependent vibrational branching ratios and asymmetry parameters for the $v' = 3$ level of the O_2 $d\,^1\Pi_g$ state leading to the $v^+ = 0$–5 levels of the ion.

cally open. The distributions are normalized such that a sum at any photon energy equals unity.

The $\Delta v = 0$ component dominates at all photon energies. For $\Delta v \neq 0$ distributions, the $v' = 3 \rightarrow v^+ = 4$ ratio is the dominant component, due to strong asymmetry of the R-dependent amplitudes at larger internuclear distances where the shape resonance is most intense. Due to nodal structure of the vibrationally excited initial state wave functions, secondary maxima associated with the resonance may occur in the cross sections (and thus branching ratios), e.g., ~11 eV photon energy. Thus, we predict an apparent "detuning" effect from the resonance to occur near threshold, e.g., ~9 eV for the $v' = 3 \rightarrow v^+ = 2$–4 ratios, and at photon energies beyond 15 eV for all transitions.

The strong variation in asymmetry parameter β with v^+ in the bottom of Fig. 6 reflects the non-Franck–Condon effect induced by the shape resonance, as seen previously in angular distribution studies of O_2 $C\,^3\Pi_g$ photoionization,[4,5] and other studies of molecules in their ground state.[25] The structure in the $v^+ = 3$ and 4 distributions reflects the secondary maxima occuring in the vibrational branching ratios.

IV. CONCLUSION

We have presented ionic vibrational branching ratios and vibrationally resolved photoelectron angular distributions for photoionization of the $d\,^1\Pi_g$ Rydberg state of O_2. The non-Franck–Condon effects induced by the σ_u shape resonance accounts for some of the observed[14] deviations from the expected $\Delta v = 0$ propensity rule for ionization of molecular Rydberg states. However, the vibrational branching ratios calculated with the Hartree–Fock model, which include the effects of the shape resonance, differ significantly from the observed values. There are no measurements of the photoelectron angular distributions for the $d\,^1\Pi_g$ state. It would be interesting to compare these photoelectron angular distributions with those for the $C\,^3\Pi_g$ state,[4] since the present calculations predict significant differences due to the particular spin couplings in the resonant intermediate and final states.

In the present $d\,^1\Pi_g$ REMPI problem, multichannel interactions involving both repulsive and Rydberg autoionizing states likely result in the major departures from the simple Franck–Condon prediction. We have tentatively identified these interactions as arising from autoionization of singlet valence states derived from the $1\pi_u^3 1\pi_g^3$ electronic configuration, analogous to earlier assessments for the $C\,^3\Pi_g$ state.[2–5] Evidence has also been presented which indicates that Rydberg states which converge to the $a\,^4\Pi_u$ and $A\,^2\Pi_u$ ion states may be responsible for a portion of the observed $\Delta v \neq 0$ intensity, in both $C\,^3\Pi_g$ and $d\,^1\Pi_g$ state REMPI spectra. Since the singlet states associated with the $A\,^2\Pi_u$ ion core have not been observed, it may be of interest to probe them directly by inducing single-photon transitions from, e.g., the O_2 $X\,^3\Sigma_g^-$ or $^1\Delta_g$ states, or by charge-exchange translational spectroscopy.

ACKNOWLEDGMENTS

The authors are grateful to P. J. Miller and W. A. Chupka for permission to use unpublished REMPI photoelectron spectra for the O_2 $d\,^1\Pi_g$ state in this work. This work was supported by grants from the National Science Foundation (CHE-8521391), Air Force Office of Scientific Research (Contract No. 87-0039), and the Office of Health and Environmental Research of the U.S. Department of Energy (DE-FG03-87ER60513). We also acknowledge use of resources of the San Diego SuperComputer Center, which is supported by the National Science Foundation. One of us (M. B.) would like to acknowledge support from a Department of Education Fellowship.

[1] S. Katsumata, K. Sato, Y. Achiba, and K. Kimura, J. Electron Spectrosc. Relat. Phenom. 41, 325 (1986).
[2] P. J. Miller, L. Li, W. A. Chupka, and S. D. Colson, J. Chem. Phys. 89, 3921 (1988).
[3] J. A. Stephens, M. Braunstein, and V. McKoy, J. Chem. Phys. 89, 3923 (1988).
[4] P. J. Miller, W. A. Chupka, J. Winniczek, and M. G. White, J. Chem. Phys. 89, 4058 (1988).
[5] M. Braunstein, J. A. Stephens, and V. McKoy J. Chem. Phys. 90, 633 (1989).
[6] H. Park, P. J. Miller, W. A. Chupka, and S. D. Colson, J. Chem. Phys. 89, 3919 (1988).
[7] H. Park, P. J. Miller, W. A. Chupka, and S. D. Colson, J. Chem. Phys. 89, 6676 (1988).

[8] D. C. Cartwright, W. J. Hunt, W. Williams, S. Trajmar, and W. A. Goddard, Phys. Rev. A **8**, 2436 (1973).
[9] S. Trajmar, D. C. Cartwright, and R. I Hall, J. Chem. Phys. **65**, 5275 (1976).
[10] T. York and J. Comer, J. Phys. B **16**, 3627 (1983).
[11] A. Sur, C. V. Ramana, and S. D. Colson, J. Chem. Phys. **83**, 904 (1985).
[12] A. Sur, C. V. Ramana, W. A. Chupka, and S. D. Colson, J. Chem. Phys. **84**, 904 (1985).
[13] R. D. Johnson, G. R. Long, and J. W. Hudges, J. Chem. Phys. **87**, 1977 (1987).
[14] P. J. Miller and W. A. Chupka (private communication).
[15] W. J. van der Zande, W. Koot, J. R. Peterson, and J. Los, Chem. Phys. Lett. **140**, 175 (1987).
[16] W. J. van der Zande, W. Koot, J. Los, and J. R. Peterson, J. Chem. Phys. **89**, 6758 (1988).
[17] R. R. Lucchese, G. Raseev, and V. McKoy, Phys. Rev. A **25**, 2572 (1982).
[18] R. R. Lucchese, K. Takatsuka, and V. McKoy, Phys. Rep. **131**, 147 (1986), and references therein.
[19] G. Raseev, H. Lefebvre-Brion, H. LeRouzo, and A. L. Roche, J. Chem. Phys. **74**, 6686 (1981).
[20] A. Gerwer, C. Asaro, B. V. McKoy, and P. W. Langhoff, J. Chem. Phys. **72**, 713 (1980).
[21] P. M. Dittman, D. Dill, and J. L. Dehmer, J. Chem. Phys. **76**, 5703 (1982).
[22] M. Braunstein and V. McKoy, J. Chem. Phys. **90**, 2575 (1989).
[23] M. Braunstein, V. McKoy, and M. E. Smith, J. Chem. Phys. **90**, 3931 (1989).
[24] J. L. Dehmer, D. Dill, and S. Wallace, Phys. Rev. Lett. **43**, 1005 (1979); R. Stockbauer, B. E. Cole, D. L. Ederer, J. B. West, A. C. Parr, and J. L. Dehmer, *ibid.* **43**, 757 (1979); J. B. West, A. C. Parr, B. E. Cole, D. L. Ederer, R. Stockbauer, and J. L. Dehmer, J. Phys. B **13**, 1105 (1980).
[25] J. L. Dehmer, A. C. Parr, and S. H. Southworth, in *Handbook on Synchrotron Radiation*, edited by G. V. Marr (North-Holland, Amsterdam, 1987), Vol. II, p. 241.
[26] I. Nenner and J. A. Beswick, in *Handbook on Synchrotron Radiation*, edited by G. V. Marr (North-Holland, Amsterdam, 1987). Vol. II, p. 355.
[27] A. Giusti, J. Phys. B **13**, 3867 (1980).
[28] H. Lefebvre-Brion and R. W. Field, *Pertubations in the Spectra of Diatomic Molecules* (Academic, Orlando, 1986), Chap. 2, Sec. 3.1.
[29] P. Krupenie, J. Phys. Chem. Ref. Data **1**, 423 (1972).
[30] R. P. Saxon and B. Liu, J. Chem. Phys. **67**, 5432 (1977).
[31] S. L. Guberman, Planet. Space Sci. **36**, 47 (1988).
[32] S. N. Dixit, D. L. Lynch, V. McKoy, and A. U. Hazi, Phys. Rev. A **40**, 1700 (1989).
[33] A. P. Hickman, Phys. Rev. Lett. **59**, 1553 (1987).
[34] Ch. Jungen, Phys. Rev. Lett. **53**, 2394 (1984).
[35] A. Giusti-Suzor and Ch. Jungen, J. Chem. Phys. **80**, 986 (1984).
[36] W. C. Price and G. Collins, Phys. Rev. **48**, 714 (1935).
[37] C. Y. Wu, J. Quant. Spectrosc. Radiat. Transfer **37**, 1 (1987).
[38] D. M. P. Holland and J. B. West, Z. Phys. D **4**, 367 (1987).
[39] W. J. van der Zande, W. Koot, J. R. Peterson, and J. Los, Chem. Phys. **126**, 169 (1988).
[40] E. Nishitani, I. Tanaka, K. Tanaka, T. Kato, and I. Koyano, J. Chem. Phys. **81**, 3429 (1984).
[41] A. L. Smith, Philos. Trans. R. Soc. London Ser A **268**, 169 (1970); J. A. Kinsinger and J. W. Taylor, Int. J. Mass Spectrosc. Ion Phys. **11**, 461 (1973). See also Ref. 26, Sec. 3.2.3.
[42] F. H. Mies, Phys. Rev. **175**, 164 (1968).
[43] U. Fano, Phys. Rev. **124**, 1866 (1961).
[44] P. M. Dehmer and W. A. Chupka, J. Chem. Phys. **62**, 4525 (1975).
[45] R. N. Dixon and S. E. Hull, Chem. Phys. Lett. **3**, 367 (1969); See also Ref. 28, Sec. 2.2.3 for a thorough discussion of this problem.
[46] N. Honjou, K. Tanaka, K. Ohno, and H. Taketa, Mol. Phys. **35**, 1569 (1978).
[47] J. Wang, A. J. Blake, and L. Torop, J. Chem. Phys. **89**, 4654 (1988).
[48] P. J. Miller, L. Li, W. A. Chupka, and S. D. Colson, J. Chem. Phys. **88**, 2972 (1988).

Chapter 4

Studies of the photoionization of the lowest excited state, a $^1\Delta_g$, and ground state, X $^3\Sigma_g^-$, of molecular oxygen

Studies of the photoionization of the lowest excited state, a $^1\Delta_g$, and ground state, X $^3\Sigma_g^-$, of molecular oxygen

M. Braunstein and V. McKoy

Arthur Amos Noyes Laboratory of Chemical Physics

California Institute of Technology

Pasadena, California 91125

Abstract

We report photoionization cross sections and photoelectron angular distributions for O_2 from its ground state, X $^3\Sigma_g^-$, and lowest electronically excited state, a $^1\Delta_g$, leading to the ground state ion, X $^2\Pi_g$, using Hartree-Fock photoelectron orbitals obtained from the Schwinger variational method. These studies were motivated by recent line source experiments at 21.2 eV which showed substantial differences between these cross sections. We find that the low energy σ_u shape resonance previously observed in ground state photoionization of O_2 also influences the a $^1\Delta_g$ cross sections, but does not account for the differences in the ground and excited state cross sections seen experimentally. In fact our results show that these cross sections are quite similar over a broad energy range.

I. Introduction

Although photoionization of the lowest electronically excited state of molecular oxygen, a $^1\Delta_g$, is known to play an important role in the chemistry of the atmosphere,[1] relatively little is known about its photoionization cross sections and there has been no report on the photoelectron angular distributions from this excited state. Clark and Wayne,[2] using the relative measurements of Cairns and Samson,[3] have reported the absolute cross sections within about one eV of the X $^2\Pi_g$ threshold, showing a rise from ~2 Mb to ~6 Mb with sharp autoionizing structure superimposed. Recently, there has been a measurement of the a $^1\Delta_g$ $\longrightarrow$ X $^2\Pi_g$ cross section at the He I line (21.2 eV) which gave a value of 11.8 Mb,[4] which compares with a value of 7.4 Mb for the cross section from the ground state of O_2, X $^3\Sigma_g^-$ $\longrightarrow$ X $^2\Pi_g$, at the same photon energy.[5] The only available theoretical work on the a $^1\Delta_g$ photoionization cross section used orthogonalized plane waves to represent the photoelectron continuum.[6] These cross sections differ substantially from the measurements at the He I line, being nearly identical to the photoionization cross sections of the ground state, X $^3\Sigma_g^-$ $\longrightarrow$ X $^2\Pi_g$, over a broad energy range.

It has been shown, however, that there is a low energy shape resonance in the ground state photoionization of O_2.[7-9] This shape resonance is probably not well represented by the orthogonal plane wave calculations on the a $^1\Delta_g$ state and could be important in explaining the difference in magnitude between the X $^3\Sigma_g^-$ and a $^1\Delta_g$ cross sections observed experimentally. To investigate this possiblity and make a more complete picture of excited state a $^1\Delta_g$ photoionization, we have calculated cross sections and photoelectron angular distributions for photoionization of the a $^1\Delta_g$ state leading to the X $^2\Pi_g$ ion using Hartree-Fock photoelectron continuum orbitals obtained with the Schwinger variational method[10] which should accurately reflect any shape resonant structure. To provide some context for these

studies we have also calculated vibrationally-unresolved photoionization cross sections and photoelectron angular distributions for ground state photoionization of O_2 leading to the X $^2\Pi_g$ ion over a broad energy range, extending our previous study[7] on the vibrationally-resolved cross sections of the ground state at low energy.

The remainder of this study is as follows. In Section II we will discuss the relevant Hartree-Fock wave functions and static-exchange potentials. We will also briefly discuss the method we use to calculate the photoelectron orbitals. In Section III, we will present our results for X $^3\Sigma_g^-$ and a $^1\Delta_g$ photoionization leading to the X $^2\Pi_g$ ion and compare these results to experiment.

II. Method and Calculations

The electronic structure of O_2 is $1\sigma_g^2\ 1\sigma_u^2\ 2\sigma_g^2\ 2\sigma_u^2\ 3\sigma_g^2\ 1\pi_u^4\ 1\pi_g^2$. For the ground state, the $1\pi_g$ electrons are triplet coupled and are singlet coupled for the excited state, a $^1\Delta_g$. This results in an energy splitting of about 1 eV. The equilibrium bond length and spectroscopic constants remain nearly identical.[11]

Photoionization of the ground state, X $^3\Sigma_g^-$, leading to the X $^2\Pi_g$ ion gives three dipole-allowed final states:

$$\Psi(^3\Pi_u) = |1\pi_g^+\, k\sigma_u|, \tag{1a}$$

$$\Psi(^3\Sigma_u^-) = \frac{1}{\sqrt{2}}\{|1\pi_g^+\, k\pi_u^-| - |1\pi_g^-\, k\pi_u^+|\}, \tag{1b}$$

$$\Psi(^3\Pi_u) = |1\pi_g^+\, k\delta_u^-|, \tag{1c}$$

where we include implicitly the closed-shell core. For photoionization of the a $^1\Delta_g$ state the dipole-allowed final state wave functions are

$$\Psi(^1\Pi_u) = \frac{1}{\sqrt{2}}\{|1\pi_g^+ \overline{k\sigma_u}| - |\overline{1\pi_g^+}\, k\sigma_u|\}, \tag{2a}$$

$$\Psi(^1\Delta_u) = \frac{1}{\sqrt{2}}\{|1\pi_g^+ \overline{k\pi_u^+}| - |\overline{1\pi_g^+}\, k\pi_u^+|\}, \tag{2b}$$

$$\Psi(^1\Phi_u) = \frac{1}{\sqrt{2}}\{|1\pi_g^+ \overline{k\delta_u^+}| - |\overline{1\pi_g^+}\, k\delta_u^+|\}. \tag{2c}$$

With these wave functions, the static-exchange one-electron equations for the photoelectron orbital, ϕ_k, can be obtained from the variational expression, $\langle \delta\Psi | H - E|\Psi\rangle = 0$, where H is the fixed-nuclei Hamiltonian and E is the total energy. These equations have the form

$$P[f + \sum_{core}(2J_i - K_i) + \sum_{open}(a_n J_n + b_n K_n) + \alpha S''_{1\pi_g} + \beta S'_{1\pi_g} - \epsilon]P \mid \phi_k >= 0, \tag{3}$$

where J_i and K_i are Coulomb and exchange operators respectively and P is a projection operator which enforces orthogonality of the continuum orbital to the occupied orbitals.[10] The photoelectron kinetic energy is given by $\epsilon = 1/2\ \mathrm{k}^2$. The operators S'' and S' are given by

$$S''_{1\pi_g}\phi_+(\mathbf{r}_1) = \phi_-(\mathbf{r}_1)\int d^3\mathbf{r}_2[\pi_-(\mathbf{r}_2)]^*\frac{1}{r_{12}}\pi_+(\mathbf{r}_2) \tag{4a}$$

and

$$S'_{1\pi_g}\phi_+(\mathbf{r}_1) = \pi_+(\mathbf{r}_1)\int d^3\mathbf{r}_2[\pi_-(\mathbf{r}_2)]^*\frac{1}{r_{12}}\phi_-(\mathbf{r}_2). \tag{4b}$$

The one-electron operator, f, in Eq. (3) is

$$f = -\frac{1}{2}\nabla_i^2 - \sum_\alpha \frac{Z_\alpha}{r_{i\alpha}}, \tag{5}$$

where Z_α is the nuclear charge of center α. Using the wave functions given in Eqs. (1) and (2), the coefficients a_n, b_n, α, and β in Eq. (3) are given in Table I.

The photoelectron orbitals of the the static-exchange equations, Eq. (3), were obtained using the iterative Schwinger variational method, discussed extensively elsewhere.[10,12] To solve the Lippmann-Schwinger equations for the continuum orbital associated with the non-local molecular ion potential, the scattering potential is approximated by a separable form

$$U(\mathbf{r},\mathbf{r}') \cong U^S(\mathbf{r},\mathbf{r}') = \sum_{ij} \langle \mathbf{r} \mid U \mid \alpha_i \rangle (U^{-1})_{ij} \langle \alpha_j \mid U \mid \mathbf{r}' \rangle, \tag{6}$$

where the matrix U^{-1} is the inverse of the matrix with elements $U_{ij} = \langle \alpha \mid U \mid \alpha_j \rangle$ and the α_i's are discrete basis functions (see Table II). To ensure convergence of the photoionization cross sections, we use photoelectron wave functions obtained after one step in our iterative procedure.[10]

For the ground state of O_2, we used the [3s2p] Cartesian Gaussian basis set of Dunning[13] with a single d-type polarization function.[14] Calculations with this basis set at the equilibrium geometry of R_e(O-O) = 2.282 a.u. give an SCF energy of -149.635 14 a.u. For the a $^1\Delta_g$ state, we used the [4s3p] basis set of Dunning[13] with two uncontracted d-type polarization functions[14]. Calculations with this basis set at the equilibrium geometry R_e(O-O) = 2.297 a.u. for this state give an SCF energy of 149.562 19 a.u.[15] This gives a calculated singlet-triplet splitting of 1.98 eV compared to the experimental value of 0.98 eV.[11] All matrix elements and functions arising in the solution of the Lippmann-Schwinger equations associated with Eq.

(3) were evaluated via single-center expansions about the molecular center. The partial-wave expansion of the photoelectron orbital, i.e.,

$$\phi_k^{(-)} = (\frac{2}{\pi})^{1/2} \sum_{\ell=0}^{\ell_p} \sum_{m=-\ell}^{+\ell} i^\ell \phi_{k\ell m}^{(-)}(\mathbf{r}) Y_{\ell m}^*(\Omega_k), \tag{7}$$

was truncated at $\ell_p = 7$. The other partial-wave expansion parameters and radial grid were the same as those used in Ref. 16 for the ground state of O_2 and Ref. 7 for the excited state.

Finally, it is important to note that the total cross section, σ, given in terms of the final state symmetry contributions (see Table II) can be written

$$\sigma = \frac{8\pi^2\omega}{3c}[|\langle \pi_g|\hat{r}_1|k\sigma_u\rangle|]^2 + [|\langle \pi_g|\hat{r}_0|k\pi_u\rangle|]^2 + [|\langle \pi_g|\hat{r}_{-1}|k\delta_u\rangle|]^2, \tag{8}$$

where $\hat{r}_{\pm 1} = \mp(x \pm iy)/\sqrt{2}$ and $\hat{r}_0 = z$, and is the same for photoionization for transitions from the ground state and a $^1\Delta_g$ excited state of O_2 to the $X^2\Pi_g$ state of O_2^+. This means that in the high energy limit, where the slight differences between the target orbitals and static-exchange potentials become less important and away from any resonant structure, one should expect the photoionization cross sections from these two states to the ground state of the ion to be nearly the same. This has important consequences in understanding the differences in the cross sections from these two states.

III. Results and Discussion

Calculations of the vibrationally-resolved photoionization cross section and photoelectron angular distributions near threshold for photoionization of the ground state of O_2 to the ground state ion have been presented previously.[7] These studies

showed that a low energy σ_u shape resonance significantly influences the ion vibrational distributions, producing large deviations from Franck-Condon behavior. In figure 1 we show results for the vibrationally unresolved cross section along with experimental data[5,17,18] over an extended energy range to provide a context for understanding photoionization of the excited a $^1\Delta_g$ state. Below ~25 eV, there is extensive scatter in the experimental data which suggests sharp structure typical of autoionization. Several authors[19-21] have investigated this rich autoionizing structure in detail with high resolution experiments and have assigned many Rydberg states associated with excited ion cores in this energy region.[22] Above ~25 eV there is good agreement between the present results and the experimental data which shows the cross section slowly diminishing after a maximum at ~25 eV. The agreement between the calculated asymmetry parameters and the experimental data[23-26] are also quite good over a broad energy range and show a rapid variation of β from threshold to about 30 eV photon energy.

In Fig. 2, we show the partial cross sections and eigenphase sums for the transition $X\,^3\Sigma_g^- \longrightarrow X\,^2\Pi_g$. The "hump" seen in the total cross section is clearly mainly composed of the $k\pi_u$ and $k\delta_u$ partial channels which are comparable in magnitude and quite large. As shown by their eigenphase sums, these cross sections are nonresonant and their structure is caused by the energy dependence of the transition matrix elements. The $k\sigma_u$ partial cross section is largest at threshold and diminishes slowly with photon energy. As shown in previous studies,[7-9] the $k\sigma_u$ channel is shape resonant. At the equilibrium bond distance, however, the shape resonance does not influence the photoionization cross section but in fact perturbs the adjoining $(1\pi_g n\sigma_u)$ Rydberg series.[7,8] For vibrationally-resolved spectra leading to the ground state ion, shorter bond lengths are sampled by the vibrational wave function and the shape resonance is clearly seen in the photoionization cross section, inducing non-Franck-Condon effects near threshold.[7]

Figure 3 shows the photoionization cross section and photoelectron angular distributions for the a $^1\Delta_g \longrightarrow$ X $^2\Pi_g$ transition. These results are quite similar to those found in ground state photoionization. Indeed, the change in the static-exchange potentials brought about by the excited state target wavefunction is reflected in only modest differences in these cross sections near threshold. At low energies, the a $^1\Delta_g$ cross section is slightly enhanced compared to the ground state cross sections due to the more repulsive potential which shifts the oscillator strength associated with the resonant σ_u continuum. This is seen clearly in Fig. 4 which shows the partial channel cross sections and eigenphase sums for the a $^1\Delta_g \longrightarrow$ X $^2\Pi_g$ transition. The kπ_u and kδ_u cross sections and eigenphase sums are nearly the same as those in transitions from the ground state, indicating that these nonresonant partial channels are quite insensitive to differences from the ground state photoionization process. Indeed, above the shape resonant region near threshold, the a $^1\Delta_g$ and X $^3\Sigma_g^-$ cross sections are nearly the same, which agrees with expectations indicated by Eq. (8) showing the contributions to the total cross section from the ground state and a $^1\Delta_g$ state to be the same.

Clark and Wayne[2] have reported the photoionization cross section from the a $^1\Delta_g$ state within about 1 eV of threshold. These results show a rise from about 2 Mb at threshold to over 6 Mb at about 1 eV above threshold with sharp autoionizing structure superimposed. Our results show the same general behavior, but increase less steeply. More recently, there has been a measurement of the a $^1\Delta_g$ cross section at 21.2 eV photon energy which gave a value of 11.8 Mb, nearly 1.6 times that for transitions from the ground state at that energy. This is a quite different value from that predicted from the present results, which show the ground state and excited state cross sections to be nearly the same. In comparing theoretical and experimental results, it is important to note, however, that the experimental value of the a $^1\Delta_g$ cross sections was obtained from normalizing to

the $X\,^3\Sigma_g^-$ cross section at the same photon energy.[4,5] Codling *et al.*[27] have shown that Rydberg states leading to the $c\,^4\Sigma_u^-$ $(2\sigma_u^{-1})$ ion significantly affects the photoionization cross section in this energy range, creating a strong energy dependence of the cross section over a narrow spectral region. This would make such a normalization procedure at this energy somewhat uncertain, along with experimental difficulties inherent in accurately measuring photoionization cross sections of transient species such as the $a\,^1\Delta_g$ state of O_2.[4,28] Furthermore, there is the possiblity that previously unobserved Rydberg states leading to the $(2\sigma_u^{-1})$ ion, where the $1\pi_g$ electrons are *singlet* coupled, could play a role in the photoionization of the $a\,^1\Delta_g$ state and be responsible for the difference between the present results and the experimental result at 21.2 eV. Clearly, experiments with tunable sources of radiation are needed to obtain a full understanding of the photoionization of the $a\,^1\Delta_g$ state and its energy dependence. In addition, calculations which include electronic autoionization would be helpful.

Acknowledgments

This work was supported by grants from the National Science Foundation (CHE-8521391). We also acknowledge use of resources of the San Diego SuperComputer Center, which is supported by the National Science Foundation. One of us (M. B.) wishes to acknowledge a Department of Education Fellowship.

TABLE I. Coefficients of the static-exchange potential of Eq. (3).

		a_n/b_n	α/β
Initial state	Channel[a]	$1\pi_g$	$1\pi_g$
$X\ ^3\Sigma_g^-$	$^3\Pi_u(k\sigma_u)$	1/-1	0/0
	$^3\Sigma_u^-(k\pi_u)$	1/-1	-1/1
	$^3\Pi_u(k\delta_u)$	1/-1	0/0
$a\ ^1\Delta_g$	$^1\Pi_u(k\sigma_u)$	1/1	0/0
	$^1\Delta_u(k\pi_u)$	1/1	0/0
	$^1\Phi_u(k\delta_u)$	1/1	0/0

[a] Channel symmetry designation of the ion plus photoelectron system.

TABLE II. Basis sets used in separable potential, Eq. (6).

Photoionization symmetry	Type of Gaussian function[a]		Exponents
σ_u	Cartesian	s	16.0,8.0,4.0,2.0,1.0,0.5
		z	1.0,0.5
	Spherical	$\ell = 1$	4.0,2.0,1.0,0.5
		$\ell = 3$	4.0,2.0,1.0,0.5
		$\ell = 5$	1.0,0.5
π_u	Cartesian	x	8.0,4.0,2.0,1.0,0.5
		xz	0.5
	Spherical	$\ell = 1$	1.0
		$\ell = 3$	1.0
δ_u	Cartesian	xy	4.0,2.0,1.0,0.5,0.25
	Spherical	$\ell = 3$	1.0
		$\ell = 5$	1.0

[a] Cartesian functions are centered at the nuclei and the spherical functions at the molecular center. For details of the forms of these functions and their use, see Refs. 10 and 12.

References

[1] See, for example, D. M. Hunten and M. B. McElroy, J. Geophysical Research **73**, 2421 (1968).

[2] I. D. Clark and R. P. Wayne, J. Geophysical Research, **75** 699 (1970).

[3] R. B. Cairns and J. A. R. Samson, Phys. Rev. A **139**, 1403 (1965).

[4] W. J. van der Meer, P. van der Meulen, M. Volmer, and C. A. de Lange, Chem. Phys. **126**, 385 (1988).

[5] C. E. Brion, K. H. Tan, M. J. van der Wiel, and Ph.E. van der Leeuw, J. Electron Spectrosc. Relat. Phenom. **17**, 101 (1977).

[6] A.-L. Roche, K. Kirby, S. L. Guberman, and A. Dalgarno, J. Electron Spectrosc. Relat. Phenom. **22**, 223 (1981).

[7] M. Braunstein and V. McKoy, J. Chem. Phys. **90**, 2575 (1989).

[8] A. Gerwer, C. Asaro, B. V. McKoy, and P. W. Langhoff, J. Chem. Phys. **72**, 713 (1980).

[9] P. M. Dittman, D. Dill, and J. L. Dehmer, J. Chem. Phys. **76**, 5703 (1982).

[10] R. R. Lucchese, K. Takatsuka, and V. McKoy, Phys. Rep. **131**, 147 (1986).

[11] P. Krupenie, J. Phys. Chem. Ref. Data **1**, 423 (1972).

[12] R. R. Lucchese, G. Raseev, and V. McKoy, Phys. Rev. A. **25**, 2572 (1982).

[13] T. H. Dunning, J. Chem. Phys. **53**, 2823 (1971).

[14] J. Andzelm, M. Klobukowski, E. Radzio-Andzelm, Y. Sakai, and H. Tatewaki, in *Gaussian Basis Sets for Molecular Orbital Calculations*, edited by S. Huzinaga (Elsevier, Amsterdam, 1984), p. 23.

[15] This calculation imposes the condition that the $1\pi_x$ and $1\pi_y$ be equivalent. If this condition is relaxed, the SCF energy is slightly lower.

[16] M. Braunstein, V. McKoy, and M. E. Smith, J. Chem. Phys. **90**, 3931 (1989).

[17] T. Gustafsson, Chem. Phys. Lett. **75**, 505 (1980).

[18] J. A. R. Samson, J. L. Gardner, and G. N. Haddad, J. Electron Spectrosc. Relat. Phenom. **12**, 281 (1977).

[19] P. M. Dehmer and W. A. Chupka, J. Chem. Phys. **62**, 4525 (1975).

[20] D. M. P. Holland and J. B. West, Z. Phys. D **4**, 367 (1987).

[21] E. Nishitani and I. Tanaka, J. Chem. Phys. **81**, 3429 (1984).

[22] For a recent review, see C. Y. R. Wu, J. Quant. Spectrosc. Radiat. Transfer **37**, 1 (1987).

[23] D. G. McCoy, J. M. Morton, and G. V. Marr, J. Phys. B **11**, L547 (1978).

[24] T. A. Carlson, G. E. McGuire, A. E. Jonas, K. L. Cheng, C. P. Anderson, C. C. Lu, and B. P. Pullen, in *Electron Spectroscopy*, edited by D. A. Shirley (North Holland, Amsterdam, 1972), pp. 207-31.

[25] W. H. Hancock and J. A. R. Samson, J. Electron Spectrosc. Relat. Phenom. **9**, 211 (1976).

[26] M. Nakamura and Y. Iida, in *Vacuum Ultraviolet Radiation Physics*, edited by E. E. Koch, R. Haensel, and C. Kunz, (Pergamon Press, Braunschweig, 1974), pp. 170-2.

[27] K. Codling, A. C. Parr, D. L. Ederer, R. Stockbauer, J. B. West, B. E. Cole, and J. L. Dehmer, J. Phys. B **14**, 657 (1981).

[28] H. van Lonkhuyzen, and C. A. de Lange, J. Electron Spectrosc. Relat. Phenom. **27**, 255 (1982).

Figure Captions

Fig. 1: Photoionization cross sections and photoelectron angular distributions for the transition (O_2) X $^3\Sigma_g^-$ $\longrightarrow$ (O_2^+) X $^2\Pi_g$: ——, present results (length); - - - present results (velocity); $\times$, experimental data of Ref. 17; $\circ$, experimental data of Ref. 5; $\bullet$, experimental data of Ref. 18; $+$, experimental data of Ref. 23; *, experimental data of Ref. 24; $\triangle$, experimental data of Ref. 25; $\diamond$, experimental data of Ref. 26.

Fig. 2: Partial photoionization cross sections (length) and eigenphase sums (radians) for each symmetry channel for photoionization of the X $^3\Sigma_g^-$ state of O_2 leading to the X $^2\Pi_g$ state of O_2^+.

Fig. 3: Photoionization cross sections and photoelectron angular distributions for the transition (O_2) a $^1\Delta_g$ $\longrightarrow$ (O_2^+) X $^2\Pi_g$: ——, present results (length); - - -, present results (velocity).

Fig. 4: Partial photoionization cross sections (length) and eigenphase sums (radians) for each symmetry channel for photoionization of the a $^1\Delta_g$ state of O_2 leading to the X $^2\Pi_g$ state of O_2^+.

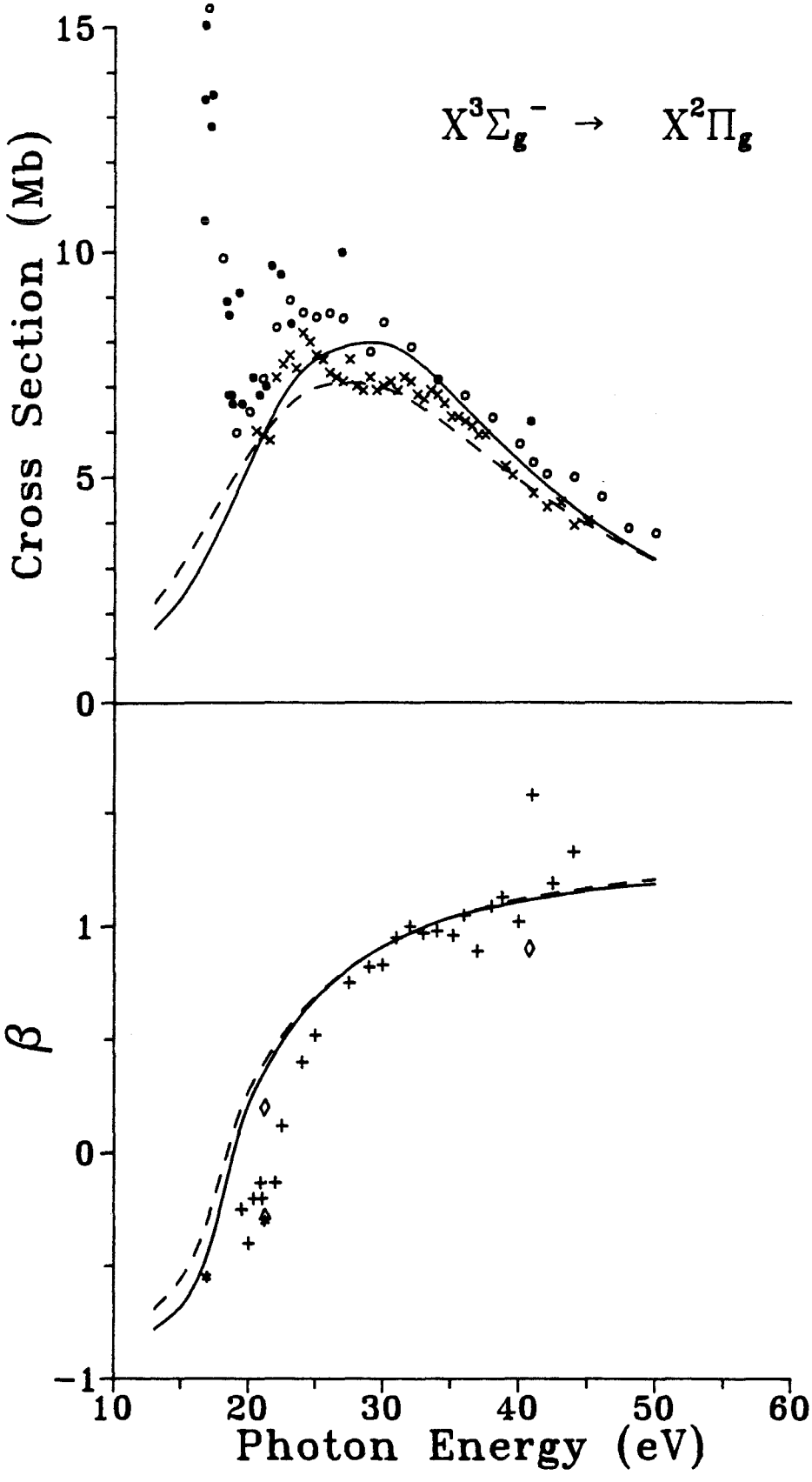
$X^3\Sigma_g^- \rightarrow X^2\Pi_g$
Cross Section (Mb)
15
10
5
0
β
1
0
−1
10
20
30
40
50
60
Photon Energy (eV)

Figure 1

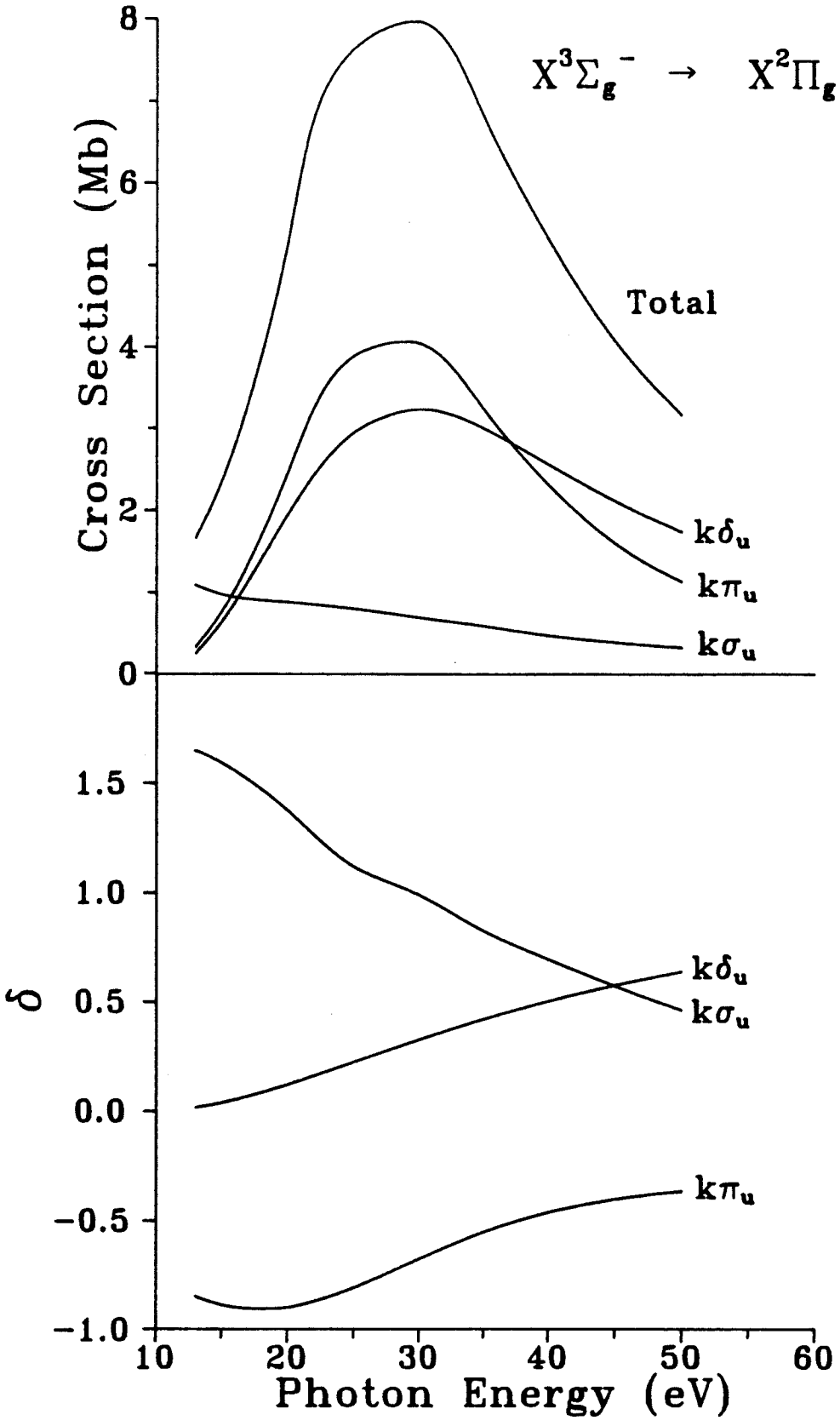
$X^3\Sigma_g^- \rightarrow X^2\Pi_g$
Total
$k\delta_u$
$k\pi_u$
$k\sigma_u$
Cross Section (Mb)
8
6
4
2
0
1.5
1.0
0.5
0.0
−0.5
−1.0
δ
$k\delta_u$
$k\sigma_u$
$k\pi_u$
10
20
30
40
50
60
Photon Energy (eV)

Figure 2

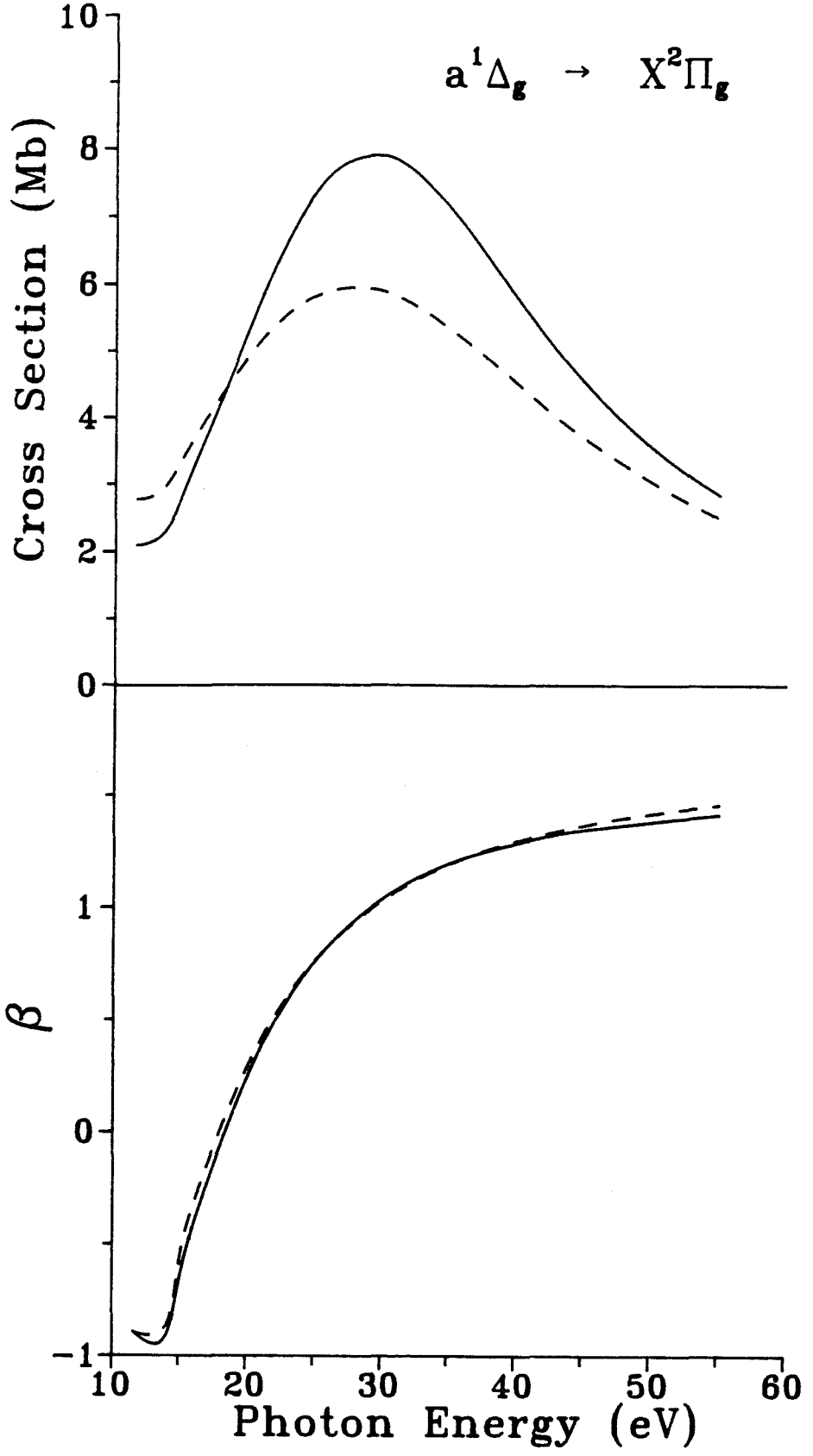
$a^1\Delta_g \rightarrow X^2\Pi_g$
Cross Section (Mb)
10
8
6
4
2
0
β
1
0
−1
10
20
30
40
50
60
Photon Energy (eV)

Figure 3

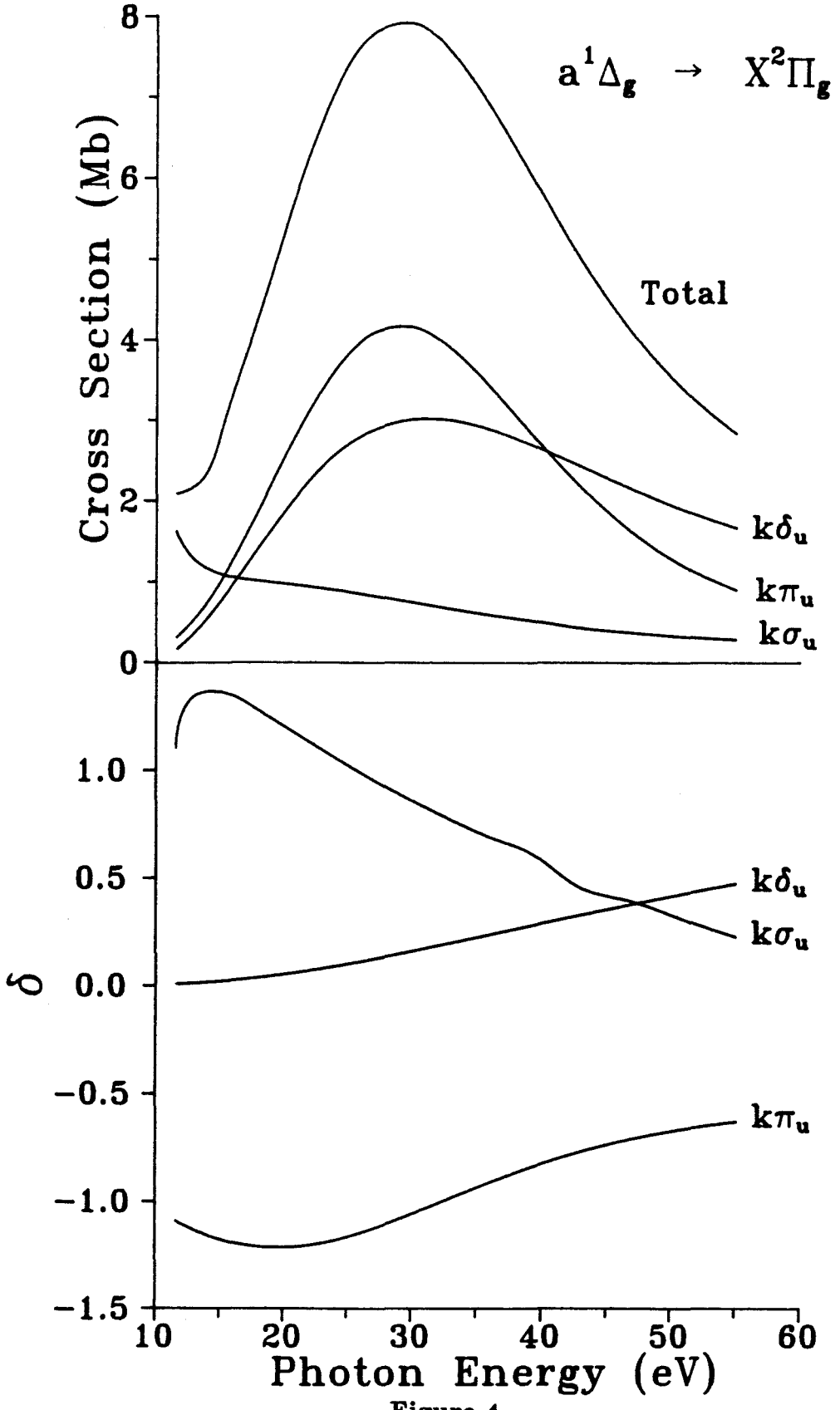
$a^1\Delta_g \rightarrow X^2\Pi_g$
Cross Section (Mb)
8
6
4
2
0
Total
$k\delta_u$
$k\pi_u$
$k\sigma_u$
1.0
0.5
0.0
−0.5
−1.0
−1.5
δ
$k\delta_u$
$k\sigma_u$
$k\pi_u$
10
20
30
40
50
60
Photon Energy (eV)

Figure 4

Chapter 5

Multiplet-specific shape resonant features in vibrationally resolved $3\sigma_g$ photoionization of O_2

(The text of this chapter appeared in: M. Braunstein and V. McKoy, J. Chem. Phys. **91**, 150 (1989).)

Multiplet-specific shape resonant features in vibrationally resolved $3\sigma_g$ photoionization of O_2

M. Braunstein and V. McKoy
A. A. Noyes Laboratory of Chemical Physics, California Institute of Technology, Pasadena, California 91125

(Received 7 February 1989; accepted 21 March 1989)

We report multiplet-specific vibrationally resolved photoionization cross sections and photoelectron angular distributions for the $3\sigma_g$ orbital of O_2 leading to the $v^+ = 0$–3 levels of the $b\,^4\Sigma_g^-$ and $B\,^2\Sigma_g^-$ states of O_2^+. These studies were motivated by recent work which shows significant nonstatistical behavior in the vibrationally unresolved spectrum at low photoelectron energies arising from the sensitivity of the $k\sigma_u$ shape resonance to the multiplet-specific exchange potentials. In addition to the anticipated non-Franck–Condon vibrational distributions arising from the $k\sigma_u$ shape resonance, we also find substantial nonstatistical effects in our vibrationally resolved cross sections and particularly in our photoelectron angular distributions over a broad energy range. Extensive electronic autoionization due to Rydberg levels leading to the $c\,^4\Sigma_u^-$ $(2\sigma_u^{-1})$ ion makes it difficult to assess these effects in the available experimental data.

INTRODUCTION

Previous theoretical studies of vibrationally unresolved $3\sigma_g$ photoionization of O_2 leading to the $B\,^2\Sigma_g^-$ and $b\,^4\Sigma_g^-$ ions have shown significant nonstatistical behavior in the spectral region of the well known σ_u shape resonance.[1,2] The sensitivity of this shape resonance to the multiplet-specific exchange potentials of these molecular ions gives rise to shifts in the oscillator strength distributions near threshold. In fact, the $b\,^4\Sigma_g^-$ cross section peaks around 4 eV above threshold, while the oscillator strength associated with the σ_u shape resonance in the $B\,^2\Sigma_g^-$ cross section shifts closer to threshold, perturbing the spectral distribution of the $n\sigma_u$ Rydberg states leading to the $B\,^2\Sigma_g^-$ ion.[2] This shift in oscillator strength associated with the σ_u shape resonance is also reflected in large differences in the multiplet-specific photoelectron angular distributions.[2] These differences are difficult to assess in the experimental spectra due to extensive electronic autoionization of Rydberg states leading to the $c\,^4\Sigma_g^-$ $(2\sigma_u^{-1})$ ion.[3–6] However, recent high-resolution measurements do show a relatively broad maximum in the $B\,^2\Sigma_g^-$ cross section at considerably lower photoelectron energies than the shape-resonant maximum seen in the $b\,^4\Sigma_g^-$ cross section.[7,8] Similar multiplet-specific behavior has also been observed in the 5σ photoionization of NO leading to the $A\,^1\Pi$ and $b\,^3\Pi$ ions, where a difference of as much as 3 eV is seen in the positions of the shape resonance.[9–11] In $(2+1)$ resonance-enhanced multiphoton ionization (REMPI) of O_2 via the $C\,^3\Pi_g$ $(\pi_g 3s\sigma_g)$ and $d\,^1\Pi(\pi_g 3s\sigma_g)$ states, significant multiplet-specific effects were also seen in the vibrationally resolved ion cross sections and photoelectron angular distributions.[12,13]

In the present work we extend our previous vibrationally unresolved studies of multiplet-specific $3\sigma_g$ photoionization in O_2 (Ref. 2) by obtaining vibrationally resolved cross sections and photoelectron angular distributions for $v^+ = 0$–3 to further assess multiplet-specific effects. Our vibrationally resolved cross sections show the expected large non-Franck–Condon effects in the region of the σ_u shape resonance as well as significant multiplet-specific behavior in the cross sections. Comparison with experimental measurements[7] is again made difficult by the role of electronic autoionization in the region of these shape resonances. The photoelectron angular distributions also show both non-Franck–Condon behavior and multiplet-specific differences well beyond the energy range of autoionizing features in the measured cross sections. Measurements of these photoelectron angular distributions using tunable radiation would be of considerable importance in understanding these multiplet-specific effects.

THEORY

Our procedure for obtaining vibrationally resolved photoionization cross sections and photoelectron angular distributions has been described extensively elsewhere.[2,14–17] Briefly, we include full kinetic energy and internuclear dependence in the bound–free transition moment,

$$M_{0\to v^+} = \int dR\, \chi_0\, \mu_{if}(k,R)\, \chi_{v^+}. \tag{1}$$

Here $\mu_{if}(k,R)$ is the transition moment between the initial bound state of O_2 $(X\,^3\Sigma_g^-)$ and final continuum state (ionic core + photoelectron). In Table I we give the internuclear distances at which the transition moments are determined. For the ground state of O_2 we used a Hartree–Fock SCF wave function obtained with a $[4s3p2d]$ Cartesian Gaussian basis set.[14] For the final state we used the frozen-core approximation with Hartree–Fock photoelectron orbitals for the dipole-allowed $^3\Sigma_u^-$ $(k\sigma_u)$ and $^3\Pi_u$ $(k\pi_u)$ channels obtained with the interative Schwinger variational technique and multiplet-specific static-exchange potentials.[2] All integrations associated with obtaining the transition moments were carried out via partial-wave expansions with the resulting radial integrals evaluated by Simpson's rule. The partial-wave expansion parameters and radial grid are the same as those of Ref. 14.

The vibrational wave functions χ of Eq. (1) were ob-

TABLE I. Internuclear distances of O_2 at which photoionization transition moments were evaluated.

Continuum symmetry	Internuclear distance[a]
$k\sigma_u$[b]	2.0,2.1,2.182,2.232,2.282 2.332,2.382,2.482,2.6,2.8,3.0
$k\pi_u$	2.0,2.182,2.282,2.382,3.0

[a] In atomic units.
[b] Resonant channel.

tained by numerical integration. For the ground and $b\,^4\Sigma_g^-$ ion states, we used the Rydberg–Klein–Rees (RKR) potentials of Krupenie.[18] A Morse potential was used for the $B\,^2\Sigma_g^-$ ion potential with spectroscopic constants given by Huber and Herzberg.[19] Franck–Condon factors obtained with these potentials are given in Table II along with other calculated values[20] and measured vibrational intensities at high energy,[21,22] well away from the influence of the $k\sigma_u$ shape resonance.

RESULTS AND DISCUSSION

In Figs. 1(a) and 1(b) we show our calculated multiplet-specific photoionization cross sections for the $3\sigma_g \rightarrow k\sigma_u$ transition in O_2 at various internuclear distances for the $b\,^4\Sigma_g^-$ and $B\,^2\Sigma_g^-$ ions, respectively. The most prominent feature here is the large maximum in the cross section caused by the well known $k\sigma_u$ shape resonance.[1–8,23–26] These resonant cross sections show the expected dependence on internuclear distance, becoming broader and peaking at higher energy with decreasing internuclear distance (R). This dependence leads to deviations from Franck–Condon behavior.[27–29] For a particular R, the peak of the shape resonance for each multiplet is at considerably different photoelectron energies. At R_e of the ground state (2.282 a.u.) the shape resonance is seen ~4 eV above threshold for the $b\,^4\Sigma_g^-$ ion, while the oscillator strength associated with the $B\,^2\Sigma_g^-$ cross section is shifted toward threshold,[1,2] and, in fact, significantly perturbs the discrete spectral distribution.[2] This shift arises from the sensitivity of the σ_u shape resonance to differences in the exchange component of the multiplet potentials and is not seen in studies using multiplet-averaged potentials.[23–26] This behavior leads to large differences in the cross sections and photoelectron angular distributions for these multiplets.

Figures 2(a) and 2(b) show our vibrationally resolved photoionization cross sections for the $b\,^4\Sigma_g^-$ and $B\,^2\Sigma_g^-$ ion states, respectively. These multiplet-specific cross sections for the $b\,^4\Sigma_g^-$ ion agree with the static-exchange multiplet-averaged calculations of Raseev *et al.*,[26] but are consistently

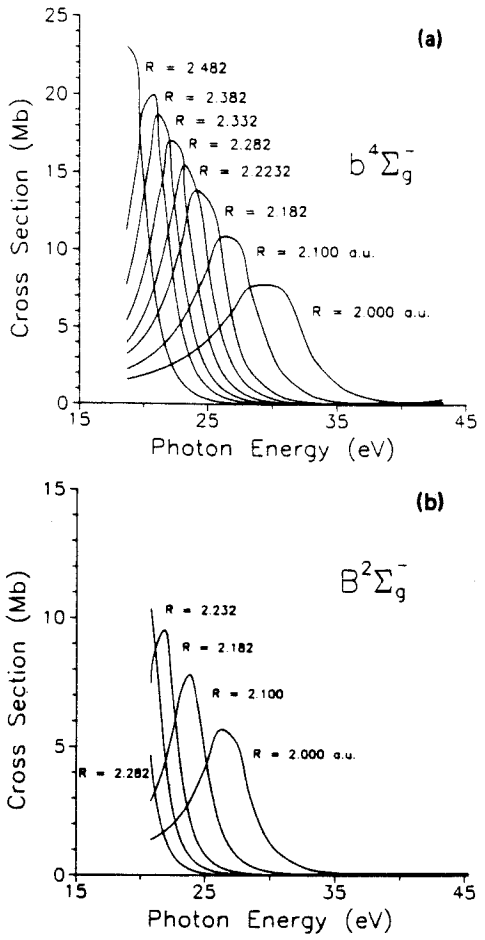

FIG. 1. (a) and (b) Photoionization cross sections (dipole length) for the shape resonant $3\sigma_g \rightarrow k\sigma_u$ channel in O_2 at several internuclear distances for the $b\,^4\Sigma_g^-$ and $B\,^2\Sigma_g^-$ ions, respectively.

TABLE II. Franck–Condon factors for transitions from the ground state of O_2 ($R_e = 2.282$ a.u.) to vibrational levels of the $b\,^4\Sigma_g^-(3\sigma_g^{-1})$ and $B\,^2\Sigma_g^-(3\sigma_g^{-1})$ states of O_2^+.

	$b\,^4\Sigma_g$ ($R_e = 2.418$ a.u.)		
v^+	Present work	Ref. 20 (theory)	Ref. 21 (experiment)[a]
0	0.408	0.411	0.452
1	0.336	0.337	0.319
2	0.164	0.163	0.154
3	0.062	0.062	0.057
	$B\,^2\Sigma_g^-$ ($R_e = 2.453$ a.u.)		
v^+	Present work	Ref. 22 (experiment)	Ref. 21 (experiment)
0	0.245	0.247	0.265
1	0.293	0.316	0.307
2	0.213	0.211	0.220
3	0.125	0.130	0.135

[a] Experimental quantities are obtained at the He II resonance line (40.8 eV) and have been normalized by taking the total relative intensitites to be unity. This energy is far enough away from any shape and/or autoionizing resonances so that Franck–Condon behavior is expected.

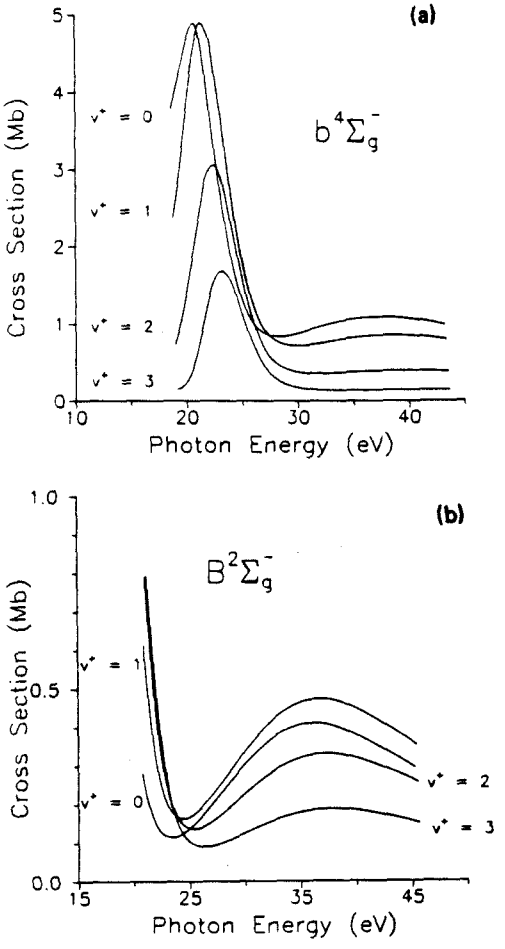

FIG. 2. (a) and (b) Vibrationally resolved photoionization cross sections (dipole length) for the $b\,^4\Sigma_g^-$ and $B\,^2\Sigma_g^-$ ions, respectively. Dipole-velocity results are nearly the same but are sometimes slightly less in magnitude. See Ref. 2 for more details.

slightly larger. The vibrationally resolved cross sections of both studies peak at successively higher photon energies with increasing vibrational excitation. For the vibrationally resolved $B\,^2\Sigma_g^-$ cross sections, however, there are significant differences between the multiplet-averaged calculations of Raseev *et al.*,[26] which are expectedly similar to the $b\,^4\Sigma_g^-$ cross sections, and the present multiplet-specific results. These differences reflect the strong multiplet-specific behavior seen in the fixed-nuclei cross sections. Shape-resonant behavior appears closer to threshold in the vibrationally resolved $B\,^2\Sigma_g^-$ cross sections than in the $b\,^4\Sigma_g^-$ cross sections. The $B\,^2\Sigma_g^-$ cross sections also show a strong minimum around a photoelectron energy of 5 eV. This is due to cancellation between partial-wave contributions to the transition moment in the $k\sigma_u$ channel and can be understood by examining the partial-wave composition of the initial bound $3\sigma_g$ and final continuum $k\sigma_u$ orbitals. The $3\sigma_g$ orbital is ~50% s wave and ~50% d wave for the internuclear distances of interest here. These s and d waves both show a radial node at ~1.2 a.u. from the molecular center. The principle-value transition moments for the $\ell_k = 1$ and $\ell_k = 3$ continuum partial waves—made up of mostly p and f waves—go through zero at this energy producing a minimum in the $k\sigma_u$ cross section. This is akin to the so-called Cooper minimum[30,31] seen in atoms, except that the anisotropic molecular potential induces partial-wave mixing. The dominant contribution to the total cross sections arises from the $k\pi_u$ partial channel in this region. This cancellation also occurs in the $b\,^4\Sigma_g^-$ channel at a higher energy (15 eV photoelectron kinetic energy) where the $k\pi_u$ cross section is larger thus obscuring the effect in the total cross section. Studies of fluorescence polarization for the $b\,^4\Sigma_g^-$ ion do show the π_u:σ_u cross section ratio growing rapidly from threshold to ~30 eV photon energy.[32,33] Measurements of the fluores-

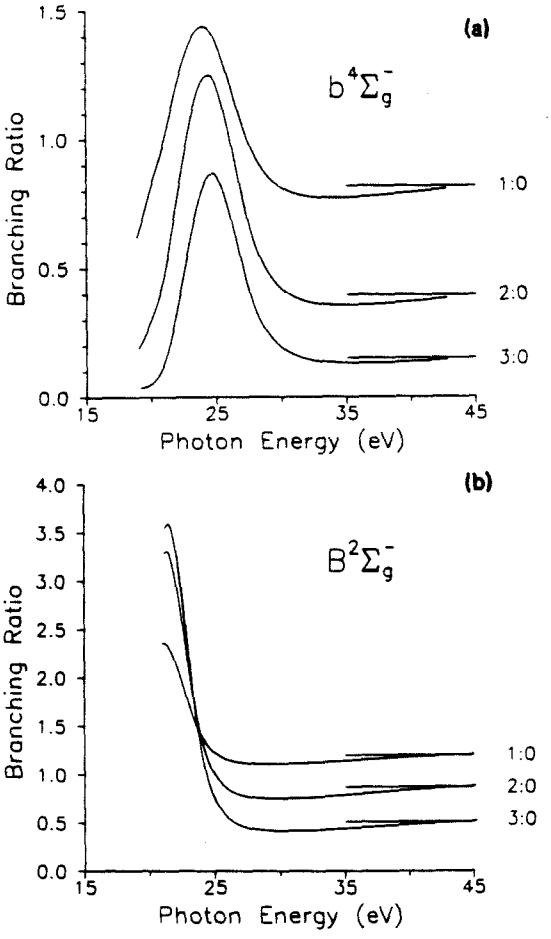

FIG. 3. (a) and (b) Vibrational branching ratios for photoionization (dipole length) for the $b\,^4\Sigma_g^-$ and $B\,^2\Sigma_g^-$ ions, respectively. Horizontal lines show the Franck–Condon ratios.

cence polarization at slightly higher energy should show this behavior clearly as the $k\sigma_u$ cross section goes through a minimum there.

High resolution vibrationally resolved photoionization measurements from threshold up to ~24 eV photon energy show differences between the vibrationally resolved multiplet cross sections.[7] However, electronic autoionization from Rydberg levels leading to the $c\,^4\Sigma_u^-$ ion (IP = 24.5 eV) in the energy region of the shape resonance makes comparisons difficult. Experiments over a broader energy range and theoretical studies which include these autoionizing states are needed to better understand these multiplet-specific effects.

Ion vibrational branching ratios for the $b\,^4\Sigma_g^-$ and $B\,^2\Sigma_g^-$ ions are shown in Figs. 3(a) and 3(b), respectively, where we use the notation n:0 to denote the branching ratio, $\sigma(v=0\rightarrow v^+=n)/\sigma(v=0\rightarrow v^+=0)$. Dramatic deviations from Franck–Condon behavior are seen in these branching ratios. For the $b\,^4\Sigma_g^-$ ion this behavior extends over a large energy range similar to that seen in $3\sigma_g$ photoionization of N_2,[17,27–29] while the $B\,^2\Sigma_g^-$ branching ratios show non-Franck–Condon behavior only in a limited energy range near threshold. These features reflect differences seen in the vibrationally resolved multiplet-specific cross sections of Figs. 2(a) and 2(b).

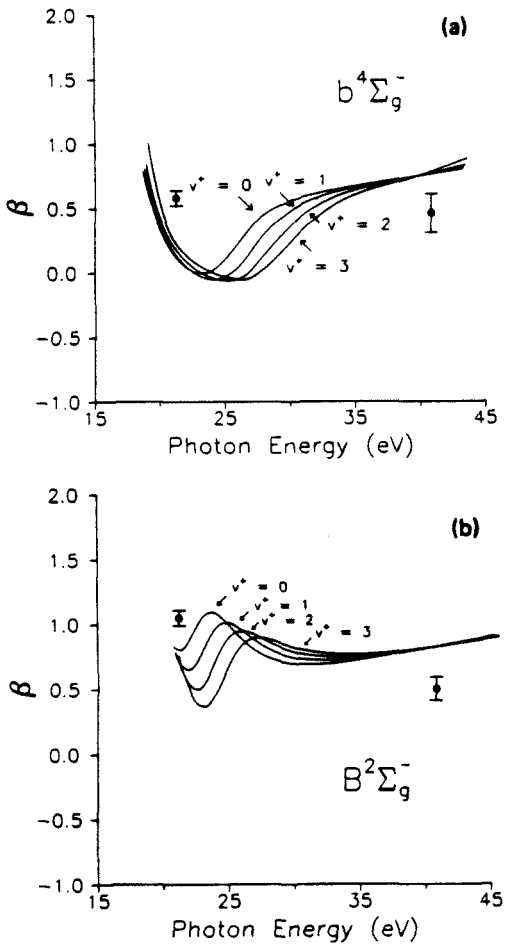

FIG. 4. (a) and (b) Vibrationally resolved photoelectron asymmetry parameters (dipole length) for the $b\,^4\Sigma_g^-$ and $B\,^2\Sigma_g^-$ ions, respectively. The open circles are experimental data from Ref. 34 for the $v^+ = 0$ level ($b\,^4\Sigma_g^-$ ion) and $v^+ = 1$ level ($B\,^2\Sigma_g^-$ ion).

Vibrationally resolved photoelectron angular distributions for these two multiplets of O_2^+ ($3\sigma_g^{-1}$) are shown in Figs. 4(a) and 4(b). These photoelectron asymmetry parameters are vibrational-state dependent. This non-Franck–Condon behavior extends over a broader energy range than in the vibrational branching ratios. The vibrationally resolved β's also show strong multiplet-specific effects. In particular, there is a shoulder in the $B\,^2\Sigma_g^-$ β's at around 25 eV photon energy, the same energy where the σ_u cross section goes through a minimum, which is not seen in the β's for the $b\,^4\Sigma_g^-$ ion. These multiplet-specific differences extend over a broad range, well beyond the complicating effects of autoionization due to states leading to the $c\,^4\Sigma_u^-$ ion. Measured photoelectron asymmetry parameters of Katsumata *et al.*[34] at 21.2 and 40.8 eV are also shown in Figs. 4(a) and 4(b). At low energy there is a significant difference between the measured multiplet β's, while at higher energy, away from the shape resonance, this difference is considerably less. Continuum source measurements are needed to fully assess the accuracy of these calculations.

ACKNOWLEDGMENTS

This material is based upon research supported by the National Science Foundation under Grant No. CHE85-21391. The authors also acknowledge use of the resources of the San Diego SuperComputer Center which is supported by the National Science Foundation.

[1] C. L. Winstead and P.W. Langhoff (to be published); see also C. L. Winstead, Ph.D. thesis, Indiana University, 1987.
[2] M. Braunstein, V. McKoy, and M. E. Smith, J. Chem. Phys. **90**, 3931 (1989).
[3] J. A. R. Samson, J. L. Gardner, and G. N. Haddad, J. Electron. Spectrosc. Relat. Phenom. **12**, 281 (1977).
[4] C. E. Brion, K. H. Tan, M. J. Van der Wiel, and Ph. E. Van der Leeuw, J. Electron. Spectrosc. Relat. Phenom. **17**, 101 (1979).
[5] T. Gustafsson, Chem. Phys. Lett. **75**, 505 (1980).
[6] A. Tabche-Fouhaile, I. Nenner, P.-M. Guyon, and J. Delwiche, J. Chem. Phys. **75**, 1129 (1981).
[7] P. Morin, I. Nenner, M. Y. Adam, M. J. Hubin-Franskin, J. Delwiche, J. Lefebvre-Brion, and A. Giusti-Suzor, Chem. Phys. Lett. **92**, 609 (1982).
[8] M. Ukai, A. Kimura, S. Arai, P. Lablanquie, K. Ito, and A. Yagashita, Chem. Phys. Lett. **135**, 51 (1987).
[9] M. E. Smith, V. McKoy, and R. R. Lucchese, J. Chem. Phys. **82**, 4147 (1985).
[10] M. R. Hermann, C. W. Bauschlicher Jr., W. M. Huo, S. R. Langhoff, and P. W. Langhoff, Chem. Phys. **109**, 1 (1986).
[11] M. R. Hermann, S. R. Langhoff, T. J. Gill, and P. W. Langhoff, Chem. Phys. Lett. **125**, 336 (1986).
[12] P. J. Miller and W. A. Chupka (private communication).
[13] J. A. Stephens, M. Braunstein, and V. McKoy (to be published).
[14] M. Braunstein and V. McKoy, J. Chem. Phys. **90**, 2575 (1989).
[15] R. R. Lucchese, K. Takatsuka, and V. McKoy, Phys. Rep. **131**, 147 (1986).
[16] R. R. Lucchese, R. Raseev, and V. McKoy, Phys. Rev. A **25**, 2572 (1982).
[17] R. R. Lucchese and V. McKoy, J. Phys. B **14**, L629 (1981).

[18]P. H. Krupenie, J. Phys. Chem. Ref. Data 1, 423 (1972).
[19]K. P. Huber and G. Herzberg, *Molecular Spectra and Molecular Structure, Vol. IV. Constants of Diatomic Molecules* (Van Nostrand Reinhold, New York, 1979).
[20]D. L. Albritton, A. L. Schmeltekopf, and R. N. Zare, *Diatomic Intensity Factors* (Wiley, New York, to be published).
[21]J. L. Gardner and J. A. R. Samson, J. Electron. Spectrosc. Relat. Phenom. 13, 7 (1978).
[22]O. Edqvist, E. Lindholm, L. E. Selin, and L. Asbrink, Phys. Scr. 1, 25 (1970).
[23]P. M. Dittman, D. Dill, and J. L. Dehmer, J. Chem. Phys. 76, 5703 (1982).
[24]P. W. Langhoff, A. Gerwer, C. Asaro, and B. V. McKoy, Int. J. Quant. Chem.: Quant. Chem. Symp. 13, 645 (1979).
[25]A. Gerwer, C. Asaro, B. V. McKoy, and P. W. Langhoff, J. Chem. Phys. 72, 713 (1980).
[26]G. Raseev, H. Lefebvre-Brion, H. Le Rouzo, and A. L. Roche, J. Chem. Phys. 74, 6686 (1981).
[27]J. L. Dehmer, D. Dill, and S. Wallace, Phys. Rev. Lett. 43, 1005 (1979).
[28]J. B. West, A. C. Parr, B. E. Cole, D. L. Ederer, R. Stockbauer, and J. L. Dehmer, J. Phys. B 13, L105 (1980).
[29]See, for example, J. L. Dehmer, A. C. Parr, and S. H. Southworth, in *Handbook on Synchrotron Radiation*, edited by G. V. Marr (North-Holland, Amsterdam, 1986), Vol. II.
[30]U. Fano and J. W. Cooper, Rev. Mod. Phys. 40, 441 (1968).
[31]S. T. Manson, Phys. Rev. 31, 3968 (1985).
[32]J. W. Keller, W. T. Hill III, D. L. Ederer, T. J. Gil, and P. W. Langhoff, J. Chem. Phys. 87, 3299 (1987).
[33]M. A. O'Halloran, J. A. Guest, and R. N. Zare, SSRL Activity Report, May 11, 1983.
[34]S. Katsumata, Y. Achiba, and K. Kimura, J. Electron. Spectrosc. Relat. Phenom. 17, 229 (1979).

Chapter 6

Shape resonance behavior in $1\pi_g$ photoionization of O_2

(The text of this chapter appeared in: M. Braunstein and V. McKoy, J. Chem. Phys. **90**, 2575 (1989).)

Shape resonance behavior in $1\pi_g$ photoionization of O_2

M Braunstein and V. McKoy
A. A. Noyes Laboratory of Chemical Physics, California Institute of Technology, Pasadena, California 91125

(Received 10 October 1988; accepted 9 November 1988)

We report calculations of vibrationally resolved cross sections and photoelectron angular distributions for photoionization of O_2 leading to the $X\,^2\Pi_g$ ($v^+ = 0$–4) states of O_2^+ using Hartree–Fock continuum photoelectron orbitals. These studies were motivated by recent results which show that a σ_u shape resonance plays a dominant role in producing non-Franck–Condon vibrational distributions in resonant multiphoton ionization of O_2 via the $C\,^3\Pi_g$ ($1\pi_g 3s\sigma_g$) Rydberg state. In the present study, we investigate how this shape resonance influences photoionization dynamics in single-photon ionization. Below 21 eV photon energy, we find significant non-Franck–Condon effects in the vibrational branching ratios as well as in the vibrationally resolved photoelectron angular distributions. Substantial autoionization hinders a direct comparison between theory and experiment.

I. INTRODUCTION

Recent resonant multiphoton ionization studies via the $C\,^3\Pi_g$ ($1\pi_g 3s\sigma_g$) state of O_2 have shown that a shape resonance has a substantial influence on the vibrational distribution of the ground state $X\,^2\Pi_g$ ion.[1–4] For single-photon ionization leading to the same ion, however, experimental evidence of any corresponding shape-resonant feature is inconclusive. Experimental studies of O_2 in the near-threshold region by single-photon ionization is complicated by extensive autoionization features[5,6] which, to date, have hindered assessment of the possible role of a low-energy shape resonance in the photoionization dynamics. To some extent this complication was avoided in the resonant multiphoton ionization studies[1–4] through specific and limited selection of the photon wavelength.

To further elucidate the role of the σ_u shape resonance in single-photon ionization, we have calculated vibrationally resolved cross sections and photoelectron angular distributions for photoionization leading to the $X\,^2\Pi_g$ state of O_2^+ using frozen-core Hartree–Fock photoelectron orbitals.[7,8] These results show that a σ_u shape resonance becomes very evident in the cross section near the ionization threshold as the internuclear distance R is decreased. This dependence of the transition moment on R, particularly for R values less than R_e of O_2 in this case, leads to significant deviations in the calculated branching ratios from Franck–Condon values for energies from theshold to ~21 eV. The non-Franck–Condon effects are also apparent in our photoelectron asymmetry parameters. Comparison and subsequent interpretation of existing measured branching ratios (obtained from line-source measurements) is inconclusive, giving impetus for measurements that employ tunable radiation and extend to the ionization threshold.

An outline of the paper is as follows. In Sec. II we briefly discuss the Schwinger variational method used to obtain the Hartree–Fock photoelectron orbitals and the procedures with which we obtain our vibrationally resolved cross sections and photoelectron angular distributions. In Sec. III our results are discussed and compared with available experimental data, and in Sec. IV concluding remarks are given.

II. METHOD AND CALCULATIONS

The continuum wave functions were obtained using the iterative Schwinger variational method[7,8] to solve the one-electron Schrödinger equation which the photoelectron orbitals satisfy in the frozen-core Hartree–Fock approximation. In this procedure, the (l,m) partial-wave component of the continuum orbital is given by the equation[8]

$$\psi^{(0)}_{klm}(\mathbf{r}) = \phi^c_{klm}(\mathbf{r}) + \sum_{i,j} \langle \mathbf{r}|G_c^{(-)}U|\alpha_i\rangle \times [D^{-1}]_{ij}\langle\alpha_j|U|\phi^c_{klm}\rangle, \quad (1)$$

where

$$D_{ij} = \langle\alpha_i|U - UG_c^{(-)}U|\alpha_j\rangle, \quad (2)$$

U is twice the static-exchange interaction potential of the ion core with the Coulomb potential removed, $G_c^{(-)}$ is the Coulomb Green's function, ϕ^c_{klm} is the (l,m) component of the Coulomb scattering function, and the α's are discrete basis functions, the same as those used in Ref. 9. This large basis was sufficient to obtain well-converged results without resorting to an iterative procedure for improving $\psi^{(0)}_{klm}$.[8] All integrations were carried out via partial-wave expansions with the resulting radial integrals evaluated by Simpson's rule. The parameters used in the expansion of the static-exchange potential were the same as those in our previous studies of O_2 (Ref. 9) except that the maximum l included in the expansion of the occupied orbitals in the exchange terms were made slightly larger so that $l_i^{ex} = 24$ ($1\sigma_g$), 24 ($1\sigma_u$), 14 ($2\sigma_g$), 14 ($2\sigma_u$), 12 ($3\sigma_g$), 12 ($1\pi_u$), 12 ($1\pi_g$). The grid used to compute the radial integrals consisted of 900 points and extended out to 96.0 a.u. The continuum solutions are constrained to be orthogonal to the bound orbitals of the same symmetry. More details can be found in earlier studies.[7]

The Hartree–Fock wave function for O_2 was constructed from a $[9s5p]/(4s3p)$ contracted Gaussian basis set[10] and two d-type polarization functions with exponents of 2.7040 and 0.5350.[11] The Hartree–Fock energy with this basis at the equilibrium internuclear distance of 2.282 a.u. is − 149.634 130 a.u.

We have obtained the photoionization transition matrix elements in both the dipole-length form

$$I^{L}_{lm\mu}(R) = k^{1/2}\langle \Psi_i(\mathbf{r}, R)|\mathbf{r}_\mu|\Psi^{(-)}_{f,klm}(\mathbf{r}, R)\rangle, \quad (3)$$

and the dipole-velocity form

$$I^{V}_{lm\mu}(R) = (k^{1/2}/E)\langle \Psi_i(\mathbf{r}, R)|\nabla_\mu|\Psi^{(-)}_{f,klm}(\mathbf{r}, R)\rangle \quad (4)$$

at the internuclear distances listed in Table I. In Eqs. (3) and (4), Ψ_i represents the initial N-electron wave function and Ψ_f is the wave function for the final ionized state, i.e., an $N-1$ molecular ion plus photoelectron, R specifies the nuclear coordinates, and $\mathbf{r}$ stands collectively for all electronic coordinates. These matrix elements were then interpolated with a cubic spline function. The length and velocity forms of the cross section for ionization of the $v=0$ level of O_2 to the nth vibrational state of O_2^+ are then given by

$$\sigma^{L,V}_{v=0,v^+=n} = \frac{4\pi^2}{3c} E \sum_{lm\mu} |\langle \chi_i^{v=0}|I^{L,V}_{lm\mu}|\chi_f^{v^+=n}\rangle|^2, \quad (5)$$

where χ are appropriate vibrational wave functions, E is the photon energy, and c is the speed of light. The vibrationally resolved photoelectron asymmetry parameter β_k is defined from the photoelectron differential cross section by

$$\frac{d\sigma^{L,V}_{v=0,v^+=n}}{d\Omega_k} = \frac{\sigma^{L,V}_{v=0,v^+=n}}{4\pi} \times [1+\beta^{L,V}_{k,v=0,v^+=n}P_2(\cos\theta)], \quad (6)$$

where θ is the angle between the direction of polarization of the light and the photoelectron momentum.

The vibrational wave functions were obtained by numerical integration of the Schrödinger equation using the Rydberg–Klein–Rees potentials of Krupenie.[12] The Franck–Condon factors thus obtained agreed with those of Ref. 12, i.e. $(v=0,v^+=0)=0.1884$, $(v=0,v^+=1)=0.3645$, $(v=0,v^+=2)=0.2901$, $(v=0,v^+=3)=0.1227$, $(v=0,v^+=4)=0.0298$.

III. RESULTS AND DISCUSSION

In previous studies of O_2, a σ_u shape resonance has been assigned experimentally[13,14] and investigated theoretically in near-threshold $3\sigma_g$ photoionization.[9,15–18] For $1\pi_g$ photoionization, an earlier fixed-nuclei Stieltjes moment theory (SMT) study showed an apparently weak set of $n\sigma_u$ transitions converging to the first ionization threshold.[17] From consideration of the energy dependence of the quantum defect associated with these states, the spectral distribution of these transitions actually display the onset of resonance behavior and connect smoothly[19] to the adjoining $k\sigma_u$ continuum, as illustrated in Fig. 1. However, the magnitude and variation of the $k\sigma_u$ partial cross section is masked by large nonresonant $k\pi_u$ and $k\delta_u$ contributions to the total cross section. The larger equilibrium internuclear distance of O_2 ($R_e = 2.282$ a.u.) compared to N_2 ($R_e = 2.068$ a.u.) and CO ($R_e = 2.132$ a.u.), where the σ shape resonance is well above threshold, shifts the resonance down to near thresh-

TABLE I. Internuclear geometries of O_2 at which photoionization matrix elements were evaluated.

Continuum symmetry	Internuclear distance (a.u.)
$k\sigma_u$*	1.8, 1.9, 2.0, 2.1, 2.14, 2.182, 2.232, 2.282, 2.382, 2.482, 2.6
$k\pi_u$	1.8, 2.1, 2.282, 2.6
$k\delta_u$	1.8, 2.1, 2.282, 2.6

*Resonant channel.

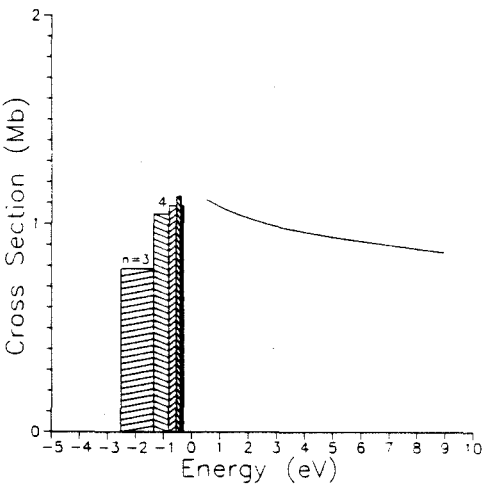

FIG. 1. Oscillator strength distribution in the discrete and continuous spectra for the $1\pi_g \rightarrow \sigma_u$ transition at R_e. The energy scale is relative to the ionization threshold at 12.07 eV. Calculations of Ref. 17 were used to construct the discrete part and the present results (dipole length) are shown above threshold.

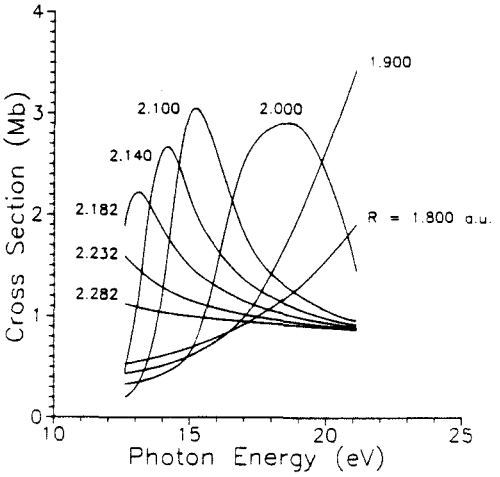

FIG. 2. Photoionization cross sections (dipole length) for the $1\pi_g \rightarrow k\sigma_u$ channel in O_2 at several values of the internuclear distance.

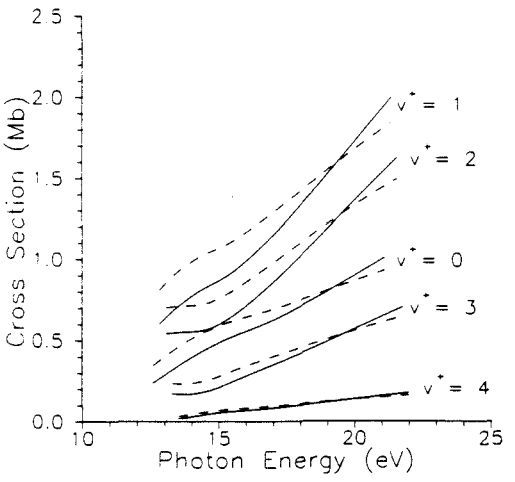

FIG. 3. Vibrationally resolved cross sections leading to the $X\,^2\Pi_g$ state of O_2^+: —, present results (dipole length); ---, present results (dipole velocity).

old, obscuring its presence.

For purposes of illustration, in Fig. 2 we show the $k\sigma_u$ partial cross sections for photoionization out of the $1\pi_g$ orbital of O_2 at eight internuclear distances. The photon energy scale in this figure assumes an ionization potential of 12.07 eV. The dependence of the shape-resonant cross section on internuclear distance is as expected,[20-23] becoming broader and shifting to higher energy as the internuclear distance is decreased. This dependence leads to non-Franck–Condon behavior in the calculated ionic vibrational distributions. In Fig. 3 we show the vibrationally resolved photoionization cross sections for the $v^+ = 0$–4 states of the $X\,^2\Pi_g$ ion. The

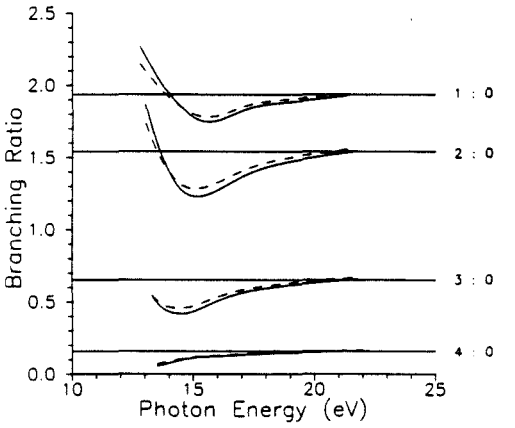

FIG. 4. Vibrational branching ratios for photoionization leading to the $X\,^2\Pi_g$ state of O_2^+: —, present results (dipole length); ---, present results (dipole velocity). The horizontal lines are the Franck–Condon values.

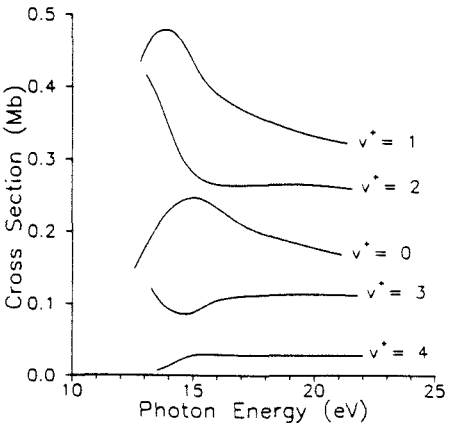

FIG. 5. Vibrationally resolved photoionization cross sections for the $1\pi_g \rightarrow k\sigma_u$ transition (dipole length).

shape resonance partially obscured by the nonresonant $k\pi_u$ and $k\delta_u$ channels, appears as a weak feature in the total cross section at low energy. These variations are sufficient to cause significant deviations from Franck–Condon values in the branching ratios, $\sigma(v=0\rightarrow v^+=n)/\sigma(v=0\rightarrow v^+=0)$, at energies below 21 eV photon energy. We use the notation n:0 to denote the branching ratio for the nth vibrational level. As seen in Fig. 4 the non-Franck–Condon behavior is quite substantial near threshold but by 21 eV the branching ratios reach their Franck–Condon values. For the

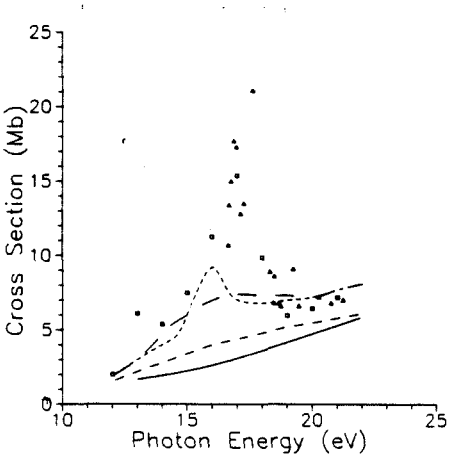

FIG. 6. Photoionization cross section for the $X\,^2\Pi_g$ state of O_2^+: —, present results (dipole length) obtained by summing contributions from $v^+ = 0$–4 vibrational levels; — (short dash), fixed-nuclei results of Ref. 15 at R_e (MSM); — — — (long dash), vibrationally averaged results of Ref. 15 (MSM); - - - (medium dash), fixed-nuclei results of Ref. 17 at R_e (SMT); □ experimental (e, $2e$) results of Brion *et al.* (Ref. 6); △, experimental line-source results of Samson *et al.* (Ref. 5). Our fixed-nuclei results at R_e are nearly identical to our vibrationally summed results and are not shown.

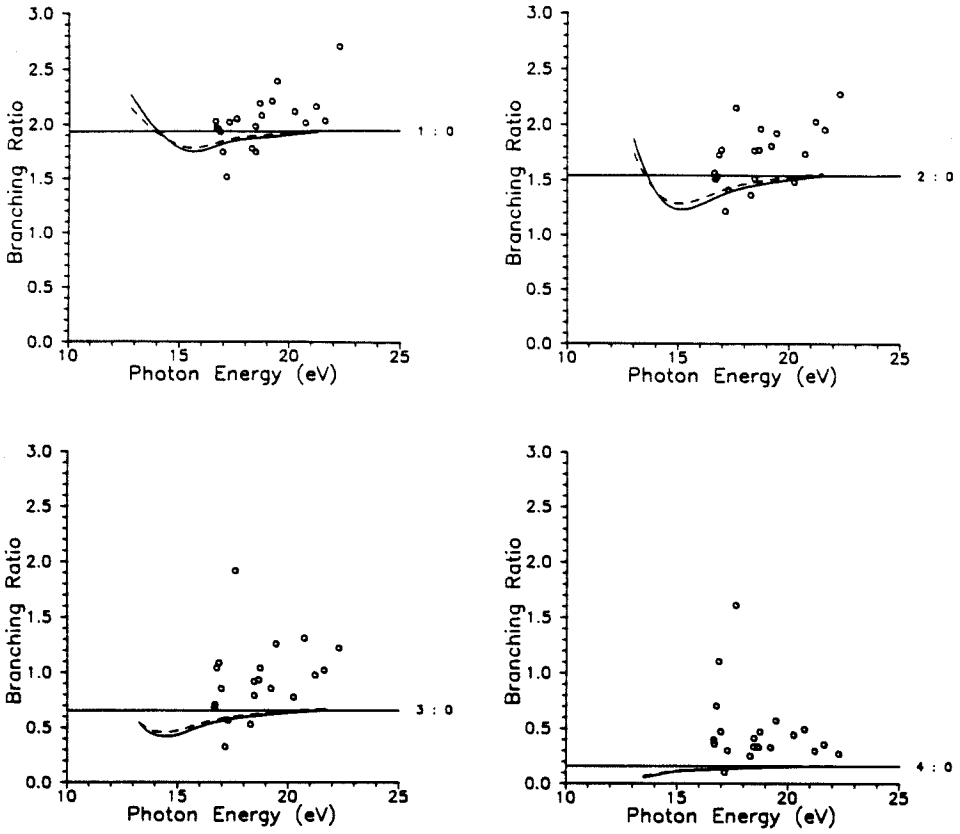

FIG. 7. The same as Fig. 4, plus the experimental line-source data of Gardner *et al.* (Ref. 26) shown by the symbol O.

lower vibrational levels ($v^+ = 0$–2), the behavior of the branching ratios can be understood by examining the dependence of the integrand in Eq. (5) on internuclear distance for the shape-resonant σ_u channel. For these levels the integrand is strongly peaked around one value of the internuclear distance R for the energy range studied. As the vibrational level increases, the largest contribution to the integrand comes from increasing values of R. The resulting shape-resonant σ_u cross sections peak at successively lower values of the photoelectron kinetic energy for increasing vibrational excitation. This behavior is best illustrated in Fig. 5 by showing vibrationally resolved $k\sigma_u$ partial cross sections. The ratios of the total cross sections therefore give rise to the sharp increase at threshold and dip at ~15.0 eV photon energy for the 1:0 and 2:0 branching ratios. For the higher ionic vibrational levels, larger internuclear distances are sampled, but the behavior of the integrands is more complex and cannot be as straightforwardly interpreted.

In Fig. 6 we show the vibrationally summed cross sections for $v^+ = 0$–4. Our results calculated at equilibrium geometry are nearly identical to the vibrationally summed results and are not shown. We also show both the fixed-nuclei results at R_e and the vibrationally averaged cross sections of the multiple scattering model (MSM) study of Dittman *et al.*[15], and the fixed-nuclei results at equilibrium of the SMT study of Gerwer *et al.*[17] We find that vibrational averaging hardly affects the present cross sections, in contrast to what is seen in the MSM study. This exaggeration of the effects of vibrational averaging in the MSM treatment has also been noted in earlier studies on N_2.[21] Moreover, the shape resonance is much more pronounced and at higher energy than in the present study. Figure 6 also shows the experimental results of Samson *et al.*[5] and Brion *et al.*[6] The prominent structure in the experimental data indicates that autoionization may play a significant role in the low-energy cross section for the $X\,^2\Pi_g$ state of O_2^+. Holmes *et al.*[24] suggest that Rydberg states leading to the $b\,^4\Sigma_g^-$ ion (ionization potential equal to 18.17 eV) are responsible for some of the autoionization in the vibrationally unresolved angular distributions. Moreover, the high-resolution photoionization efficiency study of Dehmer *et al.*[25] identifies several other Rydberg states which may contribute to autoionization features in the vibrationally resolved photoionization cross sections. Clearly, the autoionization structure is rich and com-

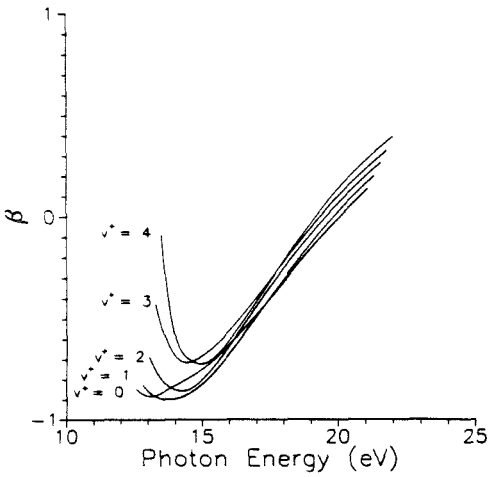

FIG. 8. Vibrationally resolved photoelectron asymmetry parameters (dipole length) leading to the $X\,^2\Pi_g$ state of O_2^+.

plex, and warrants further detailed experimental and theoretical study, as has been done on $3\sigma_g$ photoionization.[14]

In Fig. 7 we compare our calculated branching ratios to the line source data of Gardner *et al.*[26] As discussed above, autoionization structure complicates a comparison of the branching ratios with experimental data. Experiments employing a synchrotron source are needed to investigate the role of autoionization on these spectra.

Finally, in Fig. 8 we show our calculated vibrationally resolved photoelectron asymmetry parameters. These β's are strongly state dependent, particularly near threshold. This non-Franck–Condon behavior should be observable experimentally, barring additional complicating structure due to autoionization.

IV. CONCLUDING REMARKS

We have studied the vibrationally resolved cross sections and photoelectron angular distributions for photoionization leading to the $X\,^2\Pi_g$ ($v^+ = 0$–4) states of O_2^+. These studies were motivated by recent work showing the prominent role of a shape resonance in producing non-Franck–Condon effects in resonant multiphoton ionization of O_2 via the $C\,^3\Pi_g$ Rydberg state.[1–4] A σ_u shape resonance strongly influences these cross sections near the ionization threshold. This σ_u shape resonance leads to significant non-Franck–Condon behavior in ionization of the $1\pi_g$ level, and is evident in both the branching ratios and a vibrational state dependence of the photoelectron angular distributions below 21 eV photon energy. Comparison of our vibrationally resolved cross sections with available line-source data is seriously hindered by autoionization. Continuum source experiments are needed to further understand this structure, and to elucidate the shape-resonant continuum.

ACKNOWLEDGMENTS

This material is based upon research supported by the National Science Foundation under Grant No. CHE85-21391. The authors acknowledge use of the resources of the San Diego SuperComputer Center which is supported by the National Science Foundation. The authors also thank Dr. J. A. Stephens for helpful discussions and suggestions.

[1] P. J. Miller, L. Li, W. A. Chupka, and S. D. Colson, J. Chem. Phys. **89**, 3921 (1988).
[2] J. A. Stephens, M. Braunstein, and V. McKoy, J. Chem. Phys. **89**, 3923 (1988).
[3] P. J. Miller, W. A. Chupka, J. Winniczek, and M. G. White, J. Chem. Phys. **89**, 4058 (1988).
[4] M. Braunstein, J. A. Stephens, and V. McKoy, J. Chem. Phys. **90**, 633 (1989).
[5] J. A. R. Samson, J. L. Gardner, and G. N. Haddad, J. Electron Spectrosc. Relat. Phenom. **12**, 281 (1977).
[6] C. E. Brion, K. H. Tan, M. J. van der Wiel, and Ph. E. van der Leeuw, J. Electron Spectrosc. Relat. Phenom. **17**, 101 (1979).
[7] R. R. Lucchese, K. Takatsuka, and V. McKoy, Phys. Rep. **131**, 147 (1986).
[8] R. R. Lucchese, R. Raseev, and V. McKoy, Phys. Rev. A **25**, 2572 (1982).
[9] M. Braunstein, M. E. Smith, and V. McKoy, J. Chem. Phys. (to be published).
[10] T. H. Dunning, Jr., J. Chem. Phys. **53**, 2823 (1970).
[11] S. Huzinaga, *Gaussian Basis Sets for Molecular Calculations* (Elsevier, New York, 1984), p. 23.
[12] P. H. Krupenie, J. Phys. Chem. Ref. Data **1**, 423 (1972).
[13] T. Gustafsson, Chem. Phys. Lett. **75**, 505 (1980).
[14] P. Morin, I. Nenner, M. Y. Adam, M. J. Hubin-Franskin, J. Delwiche, J. Lefebvre-Brion, and A. Giusti-Suzor, Chem. Phys. Lett. **92**, 609 (1982).
[15] P. M. Dittman, D. Dill, and J. L. Dehmer, J. Chem. Phys. **76**, 5703 (1982).
[16] G. Raseev, H. Lefebvre-Brion, H. Le Rouzo, and A. L. Roche, J. Chem. Phys. **74**, 6686 (1981).
[17] A. Gerwer, C. Asaro, B. V. McKoy, and P. W. Langhoff, J. Chem. Phys. **72**, 713(1980).
[18] P. W. Langhoff, A. Gerwer, C. Asaro, and B. V. McKoy, Int. J. Quantum Chem. **13**, 645 (1979).
[19] U. Fano and J. W. Cooper, Rev. Mod. Phys. **40**, 441 (1968).
[20] J. L. Dehmer, D. Dill, and S. Wallace, Phys. Rev. Lett. **42**, 1005 (1979).
[21] R. R. Lucchese and V. McKoy, J. Phys. B **14**, L629 (1981).
[22] M. E. Smith, D. L. Lynch, and V. McKoy, J. Chem. Phys. **85**, 6455 (1986).
[23] See, for example, J. L. Dehmer, A. C. Parr, and S. H. Southworth, in *Handbook on Synchrotron Radiation*, edited by G. V. Marr (North-Holland, Amsterdam, 1986), Vol. II.
[24] R. M. Holmes and G. V. Marr, J. Phys. B **13**, 945 (1980).
[25] P. M. Dehmer and W. A. Chupka, J. Chem. Phys. **62**, 4525 (1975).
[26] J. L. Gardner and J. A. R. Samson, J. Electron Spectrosc. Relat. Phenom. **13**, 7 (1978).

Chapter 7

Shape-resonance-induced non-Franck-Condon effects in (2+1) resonance enhanced multiphoton ionization of the C $^3\Pi_g$ state of O_2

(The text of this chapter appeared in: J. A. Stephens, M. Braunstein, and V. McKoy, J. Chem. Phys. **89** 3923 (1989).)

Shape-resonance-induced non-Franck–Condon effects in (2+1) resonance enhanced multiphoton ionization of the $C\,^3\Pi_g$ state of O_2

J. A. Stephens, M. Braunstein, and V. McKoy
Arthur Amos Noyes Laboratory of Chemical Physics,[a] California Institute of Technology, Pasadena, California 91125

(Received 16 May 1988; accepted 6 July 1988)

Resonance enhanced multiphoton ionization (REMPI) coupled with high resolution, angle-resolved photoelectron spectroscopy is becoming an important probe of the photoionization dynamics of excited molecular states.[1] Recent measurements of (2 + 1) REMPI spectra of the $C\,^3\Pi_g$ ($3s\sigma_g$) Rydberg state of O_2 by Miller *et al.*[2] (preceeding paper) and Katsumata *et al.*[3] show pronounced non-Franck–Condon effects, as evident by the observation of intense off-diagonal ($\Delta v = v^+ - v' \neq 0$) peaks for alternative vibrational states of the ground state ion. Miller *et al.* have also suggested that the non-Franck–Condon behavior arises from autoionization of the $(1\pi_g 3\sigma_u)\,^3\Pi_u$ valence state which would be equivalent, in the present context, to the formation of a shape resonance in the σ_u ionization continuum.[4] The dependence of the energy and width of shape resonances on internuclear distance induces strong variations in the electronic transition dipole moment to specific vibrational states of the ion. This mechanism for inducing non-Franck–Condon vibrational distributions in the photoionization of ground state molecules was first predicted and observed in N_2 and CO.[5]

The purpose of this Letter is to present *ab initio* calculations of the O_2 $C\,^3\Pi_g$ state photoelectron spectra which have been measured by Miller *et al.* These calculations establish that in photoionization of this resonantly prepared Rydberg state, a shape resonance at threshold signficantly alters vibrational distributions from those based on the Franck–Condon principle. Such resonantly induced distributions will strongly influence the preparation of state-selected ions by REMPI, and perhaps more importantly, complicate the extraction of state populations from REMPI signals. Although these calculations account for a significant part of the observed non-Franck–Condon intensity, some discrepancies between theory and experiment remain for certain portions of the spectrum. These discrepancies are tentatively interpreted by invoking mechanisms involving initial-state correlation and final-state channel interaction with excited valence states.

To account for non-Franck–Condon effects due to the shape resonance, we have included[6,7] full kinetic energy and R dependence in the bound–free transition dipole moment $\mathbf{r}_{fv^+,iv'} = \int dR\, \chi^*_{v^+}(R) r_{fi}(k;R) \chi_{v'}(R)$. Here $r_{fi}(k;R)$ is the transition moment calculated at fixed internuclear distance R and electron momentum k, for a bound (Rydberg) initial state $|i\rangle$ and continuum (photoelectron + ionic core) final states $|f\rangle$. For the $C\,^3\Pi_g$ initial state we used a Hartree–Fock SCF wave function,[8,9] and for the final state we used continuum Hartree–Fock orbitals for the dipole-allowed $^3\Pi_u$, $^3\Delta_u$, $^3\Sigma_u^+$, and $^3\Sigma_u^-$ channels. The continuum orbitals were obtained using the iterative Schwinger variational technique.[10] For the $C\,^3\Pi_g$ state vibrational wave functions we constructed and numerically integrated an RKR potential curve, employing vibrational constants measured by York and Comer[11] and the rotational constant measured by Sur *et al.*[12] The vibrational wave functions for the $X\,^2\Pi_g$ ion were obtained by numerically integrating the RKR potential curve given by Krupenie.[13] The range of R included in calculating all transition matrix elements $\mathbf{r}_{fv^+,iv'}$ varied from 1.7 to 3.2 a_0. Further details of the calculations will be reported in a separate paper.

The calculated photoionization cross sections for the $(1\pi_g 3s\sigma_g^{-1}\, k\sigma_u)\,^3\Pi_u$ channel (not shown) predict a σ_u (f-wave) shape resonance, whose position and width are extremely sensitive to changes in the internuclear distance. The R dependence of the transition moment, particularly near the equilibrium bond distance and ~0–2 eV photoelectron kinetic energy, is responsible for the non-Franck–Condon effects in the vibrational distributions. The cross sections for final states associated with $k\pi_u$ ionization channels are relatively small and reveal almost negligible variation with R. The ground state, fixed-nuclei calculations of Gerwer *et al.*[14] for $3\sigma_g$ and $1\pi_g$ photoionization predict this resonance near the ionic thresholds. Theoretical studies[15] which include R dependence in ground state photoionization confirm the presence of the low-energy σ_u resonance, and further predict significant non-Franck–Condon effects.

In Fig. 1 we show our calculated branching ratios for the $v' = 1$–3 levels of the $C\,^3\Pi_g$ state, compared with the peak intensities obtained from the measured photoelectron spectra. The calculations predict for all v' levels pronounced non-Franck–Condon distributions: the vibrational wave functions for the $C\,^3\Pi_g$ and $X\,^2\Pi_g$ potentials are nearly identical, and the ratios $\Delta v \neq 0$ of Franck–Condon factors are *negligible* when plotted on the scale in Fig. 1. For the $v' = 2$ and 3 levels, the $\Delta v < 0$ ratios are in satisfactory agreement with experiment, while those for $\Delta v > 0$ appear to show systematic deviation. Our results for the $v' = 1$ level account for some of the observed $\Delta v \neq 0$ intensity, although there is substantial disagreement. We mention two mechanisms which could underly these discrepancies. First, several experiments[9,12,16] have suggested perturbations of the low vibrational levels of the $C\,^3\Pi_g$ state, particularly involving the $v' = 1$ level. It has been proposed[9,12] that the perturbations arise from weak configuration interaction with the $(3\sigma_g 1\pi_g^3)\,^3\Pi_g$ valence state. Inclusion of this configuration in the present theory (as initial-state correlation) would introduce R-dependent expansion coefficients into the dipole amplitude $r_{fi}(R)$. Due to the R dependence induced by the resonance, these coefficients could alter the calculated distributions for the $v' = 1$ transition such that the off-diagonal v^+ components in-

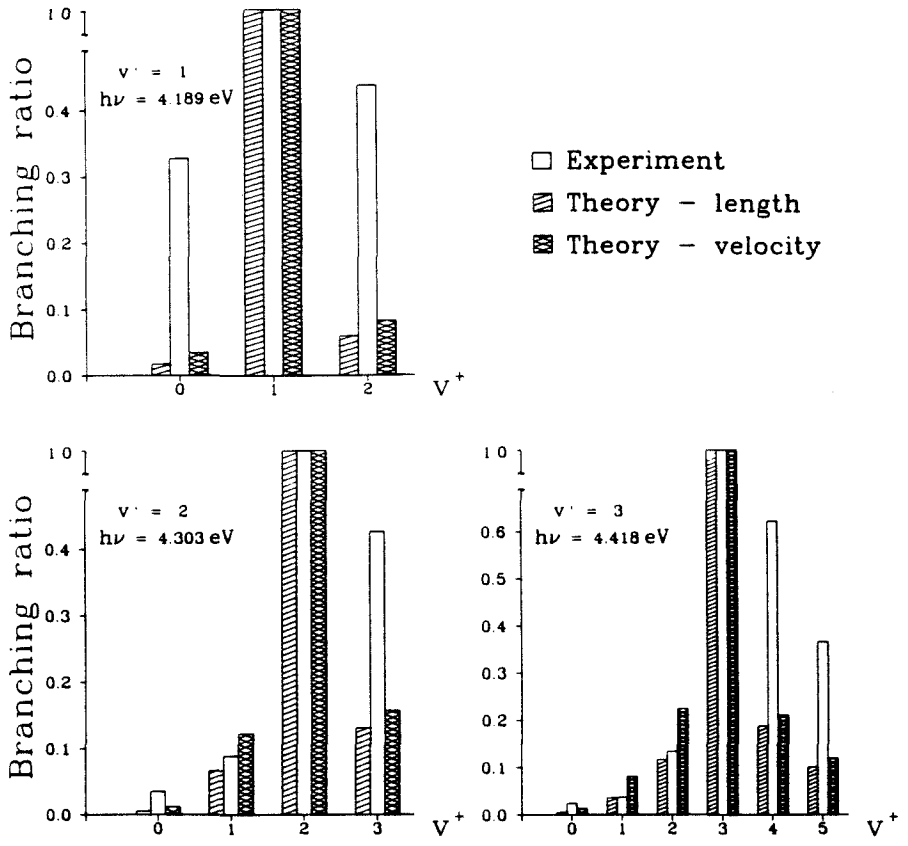

FIG. 1. Calculated vibrational branching ratios for O_2 $C\,^3\Pi_g$ ($v' = 1$–3) photoionization, compared with the measurements of Miller *et al.* (Ref. 2). The theoretical results were normalized to experiment by dividing by the $\Delta v = 0$ peak.

crease their relative magnitudes. Second, the deviations observed in the $\Delta v > 0$ components of the $v' = 2,3$ levels could arise from electronic autoionization of $^3\Pi_u$, $^3\Delta_u$, $^3\Sigma_u^+$, and $^3\Sigma_u^-$ bound states into the four continuum final states of identical symmetry. Accurate bound-state calculations[17,18] predict $^3\Delta_u$ and $^3\Sigma_u^+$ dissociative states arising from terms of the $1\pi_u^3 1\pi_g^3$ electronic configuration, which intersect the inner region of the ion curve near the $v^+ = 3$–5 levels. Autoionization of the $B\,^3\Sigma_u^-$ state could perturb the vibrational intensity for the $v^+ = 1$ level as well. These valence-shell excitations are not dipole accessible from the $C\,^3\Pi_g$ state, however, residual Coulomb interactions exist between continuum and bound configurations which differ by two molecular orbitals. The energy and R dependence of the bound–continuum mixing coefficients could substantially modify the present one-electron results for the higher v^+ levels.

The authors gratefully acknowledge helpful discussions with Sham Dixit. This work was supported by grants from the National Science Foundation (CHE-8521391), Air Force Office of Scientific Research (Contract No. 87-0039), and the Office of Health and Environmental Research of the U. S. Department of Energy (DE-FG03-87ER60513). We also acknowledge use of resources of the San Diego Supercomputer Center, which is supported by the National Science Foundation.

[a] Contribution No. 7777.
[1] See, for example, S. T. Pratt, P. M. Dehmer, and J. L. Dehmer, Chem. Phys. Lett. **105**, 28 (1984).
[2] P. J. Miller, L. Li, W. A. Chupka, and S. D. Colson, J. Chem. Phys. **89**, 3921 (1988).
[3] S. Katsumata, K. Sato, Y. Achiba, and K. Kimura, J. Electron Spectrosc. Relat. Phenom. **41**, 325 (1986).
[4] P. Morin, I. Nenner, M. Y. Adam, M. J. Hubin-Franskin, J. Delwiche, H. Lefebvre-Brion, and A. Giusti-Suzor, Chem. Phys. Lett. **92**, 609 (1982).
[5] J. L. Dehmer, D. Dill, and S. Wallace, Phys. Rev. Lett. **43**, 1005 (1979); R. Stockbauer, B. E. Cole, D. L. Ederer, J. B. West, A. C. Parr, and J. L. Dehmer, *ibid.* **43**, 757 (1979); J. B. West, A. C. Parr, B. E. Cole, D. L. Ederer, R. Stockbauer, and J. L. Dehmer, J. Phys. B **13**, 1105 (1980).
[6] R. R. Lucchese and V. McKoy, J. Phys. B **14**, L629 (1981).
[7] S. N. Dixit, D. L. Lynch, and V. McKoy, Phys. Rev. A **30**, 3332 (1984).
[8] T. H. Dunning, J. Chem. Phys. **53**, 2823 (1971).
[9] D. C. Cartwright, W. J. Hunt, W. Williams, S. Trajmar, and W. A. Goddard, Phys. Rev. A **8**, 2436 (1973).
[10] R. R. Lucchese, K. Takatsuka, and V. McKoy, Phys. Rep. **131**, 147 (1986), and references therein.
[11] T. York and J. Comer, J. Phys. B **16**, 3627 (1983).
[12] A. Sur, C. V. Ramana, W. A. Chupka, and S. D. Colson, J. Chem. Phys. **84**, 69 (1986).
[13] P. Krupenie, J. Phys. Chem. Ref. Data **1**, 423 (1972).
[14] A. Gerwer, C. Asaro, B. V. McKoy, and P. W. Langhoff, J. Chem. Phys. **72**, 713 (1980).

[15]G. Raseev, H. Lefebvre-Brion, H. LeRouzo, and A. L. Roche, J. Chem. Phys. **74**, 6686 (1981); P. M. Dittman, D. Dill, and J. L. Dehmer, *ibid.* **76**, 5703 (1982).
[16]R. H. Huebner, R. J. Celotta, S. R. Mielczarek, and C. E. Kuyatt, J. Chem. Phys. **63**, 241 (1975).
[17]R. J. Buenker and S. D. Peyerimhoff, Chem. Phys. Lett. **34**, 225 (1975); R. P. Saxon and B. Liu, J. Chem. Phys. **67**, 5432 (1977).
[18]S. L. Guberman, Int. J. Quantum Chem. Symp. **13**, 531 (1979).

Chapter 8

Shape resonance and non-Franck-Condon effects in (2+1) resonance enhanced multiphoton ionization of O_2 via the C $^3\Pi_g$ state

(The text of this chapter appeared in: M. Braunstein, J. A. Stephens, and V. McKoy, J. Chem. Phys. **90**, 633 (1989).)

Shape resonance and non-Franck–Condon effects in (2+1) resonant enhanced multiphoton ionization of O_2 via the $C\,^3\Pi_g$ state

M. Braunstein, J. A. Stephens, and V. McKoy
Arthur Amos Noyes Laboratory of Chemical Physics,[a] California Institute of Technology, Pasadena, California 91125

(Received 1 August 1988; accepted 29 September 1988)

We report vibrationally resolved photoelectron angular distributions for photoionization of the $C\,^1\Pi_g$ Rydberg state of O_2. Comparison is made with recent experimental measurements of angular distributions which employ (2 + 1) resonant enhanced multiphoton ionization of the $C\,^1\Pi_g$ state. The present theory treats the process as single-photon ionization from an unaligned Rydberg state, and qualitatively accounts for much of the observed trends. Non-Franck–Condon effects induced by the $k\sigma_u$ shape resonance lead to a substantial dependence of the angular distributions on the vibrational state of the $X\,^2\Pi_g$ ion. Discrepancies between our theoretical results and experiment are qualitatively discussed and tentatively attributed to residual electron correlations.

I. INTRODUCTION

The photoionization dynamics of the $(1\pi_g 3s\sigma_g)$ $^1\Pi_g$ and $^1\Pi_g$ Rydberg states of O_2 have been recently studied using (2 + 1) resonant enhanced multiphoton ionization (REMPI) spectroscopy.[1–3] Analysis of the ion-current and associated photoelectron spectra have yielded the rotational and vibrational constants of these states which are seen to be nearly equivalent to that of the $X\,^2\Pi_g$ ion. In addition they have probed specific electronic interactions with repulsive $(3\sigma_g 1\pi_g^3)$ $^{1,3}\Pi_g$ valence states, which had earlier been investigated by employing electron-impact excitation spectroscopy.[4–7] Most recently, measurements of vibrationally resolved photoelectron spectra of the $v' = 1$–3 levels of the $C\,^1\Pi_g$ state revealed intense, off-diagonal $(\Delta v = v^+ - v' \neq 0)$ peaks for alternative vibrational states of the $^2\Pi_g$ state of the ion.[8,9] This observation was unexpected since for an unperturbed, single-configuration Rydberg state (converging to a specific ion core), the Franck–Condon principle predicts the propensity rule $\Delta v = 0$.[10] The observed non-Franck–Condon behavior was interpreted[8,9] as arising from the formation of a low-energy shape resonance in the σ_u ionization continuum. The dependence of the energy and width of shape resonances on internuclear distance induces strong variations in the electronic transition moment to specific vibrational states of the ion. This mechanism for inducing non-Franck–Condon vibrational distributions was initially investigated in the photoionization dynamics of ground state diatomic molecules.[11–14] The present multiphoton ionization studies of O_2 establish shape-resonant, non-Franck–Condon effects as a prototypical case for study in the context of photoionization of molecular excited states.

In this paper we present studies of photoelectron angular distributions for ionization of the $C\,^1\Pi_g$ Rydberg state of O_2, and also report further details of the *ab initio* calculations published in Ref. 9. Following the measurements[8] and calculations[9] of vibrationally resolved photoelectron spectra, Miller *et al.*[15] have recently measured vibrationally resolved photoelectron angular distributions for photoionization of this same state. Comparison of our calculated angular distributions with the measurements of Miller *et al.* reveal that the σ_u shape resonance, through its angular momentum composition and dependence on nuclear motion, is responsible for much of the observed trends. The present theory treats the process as single-photon ionization from an unaligned Rydberg state, thus neglecting any consideration of alignment arising in the two-photon excitation process. We ascribe the remaining discrepancies between our calculations and experiment to our neglect of alignment of the $C\,^3\Pi_g$ state, and probably more importantly, neglect of electron correlations (beyond the Hartree–Fock level) in the theory. These aspects of the problem are now being investigated, and will be discussed in later publications.

II. THEORY

A. Wave functions and potentials

Within the frozen-core Hartree–Fock approximation, there are four dipole-allowed channels for ionization of the $C\,^3\Pi_g$ state, corresponding to photoionization of the singly occupied $3s\sigma_g$ Rydberg orbital. The electronic continuum wave functions are

$$\Psi(^3\Pi_u) = |[\text{core}]1\pi_g^+ k\sigma_u|\,, \tag{1a}$$

$$\Psi(^3\Sigma_u^+) = \frac{1}{\sqrt{2}}\{|[\text{core}]1\pi_g^+ k\pi_u^-| + |[\text{core}]1\pi_g^- k\pi_u^+|\}\,, \tag{1b}$$

$$\Psi(^3\Sigma_u^-) = \frac{1}{\sqrt{2}}\{|[\text{core}]1\pi_g^+ k\pi_u^-| - |[\text{core}]1\pi_g^- k\pi_u^+|\}\,, \tag{1c}$$

$$\Psi(^3\Delta_u) = |[\text{core}]1\pi_g^+ k\pi_u^+|\,, \tag{1d}$$

where $[\text{core}] = 1\sigma_g^2 1\sigma_u^2 2\sigma_g^2 2\sigma_u^2 3\sigma_g^2 1\pi_u^4$. With these wave functions the static-exchange, one-particle Schrödinger equations for the continuum orbitals can be derived straightforwardly,[16,17] and are of the form

[a] Contribution No. 7822.

$$^3\Pi_u: P\Big[f + \sum_{\text{core}} (2J_i - K_i) + J_{1\pi_g} - K_{1\pi_g} - \epsilon\Big] P|k\sigma_u\rangle = 0 \tag{2a}$$

$$^3\Sigma_u^+: P\Big[f + \sum_{\text{core}} (2J_i - K_i) + J_{1\pi_g} - K_{1\pi_g} + S''_{1\pi_g} - S'_{1\pi_g} - \epsilon\Big] P|k\pi_u^+\rangle = 0, \tag{2b}$$

$$^3\Sigma_u^-: P\Big[f + \sum_{\text{core}} (2J_i - K_i) + J_{1\pi_g} - K_{1\pi_g} - S''_{1\pi_g} + S'_{1\pi_g} - \epsilon\Big] P|k\pi_u^+\rangle = 0, \tag{2c}$$

$$^3\Delta_u: P\Big[f + \sum_{\text{core}} (2J_i - K_i) + J_{1\pi_g} - K_{1\pi_g} - \epsilon\Big] P|k\pi_u^+\rangle = 0. \tag{2d}$$

In these equations J_i and K_i are the Coulomb and exchange operators, and P is a projection operator which enforces orthogonality of the continuum orbital to the occupied orbitals, and ϵ is the photoelectron kinetic energy. The operators S'' and S' are defined by

$$S''_\pi \phi_+(\mathbf{r}_1) = \phi_-(\mathbf{r}_1) \int d^3r_2 [\pi_-(\mathbf{r}_2)]^* \frac{1}{r_{12}} \pi_+(\mathbf{r}_2) \tag{3}$$

and

$$S'_\pi \phi_+(\mathbf{r}_1) = \pi_+(\mathbf{r}_1) \int d^3r_2 [\pi_-(\mathbf{r}_2)]^* \frac{1}{r_{12}} \phi_-(\mathbf{r}_2), \tag{4}$$

and the one-electron operator in Eq. (2) is

$$f = -\frac{1}{2}\nabla_i^2 - \sum_\alpha \frac{Z_\alpha}{r_{i\alpha}}, \tag{5}$$

where Z_α is a nuclear charge.

An iterative procedure for solving the Lippmann–Schwinger equations associated with Eq. (2) has been developed based on the Schwinger variational principle.[16,17] This procedure, discussed in detail elsewhere,[17] begins by solving the Lippmann–Schwinger equations for a separable approximation to the potential U of the form

$$U(\mathbf{r},\mathbf{r}') = \sum_{i,j} \langle \mathbf{r}|\alpha_i\rangle [U^{-1}]_{i,j} \langle \alpha_j|\mathbf{r}'\rangle, \tag{6}$$

where the matrix U^{-1} is the inverse of the matrix with elements $U_{ij} = \langle \alpha_i|U|\alpha_j\rangle$ and the α's are discrete basis functions such as Cartesian or spherical Gaussian functions, and U is twice the static-exchange potential in Eq. (2) with the long-range Coulomb potential removed. Solutions obtained with this separable potential can be iteratively improved to yield the converged solutions of the Lippmann–Schwinger equations.[16,17] In this study we used the zero-order solutions, i.e., no iteration, but employed a large basis set $\{\alpha_i\}$ in Eq. (6). Previous studies have shown that such use of a sufficiently large basis ensures convergence of the photoelectron wave function without the need for iterative improvement.

B. Computational details

Determination of the vibrationally resolved cross sections and asymmetry parameters requires the photoionization transition moment, $\langle \Psi_f(\mathbf{r},R)|\mathbf{d}|\Psi_i(\mathbf{r},R)\rangle$, at several values of the internuclear distance R spanning the range of the vibrational motion.[11,18,19] Here $\mathbf{d}$ is the electric dipole operator and $\mathbf{r}$ represents the electronic coordinates. In the adiabatic-nuclei approximation the photoionization cross section for a transition from the v' vibrational level of the $C\,^1\Pi_g$ Rydberg state to the v^+ vibrational level of the $X\,^2\Pi_g$ ion is given by

$$\sigma_{v',v^+}^{L,V} = \frac{4\pi^2}{3c} E \sum_{lm\mu} |\langle \chi(v^+)|I_{lm\mu}^{L,V}|\chi(v')\rangle|^2. \tag{7}$$

Here $I_{lm\mu}^{L,V}$ are partial-wave components of the length (L) or velocity (V) incoming-wave normalized transition moment,[18] E is the photon energy, c is the speed of light, and $\chi(v')$ and $\chi(v^+)$ are the vibrational wave functions of the Rydberg state and the ion, respectively. The vibrationally resolved asymmetry parameter $\beta_{v',v^+}^{L,V}$ is defined through the differential photoionization cross section

$$\frac{d\sigma_{v',v^+}^{L,V}}{d\Omega_k} = \frac{\sigma_{v',v^+}^{L,V}}{4\pi}\left[1 + \beta_{v',v^+}^{L,V} P_2(\cos\theta)\right], \tag{8}$$

where θ is the angle between the direction of the light polarization and photoelectron momentum $\mathbf{k}$, and P_2 is a Legendre polynomial of degree two. The transition moments $I_{lm\mu}^{L,V}$ for the $k\sigma_u$ and $k\pi_u$ channels were evaluated at the internuclear distances given in Table I, and interpolated using cubic spline functions. The initial state $C\,^1\Pi_g$ SCF wave functions were calculated using a (9*s*5*p*2*d*/4*s*3*p*2*d*) contracted Gaussian basis set, augmented to include four (with exponents 0.08, 0.02, 0.005, 0.001 25), three (0.05, 0.0125, 0.003 125), and two (0.036 358, 0.010 769) *s*, *p*, and *d*-type diffuse functions, respectively.[4,20–22] The total SCF energy of the $C\,^1\Pi_g$ state at $R = 2.282\ a_0$ with this basis is $-149.288\,556$ a.u.

For the final state, we assume the frozen-core Hartree–Fock model, in which the ionic orbitals are constrained to be identical to those of the neutral molecule and the photoelectron orbital is a solution of the one-electron Schrödinger equations given above. For the basis functions α_i in the expansion of Eq. (6) (see Table II) we used Cartesian Gaussian functions centered on each atom and spherical Gaussian functions at the center of mass. All matrix elements in the solution of the Lippmann–Schwinger equations were evaluated using single-center expansions about the center of mass.[17] The partial-wave expansion of the photoelectron or-

TABLE I. Internuclear distances of O_2 where photoionization matrix elements were evaluated.

Photoionization symmetry	Internuclear distance (a.u.)
$3s\sigma_g \rightarrow k\sigma_u$ [a]	1.7,1.894,2.088,2.188,2.238, 2.282 2.311,2.34,2.4,2.588,2.894,3.2
$3s\sigma_g \rightarrow k\pi_u$	1.7,2.088,2.282,2.588,3.2

[a] Shape-resonant channel.

TABLE II. Basis sets used in separable potential, Eq. (6).

Photoionization symmetry	Type of Gaussian function[a]	Exponents
$3s\sigma_g \rightarrow k\sigma_u$	Cartesian s	16.0,8.0,4.0,2.0,1.0,0.5
	z	1.0,0.5
	Spherical $l=1$	4.0,2.0,1.0,0.5,0.25
	$l=3$	4.0,2.0,1.0,0.5,0.25
	$l=5$	1.0,0.5,0.25
$3s\sigma_g \rightarrow k\pi_u$	Cartesian x	16.0,8.0,4.0,2.0,1.0,0.5
	xz	1.0,0.5
	Spherical $l=1$	4.0,2.0,1.0,0.5,0.25
	$l=3$	4.0,2.0,1.0,0.5,0.25
	$l=5$	1.0,0.5,0.25

[a] Cartesian Gaussian basis functions are defined as $\phi^{n,l,m,A}(r) = N(x-A_x)^l (y-A_y)^m (z-A_z)^n \exp(-\alpha|r-A|^2)$ and spherical Gaussian functions are defined as $\phi^{n,l,m,A}(r) = N|r-A|^l \exp(-\alpha|r-A|^2) Y_{lm}(\Omega_{r-A})$. The Cartesian functions are centered on the nuclei and spherical functions are centered on the bond midpoint.

bitals were truncated at $l = 7$. The other expansion parameters[16] were chosen as follows:

(i) maximum partial wave in the expansion of the occupied orbitals in the direct potential = 30,

(ii) maximum partial wave in the expansion of the occupied orbitals in the exchange potential = 26 ($1\sigma_g$), 26 ($1\sigma_u$), 14 ($2\sigma_g$), 14 ($2\sigma_u$), 14 ($3\sigma_g$), 14 ($1\pi_u$), 14 ($1\pi_g$),

(iii) maximum partial wave expansion of $1/r_{12}$ in the direct and exchange terms = 60 and 30, respectively,

(iv) maximum partial wave expansion of the nuclear potential = 60,

(v) all other partial wave expansions were truncated at $l = 30$.

These parameters provide photoionization cross sections that are within a few percent of the converged values. The associated radial integrals were obtained with a Simpson's rule quadrature. The grid contained 900 points and extended to 96 a.u. with a step size of 0.01 a.u. from the origin to 2.0 a.u. Beyond 2.0 a.u. the largest step size was 0.32 a.u.

For the $C\,^3\Pi_g$ state vibrational wave functions, an RKR potential curve was constructed, and is reported for the first time in Table III, with calculated Franck–Condon factors given in Table IV. The vibrational wave functions for the $X\,^2\Pi_g$ ion were obtained by numerically integrating the RKR potential curve given by Krupenie,[23] in the range of $1.7 < R < 3.2$ a.u.

III. DISCUSSION OF RESULTS

A. Fixed-nuclei calculations

In Fig. 1 we show the eigenphase sums for the $3s\sigma_g \rightarrow k\sigma_u$ channel calculated at various internuclear distances. The eigenphase sum δ is given by

$$\delta = \sum_{lm} \arctan(U^\dagger K U)_{lm,lm}, \qquad (9)$$

where here U is the matrix which diagonalizes the real, symmetric K matrix. A rapid rise of $\sim\pi$ with increasing photoelectron kinetic energy signals the presence of a shape resonance,[14] and examination of the contributions to δ indicates

TABLE III. Spectroscopic constants and RKR potential energy curve for the $C\,^1\Pi_g$ state of O_2.[a]

$\omega_e = 1951$[b]	$\omega_e x_e = 20.16$[b]	$B_e = 1.68$[c]
$D_e = 4.98\times10^{-6}$[d]	$\alpha_e = 0.0214$[d]	$D_0 = 46264.9$[d]

v'	V	r_{min}	r_{max}
−0.5	0.0	2.1111	
0.0	0.004 423 74	2.031 406 5	2.207 327 2
1.0	0.013 133 18	1.975 560 5	2.280 672 7
2.0	0.021 658 53	1.939 235 4	2.333 778 7
3.0	0.029 999 81	1.911 051 7	2.378 678 5
4.0	0.038 157 02	1.887 658 4	2.418 821 3
5.0	0.046 130 15	1.867 517 0	2.455 777 8
6.0	0.053 919 20	1.849 769 9	2.490 420 8
7.0	0.061 524 18	1.833 881 2	2.523 294 6
8.0	0.068 945 08	1.819 489 4	2.554 766 4

[a] All spectroscopic constants are in cm^{-1}. The potential V, r_{min}, and r_{max} are in a.u.

[b] From Ref. 7.

[c] From Ref. 2.

[d] These constants were obtained from the following relations: $D_e = B_e^2/\omega_e^2$; $\alpha_e = (6\sqrt{\omega_e x_e B_e^3}/\omega_e) - (6B_e^2/\omega_e)$; $D_0 = (\omega_e^2/4\omega_e x_e) - \omega_e/2 - \omega_e x_e/4$.

its f-wave ($l = 3$) character. The behavior of the eigenphase sum in the $3s\sigma_g \rightarrow k\sigma_u$ channel shows that the resonance is extremely sensitive to changes in R, and in this case extends its spectral variation into the discrete portion of the $k\sigma_u$ channel near the equilibrium bond distance of the ion. Analysis of the fixed-R quantum defects reported by Gerwer *et al.*[24] for $1\pi_g$ photoionization reveals the resonant enhancement of the $n\sigma_u$ Rydberg series which converges to the first ionic threshold. Near-threshold shape resonance behavior was discussed by Raseev *et al.*[25] for the $3\sigma_g$ level of O_2, and by Dittman *et al.*[26] for the $3\sigma_g$ and $1\pi_g$ levels.

The calculated photoionization cross sections for the

TABLE IV. Calculated Franck–Condon factors for the transitions $O_2\ C\,^1\Pi_g(v') \rightarrow O_2^+\ X\,^2\Pi_g(v^+)$.[a]

v'	v^+	$\lvert\langle v^+\rvert v'\rangle\rvert^2$
0	0	0.999 845
1	0	$0.416\,395\times10^{-4}$
1	1	0.999 381
1	2	$0.132\,412\times10^{-3}$
2	0	$0.109\,287\times10^{-3}$
2	1	$0.106\,457\times10^{-3}$
2	2	0.995 847
2	3	$0.322\,933\times10^{-2}$
3	0	$0.163\,960\times10^{-5}$
3	1	$0.421\,358\times10^{-4}$
3	2	$0.284\,685\times10^{-2}$
3	3	0.983 515
3	4	$0.123\,974\times10^{-1}$
3	5	$0.699\,919\times10^{-4}$

[a] Franck–Condon factors were obtained with the potential described in Table II for the $O_2\ C\,^1\Pi_g$ state, and with the RKR potential of Ref. 23 for the $O_2^+\ X\,^2\Pi_g$ state.

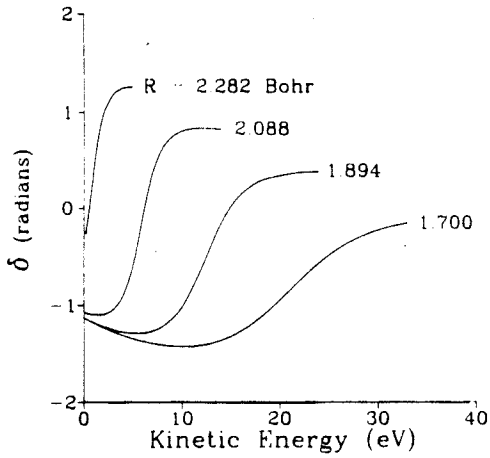

FIG. 1. Calculated eigenphase sums for the σ_u symmetry at various internuclear distances.

$3s\sigma_g \rightarrow k\sigma_u$ channel, shown in Fig. 2, display the corresponding $k\sigma_u$ shape resonance. The R dependence of the transition moment, particularly near the equilibrium bond distance (2.282 a_0) and ~0–2 eV photoelectron kinetic energy, is primarily responsible for the non-Franck–Condon effects observed in the photoelectron angular distributions and branching ratios.

B. Photoelectron angular distributions and branching ratios

In Figs. 3–6 we show our calculated vibrationally resolved photoelectron angular distributions and branching ratios for photoionization of the $v' = 1$–3 levels of the $C\,^3\Pi_g$ Rydberg state. Also plotted are the experimental results of

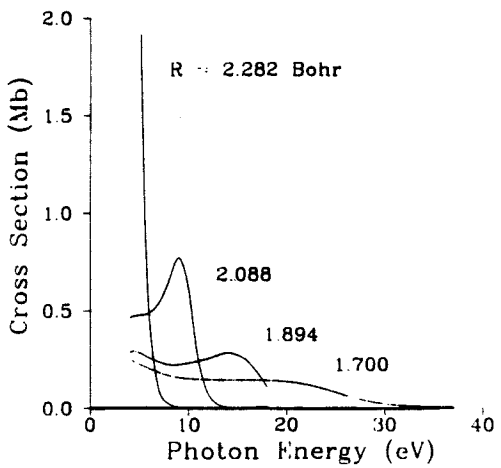

FIG. 2. Calculated (velocity form) photoionization cross sections for the $3s\sigma_g \rightarrow k\sigma_u$ channel at various internuclear distances.

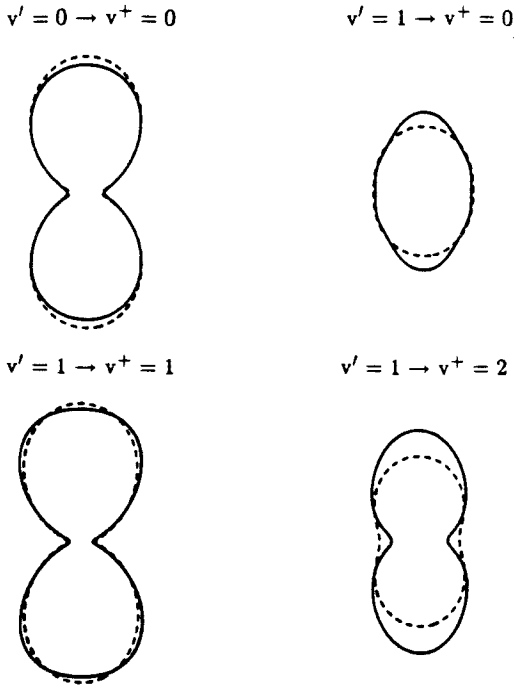

FIG. 3. Calculated (dash curve, velocity form) photoelectron angular distributions for the $v' = 0$ and 1 levels of the $C\,^1\Pi_g$ state, compared with the measurements of Miller *et al.* (Ref. 15, solid curve).

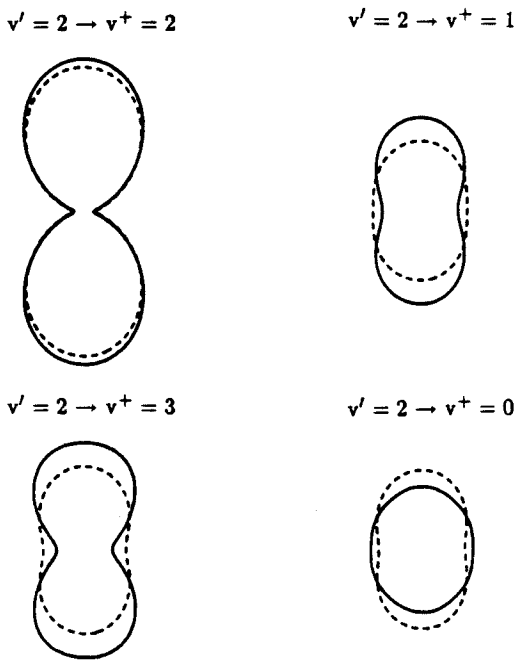

FIG. 4. Calculated (dash curve, velocity form) photoelectron angular distributions for the $v' = 2$ level of the $C\,^1\Pi_g$ state, compared with the measurements of Miller *et al.* (Ref. 15, solid curve).

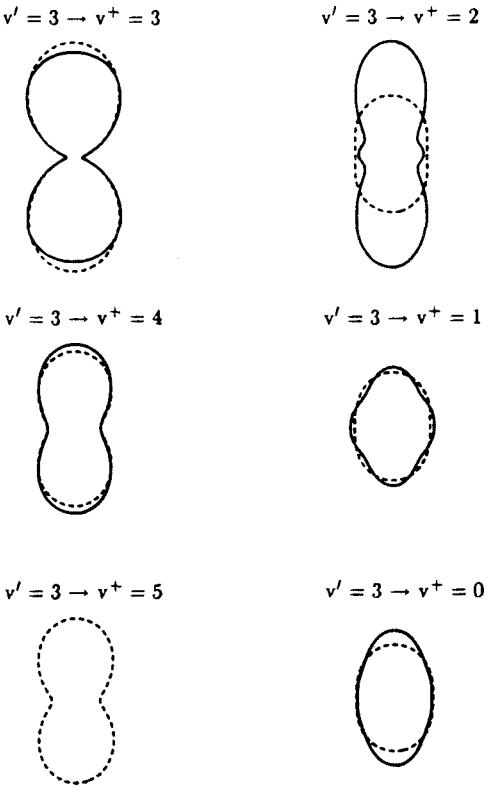

FIG. 5. Calculated (dash curve, velocity form) photoelectron angular distributions for the $v' = 3$ level of the $C\,^1\Pi_g$ state, compared with the measurements of Miller *et al.* (Ref. 15, solid curve).

Miller *et al.*[8,15] Figures 3–5 compare the angular distribution of photoelectron current obtained from theory and the experiment. As shown, each angular distribution is normalized so that in the expansion of the angular distribution, i.e.,

$$\frac{d\sigma}{d\Omega} \propto \sum_{k=0} a_{2k} P_{2k}(\cos\theta) ,$$

the a_0 term equals unity. Note that for an unaligned state only a_0 and a_2 are nonvanishing, and $\beta = a_2/a_0$. The branching ratios have been discussed previously,[8,9] and we include them here (Fig. 6) for completeness, and for comparison with the photoelectron angular distributions. Tables V and VI summarize our calculated results in addition to the measurements.

Referring to Table VI, comparison of our calculated β_{v',v^+} asymmetry parameters with experiment shows that results for the diagonal ($\Delta v = 0$) transitions are in near quantitative agreement. Our calculated off-diagonal ($\Delta v \neq 0$) coefficients essentially reproduce the observed trends (smaller a_2 values), however, discrepancies between theory and experiment previously noted[8,9] for the vibrational branching ratios are also apparent here. The most prominent observation in both theoretical and experimental results is the difference in angular distribution between the diagonal and off-diagonal transitions.

The $k\sigma_u$ shape resonance exerts its influence in both diagonal and off-diagonal transitions, and actually constitutes much of the "direct" (i.e., one-electron) transition strength. For example, in the $v' = 1 \rightarrow v^+ = 1$ transition, the $k\sigma_u$ channel accounts for $\sim 53\%$ of the total dipole strength, with the remaining strength partitioned among the $^3\Delta_u$, $^3\Sigma_u^+$, and $^3\Sigma_u^- k\pi_u$ channels. Within the $k\sigma_u$ channel of the $v' = 1 \rightarrow v^+ = 1$ transition, the dipole strength is composed of $\sim 30\%$ *f*-wave, and $\sim 70\%$ *p*-wave contributions, the *p–f* coupling being essential for formation of the shape resonance. Because the $k\pi_u$ channels are nonresonant and hence strongly dominated by the $3s\sigma_g \rightarrow k\pi_u$ ($l = 1$) component at these energies, the angular distributions for the $\Delta v = 0$ transitions display characteristic *p*-wave-type patterns, as seen in Figs. 3–5 for all diagonal transitions. In contrast, for the *off-diagonal* transitions, the $k\sigma_u$ channel accounts for $\sim 88\%$ of the total ($k\sigma_u + k\pi_u$) dipole strength. The *f*-wave component of the $k\sigma_u$ resonance causes substantial deviations from "$s \rightarrow p$"-type photoejection (see e.g., the $v' = 1 \rightarrow v^+ = 2$ distribution in Fig. 3). The $3s\sigma_g \rightarrow k\pi_u$ dipole strengths are quite small ($\sim 1\%$–5%) compared to that of the $k\sigma_u$ channel for $\Delta v \neq 0$ transitions, due to the validity of Franck–Condon factorization in these channels. This enormous difference in transition strength for these two continua ($k\sigma_u$ and $k\pi_u$) in $\Delta v \neq 0$ transitions accounts for the calculated and observed differences in the asymmetry parameters.

The a_4 and a_6 coefficients measured by Miller *et al.*[15] become particularly significant for the $v' = 3$ intermediate level, which is also evident by inspection of our Fig. 5. The magnitude of the a_4 and a_6 terms depend on the degree of alignment of the resonant intermediate $C\,^3\Pi_g$ state, as well as the relative phase (and hence interference) between amplitudes for the one-photon ionization step.[27,28] Since the present experiments and theoretical analysis have not attempted to investigate specific rotational excitation branches, it is difficult to rationalize the small magnitudes of a_4 and a_6.

In some cases the magnitude of the discrepancy between the theoretical and measured quantities in Figs. 3–6 appears different whether angular distributions or vibrational branching ratios are compared. For example, the calculated $v' = 3 \rightarrow v^+ = 4$ asymmetry parameter agrees well with the measured value, while the corresponding branching ratio does not. On the other hand, the discrepancies of the calculated $v' = 1 \rightarrow v^+ = 2$ and $v' = 2 \rightarrow v^+ = 3$ asymmetry parameters appear to be consistent with those seen in the branching ratios. Such observations have been documented in single-photon studies,[14] i.e., photoionization dynamics involving shape resonances and electron correlation effects can be mirrored in different ways for the two observables. Since the diagonal transitions are dominated by direct intensity from four continuum channels, electron correlation effects are probably less apparent compared to the off-diagonal transitions, where the single $k\sigma_u$ channel is prevalent. This circumstance permits us to assess the importance of correlation effects in a qualitative, yet preliminary, manner.

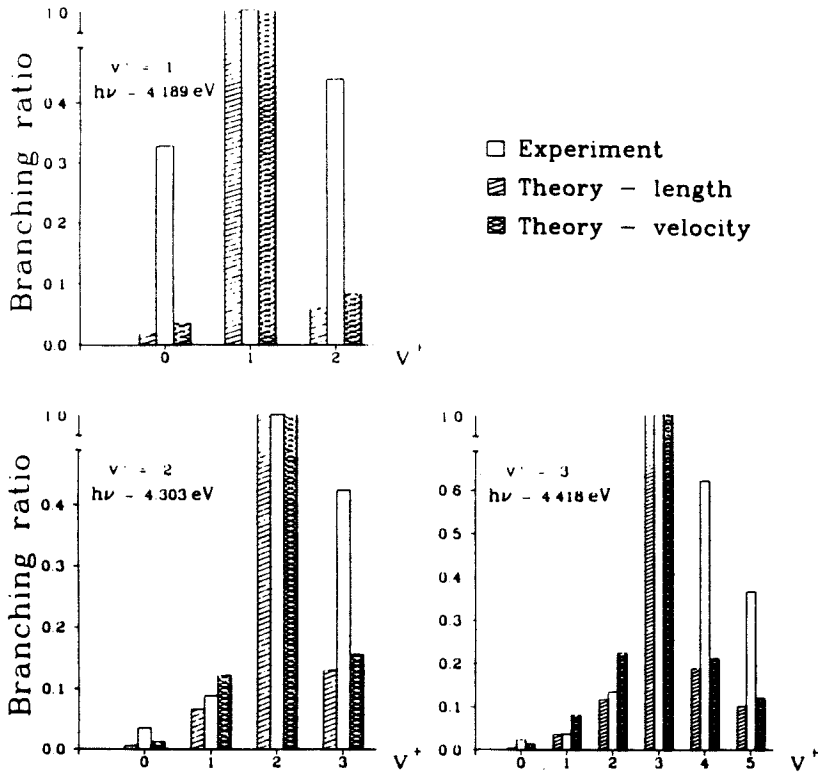

FIG. 6. Calculated vibrational branching ratios for O_2 $C\,^1\Pi_g$ ($v' = 1$–3) photoionization, compared with the measurements of Miller *et al.* (Ref. 8). The theoretical results were normalized to experiment by dividing by the $\Delta v = 0$ peak.

TABLE V. Summary of vibrationally resolved cross sections and branching ratios.

		σ_{v',v^+} (Mb)		$\sigma_{v',v^+}/\sigma(\Delta v = 0)$		
		Length velocity (Theory)		Length velocity (Theory)		$\sigma_{v',v^+}/\sigma(\Delta v = 0)$ (Experiment[a])
v'	v^+					
0	0	4.1997	1.3176	1.0000	1.0000	···
1	0	0.0756	0.0495	0.0177	0.0345	0.326
1	1	4.2836	1.4367	1.0000	1.0000	1.000
1	2	0.2580	0.1196	0.0602	0.0833	0.435
2	0	0.0212	0.0158	0.0057	0.0119	0.035
2	1	0.2452	0.1611	0.0660	0.1213	0.088
2	2	3.7172	1.3288	1.0000	1.0000	1.000
2	3	0.4830	0.2068	0.1299	0.1556	0.425
3	0	0.0140	0.0120	0.0052	0.0123	0.024
3	1	0.0964	0.0747	0.0360	0.0808	0.037
3	2	0.3118	0.2068	0.1163	0.2239	0.134
3	3	2.6802	0.9236	1.0000	1.0000	1.000
3	4	0.5027	0.1944	0.1876	0.2104	0.622
3	5	0.2720	0.1101	0.1015	0.1192	0.366

[a] From Ref. 8.

TABLE VI. Summary of vibrationally resolved photoelectron angular distributions.

		β_{v',v^+} (Theory)		
v'	v^+	Length	Velocity	a_2 (Experiment[a])
0	0	1.622	1.456	1.38
1	0	0.128	0.171	0.27
1	1	1.630	1.533	1.66
1	2	0.537	0.551	0.94
2	0	0.394	0.433	0.12
2	1	0.219	0.271	0.67
2	2	1.634	1.629	1.75
2	3	0.618	0.513	1.04
3	0	0.210	0.230	0.36
3	1	0.192	0.264	0.15
3	2	0.197	0.353	0.98
3	3	1.623	1.656	1.64
3	4	0.973	0.794	0.89
3	5	0.877	0.902	···

[a] From Ref. 15. See this reference for a_4 and a_6 coefficients.

C. Electron correlation effects

Several mechanisms which can give rise to anomalous photoelectron spectra of Rydberg states have been pointed out in the literature,[29–34] and recently discussed extensively by Chupka.[10] Such mechanisms may involve one-electron dynamical features (such as the shape resonance in the present study), autoionization of repulsive doubly excited states,[10,29–33] and Rydberg-valence mixing of the resonant intermediate state.[34–37] The latter two mechanisms are many-electron processes requiring theoretical description beyond a Hartree–Fock level for the intermediate bound and continuum final states, respectively. Mechanisms involving many-electron processes have been proposed[8,9] to account for discrepancies between the present calculations and measurements. We discuss them here in more detail to provide a guide for future theoretical effort.

Focusing on the branching ratio results in Fig. 6, there are two (possibly competing) mechanisms which could result in the observed deviations. Earlier experimental evidence suggests[4–6] perturbations of the $v' = 1$ level of the $C\,^1\Pi_g$ state, arising from weak configuration interaction with the repulsive $(3\sigma_g 1\pi_g^3)\,^3\Pi_g$ valence state.[22,38] This is corroborated by the MPI spectra of Sur *et al.*,[2] which reveal diffuse (rotationally unresolved) spectra for the low vibrational levels (except for the $v' = 2$ band), and is indicative of predissociation. If the ionization step is fast compared to the predissociation induced by the $3\sigma_g 1\pi_g^3$ state, then the relative intensities for the $v' = 1$ level should be unaffected. On the other hand, correlation of the repulsive $3\sigma_g 1\pi_g^3$ state with the Rydberg state, viz.

$$\Psi_{\mathrm{Ryd}}(R) = C_1(R)\Psi(1\pi_g 3s\sigma_g) + C_2(R)\Psi(3\sigma_g 1\pi_g^3)$$

would introduce an R-dependent coefficient into the effective transition moment,

$$\langle \Psi_k | \mathbf{d} | \Psi_{\mathrm{Ryd}} \rangle = C_1(R)\langle k\sigma_u | \mathbf{d} | 3s\sigma_g \rangle .$$

Buenker and Peyerimhoff[35] have shown that the $C\,^3\Pi_g$ state contains a significant contribution from this repulsive state (near the outer turning point of the $v' = 1$ level), in addition to the doubly excited $1\pi_u^2 1\pi_g^3 4\sigma_g$ configuration. Due to the sensitive R dependence already induced in the transition matrix element by the shape resonance, changes in the Rydberg coefficient due to configuration mixing could significantly alter the calculated branching ratios and angular distributions for the $v' = 1$ level.

A second mechanism invokes electronic autoionization of dissociative states, which possess many-electron symmetries ($^1\Sigma_u^+$, $^1\Sigma_u^-$, $^3\Delta_u$) associated with the $k\pi_u$ continua accessed from the $C\,^1\Pi_g$ state. (The known states of $^3\Pi_u$ symmetry are inaccessible for autoionization in the present experiments.) The $1\pi_u^3 1\pi_g^3$ electronic configuration gives rise to the $A\,^1\Sigma_u^+$, $B\,^3\Sigma_u^-$, and $C\,^3\Delta_u$ states, which have been studied by accurate *ab initio* calculations,[36–38] particularly in the context of dissociative recombination.[39] Considering these potential curves and the relevant range of internuclear distances (see e.g., Fig. 2 of Ref. 39), the $B\,^3\Sigma_u^-$ state may autoionize leaving O_2^+ in all v^+ levels produced for a given v' excitation. Autoionization of the $A\,^1\Sigma_u^+$ and $C\,^3\Delta_u$ states likely affects only the $v^+ = 3$–5 levels, produced via the $v' = 2,3$ excitations. With the present approximations the $A\,^1\Sigma_u^+$, $B\,^3\Sigma_u^-$, and $C\,^3\Delta_u$ states are not dipole accessible from the $C\,^3\Pi_g$ state (since the configurations differ by two spin orbitals), yet they contribute to autoionization through the dispersion term of the effective transition amplitude or q parameter. Schematically, consider the zero-order states $\psi_E = |1\pi_g k\pi_u|$, $\phi_i = |1\pi_u^3 1\pi_g^3|$, $\Phi_0 = |1\pi_g 3s\sigma_g|$, and the interaction matrix element $V_E = \langle \psi_E | H | \phi_i \rangle$. The resonant continuum wave function Ψ_E is[40,41]

$$\Psi_E = N(E)\{\Phi_i V_E^* + [E - E_i(E)]\psi_E\},$$

where $N(E)$ is a normalization factor (with maximum value at $E = E_i$), and E_i and Φ_i are the *modified* discrete energy and wave function of the autoionizing state ϕ_i. The dipole amplitude between the initial state Φ_0 and the resonant state, and the Fano q parameter are accordingly

$$\langle \Psi_E | \mathbf{d} | \Psi_0 \rangle = N(E) V_E^* \Big\{ \langle \phi_i | \mathbf{d} | \Phi_0 \rangle + P \int_0^\infty dE' \, \frac{V_{E'}^* \langle \psi_{E'} | \mathbf{d} | \Phi_0 \rangle}{E - E'} + [E - E_i(E)] \langle \psi_E | \mathbf{d} | \Phi_0 \rangle \Big\},$$

$$q = \frac{\langle \phi_i | \mathbf{d} | \Phi_0 \rangle}{\pi \langle \psi_E | \mathbf{d} | \Phi_0 \rangle V_E^*} + \frac{1}{\pi} P \int_0^\infty dE' \, \frac{1}{E - E'} \frac{f(E')}{f(E)},$$

where the function $f(E) = V_E^* \langle \psi_E | \mathbf{d} | \Phi_0 \rangle$ and P indicates principal part. For states derived from the $1\pi_u^3 1\pi_g^3$ configuration, the dipole amplitude $\langle \phi_i | \mathbf{d} | \Phi_0 \rangle$ vanishes, as noted above. Near the resonance ($E \sim E_i$), contributions to $\langle \Psi_E | \mathbf{d} | \Psi_0 \rangle$ are therefore dominated by the dispersion term. This circumstance alone supports the contention of Miller *et al.*[8] that the $B\,^3\Sigma_u^-$ state should appear as a window resonance ($q \sim 0$) in the $k\pi_u$ continuum. On the other hand, contributions to q from the dispersion term actually depend[42] on rapid variations of the *ratio* $f(E')/f(E)$ about the singularity. The resonance profile may change with internuclear distance, depending principally on the R dependence of the matrix element V_E.

IV. SUMMARY AND CONCLUSION

We have presented vibrationally resolved photoelectron angular distributions for photoionization of the $C\,^3\Pi_g$ Rydberg state of O_2. The observed trends in the measured asymmetry parameters are reproduced, in some cases quantitatively, by the theory. The large difference in angular dependence between the diagonal and off-diagonal parameters may be understood by analysis of the contributing degenerate $k\sigma_u$ and $k\pi_u$ ionization channels. Although both $\Delta v = 0$ and $\Delta v \neq 0$ transitions are enhanced by the shape resonance, the off-diagonal asymmetry parameters are dominated by contributions from the $k\sigma_u$ channel. Hence the strong f-wave component which is characteristic of the $k\sigma_u$ shape resonance causes substantial deviations from $s \rightarrow p$-type photoejection.

Non-Franck–Condon effects induced by the shape resonance have been identified as an important mechanism which causes striking deviations from the well-known $\Delta v = 0$ propensity rule for ionization of molecular Rydberg

states. From the present comparison with measurements, we conclude that specific, multichannel interactions not included in the present theory are also very important. We have tentatively identified these interactions as deriving from configuration mixing of the initial $C\,^1\Pi_g$ state with excited valence states, and autoionization of repulsive valence states derived from the $1\pi_u^1 1\pi_g^1$ electronic configuration. Future theoretical effort should aim at understanding the REMPI dynamics inclusive of these effects.

Finally, due to the ubiquity of shape resonances now documented in single-photon ionization of ground state molecules,[14] we expect them to have important implications for ionization of molecular excited states. Such resonantly induced vibrational distributions strongly influence the preparation of state-selected ions. Indeed, the present studies indicate that vibrational state selection of O_2^+ via the $C\,^1\Pi_g$ state is seriously limited.

ACKNOWLEDGMENTS

The authors acknowledge helpful discussions with Dr. Richard Dubs. This work was supported by grants from the National Science Foundation (CHE-8521391), Air Force Office of Scientific Research (Contract No. 87-0039), and the Office of Health and Environmental Research of the U.S. Department of Energy (DE-FG03-87ER60513). We also acknowledge use of resources of the San Diego SuperComputer Center, which is supported by the National Science Foundation.

[1] A. Sur, C. V. Ramana, and S. D. Colson, J. Chem. Phys. **83**, 904 (1985).
[2] A. Sur, C. V. Ramana, W. A. Chupka, and S. D. Colson, J. Chem. Phys. **84**, 69 (1986).
[3] S. Katsumata, K. Sato, Y. Achiba, and K. Kimura, J. Electron Spectrosc. Relat. Phenom. **41**, 325 (1986).
[4] D. C. Cartwright, W. J. Hunt, W. Williams, S. Trajmar, and W. A. Goddard, Phys. Rev. A **8**, 2436 (1973).
[5] S. Trajmar, D. C. Cartwright, and R. I. Hall, J. Chem. Phys. **65**, 5275 (1976).
[6] R. H. Huebner, R. J. Celotta, S. R. Mielczarek, and C. E. Kuyatt, J. Chem. Phys. **63**, 241 (1975).
[7] T. York and J. Comer, J. Phys. B **16**, 3627 (1983).
[8] P. J. Miller, L. Li, W. A. Chupka, and S. D. Colson, J. Chem. Phys. **89**, 3921 (1988).
[9] J. A. Stephens, M. Braunstein, and V. McKoy, J. Chem. Phys. **89**, 3923 (1988).
[10] W. A. Chupka, J. Chem. Phys. **87**, 1488 (1987).
[11] J. L. Dehmer, D. Dill, and S. Wallace, Phys. Rev. Lett. **43**, 1005 (1979).
[12] R. Stockbauer, B. E. Cole, D. L. Ederer, J. B. West, A. C. Parr, and J. L. Dehmer, Phys. Rev. Lett. **43**, 757 (1979).
[13] J. B. West, A. C. Parr, B. E. Cole, D. L. Ederer, R. Stockbauer, and J. L. Dehmer, J. Phys. B **13**, 1105 (1980).
[14] J. L. Dehmer, A. C. Parr, and S. H. Southworth, in *Handbook on Synchrotron Radiation*, edited by G. V. Marr (North-Holland, Amsterdam, 1986), Vol. II.
[15] P. J. Miller, W. A. Chupka, J. Winniczek, and M. G. White, J. Chem. Phys. **89**, 4058 (1988).
[16] R. R. Lucchese, G. Raseev, and V. McKoy, Phys. Rev. A **25**, 2572 (1982).
[17] R. R. Lucchese, K. Takatsuka, and V. McKoy, Phys. Rep. **131**, 147 (1986), and references quoted therein.
[18] R. R. Lucchese and V. McKoy, J. Phys. B **14**, L629 (1981).
[19] S. N. Dixit, D. L. Lynch, and V. McKoy, Phys. Rev. A **30**, 3332 (1984).
[20] T. H. Dunning, J. Chem. Phys. **53**, 2823 (1971).
[21] J. Andzelm, M. Klobukowski, E. Radzio-Andzelm, Y. Sakai, and H. Tatewaki, in *Gaussian Basis Sets for Molecular Calculations*, edited by S. Huzinaga (Elsevier, Amsterdam, 1984), p. 23.
[22] R. P. Saxon and B. Liu, J. Chem. Phys. **73**, 876 (1980).
[23] P. Krupenie, J. Phys. Chem. Ref. Data **1**, 423 (1972).
[24] A. Gerwer, C. Asaro, B. V. McKoy, and P. W. Langhoff, J. Chem. Phys. **72**, 713 (1980).
[25] G. Raseev, H. Lefebvre-Brion, H. LeRouzo, and A. L. Roche, J. Chem. Phys. **74**, 6686 (1981).
[26] P. M. Dittman, D. Dill, and J. L. Dehmer, J. Chem. Phys. **76**, 5703 (1982).
[27] S. N. Dixit and V. McKoy, J. Chem. Phys. **82**, 3546 (1985).
[28] R. L. Dubs, V. McKoy, and S. N. Dixit, J. Chem. Phys. **88**, 968 (1988).
[29] S. T. Pratt, P. M. Dehmer, and J. L. Dehmer, Chem. Phys. Lett. **105**, 28 (1984).
[30] S. T. Pratt, P. M. Dehmer, and J. L. Dehmer, J. Chem. Phys. **85**, 3379 (1986).
[31] J. C. Miller and R. N. Compton, J. Chem. Phys. **84**, 675 (1986).
[32] A. P. Hickman, Phys. Rev. Lett. **59**, 1553 (1987).
[33] C. Cornaggia, A. Giusti-Suzor, and Ch. Jungen, J. Chem. Phys. **87**, 3934 (1987).
[34] P. J. Miller, L. Li, W. A. Chupka, and S. D. Colson, J. Chem. Phys. **88**, 2972 (1988).
[35] R. J. Buenker and S. D. Peyerimhoff, Chem. Phys. **8**, 324 (1975).
[36] R. J. Buenker and S. D. Peyerimhoff, Chem. Phys. Lett. **34**, 225 (1975); **36**, 415 (1975).
[37] M. Yoshimine, K. Tanaka, H. Tatewaki, S. Obara, F. Sasaki, and K. Ohno, J. Chem. Phys. **64**, 2254 (1976).
[38] R. P. Saxon and B. Liu, J. Chem. Phys. **67**, 5432 (1977).
[39] S. L. Guberman, Int. J. Quantum Chem. Quantum Chem. Symp. **13**, 531 (1979).
[40] U. Fano, Phys. Rev. **124**, 1866 (1961).
[41] A. F. Starace, in *Handbuch der Physik*, edited by M. Mehlhorn (Springer, Berlin, 1982), Vol. 31, pp. 1–121; see especially Sect. III.
[42] U. Fano and J. Cooper, Phys. Rev. **137**, 1364 (1964).

Chapter 9

Shape resonance effects in the rotationally resolved photoelectron spectra of O_2

Shape resonance effects in the rotationally resolved photoelectron spectra of O_2

M. Braunstein and V. McKoy

*Arthur Amos Noyes Laboratory of Chemical Physics**

California Institute of Technology

Pasadena, California 91125

S. N. Dixit

Theoretical Atomic and Molecular Physics Group

Lawrence Livermore National Laboratory, L-490

Livermore, California 94550

R. G. Tonkyn and M. G. White

Chemistry Department

Brookhaven National Laboratory

Upton, New York 11973

Abstract

We report the results of theoretical and experimental studies of the rotationally resolved photoelectron spectra of O_2 at low temperature leading to the $v^+ = 0$, 1, and 2 levels of the $X\ ^2\Pi_g$ state of O_2^+. A delayed, pulsed field ionization technique is used in conjunction with a coherent VUV radiation source to obtain high resolution spectra near threshold. The data are compared with theoretical results obtained using static-exchange photoelectron orbitals and a full description of the mixed Hund's case (a)-(b) ionic ground state. Agreement with experiment is good, especially for the $v^+ = 1$ and $v^+ = 2$ levels. Analysis of the rotational branch

intensities yields detailed information on the angular momentum composition of the shape resonance near threshold. We also show that the dependence of the electronic transition moment on internuclear distance caused by the shape resonance leads to a significant dependence of the rotational branch intensity on ion vibrational level.

* Contribution No. 8145

Studies of rotationally resolved photoionization in molecules can provide insight into molecular properties and dynamics, including important details of excited electronic states,[1,2] as well as the angular momentum composition of[3-5] and the influence of autoionization on[6-8] the electronic continuum. Recently, Tonkyn *et al.*[9] used narrow band VUV laser radiation and a novel pulsed field ionization (PFI) technique to measure the photoelectron spectrum of O_2 with rotational resolution near threshold, where a shape resonance has been well documented in *vibrationally* resolved and other studies.[10-20] Analysis of *rotational* branch intensities (and photoelectron angular distributions) should reveal rich and otherwise unavailable information on the partial wave character of shape resonances. In addition, the internuclear distance dependence of the electronic transition moment associated with this shape resonance[21-24] can be expected to lead to a dependence of the rotational branch intensity on the ion vibrational state.

Figure 1 shows results of theoretical and experimental studies of rotationally resolved single-photon photoelectron spectra of O_2 leading to the $v^+ = 0$, 1, and 2 levels of the $X\ ^2\Pi_g$ state of O_2^+ at threshold. These "cold spectra" clarify the analysis of the rotationally warm ($T \sim 200°\ K$) spectrum reported in Ref. 9, which showed a great deal of spectral congestion. The photoelectron spectrometer and VUV laser source have been described in detail elsewhere.[9,25] The spectrometer has been modified here to incorporate a differentially pumped pulsed molecular beam source for rotational cooling of the target molecules. The rotationally resolved photoelectron spectra are calculated by generalizing the earlier treatment[26] to include a complete description of the mixed Hund's case (a)-(b) ionic ground state, the details of which will be given elsewhere.[27] The required bound-free amplitudes are obtained with static-exchange photoelectron orbitals[28,29] and include

a full treatment of the internuclear distance dependence of the electronic transition moment caused by the shape resonance.[10]

The calculated rotational spectra at 5° K, where only the K = 1 rotational level of the ground state is significantly populated, are dominated by low $\Delta K = (K^+ - K)$ branches (Q-S for F1; R-T for F2). Analysis of the transition amplitudes shows that these branches are mostly due to $\ell = 1$ partial waves. The high ΔK branches (T-V for F1; U-V for F2), on the other hand, are dominated by $\ell = 3$ partial waves. The difference in the angular momentum composition of the photoelectron wave function for low ΔK peaks versus high ΔK peaks is especially evident in the photoelectron angular distributions which will be discussed in a future publication.[27] Higher resolution spectra (not shown) which can distinguish between different ground state J levels (J = 0, 1 and 2 for K = 1)[30] reveal even richer information on the partial wave character of the photoelectron continuum. For example, for certain J resolved branches, *only* $\ell = 3$ and higher waves are allowed.[27]

As the vibrational excitation increases from $v^+ = 0$ to 1 to 2 in the 5° spectra, the ratio of low ΔK peaks to high ΔK peaks increases significantly. This mirrors the fact that the $\ell = 1$ photoelectron amplitudes become much larger with vibrational excitation compared to the $\ell = 3$ components, and *is the direct result of the internuclear distance dependence of the electronic transition moment due to the shape resonance.* Without the shape resonance, we would expect the same ratio of $\ell = 1$ to $\ell = 3$ amplitudes for all vibrational levels and therefore the same relative peak heights in all spectra. In analyzing these rotational intensities, it is important to stress that the angular momentum components of the σ_u shape resonance are highly coupled;[13] and hence the shape resonance cannot be solely attributed to the dominating $\ell = 1$ partial wave.

At T = 10° K, these differences in the rotational branch intensities with vibrational level are still evident in the theoretical and experimental spectra, but are more difficult to quantify due to the overlapping transitions originating from the K = 3 level, which now has an appreciable population (approximately 30% of the total intensity comes from K = 3 at 10°). The agreement between these 10° spectra is encouraging, especially for the v^+ = 1 and 2 levels. Some important differences do exist, and will be addressed in a future publication.[27]

Research at the California Institute of Technology was supported by grants from the National Science Foundation (CHE-85121391), AFOSR (87-0039), and the Office of Health and Environmental Research of DOE (DE-FG03-87ER60513). We also acknowledge use of resources of the San Diego Supercomputer Center, which is supported by the National Science Foundation. M. B. acknowledges a Pacific Northwest Laboratories graduate fellowship. Research at Brookhaven National Laboratory was supported under contract No. DE-AC02-76CH00016 with the U. S. Department of Energy and by its Division of Chemical Sciences, Office of Basic Energy Sciences. Work done by S. N. D. was performed under the auspices of the U. S. Department of Energy by Lawrence Livermore National Laboratory under contract W-7405-Eng-48.

References

[1] X. Song, E. Sekreta, J. P. Reilly, H. Rudolph, and V. McKoy, J. Chem. Phys. **91**, 6062 (1989).

[2] H. Rudolph, J. A. Stephens, V. McKoy, and M. T. Lee, J. Chem. Phys. **91**, 1374 (1989).

[3] K. S. Viswanathan, E. Sekreta, E. R. Davidson, and J. P. Reilly, J. Chem. Phys. **90**, 5078 (1986).

[4] H. Rudolph, S. N. Dixit, V. McKoy, and W. M. Huo, Chem. Phys. Lett. **137**, 521 (1987).

[5] H. Rudolph, V. McKoy, and S. N. Dixit, J. Chem. Phys. **88**, 637 (1988).

[6] E. D. Poliakoff, J. C. K. Chan, and M. G. White, J. Chem. Phys. **85**, 6232 (1986).

[7] Ch. Jungen and D. Dill, J. Chem. Phys. **73**, 3338 (1980).

[8] D. Dill, Phys. Rev. A **6**, 160 (1972).

[9] R. G. Tonkyn, J. W. Winniczek, and M. G. White, Chem. Phys. Lett. **164**, 137 (1989).

[10] M. Braunstein and V. McKoy, J. Chem. Phys. **90**, 2575 (1989).

[11] T. Gustafsson, Chem. Phys. Lett. **75**, 505 (1980).

[12] P. M. Dittman, D. Dill, and J. L. Dehmer, J. Chem. Phys. **76**, 5703 (1982).

[13] G. Raseev, H. Lefebvre-Brion, H. Le Rouzo, and A. L. Roche, J. Chem. Phys. **74**, 6686 (1981).

[14] A. Gerwer, C. Asaro, B. V. McKoy, and P. W. Langhoff, J. Chem. Phys. **72**, 713 (1980).

[15] P. J. Miller, L. Li, W. A. Chupka, and S. D. Colson, J. Chem. Phys. **89**, 3921 (1988).

[16] J. A. Stephens, M. Braunstein, and V. McKoy, J. Chem. Phys. **89**, 3923 (1988).

[17] P. J. Miller, W. A. Chupka, J. Winniczek, and M. G. White, J. Chem. Phys. **89**, 4058 (1988).

[18] M. Braunstein, J. A. Stephens, and V. McKoy, J. Chem. Phys. **90**, 633 (1989).

[19] J. A. Stephens, M. Braunstein, and V. McKoy, J. Chem. Phys. **92**, 5319 (1990).

[20] P. J. Miller and W. A. Chupka, (private communication).

[21] J. L. Dehmer, D. Dill, and S. Wallace, Phys. Rev. Lett. **43**, 1005 (1979).

[22] R. Stockbauer, B. E. Cole, D. L. Ederer, J. B. West, A. C. Parr, and J. L. Dehmer, Phys. Rev. Lett. **43**, 757 (1979).

[23] J. B. West, A. C. Parr, B. E. Cole, D. L. Ederer, R. Stockbauer, and J. L. Dehmer, J. Phys. B **13**, 1105 (1980).

[24] J. L. Dehmer, A. C. Parr, and S. H. Southworth, in *Handbook of Synchrotron Radiation*, edited by G. V. Marr (North-Holland, Amsterdam, 1986), Vol. II.

[25] R. G. Tonkyn and M. G. White, Rev. Sci. Instrum. **60** 1245 (1989).

[26] S. N. Dixit and V. McKoy, J. Chem. Phys. **82**, 3546 (1985).

[27] M. Braunstein, V. McKoy, and S. N. Dixit, (to be published).

[28] R. R. Lucchese, K. Takatsuka, and V. McKoy, Phys. Rep. **131**, 147 (1986).

[29] R. R. Lucchese, R. Raseev, and V. McKoy, Phys. Rev. A **25**, 2572 (1982).

[30] G. Herzberg, *Molecular Spectra and Molecular Structure: I. Spectra of Diatomic Molecules* (Krieger, Malabar, Florida, 1989).

Figure Caption

Fig. 1 : Threshold photoelectron spectra for single-photon ionization of O_2 ($X\ ^3\Sigma_g^-$) leading to O_2^+ ($X\ ^2\Pi_g$). The branch designations refer to $\Delta K = (K^+ - K)$ transitions. For example, an"S" branch under F1 on the bottom row of letters

refers to a transitions from the K = 1 rotational level of the ground state to the K^+ = 3 level of the F1 spin-orbit manifold of the ion. The theoretical spectra have an assumed linewidth of 2 cm^{-1}. The experimental spectra have arbitrary intensity units. The baselines of the 10° spectra have been shifted upward by a constant amount.

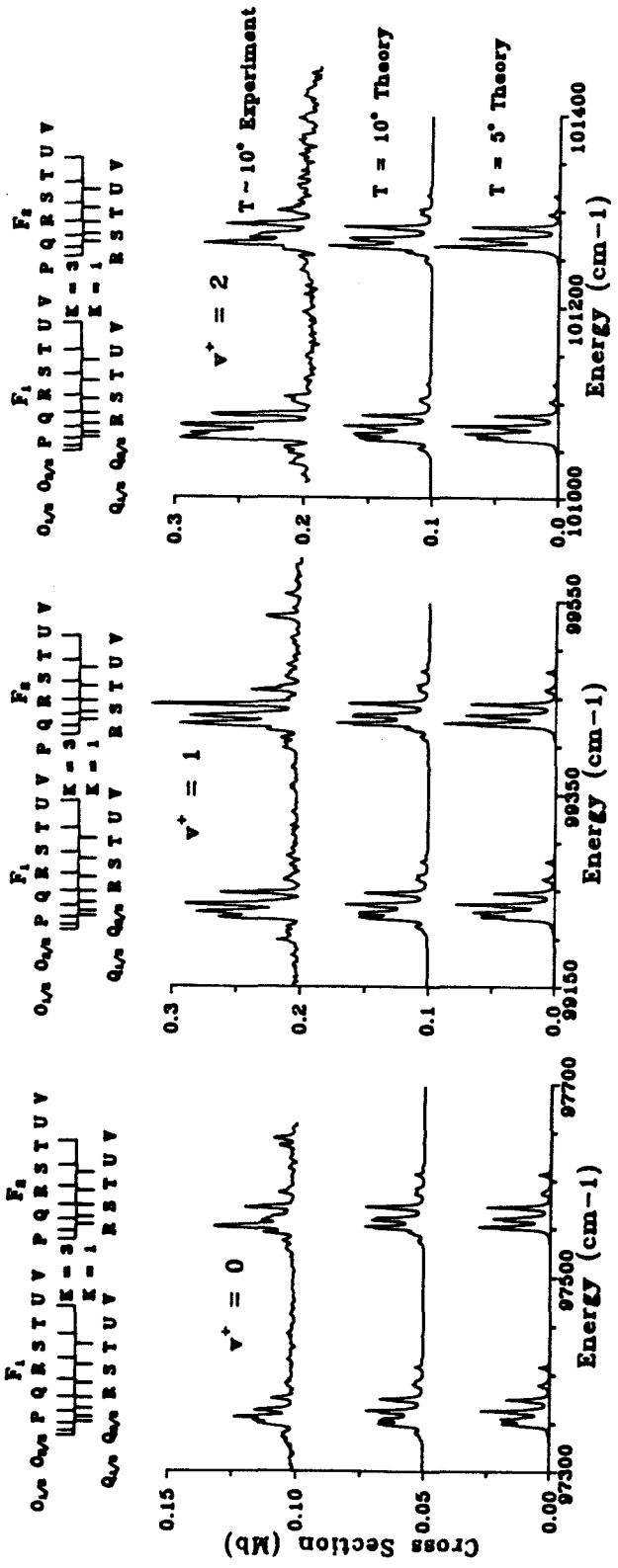
Cross Section (Mb)
Energy (cm-1)
v+ = 0
v+ = 1
v+ = 2
T = 5° Theory
T = 10° Theory
T - 10° Experiment
F1
F2
K = 3
K = 1

Figure 1

Chapter 10

Shape resonances in the photoionization of N_2O

(The text of this chapter appeared in: M. Braunstein and V. McKoy, J. Chem. Phys. **87**, 224 (1987).)

Shape resonances in the photoionization of N_2O

M. Braunstein and V. McKoy
Arthur Amos Noyes Laboratory of Chemical Physics,[a] *California Institute of Technology, Pasadena, California 91125*

(Received 12 February 1987; accepted 25 March 1987)

We report the results of studies of the cross sections and photoelectron asymmetry parameters for photoionization of the 7σ level of N_2O using Hartree–Fock photoelectron continuum orbitals. These studies were motivated by recent measurements which showed significant non-Franck–Condon vibrational distributions at low photoelectron energies where previously only autoionizing resonances, but no shape resonance, had been identified. Our results establish that there are two σ shape resonances in the 7σ ionization continuum, a pronounced resonance at low photoelectron energies, and another at higher energy which is essentially obscured in the vibrationally unresolved cross sections. The shape resonant structure that emerges from these studies differs significantly from the predictions of previous model studies. Studies in progress reveal a rich and unusual dependence of these resonances on changes in internuclear distances.

I. INTRODUCTION

Shape resonances play a central role in studies of the dynamics of molecular photoionization. These resonances or quasibound states, formed by the trapping of photoelectrons by the centrifugal barrier of the molecular force field, give rise to several distinct features in the photoionization spectra of molecules such as enhancement of the cross sections, a pronounced influence on photoelectron angular distributions, and non-Franck–Condon effects in vibrationally resolved spectra.[1] Furthermore, shape resonances are being identified in an increasingly wide range of small molecules.

The effects of shape resonances have been studied in many molecules using the intense tunable radiation provided by synchrotron sources. Such experimental studies and related theoretical efforts have served to clarify many of the properties associated with shape resonances such as their positions and symmetries in several diatomic molecules, e.g., N_2, CO, O_2, and NO and in polyatomic molecules, e.g., CO_2, C_2H_2, and C_2N_2.[2]

These results have already shown that resonance features in the photoionization of polyatomic molecules, e.g., CO_2[3,4] and C_2N_2[5,6] can behave quite differently from what could be expected on the basis of simple diatomic molecules. For example, although it is uncommon to find two shape resonances in the same continuum channel, studies of the photoionization of cyanogen have identified two such resonances in the $k\sigma_u$ continuum within about 20 eV of photoelectron kinetic energy of each other.[7] Furthermore, shape resonant vibrational branching ratios and their associated photoelectron angular distributions have been more extensively studied in diatomic molecules, e.g., N_2[8] and CO,[9,10] than in polyatomic systems such as CO_2[11] and N_2O.[12–14] With their alternative vibrational modes, vibrationally resolved studies of shape resonances in polyatomic molecules can provide rich dynamical insight into molecular photoionization. In many of these polyatomic molecules, shape resonances may result from the interaction between resonances associated with subgroups of the molecule. Vibrationally resolved data will be needed in order to understand the behavior of these shape resonances for alternative internuclear configurations and to develop a more intuitive understanding of shape resonances in polyatomic molecules.

From dispersed fluoresence measurements, Poliakoff *et al.*[14] recently determined the vibrational branching ratios for the symmetric and asymmetric stretching modes in photoionization of the 7σ level of N_2O leading to the $A\,^2\Sigma^+$ state of N_2O^+. The ionization potential of this 7σ level is about 16.4 eV and measurements were carried out for photon energies from about 17 to 22 eV. The vibrational branching ratios were found to be energy dependent, implying a breakdown of the Franck–Condon approximation due to underlying resonances in this spectral region. Poliakoff *et al.*[14] suggested that these results were due to the wings of a shape resonance with autoionizing resonances superimposed in certain narrow spectral subregions. Earlier vibrationally unresolved and resolved photoelectron studies of this channel[12,13] had identified resonance behavior in this same region. However, in these studies this non-Franck–Condon behavior was generally interpreted in terms of autoionizing resonances. This assignment was partially motivated by the results of multiple scattering model studies of these cross sections which did not show any shape resonance within a few electron volts of the 7σ ionization threshold.[12]

We have initiated vibrationally resolved studies of the 7σ photoionization of N_2O so as to provide some further quantitative insight into the effect of shape resonances on the branching ratios and photoelectron angular distributions for the symmetric and asymmetric stretching modes over a wide spectral range.[15] Here we present the results of these studies at the equilibrium geometry of the ground state. These results reveal an interesting shape resonant structure which, we believe, is perhaps representative of what can be expected in the photoionization spectra of related polyatomic molecules. The results show two shape resonances in the σ electronic continuum in 7σ photoionization of N_2O. The low-energy resonance is intense and narrow with a peak cross

[a] Contribution No. 7545.

section of about 15 Mb just below 20 eV photon energy or a photoelectron energy of about 3 eV. The higher energy shape resonance at a photon energy of about 38 eV is essentially not evident in the vibrationally unresolved cross sections but does lead to a broad, but pronounced, minimum in the photoelectron asymmetry parameter. Both of these resonances can be identified from the behavior of their associated eigenphase sums, illustrating the utility of obtaining eigenphase sums in molecular photoionization studies. The dependence of these eigenphase sums on changes in the N–O and N–N distances suggest that these resonances cannot be readily associated with a specific region of the molecule. The shifts in the positions of these shape resonances with alternative vibrational modes and their influence on the vibrational branching ratios will be discussed in a future publication.[15]

An outline of the paper is as follows. In Sec. II we briefly discuss the Schwinger variational method which we use to obtain the Hartree–Fock electronic continuum orbitals needed in studies of molecular photoionization and then give some relevant details of the numerical methods used in these studies. In Sec. III our results are presented and compared with available synchrotron radiation data and the results of earlier multiple scattering calculations.

II. METHOD AND CALCULATIONS

The rotationally unresolved fixed-nuclei photoionization cross section is given by

$$\sigma(R) = \frac{4\pi^2\omega}{3c} |\langle \Psi_i(\mathbf{r},R)|\boldsymbol{\mu}|\Psi_f(\mathbf{r},R)\rangle|^2, \tag{1}$$

where $\boldsymbol{\mu}$ is the electric dipole operator, ω is the photon frequency, and $(\mathbf{r},R)$ represents the electronic and nuclear coordinates. In Eq.(1), Ψ_i represents the initial state wave function and Ψ_f is the wave function for the final ionized state, i.e., molecular ion plus photoelectron. In these studies we use a Hartree–Fock wave function for Ψ_i. For Ψ_f we assume the frozen-core Hartree–Fock model in which the ionic orbitals are constrained to be identical to those of the neutral molecule and the photoelectron orbital is a solution of the one-electron Schrödinger equation

$$\left[-\frac{1}{2}\nabla^2 + V_{N-1}(\mathbf{r},R) - \frac{k^2}{2}\right]\phi_{\mathbf{k}}(\mathbf{r},R) = 0, \tag{2}$$

where $V_{N-1}(\mathbf{r},R)$ is the static-exchange potential of the molecular ion charge density, $k^2/2$ is the photoelectron kinetic energy, and $\phi_{\mathbf{k}}$ satisfies the appropriate scattering boundary conditions.

To solve for $\phi_{\mathbf{k}}$ we work with the integral form of Eq.(2), i.e., the Lippmann–Schwinger equation

$$\phi_{\mathbf{k}}(\mathbf{r}) = \phi_{\mathbf{k}}^c + G_c^{(-)}V\phi_{\mathbf{k}}, \tag{3}$$

where $\phi_{\mathbf{k}}^c$ is the Coulomb scattering wave function, V is the molecular ion potential V_{N-1} with the Coulomb potential removed, i.e.,

$$V = V_{N-1} + \frac{1}{r}, \tag{4}$$

and $G_c^{(-)}$ is the Coulomb Green's function with incoming-wave boundary conditions. Expansion of $\phi_{\mathbf{k}}$ in partial waves, i.e.,

$$\phi_{\mathbf{k}}(\mathbf{r}) = \left(\frac{2}{\pi}\right)^{1/2} \sum_{l=0} \sum_{m=-l}^{l} i^l \psi_{klm}(\mathbf{r})\, Y_{lm}^*(\hat{k}), \tag{5}$$

and substitution into Eq.(3) shows that *each* ψ_{klm} satisfies its own Lippmann–Schwinger equation:

$$\psi_{klm}(\mathbf{r}) = S_{klm} + G_c^{(-)}V\psi_{klm}. \tag{6}$$

We have developed an iterative procedure for solving Eq.(6) which is based on the Schwinger variational method. Details of this technique have been discussed elsewhere[17] and here we will only outline a few essential features of the procedure. We first obtain an approximate solution to Eq.(6) by assuming a separable approximation to the potential V of Eq.(4) of the form

$$V(\mathbf{r},\mathbf{r}') \cong V'(\mathbf{r},\mathbf{r}')$$

$$= \sum_{ij} \langle \mathbf{r}|V|\alpha_i\rangle (V^{-1})_{ij} \langle \alpha_j|V|\mathbf{r}'\rangle, \tag{7}$$

where the matrix V^{-1} is the inverse of the matrix with elements $V_{ij} = \langle \alpha_i|V|\alpha_j\rangle$ and the α_i's are discrete basis functions such as Cartesian[18] or spherical[19] Gaussian functions which are known to be effective in representing the multicenter nature of molecular ion potentials. With this approximation to V in Eq.(6), the solutions of this integral equation can be written as

$$\psi_{klm}^{(0)}(\mathbf{r}) = S_{klm}(\mathbf{r})$$

$$+ \sum_{ij} \langle \mathbf{r}|G_c^{(-)}V|\alpha_i\rangle (D^{-1})_{ij} \langle \alpha_j|V|S_{klm}\rangle, \tag{8}$$

where the matrix D^{-1} is the inverse of the matrix with elements

$$D_{ij} = \langle \alpha_i|V - VG_c^{(-)}V|\alpha_j\rangle. \tag{9}$$

With adequate basis sets, α_i's, these approximate solutions $\psi_{klm}^{(0)}$, which satisfy scattering boundary conditions, can provide quantitatively reliable photoionization cross sections. These cross sections can, furthermore, be shown to be variationally stable.[20] Starting with these solutions $\psi_{klm}^{(0)}$, converged solutions of Eq. (5) can be obtained through an iterative procedure.[17]

For the ground state of N_2O, with the electronic configuration $1\sigma^2 2\sigma^2 3\sigma^2 4\sigma^2 5\sigma^2 6\sigma^2 1\pi^4 7\sigma^2 2\pi^4$, we used the SCF Slater basis of McLean and Yoshimine.[21] Calculations were done at the equilibrium geometry with N–N and N–O bond distances of 2.1273 and 2.2418 a.u., respectively. At this geometry, this basis gives an SCF energy of -183.756 68 a.u. For the basis functions, $\alpha_i(\mathbf{r})$, in the expansion of Eq. (7) we used spherical Gaussian functions defined by

$$\chi(\mathbf{r}) = N|\mathbf{r} - \mathbf{A}|^l \exp(-\alpha|\mathbf{r} - \mathbf{A}|^2) Y_{lm}(\Omega_{\mathbf{r}-\mathbf{A}}), \tag{10}$$

where **A** locates the origin of the basis function. The basis sets for the σ and π ionization continua are given in Table I.

All matrix elements and functions arising in the solution of Eq.(8) are evaluated using single-center expansions about the central nitrogen atom. The partial wave expansion of the photoelectron orbital, Eq.(5), was truncated at $l_p = 8$. The other partial wave expansion parameters were chosen as follows:

TABLE I. Scattering basis sets used in obtaining the photoelectron orbitals.*

Channel	Center	l	m	Exponent
σ	N(terminal)	0	0	16, 8, 4, 2, 1, 0.5
		1	0	4, 2, 1, 0.5
		2	0	2, 1, 0.5
	N(central)	0	0	16, 8, 4, 2, 1, 0.5
		1	0	4, 2, 1, 0.5
		2	0	2, 1, 0.5
		3	0	1
		4	0	1
		5	0	1
	O	0	0	16, 8, 4, 2, 1, 0.5
		1	0	4, 2, 1, 0.5
		2	0	2, 1, 0.5
π	N(terminal)	1	1	8, 4, 2
		2	1	8, 4, 2
	N(central)	1	1	8, 4, 2
		2	1	8, 4, 2
	O	1	1	16, 8, 4, 2
		2	1	8, 4, 2

*See Eq. (10) in the text.

(i) maximum partial wave in the expansion of the occupied orbitals in the direct potential = 58,

(ii) maximum partial wave in the expansion of the occupied orbitals in the exchange potential = 40 (oxygen K shell), 40 (terminal nitrogen K shell), 10 (central nitrogen K shell), 20(4σ), 23(5σ), 19(6σ), 15(1π), 19(7σ), 15(2π),

(iii) maximum partial wave in the expansion of $1/r_{12}$ in the direct and exchange terms = 116 and 58, respectively,

(iv) all other partial wave expansions were truncated at $l = 58$.

Based on our convergence studies of such expansions, this choice of expansion parameters should provide photoionization cross sections which are within a few percent of the converged values. The associated radial integrals were obtained using a Simpson's rule quadrature. The grid contained 750 points and extended out to 90.5 a.u. with a step size of 0.01 a.u. from the origin out to 3.5 a.u. Beyond 3.5 a.u. the largest step size was 0.4 a.u.

III. RESULTS AND DISCUSSION

Figure 1 shows our calculated σ and π contributions to the photoionization cross section for the 7σ orbital of N_2O leading to the $A\,^2\Sigma^+$ state of N_2O^+ along with the total cross section. The photon energy scale in this and other figures assumes the experimental ionization potential of 16.4 eV.[13] These results were obtained using the dipole length form for the photoionization cross section. The cross sections obtained with the dipole velocity form for these cross sections differ only slightly from these results and are not shown in Fig. 1. Furthermore, these cross sections were calculated with the uniterated solutions of Eq. (8) for the photoelectron continuum orbitals. Calculations at several photon energies using more converged photoelectron orbitals

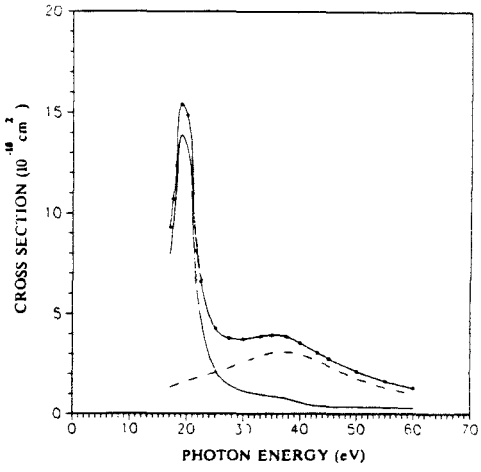

FIG. 1. Calculated photoionization cross sections for the $A\,^2\Sigma^+(7\sigma^{-1})$ state of N_2O: —, $7\sigma \rightarrow k\sigma$ component (dipole length); ---, $7\sigma \rightarrow k\pi$ component; -•-, total. Energies at which the cross sections were actually determined are indicated by •.

obtained with our iterative procedure for solving Eq. (6)[17] show that the cross sections are, at worst, within 7% of the converged values.

The most significant feature in the cross sections of Fig. 1 is the prominent shape resonance in the $7\sigma \rightarrow k\sigma$ channel just below 20 eV. The $7\sigma \rightarrow k\pi$ contribution to the photoionization cross section is nonresonant and the broad enhancement around 38 eV is due to the expected energy dependence of the dipole matrix element. Figure 2 shows the eigenphase sum for the $k\sigma$ continuum of this $N_2O^+(7\sigma^{-1})$ ion. The behavior of this eigenphase sum shows clearly that there are two resonances in this continuum. The low energy resonance associated with the increase in the eigenphase sum around 20 eV is very pronounced in the cross sections. However, the higher energy shape resonance, seen just below 40 eV in the

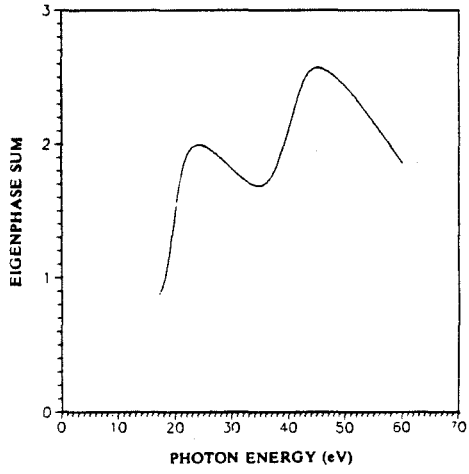

FIG. 2. Eigenphase sum for the $7\sigma \rightarrow k\sigma$ channel in N_2O.

eigenphase sum, is completely obscured in both the calculated and, as will be discussed, measured vibrationally unresolved photoionization cross sections. The composition of these resonances in terms of possible contributions from resonances associated with molecular subgroups, e.g., N–N and N–O, will provide important physical insight into polyatomic shape resonances. Although the position of the low-energy shape resonance in N_2O would be consistent with shifts expected on the basis of changes in NO bond distances between NO and N_2O, i.e., 2.173 a_0 to 2.2418 a_0,[16] the dependence of the eigenphase sum on the N–O and N–N distances in N_2O shows that this resonance cannot be viewed as predominantly associated with the N–O fragment.[15] The behavior of these two shape resonances with changes in alternative vibrational modes, and combinations thereof, and the related vibrational branching ratios will be discussed in detail in a future publication.[15]

In Fig. 3 we compare our calculated cross sections with the experimental data of Truesdale *et al.*[13] and of Carlson *et al.*[12] The agreement between our cross sections calculated in the frozen-core Hartree–Fock fixed-nuclei approximation and the experimental data is quite good. This comparison clearly identifies the resonance feature around 20 eV as due to a shape resonance. From these results it becomes clear that the slight enhancement of the cross sections around 35 eV is not shape resonant but comes from the usual energy dependence of the nonresonant $7\sigma \rightarrow k\pi$ channel. Figure 3 also shows the cross sections obtained using the multiple scattering model with two different choices for the potential, i.e., the ground and transition state potentials.[12] These results show a distinct shape resonant feature in the cross sections at 8 or 13 eV photoelectron energy depending on the choice of potential. On this basis, Carlson *et al.*[12] assigned the weak maximum around 32 eV in the measured cross sections as due to a shape resonance. The present results show no such shape resonant enhancement of the vibrationally unresolved cross sections in this energy range. Furthermore, on the basis of these multiple scattering results the rapid increase in the cross sections at lower photoelectron energy was not interpreted as arising from the low-energy shape resonance seen in the present Hartree–Fock results at a photoelectron energy around 3 eV. In fact, in the studies of Carlson *et al.*[12] this low-energy resonance feature was attributed to autoionization. Although autoionization is known to occur in this spectrum below 20 eV,[22] our results show that a shape resonance must play a significant role in photoionization out of this 7σ level at low photoelectron energy. In summary, the role of shape resonances in these photoionization spectra emerging from the present studies is quite different from that seen in the earlier multiple scattering results.[12]

In Fig. 4 we compare our calculated photoelectron asymmetry parameters for the 7σ level of N_2O with the measured values of Carlson *et al.*[12] and of Truesdale *et al.*[13] The pronounced minimum at around 19 eV in the calculated asymmetry parameters is obviously associated with the low-energy shape resonance seen earlier in both the cross sections and eigenphase sums of Figs. 1 and 2, respectively. The agreement between the calculated and measured photoelectron asymmetry parameters for photon energies up to about 30 eV is excellent. This agreement establishes that the rapid increase in the asymmetry parameters for photon energies above 19 eV seen in the experimental data is due to a shape resonance. Our calculated asymmetry parameters show a second and broader minimum around 40 eV arising from the higher energy shape resonance seen at about the same energy in the eigenphase sums of Fig. 2. It is important to note that this shape resonance was not seen in the vibrationally unresolved cross sections of Figs. 1 and 3. This broad minimum in the calculated asymmetry parameters around 40 eV is in qualitative agreement with the somewhat more pronounced

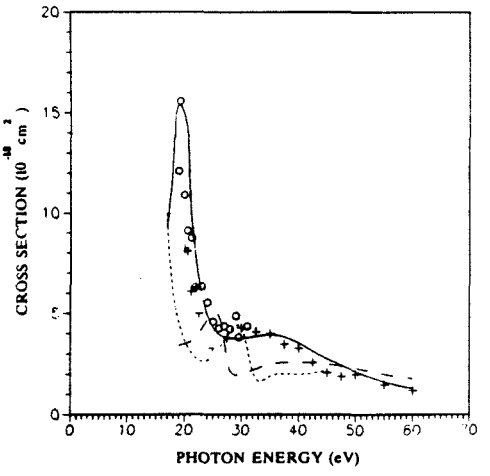

FIG. 3. Photoionization cross sections for the $A\,^2\Sigma^+(7\sigma^{-1})$ state of N_2O: —, present results; O, experimental data of Ref. 13; +, experimental data of Ref. 12; ---, multiple scattering results (ground state potential) of Ref. 12; – – –, multiple scattering results (transition state potential) of Ref. 12.

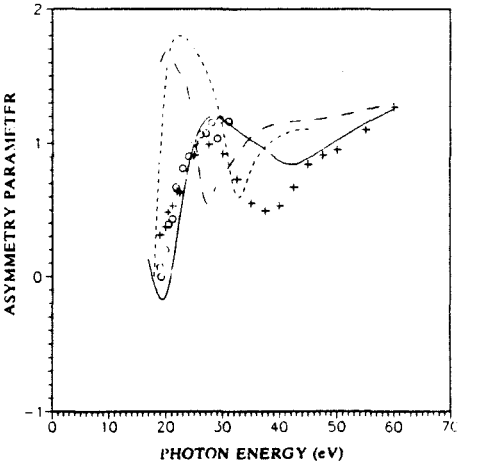

FIG. 4. Photoelectron asymmetry parameter for the $A\,^2\Sigma^+(7\sigma^{-1})$ state of N_2O^+: —, present results (dipole length); O, experimental data of Ref. 13; +, experimental data of Ref. 12; ---, multiple scattering results (ground state potential) of Ref. 12, – – –, multiple scattering results (transition state potential) of Ref. 12.

minimum seen in the experimental data at 38 eV. Measurements of the vibrationally-resolved photoelectron spectra around this minimum would clearly help to identify possible reasons for the differences seen in the calculated and measured asymmetry parameters between 30 and 45 eV. Note that the data of Carlson *et al.*[12] falls off more rapidly than that of Truesdale *et al.*[13] just above 30 eV. Finally, the calculated and measured asymmetry parameters agree very well beyond 45 eV.

Figure 4 also shows the photoelectron asymmetry parameters obtained using the multiple scattering model with different choices of the potential, i.e., the ground and transition potentials.[12] These multiple scattering asymmetry parameters are substantially different from the present results calculated with frozen-core Hartree–Fock photoelectron orbitals. The differences between the multiple scattering and Hartree–Fock results for this polyatomic system are larger than generally seen previously in diatomic molecules.[1] The multiple scattering results, particularly those using the ground state potential, do, however, show the presence of two shape resonances in these photoionization spectra.

IV. CONCLUDING REMARKS

In this paper we have presented the cross sections and photoelectron asymmetry parameters for photoionization of the 7σ level of N_2O. These studies were motivated by recent dispersed fluorescence measurements[14] which showed significant non-Franck–Condon behavior in the vibrational branching ratios for both the symmetric and asymmetric stretching modes at low photoelectron energies where previously only autoionizing resonances, but no shape resonance, had been identified.[12,13] Earlier vibrationally unresolved measurements of these cross sections had been interpreted, partly on the basis of multiple scattering studies, in terms of autoionizing resonances at low photoelectron energies and one shape resonance at considerably higher energy in the $k\sigma$ channel. Our results establish that there are two σ shape resonances in the 7σ photoionization of N_2O. One is a low-energy resonance which is very evident in both the cross sections and asymmetry parameters. The other occurs at higher energy where it is essentially obscured in the vibrationally unresolved cross sections but is clearly seen in the asymmetry parameters. Although unusual, certainly for diatomic molecules, the presence of two shape resonances in the same continuum as seen here promises to be more common for polyatomics.[7] Studies of the vibrationally resolved cross sections in the region of these shape resonances which are in progress reveal a rich and unusual dependence of these resonances on changes in internuclear distance.[15] Such studies along with experimental measurements of vibrational branching ratios using dispersed fluorescence techniques can be expected to provide much needed insight into the nature of resonant photoionization in polyatomic molecules.

ACKNOWLEDGMENTS

This material is based upon research supported by the National Science Foundation under Grant No. CHE85-21391. The authors also acknowledge use of the resources of the San Diego SuperComputer Center which is supported by the National Science Foundation.

[1] J. L. Dehmer, D. Dill, and A. C. Parr, in *Photophysics and Photochemistry in the Vacuum Ultraviolet*, edited by S. McGlynn, G. Findley, and R. Huebner (Reidel, Dordrecht, 1985), pp. 341–408.
[2] See, for example, J. L. Dehmer, A. C. Parr, and S. H. Southworth, in *Handbook on Synchrotron Radiation*, edited by G. V. Marr (North-Holland, Amsterdam, 1986), Vol. II.
[3] T. A. Carlson, M. O. Krause, F. A. Grimm, J. D. Allen, D. Mehaffy, P. R. Keller, and J. W. Taylor, Phys. Rev. A **23**, 3316 (1981).
[4] R. P. Lucchese and V. McKoy, Phys. Rev. A **26**, 1406 (1982).
[5] D. M. P. Holland, A. C. Parr, D. L. Ederer, J. B. West, and J. L. Dehmer, Int. J. Mass. Spectrom. Ion Phys. **52**, 195 (1983).
[6] J. Kreile, A. Schweig, and W. Thiel, Chem. Phys. Lett. **100**, 351 (1983).
[7] D. L. Lynch, S. N. Dixit, and V. McKoy, J. Chem. Phys. **84**, 5504 (1986).
[8] J. B. West, A. C. Parr, B. E. Cole, D. L. Ederer, R. Stockbauer, and J. L. Dehmer, J. Phys. B **13**, L105 (1980).
[9] R. Stockbauer, B. E. Cole, D. L. Ederer, J. B. West, A. C. Parr, and J. L. Dehmer, Phys. Rev. Lett. **43**, 757 (1979).
[10] B. E. Cole, D. L. Ederer, R. Stockbauer, K. Codling, A. C. Parr, J. B. West, E. D. Poliakoff, and J. L. Dehmer, J. Chem. Phys. **72**, 6308 (1980).
[11] See, for example, P. Roy, I. Nenner, M. Y. Adam, J. Delwiche, M. J. Hubin-Franskin, P. Lablanquie, and D. Roy, Chem. Phys. Lett. **109**, 607 (1984).
[12] T. A. Carlson, P. R. Keller, J. W. Taylor, T. Whitley, and F. Grimm, J. Chem. Phys. **79**, 97 (1983).
[13] C. M. Truesdale, S. Southworth, P. H. Kobrin, D. W. Lindle, and D. A. Shirley, J. Chem. Phys. **78**, 7117 (1983).
[14] E. D. Poliakoff, M.-H. Ho, M. G. White, and G. E. Leroi, Chem. Phys. Lett. **130**, 91 (1986).
[15] M. Braunstein and V. McKoy, J. Chem. Phys. (to be published).
[16] T. Gustafsson and H. J. Levinson, Chem. Phys. Lett. **78**, 28 (1981).
[17] R. R. Lucchese and V. McKoy, Phys. Rev. A **24**, 770 (1981).
[18] See, for example, T. H. Dunning, Jr. and P. J. Hay, in *Methods of Electronic Structure Theory*, edited by H. F. Schaefer III (Plenum, New York, 1977).
[19] R. R. Lucchese and V. McKoy, Phys. Rev. A **26**, 1406 (1982).
[20] R. R. Lucchese and V. McKoy, Phys. Rev. A **28**, 1382 (1983).
[21] A. D. McLean and M. Yoshimine, *Tables of Linear Molecular Wave Functions* (IBM Research Laboratory, San Jose, 1967), p. 200.
[22] See, for example, E. D. Poliakoff, M.-H. Ho, G. E. Leroi, and M. G. White, J. Chem. Phys. **85**, 5529 (1986).

Chapter 11

Vibrational branching ratios and shape resonant photoionization dynamics in N_2O

(The text of this chapter appeared in: M. Braunstein and V. McKoy, J. Chem. Phys. **90** 1535 (1989).)

Vibrational branching ratios and shape resonant photoionization dynamics in N_2O

M. Braunstein and V. McKoy
Arthur Amos Noyes Laboratory of Chemical Physics,[a] California Institute of Technology, Pasadena, California 91125

(Received 15 September 1988; accepted 28 October 1988)

Vibrational branching ratios and photoelectron asymmetry parameters for alternative vibrational modes in the photoionization of $N_2O(7\sigma^{-1})$ have been studied using accurate photoelectron continuum orbitals. Earlier dispersed ionic fluorescence measurements [E. D. Poliakoff, M. H. Ho, M. G. White, and G. E. Leroi, Chem. Phys. Lett. **130**, 91 (1986)] revealed strong non-Franck–Condon vibrational ion distributions for both the symmetric and antisymmetric stretching modes at low photoelectron energies. Our results establish that these features arise from a σ shape resonance which, based on its dependence on internuclear geometry, must be associated with the molecular framework as a whole and not with either of its fragments, N–N or N–O. This behavior accounts for the more pronounced deviations of the vibrational branching ratios from Franck–Condon values observed in the symmetric than in the antisymmetric mode. The σ continuum also supports a second shape resonance at higher energy which does not influence the vibrational branching ratios but is quite evident in the photoelectron asymmetry parameters around a photon energy of 40 eV. These vibrationally resolved studies of the photoelectron spectra of this polyatomic system provide an interesting example of the rich shape resonant behavior that can be expected to arise in polyatomic molecules with their alternative vibrational modes.

I. INTRODUCTION

Shape resonant features have been studied in the photoionization spectra of a wide range of molecules.[1] One of the more significant dynamical features arising in molecular photoionization cross sections from such resonances is the non-Franck–Condon behavior seen in the vibrationally resolved photoelectron spectra where the ionic vibrational distribution is no longer given simply by Franck–Condon factors and photoelectron angular distributions depend on the vibrational level. This breakdown of the Franck–Condon principle, first identified by Dehmer *et al.*[2] in the N_2 spectra and subsequently studied both experimentally and theoretically by others,[1-5] is due to the strong dependence of the position and lifetime of the resonance on internuclear separation and is obviously an important probe of photoelectron dynamics. Much of our physical understanding of the role of shape resonances in vibrationally resolved photoelectron spectra is based on the simple picture of their behavior in diatomics,[2] i.e., shifts to higher energies with shorter bond distances. With their alternative vibrational modes and the possibility of shape resonances associated with specific bonds in the molecule, as well as intramolecular interaction among such resonances,[6] shape resonant behavior in polyatomics can be expected to be potentially richer than in the simpler diatomic molecules. Vibrationally resolved studies are required to probe the behavior of shape resonances with alternative internuclear configurations.

Recently, Poliakoff *et al.*,[7] using dispersed ionic fluorescence—a technique which shows considerable promise for studies of vibrationally resolved photoelectron spectra of polyatomic molecules—have measured branching ratios for the (1,0,0) and (0,0,1) vibrational levels, the symmetric and antisymmetric stretching modes, respectively, of the $A\,^2\Sigma^+(7\sigma^{-1})$ state of N_2O^+ for photoelectron energies ranging from about 0.5 to 5 eV. These branching ratios were seen to be dependent on excitation energy, implying a breakdown of the Franck–Condon approximation. More recent ion fluorescence studies and photoelectron measurements of Kelly *et al.*[8] and Ferrett *et al.*,[9] respectively, at higher energy also show significant non-Franck–Condon branching ratios for these vibrational levels, particularly in the symmetric stretching mode. Earlier vibrationally unresolved studies[10] of the 7σ photoionization of N_2O identified two shape resonances in the σ ionization continuum, a low-energy pronounced resonance centered around 20 eV—the 7σ ionization potential is about 16.4 eV—responsible for the non-Franck–Condon vibrational branching ratios seen by Poliakoff *et al.*,[7] and a higher energy one around 38 eV which is essentially not evident in either the vibrationally resolved or unresolved cross sections but leads to a broad minimum in the photoelectron asymmetry parameters.

In this paper we present the results of vibrationally resolved studies of the cross sections and photoelectron asymmetry parameters for photoionization of the 7σ level in N_2O in the region of these two shape resonances. An important objective of these studies is to obtain some insight into the behavior of shape resonances for alternative internuclear configurations in a polyatomic molecule and hence their influence on specific vibrational branching ratios. For example, in a molecule such as N_2O do the shape resonances seen around 20 and 38 eV "belong" primarily to specific regions

[a] Contribution No. 7858.

of the molecule, i.e., N–N or N–O bonds, or would their behavior at different internuclear configurations suggest that they belong to the molecule as a whole? The answer to this question would obviously determine the influences these resonances can be expected to have on the branching ratios for symmetric and antisymmetric stretching modes. What we do find, perhaps in contrast to the more intuitive notion that these resonances in N_2O, particularly the low-energy one, should be associated with the localized N–N or N–O region of the molecule, is that they behave as though they belong to the molecule as a whole. As a result we expect that the shape resonance at 20 eV would more strongly influence the vibrational branching ratios for the symmetric stretch than for the antisymmetric stretch. In fact, although our calculated vibrational branching ratios show non-Franck–Condon behavior for both vibrational modes, the deviations are much more pronounced in the symmetric mode, in agreement with what is seen experimentally.[7-9]

An outline of the remaining sections of this paper is as follows. In Sec. II we briefly discuss the method we use to obtain the molecular photoelectron orbitals needed to determine the photoionization cross sections. In this section we also discuss the vibrational wave functions used. In Sec. III we present the results of fixed-nuclei calculations at 16 internuclear geometries. In Sec. IV our vibrationally resolved cross sections are discussed and compared with available experimental data.

II. METHOD AND CALCULATIONS

In these studies of the photoionization cross sections we use a Hartree–Fock wave function for the initial state. For the final state we use a frozen-core model in which the bound orbitals are assumed identical to those in the initial state Hartree–Fock wave function and the photoelectron wave function is determined in the field of these $(N-1)$ unrelaxed core orbitals. The static-exchange photoelectron continuum orbital then satisfies the one-electron Schrödinger equation,

$$(-1/2\nabla^2 + V_{N\ \ 1}(\mathbf{r},R) - k^2/2)\phi_{\mathbf{k}}(\mathbf{r},R) = 0, \quad (1)$$

where $V_{N\ \ 1}(\mathbf{r},R)$ is the nonlocal, nonspherical ion core potential, $k^2/2$ is the photoelectron kinetic energy, R denotes the internuclear geometry and $\phi_{\mathbf{k}}$ satisfies the appropriate boundary conditions. If $\phi_{\mathbf{k}}$ is expanded in spherical harmonics defined about $\hat{k}$, i.e.,

$$\phi_{\mathbf{k}}(\mathbf{r},R) = \left(\frac{2}{\pi}\right)^{1/2} \sum_{lm} i^l \varphi_{klm}(\mathbf{r},R)\, Y^*_{lm}(\hat{k}), \quad (2)$$

the functions $\varphi_{klm}(\mathbf{r},R)$ satisfy the same Schrödinger equation as $\phi_{\mathbf{k}}$ itself. We will discuss our procedure for solving Eq. (1) for these functions φ_{klm} later. With these functions φ_{klm} we define the length and velocity forms of the photoelectron matrix element as

$$I^{L}_{lm\mu}(R) = k^{1/2}\langle \phi_{7\sigma}(\mathbf{r},R)|r_\mu|\varphi_{klm}(\mathbf{r},R)\rangle, \quad (3)$$

$$I^{V}_{lm\mu}(R) = (k^{1/2}/E)\langle \phi_{7\sigma}(\mathbf{r},R)|\nabla_\mu|\varphi_{klm}(\mathbf{r},R)\rangle, \quad (4)$$

where $\phi_{7\sigma}$ is the occupied 7σ level of N_2O and E is the photon energy. The vibrationally resolved photoionization cross section $\sigma(v,v')$ can then be written as

$$\sigma^{L,V}_{v\ \ v'\ \ n} = \frac{4\pi^2}{3c} E \sum_{lm\mu} |\langle \chi^{v}_{i}\ \ ^{v'}(R)|I^{L,V}_{lm\mu}(R)|\chi^{v}_{f}\ \ ^{v'}(R)\rangle|^2, \quad (5)$$

where χ_i and χ_f are vibrational wave functions for N_2O and N_2O^+, respectively, and c is the speed of light. The corresponding photoelectron asymmetry parameter is defined as

$$\frac{d\sigma^{L,V}_{v\ \ v'\ \ n}}{d\Omega_{\hat{k}}} = \frac{\sigma_{v\ \ v'\ \ n}}{4\pi}\left[1 + \beta^{L,V}_{v\ \ v'\ \ n} P_2(\cos\theta)\right], \quad (6)$$

where θ is the angle between the polarization vector of the light and the photoelectron momentum $\hat{k}$.

To obtain the photoelectron continuum orbital $\varphi_{klm}(\mathbf{r},R)$, φ_{klm} is further expanded in spherical harmonics, $Y_{l'm}(\hat{r})$. The resulting coupled equations are solved using an adaption of the Schwinger variational principle for long-range potentials in which the direct component V_{dir} of the molecular ion potential $V_{N\ \ 1}$ is treated exactly by numerical integration and the exchange interaction V_{ex} is approximated by a separable form of the potential of the Schwinger type, i.e.,

$$V_{ex} \cong V^{s}_{ex} = \sum_{ij} V_{ex}|\alpha_i\rangle (V_{ex}^{-1})_{ij}\langle \alpha_j|V_{ex}, \quad (7)$$

where α_i are discrete basis functions. The approach yields variationally stable photoionization cross sections and includes an iterative procedure for obtaining the converged scattering solutions, φ_{klm}.[11] We have shown that the method can provide good approximations to the photoelectron orbitals even with modest expansions in Eq. (7).[11] For the expansion in Eq. (7) in these studies we used the basis shown in Table I of Ref. 10. With this basis the "zero-order" solutions were essentially converged and it was not necessary to resort to an iterative procedure. All matrix elements arising in the equations associated with this procedure are evaluated via single-center expansions about the central nitrogen atom and a Simpson's rule quadrature. The partial wave expansion parameters and the grids for the Simpson's rule quadrature of the radial integrals used here are the same as those given in Ref. 10.

For the ground state of N_2O, with an electron configuration $1\sigma^2 2\sigma^2 3\sigma^2 4\sigma^2 5\sigma^2 6\sigma^2 1\pi^4 7\sigma^2 2\pi^4$, we used the Slater basis SCF wave functions of McLean and Yoshimine[12,13] for the 16 internuclear distances at which we obtained the photoionization cross sections. At four of these geometries the wave functions were taken from Ref. 12. The wave functions at the other geometries were kindly provided by McLean.[13] At the N–N and N–O equilibrium bond distances of 2.1273 and 2.2418 a.u., respectively, this basis gives an SCF energy of $-183.756\,68$ a.u.

TABLE I. Force constants for N_2O and $N_2O^+(7\sigma^{-1})$ used in Eq. (8).[a]

	N_2O	$N_2O^+(7\sigma^{-1})$
k_{11}	18.01[b]	19.33
k_{22}	11.33	13.93
k_{12}	−0.71	0.07

[a] Reference 14.
[b] In units of 10^5 dyn cm^{-1}

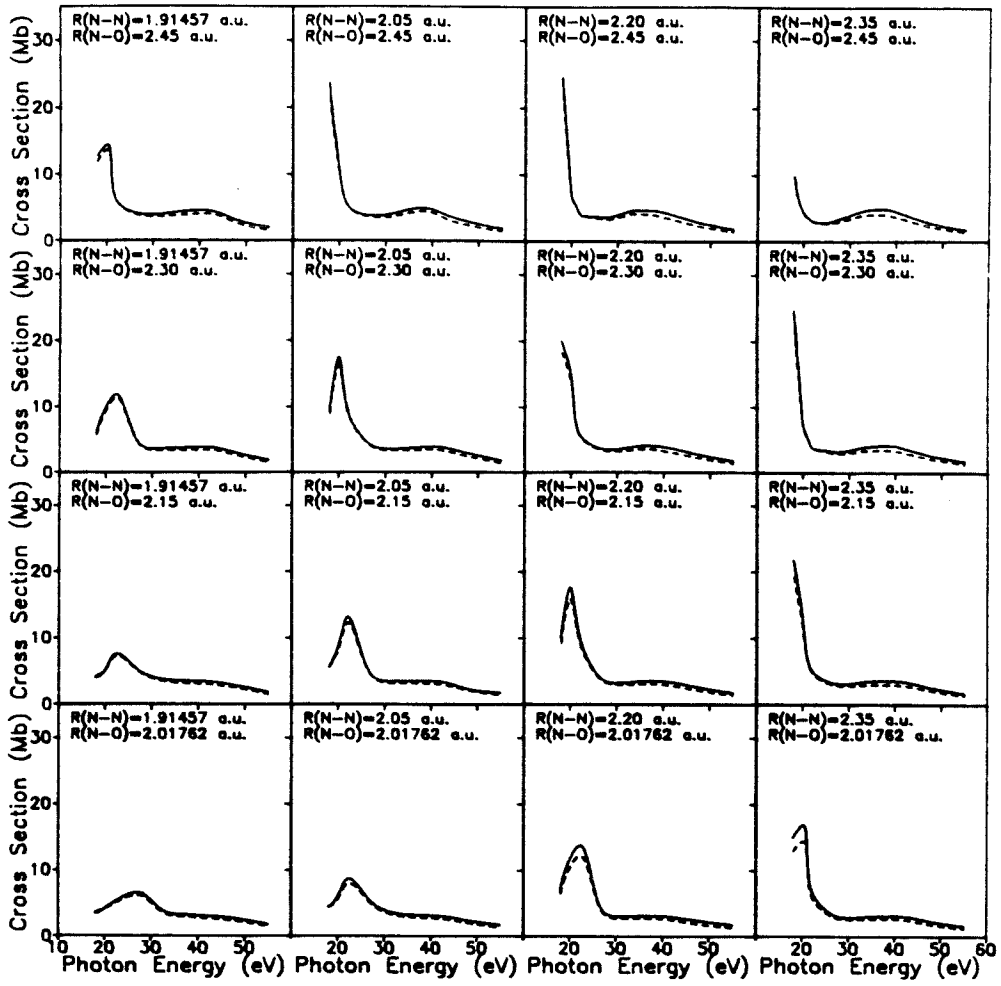

FIG. 1. Calculated cross sections (Mbs) for photoionization of the 7σ level of N_2O: —, total cross section (dipole length); ---, total cross section (dipole velocity). Along the horizontal axis from left to right, each frame corresponds to an N–N internuclear distance of 1.914 57, 2.05, 2.2, and 2.35 a.u., respectively. Along the vertical axis from bottom to top, each frame corresponds to an N–O internuclear distance of 2.017 62, 2.15, 2.3, and 2.45 a.u., respectively. The photon energy scale here and in Figs. 2 and 3 assumes an ionization potential of 16.4 eV ($1\ \text{Mb} = 10^{-18}\ \text{cm}^2$).

The vibrational wave functions for the symmetric and antisymmetric stretching modes of the ground state of N_2O and the $A\ ^2\Sigma^+$ state of N_2O^+ were obtained by solving the vibrational Schrödinger equation for a nonbending, nonrotating linear triatomic molecule. Highly accurate potentials have not been determined for the $A\ ^2\Sigma^+$ state for N_2O^+. For this state and for the ground state we hence used effective harmonic force fields with potentials of the form

$$2V = k_{11}\Delta r(\text{N–N})^2 + k_{22}\Delta r(\text{N–O})^2 + 2k_{12}\Delta r(\text{N–N})\Delta r(\text{N–O}), \quad (8)$$

where $\Delta r(\text{N–N}) = R(\text{N–N}) - R_e(\text{N–N})$, $\Delta r(\text{N–O}) = R(\text{N–O}) - R_e(\text{N–O})$. The values of the force constants, taken from Callomon and Creutzberg,[14] are listed in Table I.

The form of the kinetic energy operator is given by Wilson *et al.*[15] The vibrational wave functions were expanded in a basis of the form $\Phi_{ij} = \phi_i(R_{\text{N–N}})\phi_j(R_{\text{N–O}})$ with the bond displacement functions ϕ_i chosen as harmonic oscillator functions. Diagonalization of the vibrational Hamiltonian in such a product basis containing the first five harmonic oscillator functions gave converged solutions. The resulting Franck–Condon factors were (000,000) = 0.583, (000,100) = 0.198, and (000,001) = 0.099. These vibrational wave functions for this polyatomic molecule obtained using harmonic potentials can certainly be expected to be of lower quality than for other ions for which more refined potentials are available. Measurements of the vibrational branching ratios at high photoelectron energies would be

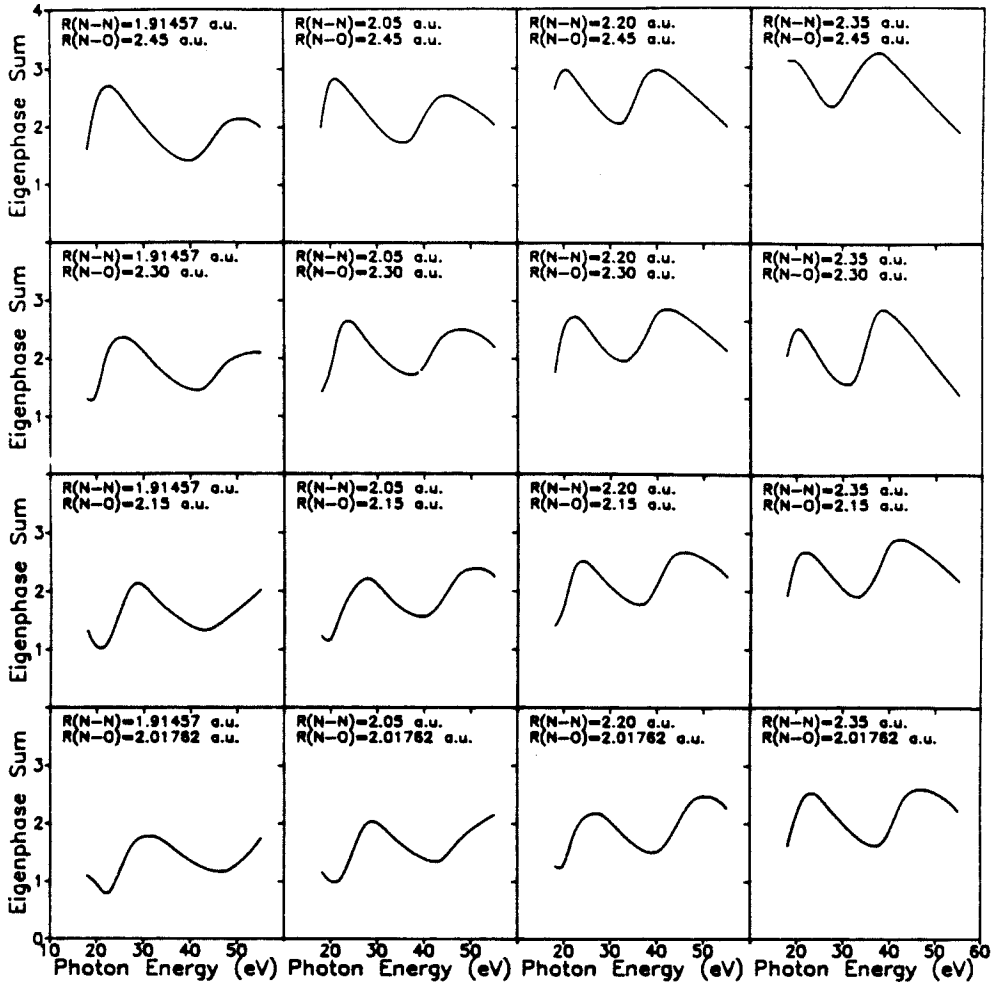

FIG. 2. Eigenphase sums in radians at several internuclear configurations for the $7\sigma - k\sigma$ channel in N_2O. Each frame corresponds to the geometry described in Fig. 1.

useful in assessing the accuracy of the calculated Franck–Condon factors.

The photoelectron matrix elements $I_{lm\mu}(R)$ of Eqs. (3) and (4) were determined at 16 internuclear geometries chosen as points of a 4×4 grid with $R_{N\text{-}N} = 1.914\,57$, 2.05, 2.2, and 2.35 a.u. and $R_{N\text{-}O} = 2.017\,62$, 2.15, 2.3, and 2.45 a.u. The real and imaginary parts of the photoelectron matrix elements at these internuclear distances were fitted to a bicubic spline which was then interpolated to obtain values needed in the Simpson's rule quadrature of Eq. (5). As a check on this procedure the interpolated values of $I_{lm\mu}$ for 18 eV at the equilibrium geometry of $R_{N\text{-}N} = 2.1273$ a.u. and $R_{N\text{-}O} = 2.2418$ a.u. were found to be within 5% of the values explicitly calculated at this geometry.

III. FIXED-NUCLEI RESULTS

Figure 1 shows our calculated photoionization cross sections for the 7σ level of N_2O at 16 internuclear geometries. The most significant feature of these cross sections is the behavior of the pronounced shape resonance with internuclear geometry. This resonance moves to lower or higher energies with an increase or decrease respectively in *either* the N–N or N–O bond distance. As can be seen from the appropriate frames of Fig. 1, the position of the resonance depends primarily on the overall length of the molecule and not on the individual N–N and N–O bond distances. It is interesting, however, to compare the position of the σ shape resonance in the 7σ photoionization of N_2O with the σ shape

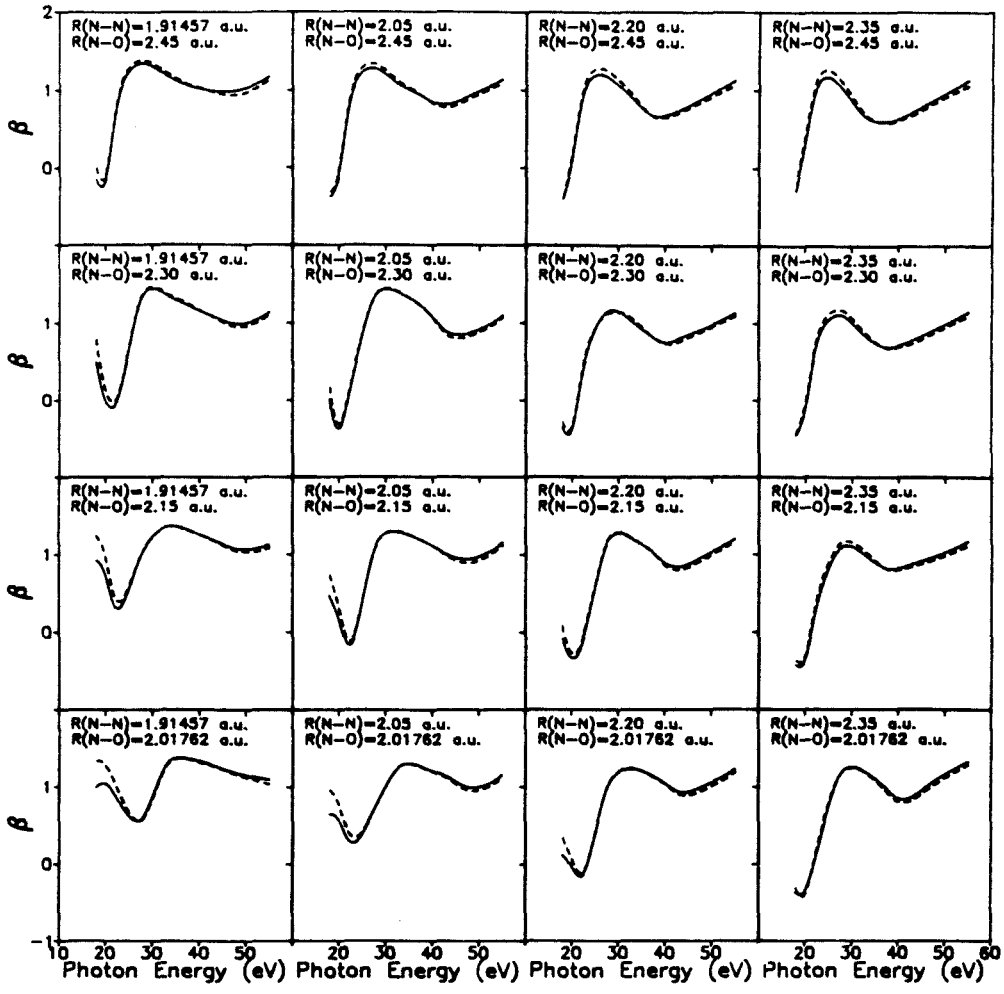

FIG. 3. Photoelectron asymmetry parameters at several internuclear configurations for the $7\sigma^{-1}$ photoionization of N_2O: —, present results (dipole length), ---, present results (dipole velocity). Each frame corresponds to the geometry described in Fig. 1.

resonance in the photoionization cross section of the 5σ level of NO seen at a photoelectron energy of about 7–8 eV.[16,17] The simple model of the shifts in resonance positions with internuclear separation in diatomics[2] would suggest that this σ shape resonance in NO with an R_e of 2.173 a.u. would move down to a photoelectron energy of 3–4 eV for the N–O separation of 2.2418 a.u. in N_2O.[16] Although this relationship is suggestive, the results of Fig. 1 show that this σ shape resonance in N_2O does not behave as though it is localized in the NO bond. In fact, a plot of these resonance positions versus total bond length of the molecule l shows that the photoelectron energy on resonance varies as $1/l^2$, consistent with the naive model of the behavior expected in such a resonance. Finally, the slight enhancement in the cross sections around 35 eV at some internuclear geometries is not shape resonant but arises from the usual energy dependence of the $7\sigma \rightarrow k\pi$ contribution. This feature becomes much less evident as the width of the resonance increases.

Figure 2 shows the eigenphase sum for the $k\sigma$ continuum of the $N_2O(7\sigma^{-1})$ ion at the same internuclear geometries as in Fig. 1. Their behavior shows that there are two shape resonances in this continuum. The low-energy resonance associated with the rise in the eigenphase sum around 20 eV at the equilibrium geometry is seen prominently in the cross sections of Fig. 1. However, the higher shape resonance around 40 eV in the eigenphase sum is completely obscured in the fixed-nuclei cross sections of Fig. 1. We will see shortly that the effect of this resonance is also not evident

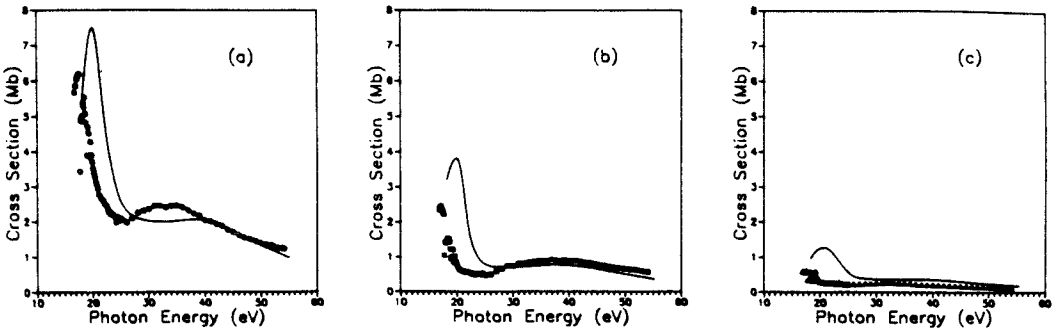

FIG. 4. Cross sections for $7\sigma^{-1}$ photoionization of N_2O to the (000), (100), and (001) vibrational levels of N_2O^+: (a) (000) level; –, present results (dipole length); O, experimental data of Ref. 8; (b) (100) level; –, present results (dipole length); □, experimental data of Ref. 8; (c) (001) level; –, present results (dipole length); △, experimental data of Ref. 8. See the text for explanation of how the experimental data has been normalized.

in the vibrationally resolved cross sections but leads to a broad dip in the photoelectron asymmetry parameters. The behavior of these eigenphase sums with N–N and N–O distances also shows that these resonances cannot be viewed as predominantly associated with either of these two regions of the molecule.

In Fig. 3 we show the fixed-nuclei photoelectron asymmetry parameters for 7σ photoionization at 16 internuclear geometries. The pronounced minimum in these asymmetry parameters at low photoelectron energies is clearly associated with the shape resonance seen in both the cross sections and eigenphase sums of Figs 1 and 2, respectively. These asymmetry parameters also show a broad minimum at higher energy which can be identified as arising from the shape resonance seen at the same energy in the eigenphase sums of Fig. 2. This broad shape resonance produces essentially no enhancement in the fixed-nuclei cross sections.

IV. VIBRATIONALLY RESOLVED RESULTS

Figures 4(a)–4(c) show calculated vibrationally resolved cross sections for photoionization leading to the (000), (100), and (001) levels of the $A\,^2\Sigma^+$ ($7\sigma^{-1}$) state of N_2O^+, respectively. Also shown are the results of Kelly *et al.*[8] derived from ionic fluorescence data (this issue) and normalized to our calculated (000) cross section at 40 eV. Although the physically significant features of these calculated cross sections agree reasonably well with measured relative cross sections, the calculated peak resonance positions are consistently about two eVs too high. We attribute this to inadequacies in our vibrational wave functions, particularly for N_2O^+, for which harmonic potentials were assumed since more refined potentials were not available. In fact, our calculated vibrationally unresolved cross sections show a resonance peak very close in energy to the measured peak position.[10] Comparison of the calculated (000), (100), and (001) cross sections, shifted down by 2 eV so as to bring the peak position of the calculated (000) cross section into agreement with the measured values, with the experimental data in Figs. 5(a)–5(c) also suggests that the potentials assumed here are not too reliable. This example serves to underscore a serious difficulty that will arise in the analysis of vibrationally resolved photoelectron spectra of polyatomic molecules.

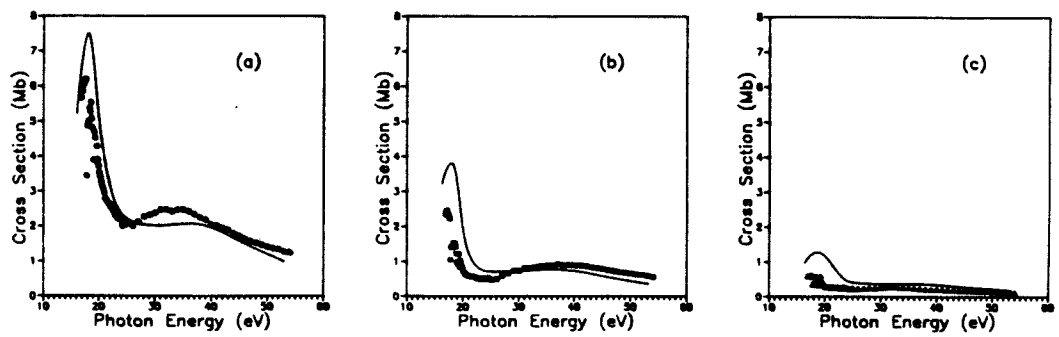

FIG. 5. Comparison of the calculated cross sections for photoionization leading to the (000), (100), and (001) levels of the $A\,^2\Sigma^+$ ($7\sigma^{-1}$) state of N_2O^+, shifted down by 2 eV, with the measured relative values of Ref. 8. See the text for explanation.

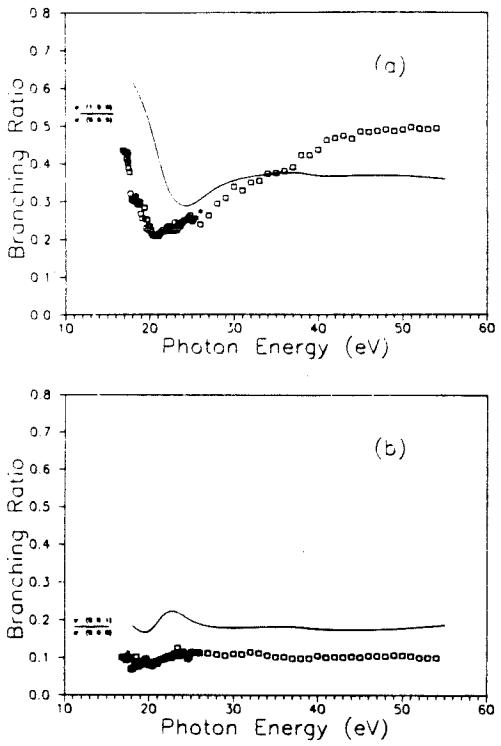

FIG. 6. Vibrational branching ratios (100)/(000) (symmetric stretch) and (001)/(000) (antisymmetric stretch) for $7\sigma^{-1}$ photoionization for N_2O: (a) symmetric stretch; –, present results (dipole length); □, experimental results of Ref. 8; *, experimental results of Ref. 9; (b) antisymmetric stretch; –, present results (dipole length); □, experimental results of Ref. 8; *, experimental results of Ref. 9.

In Figs. 6(a)–6(b) we show our calculated (100)/(000) and (001)/(000) branching ratios for 7σ photoionization of N_2O along with the ionic fluorescence and photoelectron data of Kelly *et al.*[8] and Ferrett *et al.*,[9] respectively. The most significant feature in the (100)/(000) branching ratio is its strong energy dependence (non-Franck–Condon behavior) around a photon energy of about 20 eV which arises from the $k\sigma$ shape resonance seen in the results of Fig. 1. The dip in this calculated branching ratio occurs at higher energy than the one seen experimentally. This discrepancy is probably again due to our use of approximate potentials in obtaining the vibrational wave functions for N_2O^+.[14] In fact, our calculated (100)/(000) branching ratio approaches a Franck–Condon limit significantly different from the experimental value. This discrepancy is another reflection of the limited quality of the available N_2O^+ potential energy curves. The non-Franck–Condon behavior also extends to higher energy—almost to 40 eV—in the measured than in the calculated branching ratios. It is also interesting to speculate whether the behavior seen in the measured branching ratio between 35 and 40 eV arises from the weak σ shape resonance seen at these energies in the eigenphase sums of Fig. 2. Our calculations do show non-Franck–Condon behavior in the branching ratios arising from the $k\sigma$ channel in this energy range, but it is washed out by the large nonresonant $k\pi$ channel.

The (001)/(000) branching ratio also shows non-Franck–Condon behavior around 20 eV which, however, is much less pronounced than in the (100)/(000) branching ratio and also approaches the Franck–Condon value above about 28 eV. The reason for the significantly larger deviations from the Franck–Condon behavior for the symmetric than for the antisymmetric modes can be readily seen from the fixed-nuclei cross sections shown in Fig. 1. These results show that the σ shape resonance moves to lower or higher energies with an increase or decrease respectively in *either* the N–N or N–O bond distance. The resonance hence behaves as though it belongs to the entire molecule and its position and width depend to a great extent on the overall length of the molecule. In the antisymmetric mode, (001), the total bond length of the molecule does not change much and hence the influence of the resonance on its vibrational branching ratio is less pronounced than for the symmetric

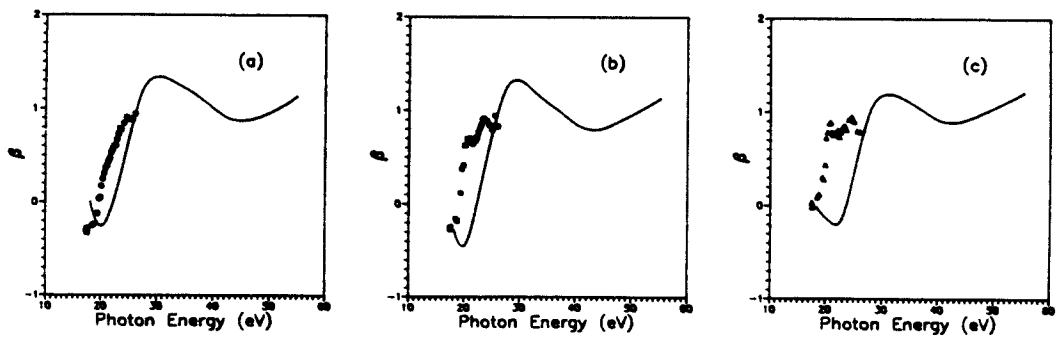

FIG. 7. Photoelectron asymmetry parameters for $7\sigma^{-1}$ photoionization of N_2O: (a) (000) level; —, present results (dipole length); O, experimental data of Ref. 9; (b) (100) level; —, present results (dipole length); □, experimental data of Ref. 9; (c) (001) level; — present results (dipole length); △, experimental data of Ref. 9.

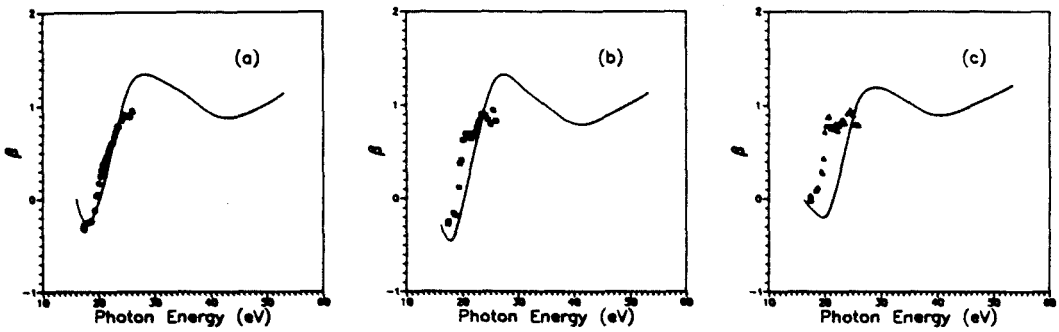

FIG. 8. Comparisons of the calculated asymmetry parameters for photoionization leading to the (000), (100), and (001) levels of the $A\ ^2\Sigma^+ (7\sigma^{-1})$ state of N_2O^+, shifted down by 2 eV, with the measured values of Ref. 9. See the text for explanation.

stretching mode, (100), where vibrational motion involves changes in the total bond length. These results provide an interesting example of how shape resonances can distinctly influence alternative vibrational modes in polyatomics.

Our calculated photoelectron asymmetry parameters for the (000), (100), and (001) levels are shown in Figs. 7(a)–7(c) along with the measured values of Ferrett *et al.*[9] The calculated asymmetry parameters show clear evidence of the low-energy shape resonance around 20 eV, in general agreement with the experimental data. These calculated asymmetry parameters also show a broad minimum around 40 eV which arises from the higher shape resonance seen in the eigenphase sums and asymmetry parameters of Figs. 2 and 3, respectively. No experimental data is available in this energy range. As in the vibrationally resolved cross sections of Figs. 4(a)–4(c), the strong dip in the asymmetry parameters also occurs at a slightly higher energy than in the experimental data. This difference again is probably due to our use of harmonic potentials in obtaining the vibrational wave functions. Purely for suggestive reasons we compare these vibrationally resolved photoelectron angular distributions, shifted to lower energy by 2 eV [the same as was done for the resonance peaks in Figs. 5(a)–5(c)] with the experimental values in Figs. 8(a)–8(c).

V. CONCLUDING REMARKS

We have studied the vibrationally resolved cross sections and photoelectron asymmetry parameters for photoionization leading to the (000), (100), and (001) levels of the $A\ ^2\Sigma^+ (7\sigma^{-1})$ state of N_2O^+. One of the main objectives of these studies was to provide some insight into shape resonance behavior for alternative internuclear configurations in polyatomics and hence to predict the expected influence of these resonances on specific vibrational branching ratios. Coupled with the experimental studies reported in the accompanying papers, these results provide an example of the rich dynamical behavior of shape resonances that can be expected in polyatomics. An important conclusion of these studies is that the more pronounced deviations of the vibrational branching ratios observed for the symmetric than for the antisymmetric stretching mode in the region of the low-energy σ shape resonance is essentially due to the fact that this shape resonance behaves as though it belongs to the molecule as a whole and hence its position and width depend on the overall length of the molecule and not on the specific N–N or N–O bond distances. It is clear that vibrationally resolved studies of the photoionization of polyatomic molecules, as illustrated here for N_2O, will provide new insight into molecular photoionization dynamics.

ACKNOWLEDGMENTS

This material is based upon research supported by the National Science Foundation under Grant No. CHE8521391. The authors also acknowledge use of the resources of the San Diego SuperComputer Center which is supported by the National Science Foundation. We would like to thank Dr. E. Poliakoff of Boston University and Dr. T. Ferrett at the National Bureau of Standards for their helpful discussions and for making the results of their experiments available before publication. Finally, we thank Dr. A. D. McLean for providing us with SCF wave functions for N_2O at many geometries.

[1] See, for example, J. L. Dehmer, A. C. Parr, and S. H. Southworth, in *Handbook of Synchrotron Radiation*, edited by G. V. Marr (North-Holland, Amsterdam, 1987), Vol. II.
[2] J. L. Dehmer, D. Dill, and S. Wallace, Phys. Rev. Lett. 43, 1005 (1979).
[3] J. B. West, A. C. Parr, B. E. Cole, D. L. Ederer, R. Stockbauer, and J. L. Dehmer, J. Phys. B 13, L105 (1980).
[4] G. Raseev, H. Le Rouzo, and H. Lefebvre-Brion, J. Chem. Phys. 72, 5701 (1980).
[5] R. R. Lucchese and V. McKoy, J. Phys. B 14, L629 (1981).
[6] For C_2N_2, as an example, see D. M. P. Holland, A. C. Parr, D. L. Ederer, J. B. West, and J. L. Dehmer, Int. J. Mass. Spectrom. Ion Phys. 52, 195 (1983); D. L. Lynch and V. McKoy, J. Chem. Phys. 84, 5504 (1986).
[7] E. D. Poliakoff, M. H. Ho, M. G. White, and G. E. Leroi, Chem. Phys. Lett. 130, 91 (1986).

[8]L. A. Kelly, L. M. Duffy, B. Space, E. D. Poliakoff, P. Roy, S. H. Southworth, and M. G. White, J. Chem. Phys. **90**, 1544 (1989).
[9]T. A. Ferrett, A. C. Parr, S. H. Southworth, J. E. Hardis, and J. L. Dehmer, J. Chem. Phys. **89**, 1551 (1989).
[10]M. Braunstein and V. McKoy, J. Chem. Phys. **87**, 224 (1987).
[11]M. E. Smith, R. R. Lucchese, and V. McKoy, Phys. Rev. A **29**, 1857 (1984).
[12]A. D. McLean and M. Yoshimine, *Tables of Linear Molecular Wave Functions* (IBM Research Laboratories, San Jose, 1967), pp. 196–204.
[13]A. D. McLean (private communication).
[14]J. H. Callomon and F. Creutzberg, Philos. Trans. R. Soc. London, Ser. A **277** 157 (1974).
[15]E. B. Wilson, Jr., J. C. Decius, and P. C. Cross, *Molecular Vibrations* (Dover, New York, 1955).
[16]T. Gustafsson and H. J. Levinson, Chem. Phys. Lett. **78**, 28 (1981).
[17]M. E. Smith, V. McKoy, and R. R. Lucchese, J. Chem. Phys. **82**, 4147 (1986).

Chapter 12

Studies of the valence shell photoionization of Cl_2

(The text of this chapter appeared in: M. Braunstein and V. McKoy, J. Chem. Phys. **92** 4887 (1990).)

Studies of valence shell photoionization of Cl_2

M. Braunstein and V. McKoy
Arthur Amos Noyes Laboratory of Chemical Physics,[a] California Institute of Technology, Pasadena, California 91125

(Received 16 October 1989; accepted 4 January 1990)

We report photoionization cross sections and photoelectron angular distributions for the $5\sigma_g$, $2\pi_u$ and $2\pi_g$ orbitals of Cl_2 from threshold to ~20 eV photoelectron energy obtained using Hartree–Fock photoelectron orbitals. These studies were motivated by recent (2 + 1) resonance enhanced multiphoton ionization (REMPI) experiments via the $2\,^1\Pi_g(2\pi_g^3 4s\sigma_g)$ state which show strong non-Franck–Condon effects in the ion vibrational distribution suggesting that shape and/or autoionizing resonances may play a role near threshold. Previous single-photon experiments on the valence orbitals of Cl_2 do not give a consistent picture of these cross sections at low energies. Our results show that there is a shape resonance in the $k\pi_u$ continuum. However, preliminary studies show that these π_u cross sections have almost no dependence on internuclear distance and could not be the cause of non-Franck–Condon effects observed in the REMPI experiments.

I. INTRODUCTION

In recent resonance enhanced multiphoton ionization (REMPI) studies of molecular chlorine via the $2\,^1\Pi_g(2\pi_g^3 4s\sigma_g)$ state, Koenders *et al.*[1] found ion vibrational distributions which could not be explained by a simple Franck–Condon picture. Such large non-Franck–Condon effects have been observed in REMPI of other diatomic molecules[2–10] and have been seen to arise from several different mechanisms.[11] In the case of molecular chlorine, studies by Li *et al.*[12,13] show that Rydberg–valence interactions involving the $1\,^1\Pi_g(\pi_u \rightarrow \sigma_u)$ valence state[14] are small, suggesting that low energy shape and/or autoionizing resonances may play a role in producing these non-Franck–Condon effects. Single-photon ionization studies of the valence orbitals of molecular chlorine have been carried out by Carlson *et al.*,[15] but these studies were mainly concerned with the region around the Cooper minimum at 30 to 40 eV above threshold and did not extend to low photoelectron energies. More recently, Samson *et al.*[16] have obtained total ion cross sections beginning around the $2\pi_u$ ionization threshold. These cross sections differ in magnitude by about a factor of 2 from those of Carlson *et al.*,[15] but show the same general dependence on energy. van de Meer *et al.*[17] have measured the photoionization cross sections for the valence oribitals of Cl_2 at the HeI line (21.2 eV). These measurements differ significantly from those of Carlson *et al.*[15] and are in better agreement but still differ with the total ion cross sections of Samson *et al.*[16] To try to understand these differences and to provide some insight into how the electronic continuum may affect REMPI experiments on Cl_2, we have obtained photoionization cross sections and photoelectron asymmetry parameters for single-photon ionization of the valence orbitals ($5\sigma_g$,$2\pi_u$,$2\pi_g$) of Cl_2 from threshold to ~20 eV photoelectron energy using Hartree–Fock photoelectron orbitals. These studies are preliminary to REMPI studies of Cl_2 via the $2\,^1\Pi_g$ state.

It is well known that interchannel coupling is important in 3*p* photoionization of chlorine atom at low photoelectron energies.[18–20] Such coupling can also be expected to be important in the photoionization of molecular chlorine. Nevertheless, the present study should illustrate some general dynamical features of the photoionization cross sections of Cl_2 and serve as a basis for future studies beyond the Hartree–Fock level. Indeed, we do find strong shape resonant structure in the $k\pi_u$ continuum which arises mainly from the $l = 3$ partial wave, not unlike but more pronounced than that seen in F_2.[21] Preliminary studies indicate, however, that these cross sections do not depend on internuclear distance. These results suggest that a shape resonant mechanism is probably not responsible for the non-Franck–Condon effects observed in the REMPI experiments of Koenders *et al.*[1] and that other mechanisms need to be investigated.

In Sec. II we give a brief description of our procedure for obtaining the Hartree–Fock photoelectron oribitals. In Sec. III we present our photoionization cross sections and photoelectron asymmetry parameters for the $5\sigma_g$,$2\pi_u$, and $2\pi_g$ orbitals of Cl_2 and compare these with experimental results.

II. METHOD AND CALCULATIONS

Our method for obtaining Hartree–Fock photoelectron orbitals has been discussed extensively elsewhere[22,23] and will only be briefly summarized here. We assume a frozen core Hartree–Fock model in which the ion orbitals are constrained to be identical to those of the neutral molecule and the photoelectron orbital is a solution of the one-electron Schrödinger equation

$$\left[-\frac{1}{2}\nabla^2 + V_{N-1}(\mathbf{r},R) - \frac{k^2}{2}\right]\phi_k(\mathbf{r},R) = 0, \qquad (1)$$

where $V_{N-1}(\mathbf{r},R)$ is the static-exchange potential of the molecular ion, $k^2/2$ is the photoelectron kinetic energy, and ϕ_k satisfies appropriate scattering boundary conditions. To solve for ϕ_k we work with the integral form of Eq. (1), i.e., the Lippmann–Schwinger equation

$$\phi_k = \phi_k^c + G_c^{(-)} V \phi_k, \qquad (2)$$

where ϕ_k^c is the Coulomb scattering wave function, V is the molecular ion potential V_{N-1} with the Coulomb potential removed, and $G_c^{(-)}$ is the Coulomb Green's function with incoming-wave boundary conditions. We first obtain an approximate solution of Eq. (2) by assuming a separable approximation to the potential V of the form

$$V(\mathbf{r},\mathbf{r}') \cong V^{\mathrm{s}}(\mathbf{r},\mathbf{r}') = \sum_{ij} \langle \mathbf{r}|V|\alpha_i\rangle [V^{-1}]_{ij} \langle \alpha_j|V|\mathbf{r}'\rangle, \tag{3}$$

where the matrix V^{-1} is the inverse of the matrix with elements $V_{ij} = \langle \alpha_i|V|\alpha_j\rangle$ and the α's are discrete basis functions such as Cartesian or spherical Gaussian functions.[22] With this approximation to V, the partial wave solution to the integral equation can be written as

$$\phi^{(0)}_{klm}(\mathbf{r}) = \phi^{c}_{klm}(\mathbf{r}) + \sum_{ij} \langle \mathbf{r}|G_c^{(-)}V|\alpha_i\rangle [D^{-1}]_{ij} \langle \alpha_j|V|\phi^{c}_{klm}\rangle, \tag{4}$$

where

$$D_{ij} = \langle \alpha_i|V - VG_c^{(-)}V|\alpha_j\rangle \tag{5}$$

and

$$\phi_{\mathbf{k}}(\mathbf{r}) = \left(\frac{2}{\pi}\right)^{1/2} \sum_{l=0}^{l_p} \sum_{m=-l}^{l} i^l \phi_{klm}(\mathbf{r}) Y^{*}_{lm}(\hat{\mathbf{k}}). \tag{6}$$

With adequate basis sets α's, these approximate solutions $\phi^{(0)}_{klm}$, which satisfy scattering boundary conditions, can provide quantitatively reliable cross sections[24] and have been used in calculating the photoionization cross sections and photoelectron asymmetry parameters reported below.

TABLE I. Basis sets used in separable potential, Eq. (3).

Photoionization symmetry	Type of Gaussian function[a]	Exponents
σ_g	Cartesian s	16.0,8.0,4.0,2.0,1.0,0.5,0.1
	z	1.0,0.5,0.1
	Spherical $l=0$	4.0,2.0,1.0,0.5,0.1
	$l=2$	4.0,2.0,1.0,0.5,0.1
	$l=4$	1.0,0.5,0.1
σ_u	Cartesian s	16.0,8.0,4.0,2.0,1.0,0.5,0.1
	z	1.0,0.5,0.1
	Spherical $l=1$	4.0,2.0,1.0,0.5,0.1
	$l=3$	4.0,2.0,1.0,0.5,0.1
	$l=5$	1.0,0.5,0.1
π_g	Cartesian x	16.0,8.0,4.0,2.0,1.0,0.5,0.1
	xz	1.0,0.5,0.1
	Spherical $l=2$	4.0,2.0,1.0,0.5,0.1
	$l=4$	4.0,2.0,1.0,0.5,0.1
π_u	Cartesian x	16.0,8.0,4.0,2.0,1.0,0.5,0.1
	xz	1.0,0.5,0.1
	Spherical $l=1$	4.0,2.0,1.0,0.5,0.1
	$l=3$	4.0,2.0,1.0,0.5,0.1
	$l=5$	1.0,0.5,0.1
δ_g	Cartesian xy	16.0,8.0,4.0,2.0,1.0,0.5,0.1
	Spherical $l=2$	4.0,2.0,1.0,0.5,0.1
	$l=4$	1.0,0.5,0.1
δ_u	Cartesian xy	16.0,8.0,4.0,2.0,1.0,0.5,0.1
	Spherical $l=3$	4.0,2.0,1.0,0.5,0.1
	$l=5$	1.0,0.5,0.1

[a] Cartesian Gaussian basis functions are defined as $\phi^{a,l,m,n,A}(\mathbf{r}) = N(x-A_x)^l(y-A_y)^m(z-A_z)^n \exp(-\alpha|\mathbf{r}-\mathbf{A}|^2)$ and spherical Gaussian functions as $\phi^{\alpha,l,m,A}(\mathbf{r}) = N|\mathbf{r}-\mathbf{A}|^l \exp(-\alpha|\mathbf{r}-\mathbf{A}|^2) Y_{lm}(\Omega_{\mathbf{r}-\mathbf{A}})$. The Cartesian functions are centered on the nuclei and spherical functions on the bond midpoint.

For the ground state SCF wave function of Cl_2 with its electronic configuration $1\sigma_g^2 1\sigma_u^2 2\sigma_g^2 2\sigma_u^2 3\sigma_g^2 3\sigma_u^2 1\pi_u^4 1\pi_g^4 4\sigma_g^2 4\sigma_u^2 5\sigma_g^2 2\pi_u^4 2\pi_g^4$ we used the [8s5p] contracted Gaussian basis set of Dunning and Hay[25] with two additional d-type polarization functions with exponents 0.797 and 0.220 on each nucleus.[26] Calculations with this basis at the equilibrium geometry of Cl_2 (R_e = 3.7568 a.u.) give an SCF energy of −918.908 278 a.u. For the basis sets $\{\alpha\}$ in Eqs. (3) and (4) we used Cartesian Gaussian functions centered on the atomic nuclei and spherical Gaussians at the center of mass. These functions for each photoelectron symmetry are given in Table I.

All matrix elements and functions arising in the solution of the Lippmann–Schwinger equation, Eq. (2), were evaluated via single-center expansions about the molecular center. The partial wave expansion of the photoelectron orbital, Eq. (6), was truncated at $l_p = 13$. The other partial wave expansion parameters were chosen as follows:

(i) maximum partial wave in the expansion of the occupied orbitals = 80,

(ii) maximum partial wave in the expansion of the occupied orbitals in the exchange potential = 80($1\sigma_g$),

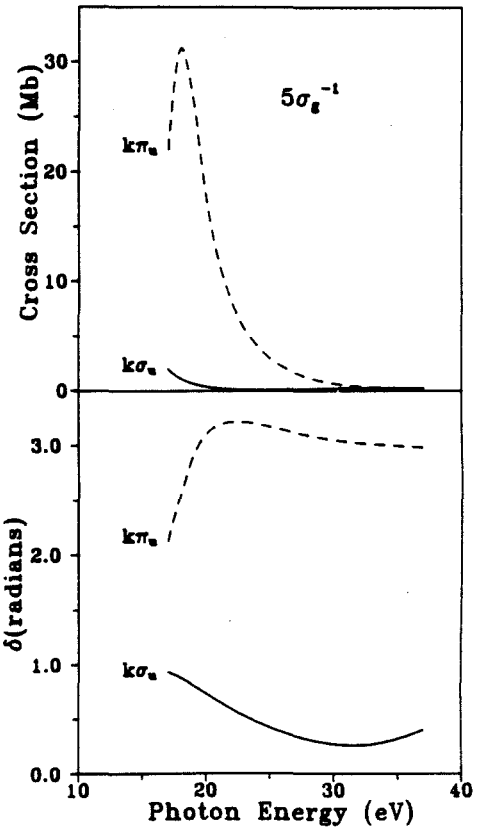

FIG. 1. Partial photoionization cross sections (length) and eigenphase sums for the $5\sigma_g$ orbital of Cl_2.

$80(1\sigma_u)$, $70(2\sigma_g)$, $70(2\sigma_u)$, $50(3\sigma_g)$, $50(3\sigma_u)$, $50(1\pi_u)$, $50(1\pi_g)$, $50(4\sigma_g)$, $50(4\sigma_u)$, $40(5\sigma_g)$, $40(2\pi_u)$, $40(2\pi_g)$,

(iii) maximum partial wave in the expansion of $1/r_{12}$ in the direct and exchange terms = 160 and 80, respectively,

(iv) all other partial wave expansions were truncated at $l = 80$.

Based on our studies with such partial-wave expansions, this choice of expansion parameters should provide cross sections within a few percent of the converged values. The associated radial integrals were obtained using a Simpson's rule quadrature. The grid contained 850 points and extended to 94.5 a.u.with a step size varying from 0.01 a.u. near the atomic nuclei to 0.5 a.u. at large distances.

III. RESULTS AND DISCUSSION

Figure 1 shows the $k\sigma_u$ and $k\pi_u$ partial cross sections and eigenphase sums for photoionization of the $5\sigma_g$ orbital of Cl_2, assuming an ionization potential (IP) of 16.1 eV.[27,28]

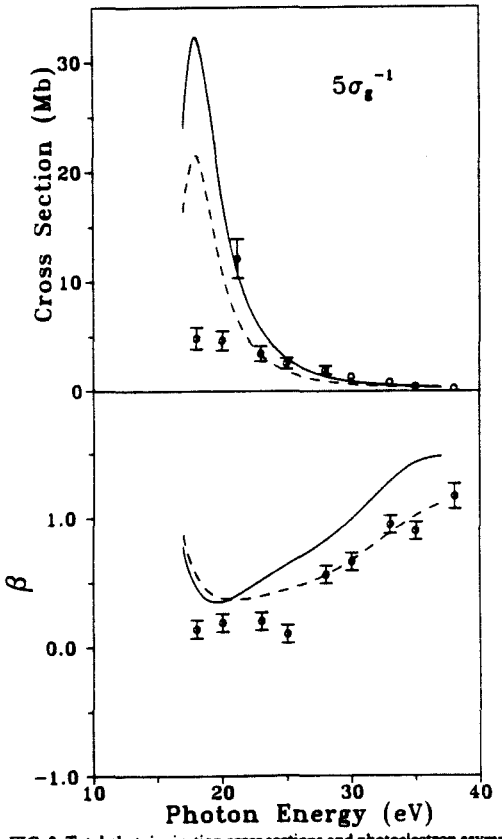

FIG. 2. Total photoionization cross sections and photoelectron asymmetry parameters for the $5\sigma_g$ orbital of Cl_2:—, present results (length);—, present results (velocity); O, synchrotron measurements of Ref. 15. Error bars are not shown at higher energies; ●, HeI line measurement of Ref. 17.

In contrast to what is seen in other lighter diatomics such as N_2 [29] and O_2 [30] with their shorter bond lengths, the $k\sigma_u$ channel is weak and shows no evidence of shape resonant behavior at these internuclear distances. The $k\pi_u$ eigenphase sum shows a rapid rise near threshold which is reflected in the large enhancement in the $k\pi_u$ partial channel cross section. Calculations at several internuclear distances show almost no change in these $k\pi_u$ cross sections, in contrast to previous studies of the behavior of $k\sigma_u$ shape resonances in other molecules.[31] For a $k\pi_u$ shape resonance, oriented perpendicular to the molecular axis, one perhaps would not expect changes in the bond length to affect the cross sections. With its insensitivity to bond distance, this shape resonant continuum *should not* lead to any significant non-Franck–Condon behavior.

Examination of the U matrix which diagonalizes the K matrix to obtain the eigenphase sum[32]

$$\delta = \sum_{lm} \arctan(U^{\dagger}KU) \tag{7}$$

shows this resonance behavior to be associated principally with the $l = 3$ partial wave. Indeed, a plot of the corresponding resonant eigenchannel function[32]

$$\psi_\alpha = \sum_{lm} \psi_{lm} U_{lm\alpha}, \tag{8}$$

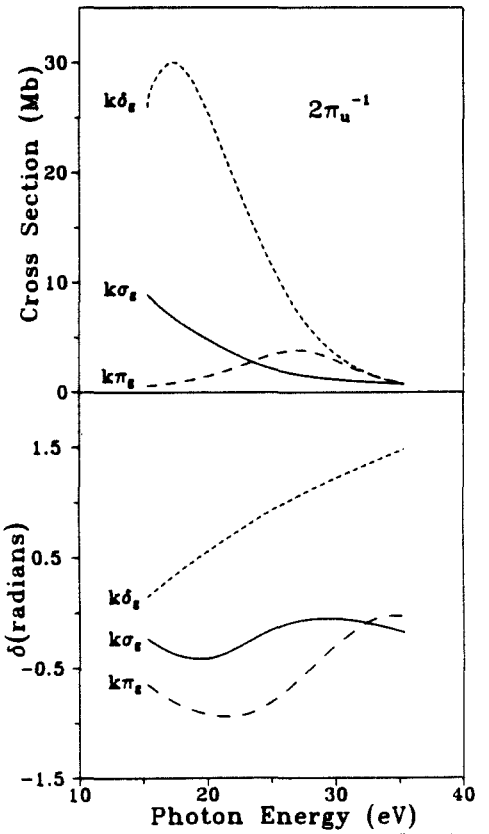

FIG. 3. Partial photoionization cross sections (length) and eigenphase sums for the $2\pi_u$ orbital of Cl_2.

where ψ_{lm} is the K-matrix normalized partial wave component of the continuum orbital and α is an eigenchannel index, shows f-wave nodal structure (not shown).

In Fig. 2 we show our calculated cross sections and photoelectron asymmetry parameters for photoionization of the $5\sigma_g$ orbital of Cl_2 along with the experimental synchrotron results of Carlson *et al.*[15] and the HeI line measurement of van der Meer *et al.*[17] Differences between the cross sections obtained in the length and velocity approximations are known to arise primarily from neglect of electronic correlations in the Hartree–Fock wave functions used here.[23] The pronounced peak in the calculated cross sections arises from the shape resonant $k\pi_u$ partial channel shown in Fig. 1. Below ~25 eV photon energy there are large differences between the measured values of Carlson *et al.*[15] and the present results. The results of multiple-scattering model (MSM) calculations of Carlson *et al.*,[15] which extend down to ~19 eV photon energy (not shown) agree well with the present calculations, showing the same enhancement near threshold. The agreement between the He I line measurement of van der Meer *et al.*[17] and the calculated cross sections is encouraging. Additional measurements at low photoelectron energies would be helpful in clarifying the resonant behavior of these cross sections. The agreement between the calculated photoelectron asymmetry parameters and the measurements of Carlson *et al.*[15] is also quite satisfactory. Further experimental studies of these asymmetry parameters in the region of the "dip" in the present results would be helpful.

Figure 3 shows our calculated partial cross sections and eigenphase sums for the $2\pi_u$ orbital of Cl_2 assuming an ionization potential of 14.4 eV.[27,28] The $k\delta_g$ cross section, which is primarily $l = 2$, shows a broad enhancement at low energy. The $k\pi_g$ cross section is small at low energy and shows a mild enhancement at ~25 eV photon energy where the eigenphase sum rises slightly due to the $l = 4$ partial wave. The total cross sections and photoelectron asymmetry parameters for the $2\pi_u$ level are shown in Fig. 4. There are again substantial differences between the present calculated results and the measurements of Carlson *et al.*[15] The cross section at the HeI line measured by van der Meer *et al.*[17] is again also in good agreement with the calculated value. The calculated photoelectron angular distributions, however, agree well with the measurements of Carlson *et al.*[15] over the entire energy range.

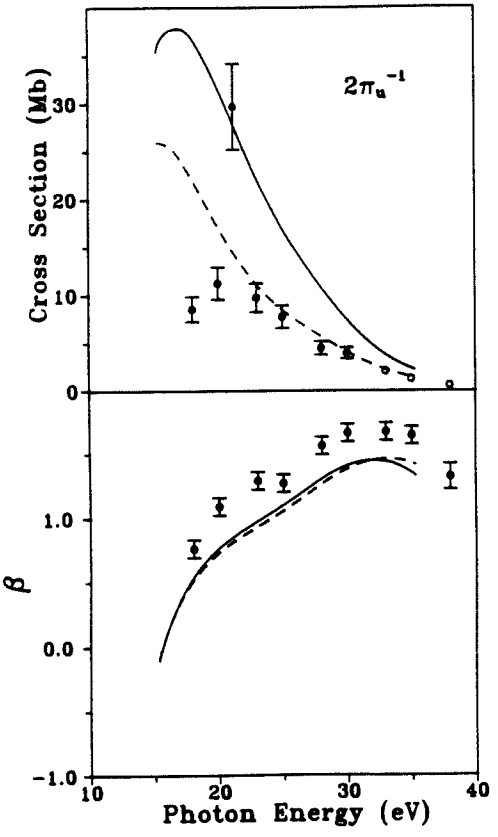

FIG. 4. Total photoionization cross sections and photoelectron asymmetry parameters for the $2\pi_u$ orbital of Cl_2:—, present results (length);---, present results (velocity); O, synchrotron measurements of Ref. 15. Error bars are not shown at higher energies; ●, HeI line measurement of Ref. 17.

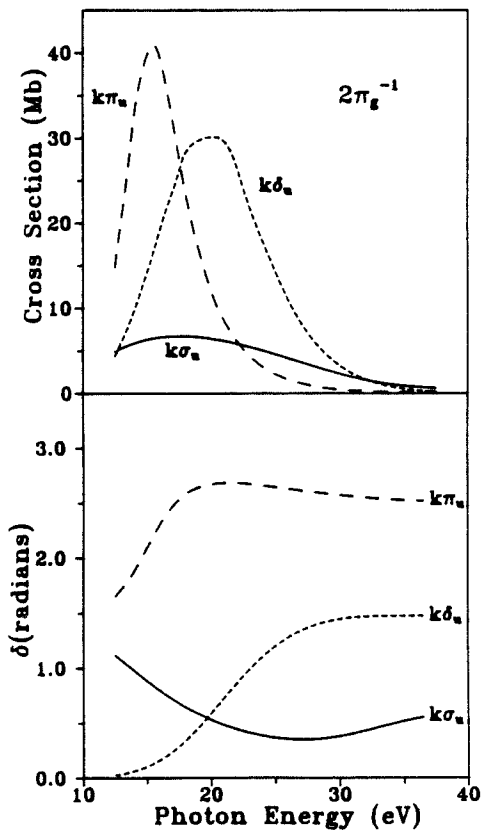

FIG. 5. Partial photoionization cross sections (length) and eigenphase sums for the $2\pi_g$ orbital of Cl_2.

In Fig. 5 we show the partial cross sections and eigenphase sums for photoionization of the $2\pi_g$ level (IP = 11.6 eV).[27,28] The $k\pi_u$ eigenphase sums show the same rise near threshold seen in $5\sigma_g$ photoionization. There is a similar but slow rise in the $k\delta_u$ eigenphase sums. This behavior in the eigenphase sums is also evident in enhancements in the $k\pi_u$ and $k\delta_u$ cross sections. Figure 6 shows the total cross sections and photoelectron asymmetry parameters for $2\pi_g$ photoionization. Our calculated cross sections agree with those of Carlson *et al.*[15] above ~25 eV photon energy, but differ significantly closer to threshold. The agreement between the calculated cross sections and the measured value of van der Meer *et al.*[17] at the HeI line is again encouraging. The calculated photoelectron asymmetry parameters are in good agreement with the measured values of Carlson *et al.*[15]

Figure 7 shows the total photoionization cross sections for the $5\sigma_g + 2\pi_u + 2\pi_g$ orbitals of molecular chlorine along with results of experiment. The "steps" at low energy in the present results indicate the onset of these ionization thresholds. These thresholds are also indicated by the arrows on the photon energy axis. Note that the data of Samson *et al.*[16] record the total ion yield and include contributions from the $4\sigma_u$ orbital (IP ~ 27 eV) and $4\sigma_g$ orbital (IP ~ 34 eV). The data of Carlson *et al.*[15] and Samson *et al.*[16] show the same general energy dependence, except for the data point of Carlson *et al.*[16] at 18 eV photon energy, but differ substantially in magnitude. Above ~20 eV photon energy the data of Samson *et al.*[16] agree well with the present results. Below the $5\sigma_g$ threshold, however, the data of Samson *et al.*[16] and the present results show a quite different energy dependence. Several studies[33–35] show rich autoionizing structure within a few electron volts of the $2\pi_g$ ionization threshold and this may account for some of these differences. The data of van der Meer *et al.*[17] at 21.2 eV differs from that of Samson *et al.*[16] Both of these experimental results are bracketed by the present length and velocity Hartree–Fock results. The difference between the length and velocity results indicates that electron correlations beyond the Hartree–Fock level are important in this region. Future theoretical studies need to include such effects and interchannel coupling to understand these experimental cross sections. In addition, further experimental studies of orbital cross sections are needed to provide a consistent picture of photoionization of Cl_2 at low energies.

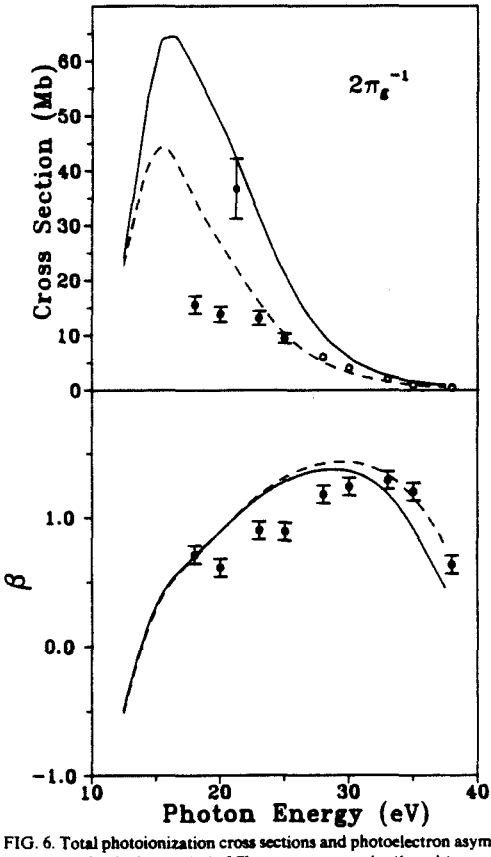

FIG. 6. Total photoionization cross sections and photoelectron asymmetry parameters for the $2\pi_g$ orbital of Cl_2:—, present results (length);---, present results (velocity); O, synchrotron measurements of Ref. 15. Error bars are not shown at higher energies; ●, HeI line measurement of Ref. 17.

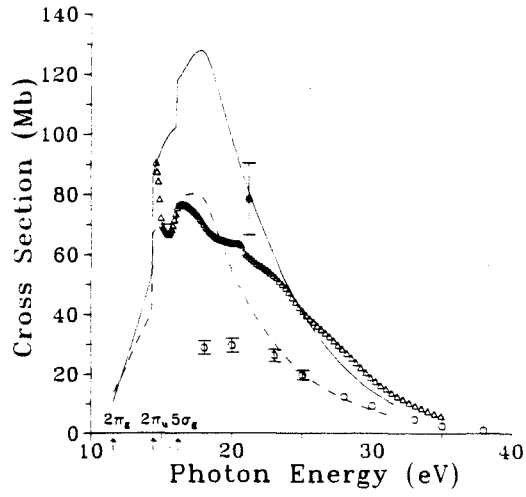

FIG. 7. Total photoionization cross sections ($5\sigma_g + 2\pi_u + 2\pi_g$) for Cl_2:—, present results (length);---, present results (velocity); O, synchrotron measurements of Ref. 15. Error bars are not shown at higher energies; ●, HeI line measurement of Ref. 17; △ experimental measurements of Ref. 16. Above ~27 eV the data of Ref. 16 contain contributions from other lower lying molecular orbitals.

ACKNOWLEDGMENTS

This work was supported by a grant from the National Science Foundation (CHE-8521391). We also acknowledge use of resources of the San Diego SuperComputer Center, which is supported by the National Science Foundation, and the Air Force SuperComputer Center-Kirtland. One of us (M.B.) would like to acknowledge support from a Department of Education Graduate Fellowship and would also like to thank Dr. J. A. Stephens for providing data on atomic chlorine phase shifts.

[1]B. G. Koenders, S. M. Koeckhoven, G. J. Kuik, K. E. Drabe, and C. A. de Lange, J. Chem. Phys. **91**, 6042 (1989).
[2]M. G. White, M. Seaver, W. A. Chupka, and S. D. Colson, Phys. Rev. Lett. **49**, 28 (1982).
[3]M. G. White, M. Seaver, W. A. Chupka, and S. D. Colson, J. Chem. Phys. **80**, 678 (1984).
[4]J. C. Miller and R. N. Compton, J. Chem. Phys. **84**, 675 (1986).
[5]S. T. Pratt, P. M. Dehmer, and J. L. Dehmer, Chem. Phys. Lett. **105**, 28 (1984).
[6]S. T. Pratt, P. M. Dehmer, and J. L. Dehmer, J. Chem. Phys. **85**, 3379 (1986).
[7]S. Katsumata, K. Sato, Y. Achiba, and K. Kimura, J. Electron Spectrosc. Relat. Phenom. **41**, 325 (1986).
[8]P. J. Miller, L. Li, W. A. Chupka, and S. D. Colson, J. Chem. Phys. **89**, 3921 (1988).
[9]J. A. Stephens, M. Braunstein, and V. McKoy, J. Chem. Phys. **89**, 3923 (1988).
[10]M. Braunstein, J. A. Stephens, and V. McKoy, J. Chem. Phys. **90**, 633 (1989).
[11]See, for example, W. A. Chupka, J. Chem. Phys. **87**, 1488 (1987).
[12]L. Li, R. Lipert, H. Park, W. A. Chupka, and S. D. Colson, J. Chem. Phys. **87**, 6767 (1987).
[13]L. Li, R. Lipert, H. Park, W. A. Chupka, and S. D. Colson, J. Chem. Phys. **88**, 4608 (1988).
[14]S. D. Peyerimhoff and R. J. Buenker, Chem. Phys. **57**, 279 (1981).
[15]T. A. Carlson, M. O. Krause, F. A. Grimm, and T. A. Whitley, J. Chem. Phys. **78**, 638 (1983).
[16]J. A. R. Samson and G. C. Angel, J. Chem. Phys. **86**, 1814 (1987).
[17]W. J. van der Meer, R. J. Butselaar, and C. A. de Lange, Aust. J. Phys. **39**, 779 (1986).
[18]E. R. Brown, S. L. Carter, and H. P. Kelly, Phys. Rev. A **21**, 1237 (1980).
[19]W. R. Fielder and L. A. Armstrong, Jr., Phys. Rev. A **28**, 218 (1983).
[20]J. A. R. Samson, Y. Shefer, and G. C. Angel, Phys. Rev. Lett. **56**, 2020 (1986).
[21]A. E. Orel, T. N. Rescigno, B. V. McKoy, and P. W. Langhoff, J. Chem. Phys. **72**, 1265 (1980).
[22]R. R. Lucchese, G. Raseev, and V. McKoy, Phys. Rev. A **25**, 2572 (1982).
[23]R. R. Lucchese, K. Takatsuka, and V. McKoy, Phys. Rep. **131**, 147 (1986).
[24]M. Braunstein and V. McKoy, J. Chem. Phys. **87**, 224 (1987).
[25]T. H. Dunning and P. J. Hay, in *Modern Theoretical Chemistry*, edited by H. F. Schaefer III (Plenum, New York, 1976), Vol. 3, Chap. 1.
[26]J. Andzelm, M. Klobukowski, E. Radzio-Andzelm, Y. Sakai, and H. Tatewaki, in *Gaussian Basis Sets for Molecular Calculations*, edited by S. Huzinaga (Elsevier, Amsterdam, 1984).
[27]A. B. Cornford, D. C. Frost, C. A. McDowell, J. L. Ragle,. and I. A. Stenhouse, J. Chem. Phys. **54**, 2651 (1971).
[28]A. W. Potts and W. C. Price, Trans. Faraday Soc. **67**, 1242 (1971).
[29]J. L. Dehmer and D. Dill, J. Chem. Phys. **65**, 5327 (1976); G. Raseev, H. Le Rouzo, and H. Lefebvre-Brion, *ibid.* **72**, 5701 (1980).
[30]A. Gerwer, C. Asaro, B. V. McKoy, and P. W. Langhoff, J. Chem. Phys. **72**, 713 (1980); P. M. Dittman, D. Dill, and J. L. Dehmer, *ibid.* **76**, 5703 (1982); T. Gustafsson, Chem. Phys. Lett. **75**, 505 (1980).
[31]See, for example, J. L. Dehmer, A. C. Parr, and S. H. Southworth, in *Handbook on Synchrotron Radiation*, edited by G. V. Marr (North-Holland, Amsterdam, 1986), Vol. II.
[32]D. Loomba, S. Wallace, and D. Dill, J. Chem. Phys. **75**, 4546 (1981).
[33]V. H. Dibeler, J. A. Walker, K. E. McCulloh, and H. M. Rosenstock, Int. J. Mass Spectrom. Ion Phys. **7**, 209 (1971).
[34]R. J. Stubba, T. A. York, and J. Comer, J. Phys. B **18**, 3229 (1985).
[35]J. Berkowitz, C. A. Mayhew, and B. Ruscic, Chem. Phys. **123**, 317 (1988).

Chapter 13

Molecular K-shell photoionization cross sections in the relaxed core Hartree-Fock approximation

(The text of this chapter appeared in: J. Schirmer, M. Braunstein, and V. McKoy, Phys. Rev. A **41** 283 (1990).)

Molecular K-shell photoionization cross sections in the relaxed-core Hartree-Fock approximation

J. Schirmer,* M. Braunstein, and V. McKoy
Arthur Amos Noyes Laboratory of Chemical Physics, California Institute of Technology, Pasadena, California 91125
(Received 30 May 1989)

The relaxed-core Hartree-Fock (RCHF) approach to the calculation of K-shell photoionization cross sections is analyzed and applied to K-shell single-hole ionization in CO. A direct method based on the Schwinger variational principle and single-center-expansion techniques is used to generate the continuum orbitals associated with the motion of the photoelectron in the direct and exchange potential of the relaxed ion. A method is presented for evaluating the N-electron transition moment, a step that has posed a considerable computational obstacle due to the lack of orthogonality between the frozen and relaxed orbitals in the initial and final N-electron states, respectively. Besides being very practical and efficient, this formulation establishes the distinction between the "direct" and "conjugate" part of the transition moment, introducing bound-free dipole and overlap integrals, respectively. Whereas for large photoelectron energies the conjugate terms can be neglected, they become important near threshold, contributing, for example, up to 30% to the $1s$ cross sections in CO. An analysis by means of low-order perturbation theory shows that the RCHF model correctly describes the effect of ionic relaxation, that is, essentially the screening of the $1s$ hole by the valence electrons. As a consequence the σ^* shape resonance is substantially shifted to higher energy and broadened compared with the frozen-core Hartree-Fock picture where the more attractive unscreened $1s$-hole potentials are used. The remaining discrepancies with the experimental results are attributed to the neglect of target polarization in the RCHF model.

I. INTRODUCTION

Photoionization of atoms or molecules with sufficiently energetic photons generates highly excited ionic states characterized by a K-shell electron vacancy.[1,2] The dominant process is the ejection of a single $1s$ electron reflected by a main peak in the photoelectron spectrum. Smaller peaks or satellites appearing at higher ionization energy are associated with shake-up (or shake-off) processes, where, in addition to the $1s$ hole, one or more valence electrons are excited.[2,3] Typically, 30–40 % of the $1s$-photoionization cross section may be diverted to these shake-up (shake-off) states. Prominent satellites states at low energy with intensities up to 10% of that of the main peak arise from the π-π^* excitations in simple unsaturated molecules like N_2 and CO.[3]

The availability of tunable synchrotron radiation has made it possible to study the dynamics of the photoionization process, that is, to map the spectral intensities (partial photoionization cross sections) of individual ionic states as a function of photon energy.[4] In the K-shell region several such studies have been carried out for the $1s$-hole main state of atoms[5] and molecules.[6,7] In the case of N_2 and CO, previously studied by electron energy loss[8] and photoabsorption spectroscopy,[9–11] the most conspicuous feature in the molecular photoelectron spectrum is the occurrence of σ-type shape resonances. In the case of K-shell satellites, where the lower intensities make experiments more difficult, synchrotron-radiation studies have been performed for the noble-gas atoms He and Ar (Ref. 5) and the CO molecule.[12]

A common feature of several approaches[13–15] used in theoretical studies of molecular photoionization is that the photoelectron continuum is determined by a single-particle (Hartree-Fock) equation with a suitably chosen potential for the electron-ion interaction. To date most applications have adopted the frozen-core Hartree-Fock (FCHF) model. In this approximation the neutral-molecule ground-state Hartree-Fock (HF) orbitals are assumed for both the initial and the final ionic states, and corresponding potentials defining the motion of the photoelectron in the field of the ion can readily be derived. The FCHF model neglects both the effects of relaxation, that is, the adjustment of the other electrons to the presence of the hole, and correlation.

Relaxation is particularly important in the case of K-shell ionization, often exceeding by far correlation corrections. Almost all previous studies of K-shell photoionization of molecules have been carried out in the FCHF approximation.[16–19] While these studies proved quite successful in establishing and clarifying the occurrence of σ-type shape resonances in the K-shell single-hole photoionization cross section, the agreement with experimental resonance positions and widths was often less than satisfactory. Recently, Lynch and McKoy[20] used a relaxed-core Hartree-Fock (RCHF) model to study the resonant K-shell photoionization cross section in N_2. In this model the ionic state and the associated potential are expressed in terms of the "relaxed" orbitals generated by a separate HF calculation for the ionic state. This RCHF potential accounts for screening of the $1s$ hole by the relaxation of the valence orbitals and is hence less attractive than the unscreened FCHF potential, leading to shifts of the resonance positions to higher energy.

Indeed, for the N_2 K shell[20] the RCHF resonance position was 7–8 eV higher than the FCHF result and 3–4 eV above the experimental position. Furthermore, the broadening of the resonance in the RCHF description results in better agreement with the experimental cross sections than seen in the FCHF model.

Although the RCHF approximation maintains the simplicity of a single-particle model, the absence of orbital orthogonality introduces several complications into its application. First, in contrast to the FCHF case, the variational principle used to derive the ion-electron scattering equation does not impose orthogonality between the continuum and the relaxed open-shell orbital, resulting in a significantly more complicated equation for the continuum electron. Fortunately, this problem is not acute in the case of K-shell (main) ionization since, to a good approximation, the $1s$-continuum nonorthogonality can be neglected. As we shall see, this is a consequence of the core-valence separation (CVS) associated with the large energy difference of K-shell and valence levels and of the weak coupling matrix elements for states with different K-shell occupation numbers. Secondly, the initial and final N-electron states are formulated in terms of mutually nonorthogonal sets of "relaxed" and "frozen" orbitals, complicating the evaluation of the N-electron transition moment. As a result the initial ground and final excited N-electron states lack strict orthogonality which introduces a dependence of the transition-moment matrix element on the origin of the molecular coordinate frame. This is clearly an artifact of the RCHF model. For K-shell ionization we will show that the CVS approximation can be used to eliminate in a well-defined manner these unphysical contributions. The remaining nonorthogonality contributions to the RCHF transition moment are, of course, meaningful and establish the improved level of description compared with the FCHF approximation.

Nonorthogonality of the relaxed continuum orbital and the frozen ground-state orbitals gives rise to specific contributions in the RCHF transition moment that contain continuum-bound overlap integrals.[21] This contribution to the transition moment, referred to as the "conjugate" part,[21,22] may be distinguished from the "direct" part containing continuum-bound dipole integrals. Obviously the relative importance of these two contributions depends on the photoelectron energy. In the high-energy or "sudden" limit[23] the overlap integrals vanish much more rapidly than the dipole integrals and the transition moment is determined by the direct part. On the other hand, for low energies, the overlap contributions could become appreciable and substantially affect the photoionization cross section. The effect of these conjugate contributions may be more significant for satellite intensities than for single-hole cross sections, since selection rules for these differ from those of the direct part.[21,22] As a consequence, satellites not detected at high photon energy might appear in a spectrum taken at near-threshold energy. Possible candidates for "conjugate shake-up" are, for example, the $2p$-$3s$ ^2P satellites in the Ne $1s$ photoelectron spectrum.[5]

To our knowledge, the role of the conjugate contribution in molecular photoionization cross sections has never been investigated very quantitatively. Even for atoms, where more sophisticated methods are available[24] the nature of these conjugate contributions is not fully understood. The striking discrepancy between theory and experiment seen in the Ne $1s$ satellites referred to above serves as an example.[5,25]

The present study continues the previous work[20] on molecular K-shell ionization in the framework of the RCHF model. We present an alternative approach for evaluating the central quantity, i.e., the N-electron transition amplitude between the frozen ground and relaxed final states. The resulting expressions for both the single-hole and satellite states of the ion are more transparent and practical than the biorthogonal orbital formulations used previously.[20] They allow us, in particular, to analyze and calculate separately the direct and conjugate contributions to the transition amplitudes and photoionization cross sections. The case of K-shell ionization of CO has been chosen for the present numerical studies. This choice focuses directly on K-shell relaxation and avoids possible complications arising from hole localization. In the present study we confine ourselves to the single-hole (main) states. Results for the $1s$ satellites will be reported in a forthcoming publication.[26]

An outline of this paper is as follows. Section II discusses our formulation of the photoionization amplitudes in the RCHF model and the CVS approximation. The choice of single-particle scattering potentials to determine the photoelectron continua is reviewed in Sec. III. In Sec. IV we analyze the energies (resonance positions) and cross sections in the RCHF description in the framework of (low-order) perturbation theory. The computational details are given in Sec. V, while Sec. VI contains the discussion of our results and comparison to experiment. A summary of our findings and conclusions are given in Sec. VII.

II. PHOTOIONIZATION CROSS SECTIONS IN THE FROZEN AND RELAXED HARTREE-FOCK APPROXIMATIONS

A. Final-state wave function

The partial photoionization cross section at a photon energy ω leading to an ionic state $|\Psi_n^{N-1}\rangle$ and a photoelectron with kinetic energy $k^2/2$ is given by the familiar golden-rule expression (in atomic units):

$$\sigma_n(\omega)=\frac{4\pi^2}{3c}\omega\sum_{\mu,\lambda,\nu}|\langle\Psi^N_{n\nu,k\lambda}|\hat{D}^{(\mu)}|\Psi^N_0\rangle|^2 . \tag{1}$$

Here $|\Psi^N_{n\nu,k\lambda}\rangle$ represents the final N-electron state describing asymptotically the ion in the state $|\Psi^{N-1}_{n\nu}\rangle$ and a photoelectron in the state $|k\lambda\rangle$. The additional quantum numbers ν and λ specify degeneracies not observed in the experiment, e.g., magnetic spin quantum numbers, and angular momentum of the photoelectron. A nondegenerate initial (ground state) $|\Psi^N_0\rangle$ is assumed in Eq. (1), and $\hat{D}^{(\mu)}$, $\mu=x,y,z$ denotes the components of the N-electron dipole operator

$$\hat{D}=\sum_{i=1}^{N} r^{(i)} . \tag{2}$$

Energy conservation requires $k^2/2=\omega-E_n^{N-1}+E_0^N$, where E_0^N and E_n^{N-1} are the energies of the initial ground state and the final ionic state, respectively. Rotational and vibrational degrees of freedom are suppressed in Eq. (1) and a fixed nuclear geometry is assumed for all electronic states.

To disentangle the many-body and continuum aspects in evaluating the bound-free N-electron transition amplitude

$$A_{n\nu,k\lambda}^{(\mu)}=\langle \Psi_{n\nu,k\lambda}^N|\hat{D}^{(\mu)}|\Psi_0^N\rangle , \tag{3}$$

a product approximation is normally assumed for the final state and $|\Psi_{n\nu,k\lambda}^N\rangle$ is written as the antisymmetrized product

$$|\Psi_{n\nu,k\lambda}^N\rangle=c_{k\lambda}^\dagger|\Psi_{n\nu}^{N-1}\rangle \tag{4}$$

of the ionic state $|\Psi_{n\nu}^{N-1}\rangle$ and the one-electron scattering orbital $|\psi_{k\lambda}^{(-)}\rangle$ (with incoming-wave boundary conditions). In Eq. (4) we use the second-quantized notation, where $c_{k\lambda}^\dagger$ represents the creation operator associated with the continuum orbital $|\psi_{k\lambda}^{(-)}\rangle$. The form of Eq. (1) for the cross section assumes the final states to be normalized by

$$\langle \Psi_{n\nu}^{N-1}|c_{k\lambda}c_{k'\lambda}^\dagger|\Psi_{n\nu}^{N-1}\rangle=\delta\left[\frac{k'^2}{2}-\frac{k^2}{2}\right] . \tag{5}$$

To proceed we may insert the second-quantized representation of the dipole operator in Eq. (3) and make use of the commutation relations for (fermion) operators. For this purpose we use a representation in terms of neutral ground-state (frozen) Hartree-Fock orbitals $|\phi_i\rangle$ and the associated operators $a_i^\dagger$ (a_i):

$$\hat{D}^{(\mu)}=\sum_i \langle \phi_i|\hat{d}^{(\mu)}|\phi_j\rangle a_i^\dagger a_j . \tag{6}$$

Since c_k may be expressed as

$$c_k=\sum_i \langle \psi_k^{(-)}|\phi_i\rangle a_i , \tag{7}$$

in terms of the operators a_i, the expression for the transition amplitude can be written[21,27,28]

$$\begin{aligned} A_{n,k}&=\langle \Psi_n^{N-1}|c_k\hat{D}|\Psi_0^N\rangle \\ &=\sum_r \langle \psi_k^{(-)}|\hat{d}|\phi_r\rangle\langle \Psi_n^{N-1}|a_r|\Psi_0^N\rangle \\ &\quad+\sum_r \langle \psi_k^{(-)}|\phi_r\rangle\langle \Psi_n^{N-1}|\hat{D}a_r|\Psi_0^N\rangle . \end{aligned} \tag{8}$$

Here and in the following the additional quantum numbers ν and λ and the specification μ of the dipole operator are suppressed whenever they are not essential. According to Eq. (8), $A_{n,k}$ is the sum of two distinct parts $A_{n,k}^{\mathrm{I}}$ and $A_{n,k}^{\mathrm{II}}$. The first part $A_{n,k}^{\mathrm{I}}$, referred to as the direct part, combines the one-electron dipole matrix elements $\langle \psi_k^{(-)}|\hat{d}|\phi_r\rangle$ with the so-called spectroscopic amplitudes

$$x_r^{(n)}=\langle \Psi_n^{N-1}|a_r|\Psi_0^N\rangle . \tag{9}$$

The second term, on the other hand, contains products of the bound-continuum overlap integrals $\langle \psi_k^{(-)}|\phi_r\rangle$ and the bound-bound transition integrals

$$y_r^{(n)}=\langle \Psi_n^{N-1}|\hat{D}a_r|\Psi_0^N\rangle . \tag{10}$$

This contribution is the conjugate or nonorthogonality part;[21,22] it only gives a contribution if the continuum orbital $|\psi_k^{(-)}\rangle$ is not "orthogonal" to $|\Psi_0^N\rangle$, i.e., $\langle \Psi_0^N|c_k^\dagger c_k|\Psi_0^N\rangle\neq 0$. It is interesting to note that the direct and conjugate amplitudes impose different selection rules among the molecular orbitals, i.e., dipole and monopole rules, respectively. The energy dependence of the conjugate amplitude has not been directly calculated previously and should provide new insight into K-shell photoionization, especially in the context of satellite intensities. If the HF ground state

$$|\Phi_0^N\rangle=|\phi_1\cdots\phi_N| \tag{11}$$

is taken as the initial state, then the summation on the right-hand side of Eq. (8) runs over occupied orbitals ($n_r=1$) only. If allowance for ground-state correlation is made, unoccupied orbitals ($\bar{n}_r=1-n_r=1$) may also give contributions.

The simplest and most widely used approximation for the transition amplitudes of Eq. (8) is the frozen-core Hartree-Fock model. Here, besides using the HF approximation $|\Phi_0^N\rangle$ for the ground state, the ionic states are also expressed in terms of the "frozen" HF orbitals of the neutral ground state. Specifically, the states

$$|\Phi_h^{N-1}\rangle=a_h|\Phi_0^N\rangle, \quad n_h=1 \tag{12a}$$

and

$$|\Phi_{jhl}^{N-1}\rangle=a_j^\dagger a_h a_l|\Phi_0^N\rangle, \quad \bar{n}_j n_h n_l=1 \tag{12b}$$

are used to represent a single-hole (main) and a two-hole–one-particle ($2h$-$1p$) satellite state, respectively. Consistently defined "frozen" potentials (see Sec. III) are used to determine the continuum orbitals $|\psi_k^{(-)}\rangle$. These FCHF potentials impose orthogonality constraints[10]

$$\langle \psi_k^{(-)}|\phi_r\rangle=0, \quad n_r=1$$

between the continuum and the occupied HF orbitals, and consequently the conjugate part of the transition amplitude vanishes. For a single-hole (main) state the spectroscopic amplitudes of Eq. (9) are trivial,

$$x_r^{(h)}=\langle \Phi_0^N|a_h^\dagger a_r|\Phi_0^N\rangle=\delta_{hr} , \tag{13}$$

so that the transition amplitude reduces to

$$A_{hk}=\langle \psi_k^{(-)}|\hat{d}|\phi_h\rangle . \tag{14}$$

For satellite states [Eq. (12b)] the FCHF model cannot be used, since both parts of the amplitude $A_{jhl,k}$ vanish. For the direct part this is so because the spectroscopic amplitudes vanish

$$x_r^{(jhl)}=\langle \Phi_0^N|a_l^\dagger a_h^\dagger a_j a_r|\Phi_0^N\rangle=0 . \tag{15}$$

For the conjugate part, on the other hand, we find nonvanishing moments,

$$y_r^{(jhl)} = \langle \Phi_0^N | a_l^\dagger a_h^\dagger a_j \hat{D} a_r | \Phi_0^N \rangle$$
$$= \delta_{rl} \langle \phi_j | \hat{d} | \phi_h \rangle - \delta_{rh} \langle \phi_j | \hat{d} | \phi_l \rangle \ . \quad (16)$$

However, the bound-free overlap integrals $\langle \psi_k^{(-)} | \phi_r \rangle$ vanish.

In the framework of many-body perturbation theory the FCHF model may be viewed as the zeroth-order approximation to the transition amplitudes (see Sec. IV B). Obviously one has to go beyond this level of description to account for relaxation and correlation. If one is only interested in the bound-bound amplitudes x_r and y_r one may, of course, resort to the well-developed methods of quantum chemistry. For the spectroscopic amplitudes x_r direct computational schemes based on the one-particle Green's function have been widely applied.[29] In the present study, rather than trying to obtain more accurate bound-bound amplitudes we are interested in a consistent treatment of the many-body and continuum aspects of the problem. Such a level of description, which goes beyond the FCHF model but maintains the essential simplifications of the single-particle picture, is provided by the relaxed-core Hartree-Fock approximation, discussed in Sec. II B.

B. Spectroscopic amplitudes and conjugate transition moments in the RCHF approximation

In the RCHF approximation distinct HF wave functions are used for the initial ground state and the final ionic state; a consistent relaxed ion core potential is used to determine the photoelectron continuum (see Sec. III). The lack of orthogonality between the frozen-core and relaxed-core HF orbitals leads to obvious complications. In the following we present a transparent and tractable approach allowing us, in particular, to distinguish readily between direct and conjugate contributions to the photoionization cross sections.

In addition to the FCHF orbitals $|\phi_l\rangle$ and the corresponding creation (destruction) operators $a_l^\dagger$ (a_l) considered in Sec. II A, we now introduce the set of relaxed orbitals $|\psi_l\rangle$ generated by an appropriate HF calculation for the ion. Denoting the associated creation (destruction) operators by $c_l^\dagger$ (c_l), the RCHF representation of a single-hole (main) state is

$$|\Psi_h^{N-1}\rangle = c_h |\bar{\Phi}_0^N\rangle, \quad n_h \doteq 1 \quad (17)$$

where

$$|\bar{\Phi}_0^N\rangle = |\psi_1 \cdots \psi_N| \quad (18)$$

is defined in analogy to $|\Phi_0^N\rangle$ as the Slater determinant of the lowest N relaxed orbitals $|\psi_l\rangle$. To obtain the spectroscopic amplitude $x_r^{(h)}$ for the single-hole state of Eq. (17) and the uncorrelated ground state $|\Phi_0^N\rangle$ we have to evaluate the overlap integral between the two $(N-1)$-electron states $c_h|\bar{\Phi}_0^N\rangle$ and $a_r|\Phi_0^N\rangle$ represented by Slater determinants of mutually nonorthogonal sets of orbitals. As shown in the Appendix the result simply is

$$x_r^{(h)} = \langle \bar{\Phi}_0^N | c_h^\dagger a_r | \Phi_0^N \rangle = (\underline{S}^{-1})_{rh} \langle \bar{\Phi}_0^N | \Phi_0^N \rangle n_r \ . \quad (19)$$

Here, $\underline{S}$ denotes the $N \times N$ matrix of the "relaxed-frozen" overlap integrals

$$S_{ij} = \langle \psi_i | \phi_j \rangle, \quad n_i = n_j = 1 \quad (20)$$

$$\langle \bar{\Phi}_0^N | \Phi_0^N \rangle = \det \underline{S} \ . \quad (21)$$

Similarly, one finds for the conjugate transition moment

$$y_r^{(h)} = \langle \bar{\Phi}_0^N | c_h^\dagger \hat{D} a_r | \Phi_0^N \rangle$$
$$= [-(\underline{S}^{-1} \underline{d} \, \underline{S}^{-1})_{rh}$$
$$+ (\underline{S}^{-1})_{rh} \mathrm{Tr}(\underline{d} \, \underline{S}^{-1})] \langle \bar{\Phi}_0^N | \Phi_0^N \rangle n_r \ , \quad (22)$$

where $\underline{d}$ denotes the $N \times N$ matrix of dipole integrals

$$d_{ij} = \langle \psi_i | \hat{d} | \phi_j \rangle, \quad n_i = n_j = 1 \quad (23)$$

for the occupied relaxed and frozen orbitals, and $\mathrm{Tr}(\underline{a})$ is the trace of $\underline{a}$. We note in passing that transition moments of this type are also encountered in the HF description of x-ray emission intensities. The final result for the single-hole state photoionization amplitude in the RCHF approximation is

$$A_{h,k} = \sum_r \{ \langle \psi_k^{(-)} | \hat{d} | \phi_r \rangle (\underline{S}^{-1})_{rh}$$
$$+ \langle \psi_k^{(-)} | \phi_r \rangle [-(\underline{S}^{-1} \underline{d} \, \underline{S}^{-1})_{rh}$$
$$+ (\underline{S}^{-1})_{rh} \mathrm{Tr}(\underline{d} \, \underline{S}^{-1})] \} \langle \bar{\Phi}^N | \Phi_0^N \rangle . \quad (24)$$

To identify clearly the major contributions in Eq. (24) we consider the simplified amplitude obtained by setting $\underline{S} = \underline{1}$ and $d_{ij} = \langle \phi_i | \hat{d} | \phi_j \rangle$:

$$A_{h,k} \approx \langle \psi_k^{(-)} | \hat{d} | \phi_h \rangle - \sum_r \langle \psi_k^{(-)} | \phi_r \rangle \langle \phi_r | \hat{d} | \phi_h \rangle n_r$$
$$+ \langle \psi_k^{(-)} | \phi_h \rangle \sum_i \langle \phi_i | \hat{d} | \phi_i \rangle n_i \ . \quad (25)$$

The "diagonal" term in Eq. (25) depends on the origin of the molecular coordinates. As discussed in Sec. II C, this is due to spurious contributions which arise from the lack of strict orthogonality between the initial ground and the final excited state.

The $2h$-$1p$ satellite states are given in the RCHF approximation by

$$|\Psi_{jhl}^{N-1}\rangle = c_j^\dagger c_h c_l |\bar{\Phi}_0^N\rangle, \quad \bar{n}_j n_h n_l = 1 \ . \quad (26)$$

The corresponding spectroscopic amplitudes $x_r^{(jhl)}$ and conjugate transition moments $y_r^{(jhl)}$ can be obtained analogously to the case of single-hole states (see Appendix). The resulting expressions are

$$x_r^{(jhl)} = \langle \bar{\Phi}_0^N | c_l^\dagger c_h^\dagger c_j a_r | \Phi_0^N \rangle$$
$$= \Big\{ [(\underline{S}^{-1})_{rl} \sum_u \langle \psi_j | \phi_u \rangle \underline{S}_{uh}^{-1}]$$
$$- [h \leftrightarrow l] \Big\} \langle \bar{\Phi}_0^N | \Phi_0^N \rangle n_r \quad (27)$$

and

$$y_r^{(jhl)} = \langle \bar{\Phi}_0^N | c_l^\dagger c_h^\dagger c_j \hat{D} a_r | \Phi_0^N \rangle$$
$$= \Big[\Big[(\underline{S}^{-1})_{rl} \sum_u \langle \psi_j | \hat{d} | \phi_u \rangle (\underline{S}^{-1})_{uh} + (\underline{S}^{-1} \underline{d} \, \underline{S}^{-1})_{rh} \sum_u \langle \psi_j | \phi_u \rangle (\underline{S}^{-1})_{ul}$$
$$+ (\underline{S}^{-1})_{rl} \sum_{u,v} \langle \psi_j | \phi_u \rangle (\underline{S}^{-1})_{uv} [\mathrm{Tr}(\hat{d} \underline{S}^{-1}) \underline{1} - \underline{d} \, \underline{S}^{-1}]_{vh} \Big] - [h \leftrightarrow l] \Big] \langle \bar{\Phi}_0^N | \Phi_0^N \rangle n_r \,, \tag{28}$$

where $[h \leftrightarrow l]$ means repeating the preceding terms, but with h and l indices interchanged. Here, besides the occupied orbital overlap and dipole matrices $\underline{S}$ and $\underline{d}$, the overlap $\langle \psi_j | \phi_r \rangle$ and dipole $\langle \psi_j | \hat{d} | \phi_r \rangle$ integrals are required for the relaxed (unoccupied) orbital $|\psi_j\rangle$ of the satellite state and the frozen occupied orbitals $|\phi_r\rangle$, $r \le N$. Again, the dominant direct and conjugate contributions to the satellite amplitude $A_{jhl,k}$ become apparent in the (zeroth-order) approximation $\underline{S} = \underline{1}$ and $d_{ij} = \langle \phi_i | \hat{d} | \phi_j \rangle$:

$$A_{jhl,k} = \Big[\langle \psi_k^{(-)} | \hat{d} | \phi_l \rangle \langle \psi_j | \phi_h \rangle + \langle \psi_k^{(-)} | \phi_l \rangle \langle \psi_j | \hat{d} | \phi_h \rangle + \sum_r \langle \psi_k^{(-)} | \phi_r \rangle \langle \phi_r | \hat{d} | \phi_h \rangle \langle \psi_j | \phi_l \rangle n_r$$
$$- \langle \psi_k^{(-)} | \phi_l \rangle \sum_r \langle \psi_j | \phi_r \rangle \langle \phi_r | \hat{d} | \phi_h \rangle n_r + \langle \psi_k^{(-)} | \phi_l \rangle \langle \psi_j | \phi_h \rangle \sum_i \langle \phi_i | \hat{d} | \phi_i \rangle n_i \Big] - [h \leftrightarrow l] \,. \tag{29}$$

It should be noted that the more intuitively derived expression for the conjugate shake-up amplitude[22]

$$A^{II} = \langle \psi_k^{(-)} | \phi_l \rangle \langle \psi_j | \hat{d} | \phi_h \rangle - \langle \psi_k^{(-)} | \phi_h \rangle \langle \psi_j | \hat{d} | \phi_l \rangle \tag{30}$$

represents only a part of the conjugate contribution in Eq. (29).

C. Nonorthogonality of initial and final states

Complications arise in the RCHF approximation due to the lack of strict orthogonality between the N-electron ground state $|\Phi_0^N\rangle$ and the final (excited) states $c_k^\dagger c_h |\bar{\Phi}_0^N\rangle$ or $c_k^\dagger c_j^\dagger c_h c_l |\bar{\Phi}_0^N\rangle$, respectively. In the case of a single-hole ionic core the overlap integral may be evaluated as follows:

$$\langle \bar{\Phi}_0^N | c_h^\dagger c_k | \Phi_0^N \rangle = \sum_r \langle \psi_k^{(-)} | \phi_r \rangle x_r^{(h)} \,, \tag{31a}$$

where the spectroscopic amplitudes $x_r^{(h)}$ are specified by Eq. (19). Similarly we find

$$\langle \bar{\Phi}_0^N | c_k c_j c_h^\dagger c_l^\dagger | \Phi_0^N \rangle = \sum_r \langle \psi_k^{(-)} | \phi_r \rangle x_r^{(jhl)} \,, \tag{31b}$$

in the case of a $2h$-$1p$ satellite; the spectroscopic amplitudes $x_r^{(jhl)}$ are given by Eq. (27). As a consequence of this nonorthogonality the dipole transition amplitudes $A_{n,k}$ [Eq. (3)] depend on the choice of origin of the molecular coordinate frame. In our explicit RCHF expressions [Eqs. (24), (25), and (27)–(29)] this becomes apparent through the occurrence of origin-dependent integrals such as $\langle \psi_k^{(-)} | \hat{d} | \phi_r \rangle$ or $\langle \psi_r | \hat{d} | \phi_r \rangle$. Clearly such contributions bear no physical meaning and are a mere artifact of the RCHF model. How can one distinguish between these artificial contributions to the transition amplitude and the genuine conjugate contributions in the RCHF approximation? In general, the answer is by no means clear. In the case of K-shell ionization, however, on which we shall focus here, the artificial nonorthogonality contributions can be discarded in a well-defined way as discussed in Sec. II D.

D. Core-valence separation approximation

Specialization to the case of K-shell ionization allows for a considerable simplification of the RCHF transition amplitudes. This is achieved by adopting the so-called core-valence separation approximation in which one neglects the coupling of states with different $1s$ occupations. Formally this decoupling is introduced by neglecting the following types of Coulomb integrals:[30]

$$V_{cvv'v''} = V_{vcv'v''} = \cdots = 0 \,,$$
$$V_{cc'c''v} = V_{cc'vc''} = \cdots = 0 \,, \tag{32}$$
$$V_{cc'vv'} = V_{vv'cc'} = 0 \,,$$

where c, c', and c'' and v, v', and v'' label K-shell and valence orbitals, respectively. The errors introduced here in the wave functions and energies are of the order of $V/\Delta\varepsilon$ and $V^2/\Delta\varepsilon$, respectively, where V stands for one of the neglected Coulomb integrals (32) and $\Delta\varepsilon$ is the core-valence energy separation. To see the effect of the core-valence separation on the RCHF amplitudes, consider the relaxed core orbital $|\psi_c\rangle$. The perturbation expansion of $|\psi_c\rangle$ in terms of the frozen orbitals $|\phi_r\rangle$ through first order,

$$|\psi_c\rangle = |\phi_c\rangle + \sum_{r \neq c} \frac{\gamma V_{cccr}}{\varepsilon_c - \varepsilon_r} |\phi_r\rangle + O(2) \,, \tag{33}$$

shows that the relaxed orbital differs from the frozen one by the admixture of valence orbitals, the mixing coefficients being of the order of $V_{cccr}/(\varepsilon_r - \varepsilon_c)$. In Eq. (33) γ is a constant, depending on the specific RCHF treatment. Obviously, in the CVS approximation, the relaxed- and frozen-core orbitals are identical (up to an eventual phase factor) leading to the following simplifications for the relaxed-frozen overlap integrals:

$$|\langle \psi_c | \phi_c \rangle| = 1 \,, \tag{34a}$$
$$\langle \psi_r | \phi_c \rangle = 0, \quad r \neq c \tag{34b}$$
$$\langle \psi_k^{(-)} | \phi_c \rangle = 0 \,. \tag{34c}$$

An immediate consequence of the CVS approximation is that the initial-final state overlaps in Eqs. (31a) and (31b), vanish, and there are no longer artificial contributions in the transition amplitudes. Applying the CVS approximation Eq. (34) to the amplitude $A_{c,k}$ for a K-shell single-

hole state c^{-1}, the RCHF result of Eq. (24) becomes

$$A_{c,k}=\left[\langle\psi_k^{(-)}|\hat{d}|\phi_c\rangle-\sum_{r,r'}\langle\psi_k^{(-)}|\phi_r\rangle(\underline{S}^{-1})_{r,r'}\times\langle\psi_{r'}|\hat{d}|\phi_c\rangle\right]\langle\bar{\Psi}_0^N|\Phi_0^N\rangle\ . \tag{35}$$

as can be readily shown, the quantity

$$\hat{P}=\sum_{r,r'}|\phi_r\rangle(\underline{S}^{-1})_{r,r'}\langle\psi_{r'}| \tag{36}$$

is a non-Hermitian projection operator, and using this definition the amplitude $A_{c,k}$ may be written as

$$A_{c,k}=\langle\psi_k^{(-)}|(1-\hat{P})\hat{d}|\phi_c\rangle\langle\bar{\Phi}_0^N|\Phi_0^N\rangle\ . \tag{37}$$

Comparing this result with the direct amplitude,

$$A_{c,k}^{\mathrm{I}}=\langle\psi_k^{(-)}|\hat{d}|\phi_c\rangle\langle\bar{\Phi}_0^N|\Phi_0^N\rangle\ , \tag{38}$$

we see that the effect of the conjugate contribution is to project out a certain part of the continuum orbital, namely, its occupied frozen-orbital components, as can be seen from the zeroth-order approximation to the projector [Eq. (36)],

$$\hat{P}^{(0)}=\sum_r|\phi_r\rangle\langle\phi_r|n_r\ . \tag{39}$$

A further understanding of the contributions to the RCHF amplitude will be gained from the perturbation point of view given in Sec. IV B.

In the case of a $2h$-$1p$ satellite (j^1,c^{-1},l^{-1}) where c denotes a core orbital, the general RCHF result [Eqs. (8), (27), and (28)] simplifies considerably in the CVS approximation [Eq. (34)] and the final result for the amplitude $A_{jcl,k}$ can be put into the compact form

$$A_{jcl,k}=[-\langle\psi_k^{(-)}|(1-\hat{P})\hat{d}|\phi_c\rangle\langle\psi_j|\phi_l\rangle^{\mathrm{eff}}+\langle\psi_j|(1-\hat{P})\hat{d}|\phi_c\rangle\langle\psi_k^{(-)}|\phi_l\rangle^{\mathrm{eff}}]\langle\bar{\Phi}_0^N|\Phi_0^N\rangle\ . \tag{40}$$

Here $\hat{P}$ is given by Eq. (36) and the "effective" overlaps are defined:

$$\langle\psi_j|\phi_l\rangle^{\mathrm{eff}}=\sum_r\langle\psi_j|\phi_r\rangle(\underline{S}^{-1})_{rl}\ , \tag{41a}$$

$$\langle\psi_k^{(-)}|\phi_l\rangle^{\mathrm{eff}}=\sum_r\langle\psi_k^{(-)}|\phi_r\rangle(\underline{S}^{-1})_{rl}\ . \tag{41b}$$

The direct amplitude above is given by

$$A_{jcl,k}^{\mathrm{I}}=\langle\psi_k^{(-)}|\hat{d}|\phi_c\rangle(-\langle\psi_j|\phi_l\rangle^{\mathrm{eff}}\langle\bar{\Phi}_0^N|\Phi_0^N\rangle)\ , \tag{42}$$

where the factor

$$x_c^{(jcl)}=-\langle\psi_j|\phi_l\rangle^{\mathrm{eff}}\langle\bar{\Phi}_0^N|\Phi_0^N\rangle \tag{43}$$

is readily identified as the spectroscopic satellite amplitude. Comparison of the direct and the full amplitudes clarifies the effect of the conjugate part: except for introducing the projection operator $\hat{P}$ in the direct part, there arises an additional term formally obtained by exchanging the role of j and k in the first ("effective" direct) part ($A_{jcl,k}^{\mathrm{I}}\rightarrow A_{kcl,j}^{\mathrm{I}}$). We may call this latter part the "effective" conjugate shake-up amplitude. It should be noted that the quantity

$$A_{c,j}=\langle\psi_j|(1-\hat{P})\hat{d}|\phi_c\rangle\langle\bar{\Phi}_0^N|\Phi_0^N\rangle \tag{44}$$

represents the transition moment for a bound K-shell single excitation (j^1c^{-1}) in the CVS approximation.

The expressions (35)–(40) for K-shell ionization amplitudes in the RCHF and CVS approximations are still in terms of (primitive) spin-orbital representations. The construction of spin-free equations for ionic states of proper spatial and spin symmetry is straightforward. The resulting expression for the 1s-hole main state in the 1s photoionization of CO will be given in Sec. V. The case of K-shell satellites will be discussed in a forthcoming publication.[26]

III. POTENTIALS FOR K-SHELL PHOTOELECTRONS

Single-particle scattering equations may be derived from the variational expression[31]

$$\langle\delta\Psi^N|\hat{H}-E|\Psi^N\rangle=0\ , \tag{45}$$

where $|\Psi^N\rangle$ is an N-electron final state expressed in terms of target-state orbitals that are kept fixed and a continuum orbital $|\psi_k^{(-)}\rangle$ which is to be determined. Here the variation $|\delta\Psi^N\rangle$ arises from the variation of the continuum orbital $|\delta\psi_k\rangle$ only. In the FCHF model for the photoionization of a closed-shell molecule the final state (with $S=0$) corresponding to a single-hole ionic state

$$|\Phi_{h\gamma}^{N-1}\rangle=a_{h\gamma}|\Phi_0^N\rangle \tag{46a}$$

may be written as

$$|\Psi_{h,\mathbf{k}}^N\rangle=\frac{1}{\sqrt{2}}(a_{\mathbf{k}\alpha}^\dagger a_{h\alpha}+a_{\mathbf{k}\beta}^\dagger a_{h\beta})|\Phi_0^N\rangle\ , \tag{46b}$$

where the second-quantized notation introduced in Sec. II A is used and α and β are the usual spin states. The analogous RCHF state reads

$$|\Psi_{h,\mathbf{k}}^N\rangle=\frac{1}{\sqrt{2}}(c_{\mathbf{k}\alpha}^\dagger c_{h\alpha}+c_{\mathbf{k}\beta}^\dagger c_{h\beta})|\bar{\Phi}_0^N\rangle\ . \tag{46c}$$

In either case the result of the variation of Eq. (45) takes on the form[15]

$$\left[\hat{\tau}+\sum_{\substack{i\\ i\neq h}}(2\hat{J}_i-\hat{K}_i)n_i+\hat{J}_h+\hat{K}_h+E_0^N-\varepsilon_h-E\right]|\mathbf{k}\rangle+|h\rangle\langle h|\mathbf{k}\rangle(E_0^N-2\varepsilon_h+J_{hh}-E)+|h\rangle\left\langle h\left|\hat{\tau}+\sum_{\substack{i\\ i\neq h}}(2\hat{J}_i-\hat{K}_i)n_i\right|\mathbf{k}\right\rangle+\left[\hat{\tau}+\sum_{\substack{i\\ i\neq h}}(2\hat{J}_i-\hat{K}_i)n_i\right]|h\rangle\langle h|\mathbf{k}\rangle=0\ , \tag{47}$$

where the notation $|i\rangle$ applies to the frozen orbitals $|\phi_i\rangle$ or the relaxed orbitals $|\psi_i\rangle$, respectively. In Eq. (47) $\hat{t}$ represents the kinetic energy and the electron-nuclei attraction, $\hat{J}_i$ and $\hat{K}_i$ denote Coulomb and exchange operators associated with the orbitals $|i\rangle$. The energy ε_h of the open-shell orbitals is given by

$$\varepsilon_h = \left\langle h \left| \hat{t} + \sum_i (2\hat{J}_i - \hat{K}_i) n_i \right| h \right\rangle , \tag{48}$$

which still applies if $|h\rangle$ is not an eigenfunction of the inserted HF operator. Furthermore,

$$J_{hh} = \langle h|\hat{J}_h|h\rangle - \langle h|\hat{K}_h|h\rangle \tag{49}$$

is the Coulomb self-energy of the orbital $|h\rangle$ and

$$E_0^N = \langle N|\hat{H}|N\rangle \tag{50}$$

represents the (first-order) energy of the frozen ($|N\rangle = |\Phi_0^N\rangle$) or relaxed ($|N\rangle = |\bar{\Phi}_0^N\rangle$) N-electron ground state. In deriving Eq. (47) orthogonality was assumed between the continuum orbital $|\mathbf{k}\rangle$ and the doubly occupied orbitals $|r\rangle$, $n_r = 1$, $r \neq h$, but no such restriction with respect to the open-shell orbital $|h\rangle$ was imposed on $|\mathbf{k}\rangle$.

To discuss the complications introduced by the possible lack of orthogonality between the orbitals $|\mathbf{k}\rangle$ and $|h\rangle$ we project both sides of Eq. (47) on $|h\rangle$, yielding the equation

$$\left\langle h \left| \hat{t} + \sum_{\substack{i \\ i \neq h}} (2\hat{J}_i - \hat{K}_i) n_i + \hat{J}_h \right| \mathbf{k} \right\rangle + (E_0^N - \varepsilon_h - E)\langle h|\mathbf{k}\rangle = 0 . \tag{51}$$

In the FCHF model, since $|h\rangle$ is an eigenfunction of the (ground-state) HF operator, this equation reduces to[15]

$$0 = (E_0^N - E)\langle h|\mathbf{k}\rangle = (\varepsilon_h - \tfrac{1}{2}k^2)\langle h|\mathbf{k}\rangle , \tag{52}$$

where the second equation follows by writing the total energy E as

$$E = E_0^N - \varepsilon_h + \tfrac{1}{2}k^2 . \tag{53}$$

Obviously, Eq. (52) requires $\langle h|\mathbf{k}\rangle = 0$ for positive energies $\frac{1}{2}k^2$ and with this orthogonality constraint one obtains the familiar improved virtual orbital (IVO) equation[32]

$$\left[\hat{t} + \sum_{\substack{i \\ i \neq h}} (2\hat{J}_i - \hat{K}_i) n_i + \hat{J}_h + \hat{K}_h - \tfrac{1}{2}k^2 \right] |\mathbf{k}\rangle = 0 . \tag{54}$$

It should be noted that the orthogonality properties,

$$\langle \mathbf{k}|i\rangle = 0, \quad n_i = 1$$

are not automatically fulfilled by the solution of Eq. (54) but rather must be introduced as an additional constraint.

Turning to the case of the RCHF model we write the continuum function as

$$|\mathbf{k}\rangle = |\mathbf{k}'\rangle + \langle h|\mathbf{k}\rangle |h\rangle , \tag{55}$$

where $\langle h|\mathbf{k}'\rangle = 0$. Equation (51) can then be transformed to the following equation:

$$\langle h|\mathbf{k}\rangle = \frac{\left\langle h \left| \hat{t} + \sum_{\substack{i \\ i \neq h}} (2\hat{J}_i - \hat{K}_i) n_i + \hat{J}_h \right| \mathbf{k}' \right\rangle}{\varepsilon_h - \frac{1}{2}k^2} \tag{56}$$

for the bound-free overlap $\langle h|\mathbf{k}\rangle$. In general, the numerator on the right-hand side of Eq. (56) does not vanish and one is faced with the situation that the variational principle explicitly requires a nonvanishing overlap $\langle h|\mathbf{k}\rangle$. Besides the much more complicated coupled equations that may result from Eq. (47) for $|\mathbf{k}'\rangle$ and $\langle h|\mathbf{k}\rangle$, it is by no means clear how a properly normalized N-particle final state could be constructed in this case.

Fortunately, specialization to K-shell ionization allows one to get rid of these complications to a very good approximation. If $|h\rangle = |c\rangle$ is a K-shell orbital the absolute value of the denominator in Eq. (56) is of the order of the core-valence energy gap. The matrix elements appearing in the numerator are small since they are of the mixed core-valence type t_{cv} and $V_{cvv'v''}$. Hence only a very small error is introduced by setting $\langle h|\mathbf{k}\rangle = 0$, i.e., by adopting the strict core-valence separation approximation discussed in Sec. II D. Thus in the RCHF model of K-shell photoionization we may safely adopt the IVO Eq. (54).

IV. ANALYSIS OF THE RCHF MODEL

A. Resonance positions through second order of perturbation theory

In the FCHF description of shape-resonant K-shell photoionization the potential does not include the effect of screening of the 1s hole by the reorganization (relaxation) of the valence electrons. The FCHF potential is hence too attractive and the resulting resonance positions are usually several eV below the experimental values. A substantial shifting to higher energies has indeed been found by Lynch and McKoy[20] for the σ^* shape resonance in N_2 by allowing for electronic relaxation through the RCHF potential. While the shape of the resonance is now in much better agreement with the experiment the calculated resonance position lies a few eV above the experimental value. This discrepancy in resonance position was tentatively attributed to an "overscreening" introduced by the RCHF potential. To clarify this concept and to get a better understanding of the frozen- and relaxed-core approximations we compare the resonance energies in the FCHF and RCHF models with the exact result through second order of perturbation theory.

We specifically consider the energy E_{vc}^N of a singlet core excitation $|\Psi_{vc}^N\rangle$ obtained from the unperturbed singly excited state

$$|\Phi_{vc}^N\rangle = \frac{1}{\sqrt{2}}(a_{v\alpha}^\dagger a_{c\alpha} + a_{v\beta}^\dagger a_{c\beta})|\Phi_0^N\rangle . \tag{57}$$

Here $|v\rangle$ represents an unoccupied (valence) orbital, e.g., π^* or σ^*, and c a 1s orbital. The term value

$$R_v = E_{vc}^N - E_c^{N-1} , \tag{58}$$

i.e., the energy with respect to that of the 1s-hole state,

$$|\Psi_{c\gamma}^{N-1}\rangle \leftarrow a_{c\gamma}|\Phi_0^N\rangle ,$$

can be positive or negative. In the former case the term value is related to a resonance position, while in the latter it refers to the position of a bound state below the 1s-ionization threshold. All perturbation expansions used in the following are defined with respect to the ground-state HF representation.

Let us begin with the FCHF model. Here the term value R_v^{FC} is given by the eigenvalue ε_v^{FC} of the FCHF Eq. (54):

$$\hat{f}^{FC}|v^{FC}\rangle=\varepsilon_v^{FC}|v^{FC}\rangle\ . \tag{59}$$

The FCHF operator $\hat{f}^{FC}$ can be written as

$$\hat{f}^{FC}=\hat{f}_0-\hat{J}_c+2\hat{K}_c\ , \tag{60}$$

where

$$\hat{f}_0=\hat{t}+\sum_i(2\hat{J}_i-\hat{K}_i)n_i \tag{61}$$

is the ground-state HF operator. The form of the right-hand side of Eq. (61) makes the perturbation expansions for $|v^{FC}\rangle$ and ε_v^{FC} obvious:

$$|v^{FC}\rangle=|v\rangle+\sum_{\substack{q\\q\neq v}}\frac{-V_{vcqc}+2V_{vccq}}{\varepsilon_v-\varepsilon_q}\bar{n}_q|q\rangle+O(2)\ , \tag{62a}$$

$$R_v^{FC}=\varepsilon_v^{FC}=\varepsilon_v-J_{vc}+2K_{vc}+2K_{vc}+\sum_{\substack{q\\q\neq v}}\frac{(V_{vcqc}-2V_{vccq})^2\bar{n}_q}{\varepsilon_v-\varepsilon_q}+O(2)+O(3)\ . \tag{62b}$$

The direct part $(-J_{vc})$ of the first-order contribution to the orbital energy accounts for the lowering of the electrostatic repulsion upon removal of a 1s electron. The second-order term for the energy (and the first-order term for the wave function) reflects the adjustment (relaxation) of the relevant orbital $|v\rangle$ to the 1s vacancy. It should be noted that the perturbation expansions (62) already include the effect of the orthogonality constraints $\langle v^{FC}|r\rangle=0$, $n_r=1$ of the FCHF model by restricting the summations to unoccupied orbitals $|q\rangle$.

In the RCHF model too, the term value R_v^{RC} is given by the single particle energy ε_v^{RC}. The RCHF operator

$$\hat{f}^{RC}=\hat{t}+\sum_{\substack{i\\i\neq h}}(2\hat{J}_i'-\hat{K}_i')n_i+\hat{J}_c'+\hat{K}_c' \tag{63}$$

has the same form as the FCHF operator but—as indicated by the primes—the Coulomb and exchange operators here are defined with respect to the relaxed orbitals $|\psi_i\rangle$ of a HF calculation for the ion. To derive the desired perturbation expansions we decompose the RCHF operator according to

$$\hat{f}^{RC}=\hat{f}_0+\hat{f}_I^{RC}\ , \tag{64a}$$

$$\hat{f}_I^{RC}=-\hat{J}_c+2\hat{k}_c+\sum_{\substack{i\\i\neq c}}(2\hat{J}_i'-\hat{K}_i'-2\hat{J}_i+\hat{K}_i)n_i+\hat{J}_c'+K_c'-\hat{J}_c-\hat{K}_c\ , \tag{64b}$$

where one has to take into account that the perturbation part $\hat{f}_I^{RC}$ itself has its perturbation expansion

$$\hat{f}_I^{RC}=\hat{f}_I^{RC}(0)+\hat{f}_I^{RC}(1)+\cdots\ . \tag{65}$$

The zeroth-order term is clearly identified as

$$\hat{f}_I^{RC}(0)=-\hat{J}_c+2\hat{K}_c \tag{66}$$

and the first-order term may be easily evaluated once the ionic HF operator generating the relaxed orbitals has been specified. Obviously this operator may deviate from the IVO form of Eq. (54); it may even be the case that the relaxed orbitals are calculated by a generalized HF procedure where the operator approach does not apply at all. In any case, we may assume the following form for the expansion of the relaxed orbitals through first order

$$|\psi_j\rangle=|j\rangle+\sum_{\substack{q\\q\neq j}}\frac{-V_{jcqc}+\gamma V_{jccq}}{\varepsilon_j-\varepsilon_q}|q\rangle+O(2)\ , \tag{67}$$

where γ is a parameter, depending on the choice of the ionic HF equations. Now the perturbation expansion of the excited RCHF orbital $|v^{RC}\rangle$ may be written as

$$|v^{RC}\rangle=|v\rangle+\sum_{\substack{q\\q\neq v}}\frac{-V_{vcqc}+2V_{vccq}}{\varepsilon_v-\varepsilon_q}\bar{n}_q|q\rangle+\sum_{\substack{q\\q\neq v}}\frac{-V_{vcqc}+\gamma V_{vccq}}{\varepsilon_v-\varepsilon_q}n_q|q\rangle+O(2)\ . \tag{68}$$

Here, in addition to the first-order FCHF form, admixtures of occupied orbitals $|q\rangle$ occur. Note that in the latter part the exchange terms have the factor γ instead of 2; this guarantees the orthogonality constraints $\langle v^{RC}|\psi_j\rangle=0$ for the occupied relaxed orbitals $|\psi_j\rangle$ [Eq. (67)] through first order. For the RCHF energy ε_v^{RC} the second-order expansion

$$R_v^{RC}=\varepsilon_v^{RC}=\varepsilon_v^{FC}(2)+\sum_q\frac{(-V_{vcqc}+\gamma V_{vccq})^2}{\varepsilon_v-\varepsilon_q}n_q+\langle v|\hat{f}_I^{RC}(1)|v\rangle+O(3) \tag{69a}$$

comprises the FCHF result $\varepsilon_v^{FC}(2)$ [Eq. (62b)] and two additional terms, the first of which is associated with the occupied-orbital admixtures to $|v\rangle$. The other term reads

$$\langle v|\hat{f}_I^{RC}|v\rangle=\sum_{\substack{r\\r\neq c}}\langle v|2\hat{J}_r'-\hat{K}_r'-2\hat{J}_r+\hat{K}_r|v\rangle n_r=2\sum_{\substack{r,q\\r\neq c}}\frac{(-V_{rcqc}+\gamma V_{rccq})(2V_{vrvq}-V_{vrqv})}{\varepsilon_r-\varepsilon_q}\times n_r\bar{n}_q\ , \tag{69b}$$

where real-valued Coulomb integrals have been assumed for simplicity. This term has the obvious physical meaning of a screening energy for the orbital $|v\rangle$, since it accounts for the change in the electrostatic respulsion between the orbital $|v\rangle$ and the occupied valence orbitals upon relaxation of the latter. It should be noted that in the core-valence separation approximation, which for simplicity will also be adopted in the present perturbation

studies, $|\psi_c\rangle = |c\rangle$ and hence the part $\hat{J}_c' + \hat{K}_c' - \hat{J}_c - \hat{K}_c$ of $\hat{f}_I^{\mathrm{RC}}$ vanishes.

Now we may compare the FCHF and RCHF approximations with the exact term values R_v through second order. The second-order expansion of the energy of the excited state $|\Psi_{vc}^N\rangle$ has the following form:

$$E_{vc}^N(2) = E_0^N(1) + \varepsilon_v - \varepsilon_c - J_{vc} + 2K_{vc} + U_{vc}^{(2)}(p\text{-}h) + U_{vc}^{(2)}(2p\text{-}2h) + U_{vc}^{(2)}(3p\text{-}3h) \,. \tag{70}$$

Here $E_0^N(1) = \langle \Phi_0^N | \hat{H} | \Phi_0^N \rangle$ is the ground-state HF energy. The three terms $U_{vc}^{(2)}(p\text{-}h)$, $U_{vc}^{(2)}(2p\text{-}2h)$, and $U_{vc}^{(2)}(3p\text{-}3h)$ represent the second-order contributions arising from the interaction of $|\Phi_{cv}^N\rangle$ with (other) p-h states, $2p$-$2h$ states, and $3p$-$3h$ states, respectively. Similarly, we find for the energy of the ionic state the expansion

$$E_c^{N-1}(2) = E_0^N(1) - \varepsilon_c + U_c^{(2)}(2h\text{-}1p) + U_c^{(2)}(3h\text{-}2p) \,, \tag{71}$$

where $U_c^{(2)}(2h\text{-}1p)$ and $U_c^{(2)}(3h\text{-}2p)$ arise from the interaction of the single-hole state with $2h$-$1p$ and $3h$-$2p$ states, respectively. Combining the expansions (70) and (71) yields for the term value

$$R_v(2) = \varepsilon_v - J_{vc} + 2K_{vc} + U_{vc}^{(2)}(p\text{-}h) + U_{vc}^{(2)}(2p\text{-}2h) - U_c^{(2)}(2h\text{-}1p) + U_{vc}^{(2)}(3p\text{-}3h) - U_c^{(2)}(3h\text{-}2p) \,. \tag{72}$$

The second-order contributions appearing here have been specified elsewhere[33,34] in the case of primitive (spin-orbital) excitations. Here we have to consider the somewhat more complicated spin-free expressions appropriate for a singlet excitation (57) and a doublet ionic state. Again using the core-valence approximation we find

$$U_{vc}^{(2)}(p\text{-}h) = \sum_{\substack{q \\ q \neq v}} \frac{(V_{vcqc} - 2V_{vccq})^2}{\varepsilon_v - \varepsilon_q} \bar{n}_q \,. \tag{73}$$

This result is readily identified as the second-order contribution of the FCHF energy (62b). The contribution

$$U_c^{(2)}(2h\text{-}1p) = -\sum_{r,q} \frac{2V_{crcq}^2 + 2V_{crqc}^2 - 2V_{crcq}V_{crqc}}{\varepsilon_q - \varepsilon_r} \bar{n}_q n_r \tag{74}$$

represents the second-order relaxation energy of the ionic state. For discussion of the $2p$-$2h$ contribution $U_{cv}^{(2)}(2p\text{-}2h)$ it is useful to split it into a part $U_{vc}'(2p\text{-}2h)$ arising from excitations of the form $(q)^1(v)^1(c)^{-1}(r)^{-1}$ and a remainder $U_{cv}''(2p\text{-}2h)$. The former part, being the essential one, can be brought into the following form:

$$U_{cv}'(2p\text{-}2h) = Q + S + P \,, \tag{75a}$$

$$Q = -2 \sum_{\substack{q,r \\ q \neq v}} \frac{q}{\varepsilon_q - \varepsilon_r} (V_{crcq}^2 - V_{crcq}V_{crqc} + V_{crqc}^2) n_r \bar{n}_q - \sum_r \frac{1}{\varepsilon_v - \varepsilon_r} (V_{crcv} + V_{crvc})^2 n_r \,, \tag{75b}$$

$$S = 2 \sum_{\substack{q,r \\ q \neq v}} \frac{1}{\varepsilon_q - \varepsilon_r} (2V_{crcq}V_{vrvq} - V_{crcq}V_{vrqv} - V_{crqc}V_{vrvq} + 2V_{crqc}V_{vrqv}) n_r \bar{n}_q + 2 \sum_r \frac{1}{\varepsilon_v - \varepsilon_r} (V_{crcv} + V_{crvc}) V_{vrvv} n_r \,, \tag{75c}$$

$$P = -2 \sum_{\substack{q,r \\ q \neq v}} \frac{1}{\varepsilon_q - \varepsilon_r} (V_{vrvq} - V_{vrvq}V_{vrqv} + V_{vrqv}^2) n_r \bar{n}_q - \sum_r \frac{1}{\varepsilon_v - \varepsilon_r} V_{vrvv}^2 n_r \,. \tag{75d}$$

Each of these parts has a distinct physical meaning. The first part Q is identical with the $1s$ relaxation energy (74), except for the term in which $q = v$. With respect to the term value this means that the $1s$ relaxation energy largely cancels out, the remainder being

$$Q - U_c^{(2)}(2h\text{-}1p) = \sum_r \frac{V_{crcv}^2 - 4V_{crcv}V_{crvc} + V_{crvc}^2}{\varepsilon_v - \varepsilon_r} n_r \,. \tag{76}$$

Up to terms with exchange integrals, this part is retrieved in the RCHF energy E_v^{RC}, namely, in the second term on the right-hand side of Eq. (69a). The next part S in Eq. (75) obviously recovers the screening energy (69b) introduced by the RCHF approximation. It should, however, be noted that there remain discrepancies with respect to exchange contributions irrespective of the choice of γ [Eq. (67)] adopted for the relaxed orbitals. Neither the FCHF nor the RCHF approximation includes the third part P accounting for the polarization of the ionic core by the bound or free electron in the orbital v. The energy associated with the polarization is clearly negative, shifting the term value or the resonance position to lower energy.

The remaining second-order contributions are the remainder of the $2p$-$2h$ part ($\mathcal{E}$ denotes the exchange energy)

$$U_{cv}''(2p\text{-}2h) = -\sum_{\substack{r,q,q' \\ q \leq q' (\neq v)}} \frac{2V_{rvqq'}^2 + \mathcal{E}}{\varepsilon_q + \varepsilon_{q'} - \varepsilon_r - \varepsilon_v} n_r \bar{n}_q \bar{n}_{q'} \,, \tag{77}$$

and the difference

$$U_{cv}^{(2)}(3h\text{-}2p) - U_c^{(2)}(3h\text{-}2p) = +\sum_{\substack{r,r' \\ r \leq r'}} \frac{2V_{vqrr'}^2 + \mathcal{E}}{\varepsilon_v + \varepsilon_q - \varepsilon_r - \varepsilon_{r'}} \bar{n}_q n_r n_{r'} \tag{78}$$

mainly reflecting the difference of correlation energies in the excited and the ionic states. Both contributions are absent in the single-particle approximations but are expected to be only of minor importance.

We can summarize our results as follows. Of all second-order contributions the FCHF energy includes only the Tamm-Dancoff (TDA) term $[U_{vc}^{(2)}(p\text{-}h)]$ arising from the mixing with other single excitations. The FCHF result (in second order) differs from the RCHF energy by the screening energy (69b) and the occupied orbital analogous to $U_{vc}^{(2)}(p\text{-}h)$, that is,

$$\sum_q \frac{(V_{vcqc}-\gamma V_{vccq})^2 n_q}{\varepsilon_v-\varepsilon_q} .$$

Both contributions are positive, explaining the higher RCHF energies. In the exact second-order result they are retrieved (up to exchange terms) as the energy S [Eq. (75b)] and the difference $Q-U_c^{(2)}(2h\text{-}1p)$ [Eq. (76)] of excited- and ionic-state relaxation energies. The major deficiency of the RCHF model appears to be the neglect of the polarization energy (75d) leading to too high term values or resonance positions.

B. Transition amplitudes

In the preceding section, Sec. IV A, we adopted perturbation theory to analyze resonance positions or term values in K-shell photoexcitation. We now look at the corresponding transition amplitudes in light of perturbation theory. Again, we consider the singlet K-shell hole state $|\Psi_{vc}^N\rangle$ resulting from the zeroth-order state $|\Phi_{vc}^N\rangle$ of Eq. (57), where $|v\rangle$ represents an unoccupied valence or continuum orbital. The expansion of the transition amplitude $A_{c,v}=\langle\Psi_{vc}^N|\hat{D}|\Psi_0^N\rangle$ [see Eq. (3)] through first order is

$$A_{c,v}(1)=\sqrt{2}\langle v|\hat{d}|c\rangle+\langle\Psi_{vc}^{(1)}|\hat{D}|\Phi_0^N\rangle + \langle\Phi_{vc}^N|\hat{D}|\Psi_0^{(1)}\rangle , \tag{79}$$

where $|\Psi_{vc}^{(1)}\rangle$ and $|\Psi_0^{(1)}\rangle$ represent the first-order excited and ground states, respectively. The first-order contribution,

$$\langle\Psi_{vc}^{(1)}|\hat{D}|\Phi_0^N\rangle=\sqrt{2}\sum_{\substack{q\\q\neq v}}\frac{-V_{vcqc}+2V_{vccq}}{\varepsilon_v-\varepsilon_q}\bar{n}_q\langle q|\hat{d}|c\rangle , \tag{80}$$

arises from the admixture of other single excitations $|\Phi_{qc}^N\rangle$ (adopting here again the CVS approximation). This part of the first-order amplitude is properly accounted for by the Tamm-Dancoff approximation to electronic excitation.[35] The other first-order contribution in Eq. (79), associated with ground-state correlation, or more precisely, with the admixture of double excitations to the HF ground state, is included in the random-phase approximation[35] (RPA) which provides a consistent first-order description of the single-excitation transition amplitudes; for a more detailed discussion see, e.g., Ref. 33. In the present context it is important to realize that for K-shell excitations in the CVS approximation the RPA reduces to the TDA and the ground-state correlation contribution $\langle\Phi_{vc}^N|\hat{D}|\Psi_0^{(1)}\rangle$ in Eq. (79) vanishes.

We can now compare the full first-order result (in the CVS approximation) with the RCHF amplitude $A_{c,v}^{RC}$ [Eqs. (35) or (40)]. To first order and in spin-free notation we find

$$A_{c,v}^{RC}(1)=\sqrt{2}\left[\langle v|\hat{d}|c\rangle+\langle v^{(1)}|\hat{d}|c\rangle - \sum_r\langle v^{(1)}|r\rangle\langle r|\hat{d}|c\rangle n_r\right] . \tag{81}$$

Obviously, the conjugate part cancels all contributions arising from the occupied orbitals in the first-order term of $|v^{RC}\rangle$ [Eq. (70)], i.e.,

$$|v^{(1)}\rangle-\sum_r|r\rangle\langle r|v^{(1)}\rangle = \sum_{\substack{q\\q\neq v}}\frac{-V_{vcqc}+2V_{vccq}}{\varepsilon_v-\varepsilon_q}\bar{n}_q|q\rangle , \tag{82}$$

and the final result is seen to be identical with the full (first-order) amplitude. Thus we have arrived at the important conclusions that the RCHF description of single photoexcitation amplitudes in the K-shell regime is complete (up to terms vanishing in the CVS approximation) through first order of perturbation theory, and is thus comparable to the level of the RPA treatment. Interestingly, the FCHF amplitudes $A_{c,v}^{FC}$ are also consistent through first order, since, due to the orthogonality constraints $\langle v^{FC}|r\rangle=0$, $n_r=1$, the first-order term of $|v^{FC}\rangle$ [Eq. (62a)] contains only unoccupied orbitals $|q\rangle$.

V. CALCULATIONS

The bound electronic wave functions required in the present applications were obtained from Hartree-Fock calculations for the $^1\Sigma^+$ ground state of CO ($1\sigma^2 2\sigma^2 3\sigma^2 4\sigma^2 1\pi^4 5\sigma^2$) and for the C 1$s$ and O 1s hole states of CO^+. The SCF basis used in these calculations consisted of the $7s/4p/2d$ contraction of $13s/8p/2d$ Cartesian Gaussians. The exponents and contraction coefficients (No. 6.72.2 for C and No. 8.76.2 for O) were taken from Huzinaga.[36] The exponents for the d functions were 0.92 and 0.256 for C, and 1.324 and 0.445 for O. The calculations were done at the equilibrium nuclear geometry of 2.132 a.u. For the ground state of the neutral molecule an SCF energy of -112.7844 a.u. was obtained; the energies for the C 1s and O 1s hole states were -101.8625 and -92.8818 a.u., respectively. The overlap integrals S_{ij} [Eq. (20)] and dipole integrals d_{ij} [Eq. (23)] between the frozen (ground-state HF) and the relaxed (ionic HF) orbitals were calculated using the single-center expansion techniques described below. The results are listed in Tables I and II.

The methods for obtaining the photoelectron continuum wave functions and bound-continuum integrals have been used in many previous applications and are amply described in Refs. 15 and 37. In brief, the continuum function is written as the partial-wave expansion

$$\psi_{\mathbf{k}}^{(-)}(\mathbf{r})=\left[\frac{2}{\pi}\right]^{1/2}\sum_{l,m}\frac{i^l}{k}\psi_{klm}^{(-)}(\mathbf{r})Y_{lm}^*(\hat{\mathbf{k}}) . \tag{83}$$

Each partial wave $\psi_{klm}(\mathbf{r})$ satisfies the Lippmann-Schwinger equation

$$\psi_{klm}^{(-)}(\mathbf{r})=\phi_{klm}^c+G_c^{(-)}\left[\hat{v}+\frac{1}{r}\right]\psi_{klm} . \tag{84}$$

Here $G_c^{(-)}$ is the Coulomb Green's function with incoming-wave boundary conditions and $\hat{v}$ is the static-exchange potential for the molecular ion [see Eq. (54)] taken either in the frozen core ($\hat{v}=\hat{v}^{FC}$) or the relaxed core ($\hat{v}=\hat{v}^{RC}$) representation. Orthogonalization be-

TABLE I. Overlap integrals S_{ij} [Eq. (20)]. These overlaps contain an arbitrary phase due to the sign of the wave function.

Relaxed \ Frozen	1σ	2σ	3σ	4σ	5σ	1π
			C $1s(2\sigma)$[a]			
1σ	0.999	-0.905×10^{-5}	-0.177×10^{-3}	-0.381×10^{-3}	0.107×10^{-3}	
2σ	-0.877×10^{-5}	-0.998	0.622×10^{-2}	0.688×10^{-2}	-0.700×10^{-2}	
3σ	-0.393×10^{-3}	-0.498×10^{-2}	-0.994	0.887×10^{-1}	-0.142×10^{-1}	
4σ	0.569×10^{-3}	-0.431×10^{-2}	0.906×10^{-1}	0.988	0.747×10^{-1}	
5σ	-0.149×10^{-3}	-0.341×10^{-2}	-0.196×10^{-1}	-0.799×10^{-1}	0.976	
1π						0.986
			O $1s(1\sigma)$[b]			
1σ	0.999	-0.696×10^{-4}	0.749×10^{-2}	0.372×10^{-2}	0.866×10^{-3}	
2σ	-0.693×10^{-4}	-0.999	0.150×10^{-3}	0.242×10^{-3}	0.107×10^{-2}	
3σ	0.561×10^{-2}	0.229×10^{-3}	-0.995	0.125×10^{-1}	-0.480×10^{-1}	
4σ	-0.232×10^{-2}	0.225×10^{-3}	0.732×10^{-2}	0.981	-0.142	
5σ	-0.656×10^{-3}	0.137×10^{-2}	-0.521×10^{-1}	0.147	0.981	
1π						-0.972

[a]The frozen orbitals are from the neutral ground state. The relaxed orbitals are from the ion state, $2\sigma^{-1}$, i.e., the C $1s^{-1}$ state of CO^+.

[b]The same as footnote a except the relaxed orbitals are from the ion state $1\sigma^{-1}$, i.e., the O $1s^{-1}$ state of CO^+.

tween the continuum and the occupied orbitals is taken into account by means of the Philips-Kleinman pseudopotential as described in Ref. 15. The solution of the Lippmann-Schwinger equations (84) is based on the Schwinger variational method. By assuming a separable approximation to the potential,

$$\hat{V}=\hat{v}+\frac{1}{r}\ , \tag{85}$$

of the form

$$\hat{V}\cong\hat{V}^s=\sum_{i,j}\langle\mathbf{r}|\hat{V}|\alpha_i\rangle(\underline{V}^{-1})_{ij}\langle\alpha_j|\hat{V}|\mathbf{r}'\rangle\ , \tag{86}$$

the solutions of the integral equations (84) can be written as

$$\psi^{(-)}_{klm}(\mathbf{r})=\phi^c_{klm}(\mathbf{r})+\sum_{i,j}\langle\mathbf{r}|G_c^{(-)}\hat{V}|\alpha_i\rangle(\underline{D}^{-1})_{ij}\times\langle\alpha_j|\hat{V}|\phi^c_{klm}\rangle\ . \tag{87}$$

Here $\underline{V}$ and $\underline{D}$ denote matrices with matrix elements

$$V_{ij}=\langle\alpha_i|\hat{V}|\alpha_j\rangle \tag{88}$$

and

$$D_{ij}=\langle\alpha_i|\hat{V}-\hat{V}G_c^{(-)}\hat{V}|\alpha_j\rangle\ . \tag{89}$$

TABLE II. Dipole integrals d_{ij} [Eq. (23)] between frozen and relaxed orbitals in a.u. For the $\sigma\to\sigma$, $\pi\to\pi$ transition $\hat{d}=z$; for $\sigma\to\pi$, $\hat{d}=(x-iy)/\sqrt{2}$; and for $\pi\to\sigma$, $\hat{d}=-(x+iy)/\sqrt{2}$.

Relaxed \ Frozen	1σ	2σ	3σ	4σ	5σ	1π
			C $1s(2\sigma)$			
1σ	0.913[a]	0.437×10^{-3}	-0.181×10^{-1}	0.472×10^{-1}	-0.234×10^{-1}	-0.511×10^{-1}
2σ	-0.114×10^{-2}	1.216	0.370×10^{-1}	-0.204×10^{-1}	0.853×10^{-1}	-0.494×10^{-1}
3σ	0.202×10^{-1}	0.499×10^{-1}	-0.257	-0.595	-0.107	0.604
4σ	0.440×10^{-1}	0.176×10^{-1}	0.705	0.879	-0.905	-0.126
5σ	-0.268×10^{-1}	0.697×10^{-1}	-0.103×10^{-2}	-0.885	-1.551	0.297
1π	0.489×10^{-1}	-0.581×10^{-1}	0.625	0.160×10^{-1}	-0.329	0.283
			O $1s(1\sigma)$			
1σ	0.912	-0.100×10^{-3}	-0.144×10^{-1}	-0.595×10^{-1}	-0.328×10^{-1}	-0.605×10^{-1}
2σ	-0.506×10^{-3}	1.216	0.369×10^{-1}	-0.188×10^{-1}	0.563×10^{-1}	-0.389×10^{-1}
3σ	0.260×10^{-1}	0.358×10^{-1}	-0.355	-0.617	-0.243×10^{-1}	0.592
4σ	0.571×10^{-1}	0.243×10^{-1}	0.621	1.002	-0.588	-0.108
5σ	-0.205×10^{-1}	-0.549×10^{-1}	0.168	-0.735	-1.742	0.327
1π	-0.668×10^{-1}	0.283×10^{-1}	-0.600	-0.143	0.183	-0.532

[a]Note that diagonal elements depend on the origin of coordinates and are not included in the calculation of the transition amplitude due to the CVS approximation discussed in Sec. II D.

The set of functions $|\alpha_i\rangle$ referred to as the scattering basis set consists of suitably chosen discrete functions such as Cartesian Gaussian functions. The scattering basis set used in the present calculations is specified in Table III.

All matrix elements and functions arising in the computation of the partial wave $\psi_{klm}^{(-)}$ according to Eqs. (87)–(89) are evaluated using single-center expansions about the center of gravity. The details of these expansions are as follows.

(i) Maximum angular momentum in the expansion of the occupied orbitals in the direct potential is 29.

(ii) Maximum angular momentum in the expansion of the occupied orbitals in the exchange potential is 25 (1σ), 25 (2σ), 15 (3σ), 15 (4σ), 10 (5σ), and 10 (1π).

(iii) Maximum angular momentum in the expansion of $1/r_{12}$ in the direct and exchange terms is 58 and 29, respectively.

(iv) All other single-center expansions were truncated at $l=29$.

The partial-wave expansion of the continuum orbital, Eq. (83), was truncated at $l_p=8$. The resulting radial integrals were obtained using a Simpson-rule quadrature. The grid contained 500 points and extended to 69.0 a.u. with a step size of 0.01 a.u. near the nuclei and a maximum step size of 0.40 a.u.

Following Eq. (35) we introduce the spin-free transition amplitudes $I_{lm\mu}$ for the partial waves ψ_{klm}

$$I_{lm\mu}=\frac{1}{\sqrt{2}}\left(A^{(\mu)}_{|s\alpha,klm\beta}+A^{(\mu)}_{|s\beta,klm\alpha}\right) \tag{90a}$$

$$=\sqrt{2}\langle\bar{\Phi}_0^N|\Phi_0^N\rangle\left[\langle\psi_{klm}^{(-)}|\hat{r}_\mu|\phi_{1s}\rangle-\sum_{r,r'}\langle\psi_{klm}^{(-)}|\phi_r\rangle(\underline{S}^{-1})_{rr'}\langle\psi_{r'}|\hat{r}_\mu|\phi_{1s}\rangle\right]. \tag{90b}$$

Here, the dipole operator components

$$\hat{r}_\mu=\begin{cases}\mp(\hat{x}\pm i\hat{y})/\sqrt{2} & \text{for } \mu=\pm1\ ,\\ \hat{z} & \text{for } \mu=0\end{cases} \tag{91}$$

are used and $|\phi_{1s}\rangle$ refers to the core orbital C $1s(2\sigma)$ or O $1s(1\sigma)$. In Eq. (90b) only spin-free (spatial) quantities are retained, and, in particular, $\underline{S}$ represents the matrix of spatial relaxed-frozen overlap integrals $\langle\psi_r|\phi_{r'}\rangle$. The N-electron overlap $\langle\bar{\Phi}_0^N|\Phi_0^N\rangle$ is given by the square of $\det(\underline{S})$. The decomposition of the full amplitude $I_{lm\mu}$ into the direct $I^{(\mathrm{I})}$ and conjugate contribution $I^{(\mathrm{II})}$,

$$I_{lm\mu}=I^{(\mathrm{I})}_{lm\mu}+I^{(\mathrm{II})}_{lm\mu}\ , \tag{92}$$

according to Eq. (90b), is obvious. The dipole integrals $\langle\psi_{klm}|\hat{r}_\mu|\phi_{1s}\rangle$ and overlaps $\langle\psi_{klm}|\phi_r\rangle$ were calculated with the single-center expansion technique specified above. The total photoionization cross section for the $1s$-hole main state averaged over all molecular orientations is obtained from the partial amplitudes (90b) by

$$\sigma=\frac{4\pi^2}{3c}\omega k\sum_{l,m,\mu}|I_{lm\mu}|^2\ . \tag{93}$$

The corresponding asymmetry parameter β of the photoelectron angular distribution (with respect to the polarization of the light) is given by

$$\beta=\frac{4\pi^2}{5c\sigma}k\sum_{\substack{l,m,\mu\\ l',m',\mu'\\ \mu''}}(-1)^{m-\mu'}I_{lm\mu}I^*_{l'm'\mu'}[(2l+1)\times(2l'+1)]^{1/2}\langle1100|20\rangle\langle ll'0|20\rangle\times\langle11-\mu\mu'|2\mu''\rangle\langle ll'-m-m'|2-\mu''\rangle\ . \tag{94}$$

Here $\langle l_1m_1l_2m_2|lm\rangle$ is the Clebsch-Gordan coefficient $(l_1m_1l_2m_2|l_1l_2lm)$ in the notation of Edmonds.[38]

TABLE III. Scattering basis sets used in Eq. (87).

Continuum symmetry	Type of Gaussian function[a]	Exponents
σ	Cartesian s	10.0,4.0,1.5,0.5,0.1
	Cartesian z	2.0,1.0,0.5,0.1
π	Cartesian p_x	10.0,4.0,1.5,0.5,0.1
	Cartesian d_{xz}	1.0,0.1

[a]Cartesian functions are centered on each nucleus. For details of the forms of these functions and their use see Ref. 15.

VI. RESULTS AND DISCUSSION

A. C (1s) ionization

Figure 1 shows the shape-resonant C $1s$ photoionization cross section in CO calculated both in the FCHF and the RCHF approximations, together with experimental results by Kay *et al.*[39] and by Truesdale *et al.*[6] As for N_2, the two results are significantly different. Without valence-electron relaxation one finds a relatively narrow and intense peak about 5 eV above the C $1s$ ionization threshold (296.2 eV). The relaxed description (RCHF), on the other hand, results in a substantial lowering, broadening, and shifting of the σ^* resonance centered at 11.2 eV above threshold. This difference is clearly an effect of the screening of the $1s$ hole by the relaxed valence electrons leading to a much less attractive potential than the "unscreened" potential of the FCHF model. The experimental resonance position, somewhat obscured by autoionization structures, appears to be between 8 and 9 eV, that is 2–3 eV below our RCHF result. According to the discussion in Sec. IV A the overshooting of the calculated resonance position seems to be primarily induced by the neglect of target polarization in the present ap-

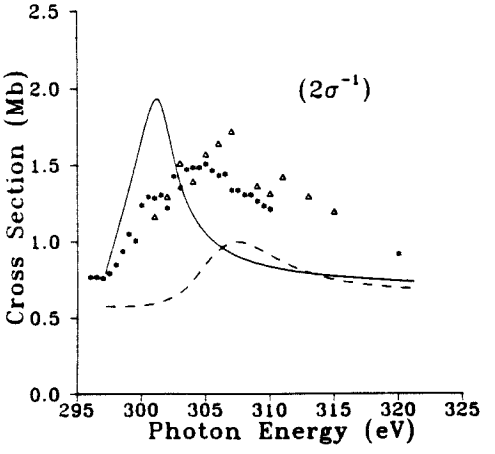

FIG. 1. Photoionization cross sections leading to the $2\sigma^{-1}$ (C $1s^{-1}$) state of CO^+. ——, present results (length) in the FCHF approximation; — — —, present results (length) in the RCHF approximation; *, experimental results of Ref. 39; △, experimental results of Ref. 6.

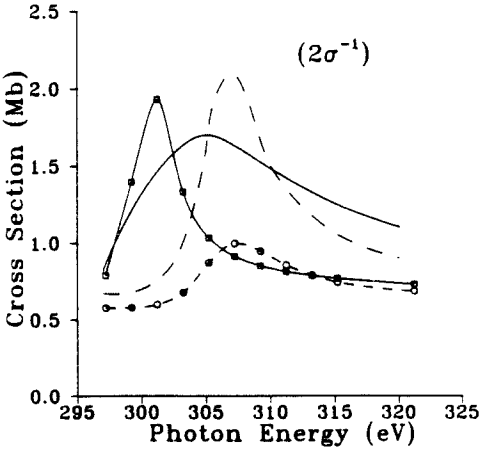

FIG. 2. Photoionization cross sections leading to the $2\sigma^{-1}$ (C $1s^{-1}$) state of CO^+. ⊟—⊟, present results (length) in the FCHF approximation; ⊖—⊖, present results (length) in the RCHF approximation; ——, calculated FCHF results of Ref. 18 using the STMT method; — — —, calculated results of Ref. 41 using the MSM method.

proach. Inclusion of the attractive polarization potential not only would lower the resonance position but would also enhance the resonance peak.

It may be worth noting that the different magnitudes in the frozen and relaxed cross sections result to some extent from the absence of the overall spectroscopic factor

$$|x_{1s}|^2=|\langle\bar{\Phi}_0^N|\Phi_0^N\rangle|^2,$$

in the expression for the FCHF cross section. This quantity specifies the amount of spectral strength diverted from the single-hole state to shake-up and shake-off states. The present RCHF calculations give a value of $|x_{1s}|^2=0.79$ which is slightly larger than the result (0.68) found in a recent Green's-function study.[40]

In Fig. 2 we compare our calculated frozen- and relaxed-core photoionization cross sections with the frozen-core results obtained previously by the Stieltjes-Tschebycheff moment theory[18] (STMT) and by the multiple scattering (MS) method.[41] The present frozen-core curves should be essentially identical to those of the STMT studies, since the underlying single-particle scattering potential is the same. Nevertheless, we see drastic discrepancies in these results. The cross section of the STMT method shows a very broad resonance feature with a maximum 9 eV above threshold, in apparent good agreement with the experimental data. The resonance peak of the MS calculation is centered at even higher energy, almost coinciding with our relaxed-core result; its width and height is somewhat larger than that given by the present FCHF calculation. According to our discussion in Sec. IV A, it is certainly not realistic to expect resonance positions at or even above the experimental value when using the unscreened core-hole potential of the frozen-core model. Similar discrepancies between the STMT result and the iterative Schwinger static-exchange (FCHF) cross sections have been found for the K-shell ionization of N_2.[20]

Figure 3 shows the decomposition of the total C $1s$ photoionization cross section into the contributions of the $k\sigma$ and $k\pi$ subchannels. To investigate the role of the conjugate contributions we have also plotted (dashed line) the "direct" $k\sigma$ and $k\pi$ cross sections obtained by omitting the conjugate (overlap) part in the amplitude (90b). Note that the overall spectroscopic factor ($|x_{1s}|^2=0.79$) is not taken into account in Fig. 3. In both

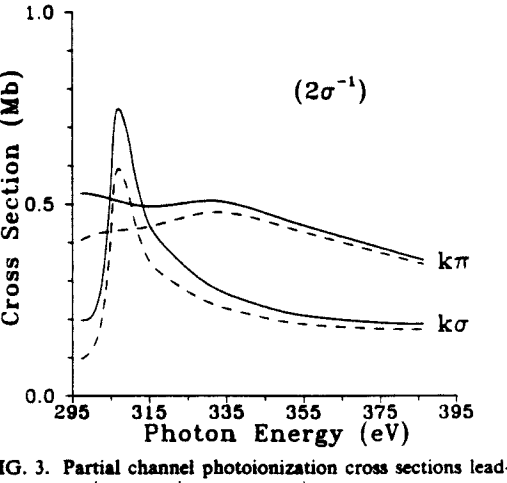

FIG. 3. Partial channel photoionization cross sections leading to the $2\sigma^{-1}$, (C $1s^{-1}$) state of CO^+ in the RCHF approximation. ——, direct plus conjugate cross sections as per Eq. (90b); — — —, only direct cross sections using the first term of Eq. (90b). Note that these cross sections omit the overall spectroscopic factor.

channels we see a significant enhancement of the cross section upon inclusion of the conjugate contribution. The modification due to the bound-free overlap terms is largest at low photoelectron energy and becomes small towards larger energies, as expected. At the resonance position in the $k\sigma$ channel the enhancement of the direct part amounts to 0.16 Mb, that is, almost 30% of the direct value. In the $k\pi$ channel the largest difference between the direct and full cross section is found at threshold, being here about 30%.

A more detailed view of the bound-free overlaps is given in Fig. 4. Here we have plotted the quantities

$$S_r(k)=\frac{8\pi^2}{3c}\omega k\sum_{l,m}|\langle\psi_{klm}^{(-)}|\phi_r\rangle|^2 \tag{95}$$

as a function of energy for the occupied (frozen) valence orbitals $r=3\sigma$, 4σ, 5σ, and 1π. Note that these quantities are dimensionless and when multiplied by the square of the appropriate bound-bound transition matrix element, correspond to a "conjugate transition cross section." It is also important to note that each l component of the conjugate amplitude may interfere with the direct part of the amplitude [see Fig. 90(b)]. In addition, in CO there may be additional interference in the sum over orbital contributions, (r,r'), in the conjugate amplitude.

In the $k\pi$ channel the squared overlap $S_{1\pi}(k)$ assumes a value of ≥ 2.75 at threshold and decreases rapidly with increasing photoelectron energy. In the $k\sigma$ curves this type of behavior is superimposed on a resonance enhancement, leading to local maxima (and minima) in the 3σ and 4σ overlap curves and a distinct shoulder in the 5σ curve. The value at threshold is largest for the outermost valence orbital 5σ [$S_{5\sigma}(0)\geq 3.5$]; distinctly lower values, namely, $S_{4\sigma}(0)\approx 0.6$ and $S_{3\sigma}(0)\approx 0.1$, respectively, are found for the inner-valence orbitals.

The squared overlap $S_r(k)$ for the core orbitals O 1s (1σ) and C 1s (2σ) are smaller than 10^{-4} and 0.03, respectively. In the strict core-valence separation approximation the frozen- and relaxed-core orbitals are identical and orthogonal to the (relaxed) continuum orbital. However, since this approximation has not been enforced in the calculation of the relaxed orbitals the frozen 1s relaxed-continuum overlap integrals are not identically zero. These deviations give an estimate of the error introduced by the core-valence separation approximation.

Figure 5 shows the photoelectron asymmetry parameter β calculated in the frozen- and relaxed-core models. The shifting and broadening of the shape resonance by the screening of the C 1s hole are apparent in these results. Both the frozen and the relaxed β curves have a distinct minimum in the energy regions of the respective frozen and relaxed resonance positions, as seen in the cross sections. Beside the shift in the position, the relaxed curve assumes a somewhat high β value at the minimum and is flatter than the frozen one. The experimental data of Truesdale *et al.*[6] seem to be in better agreement with the relaxed curve, in particular, if shifted by 2–3 eV to lower energy in order to agree with the experimental resonance position.

Figure 5 also displays the direct part of the relaxed β curve obtained by neglecting the conjugate contributions in amplitude (90b). The direct curve differs only little from the solid curve; in particular, above the minimum they are almost identical. This shows that the β parameter is little affected by the conjugate contributions.

The 1s photoelectron asymmetry parameters for CO have been calculated previously by Dill *et al.*[42] and by Grimm[43] using the multiple-scattering model (MSM). These calculations were based on the transition state self-consistent-field (SCF) treatment in which one-half of an electron was removed from the K-shell. Correspondingly, only half of the 1s-hole screening was accounted for by the scattering potential. The results of such a

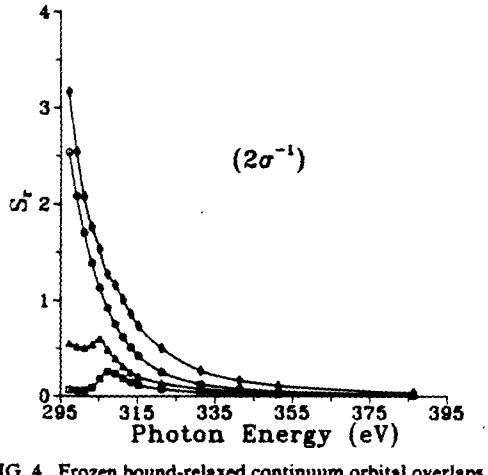

FIG. 4. Frozen bound-relaxed continuum orbital overlaps, S_r of Eq. (95). ⊟, $r=3\sigma$; △, $r=4\sigma$; ◇, $r=5\sigma$; ○, $r=1\pi$. See Sec. VI for more details.

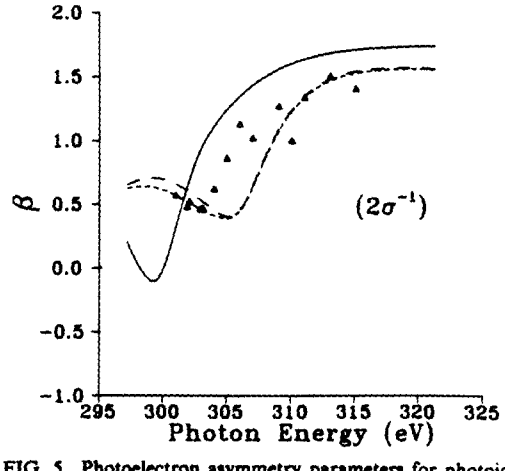

FIG. 5. Photoelectron asymmetry parameters for photoionization leading to the $2\sigma^{-1}$ (C $1s^{-1}$) state of CO^+. ——, present results (length) in the FCHF approximation; — — —, present results (length) in the RCHF approximation; —, present results (length) only using the direct part of the transition amplitude; △, experimental results of Ref. 6.

"half-relaxed" method lie, of course, somewhere between those of the frozen- and the fully relaxed-core approximations. In spite of the usually better agreement with experiment there is little physical justification for this procedure, since the shortcoming of the RCHF model is not "overscreening" but neglect of target polarization.

B. O (1s) ionization

The O 1s photoionization cross sections calculated both in the frozen- and relaxed-core approximations are shown in Fig. 6, along with experimental results of Barrus *et al.*[11] (photoabsorption) and Truesdale *et al.*[6] and previous theoretical results of Padial *et al.*[18] obtained using the FCHF model and STMT methods. As in the C 1s cross section, the shape resonance is drastically shifted and broadened in the relaxed potential compared to the frozen-core potential. However, here the differences between the frozen and relaxed calculations are more dramatic. The shift of the resonance position induced by the screening of the O 1s hole in the RCHF model is about 10.5 eV, which is over 4 eV larger than in the C 1s cross section; concommitantly the relaxed O 1s resonance peak is even flatter and more extended than its C 1s counterpart. The difference in the screening effect for the C 1s and the O 1s hole is, of course, a consequence of the larger electronic reorganization (relaxation) in the presence of a *K*-shell hole at the atom with higher nuclear charge. The relaxation shifts for the C 1s and O 1s ionization energies of about 13 and 21 eV, respectively, may serve as a measure of this difference.

As in the C 1s case, the experimental shape resonance result lies between the frozen and relaxed theoretical curves. Again, we expect that inclusion of polarization in the RCHF potential would lead to better agreement with experiment. However, here the experimental resonance position (about 7.5 eV above threshold) differs by 5.5 eV from the result of the relaxed-core calculation, and this discrepancy appears somewhat too large to be accounted for only by polarization. The overall spectroscopic factor $|x_{1\sigma}|^2$ contained in the relaxed-core result (but absent in the frozen-core result) was calculated to be 0.74, a value larger than the previous *ab initio* result[40] of 0.61. The O 1s cross section calculated by Padial *et al.*[18] in the FCHF approximation using the STMT method is again at variance with our frozen-core result even at high photon energy.

The decomposition of the relaxed-core O 1s cross section into the $k\sigma$ and $k\pi$ subchannels is shown in Fig. 7. Also plotted here are the direct parts of the respective cross sections, thus making apparent the role of the conjugate contributions. As in the C 1s ionization they result in a substantial enhancement of the cross section in both channels. Remarkably, the direct $k\pi$ cross section increases even at 100 eV above threshold, and the enhancement by the conjugate contribution is still of the order of 10%.

The frozen and relaxed photoelectron asymmetry parameters for O 1s ionization are plotted in Fig. 8. For both curves the β values at low energies are higher than for C 1s ionization. As in the cross sections, the differences between FCHF and RCHF β's are qualitatively the same as in C (1s) photoionization. The relaxed β curve exhibits a pronounced maximum near threshold. The synchrotron data by Truesdale *et al.*[6] are somewhat scarce and scattered, making the comparison between theory and experiment inconclusive.

VII. SUMMARY AND CONCLUSIONS

The relaxed-core Hartree-Fock model used here to study molecular *K*-shell photoionization cross sections and angular distributions contains the following approximations.

(i) The *N*-electron initial state is given by its HF repre-

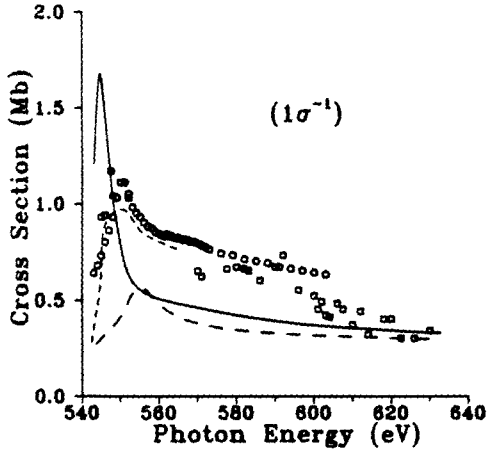

FIG. 6. Photoionization cross sections leading to the $1\sigma^{-1}$ (O $1s^{-1}$) state of CO^+. ——, present results (length) in the FCHF approximation; – – –, present results (length) in the RCHF approximation; —, calculated FCHF results of Ref. 18 using the STMT method; ○, experimental results (photoabsorption) of Ref. 11; □, experimental results of Ref. 6.

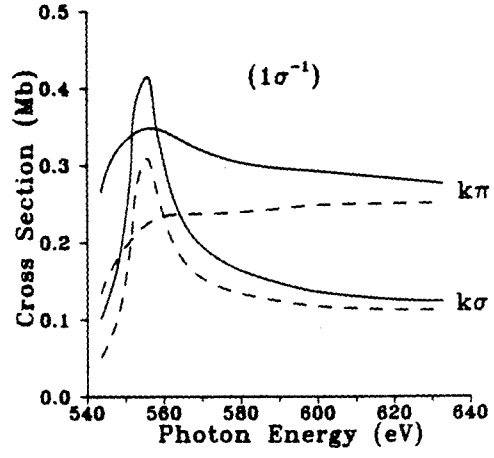

FIG. 7. Same as Fig. 3 except for photoionization leading to the $1\sigma^{-1}$ (O $1s^{-1}$) state of CO^+.

sentation, that is, as a Slater determinant of "frozen" orbitals.

(ii) The relaxed orbitals generated by a HF calculation for the 1*s*-hole state are used to represent the ion and the potential for the electron-ion scattering. The photoelectron continuum orbitals are constrained to be orthogonal to the occupied relaxed orbitals.

(iii) The *N*-electron final state is—apart from spin (and spatial symmetry) coupling—represented by an antisymmetrized product of the ionic state and the continuum orbital.

In addition, we have introduced the core-valence separation approximation, which is justified in the case of *K*-shell ionization due to the large energy separation between the 1*s* and valence levels and to the small coupling matrix elements for states with differing *K*-shell occupations. In the CVS approximation the *N*-electron initial and final states are strictly orthogonal and thus one gets rid of unphysical contributions to the RCHF *N*-electron transition moment. Furthermore, in the CVS approximation the familiar IVO form of the static-exchange potential is consistent with the general variational principle used to derive the RCHF potential.

Compared to the more widely used frozen-core Hartree-Fock calculations, the essential computational complication of the RCHF model arises from the nonorthogonality of the frozen and relaxed orbitals in the initial and final states, respectively. The method proposed here to evaluate *N*-electron matrix elements for determinants with mutually nonorthogonal orbitals has proven to be particularly practical and transparent in the case of the RCHF transition moment. Besides the computational aspect, the new formulation also leads to a conceptual clarification, since it allows one to make a distinction between the direct and the conjugate parts of the transition moment. The latter part arises due to the lack of orthogonality between the (relaxed) continuum orbital and the frozen occupied orbitals, which is reflected in the bound-free overlap integrals introduced here. The direct part, on the other hand, is characterized by the occurrence of the usual bound-free dipole (transition) integrals, and prevails, of course, also in the case of orthogonality between bound and continuum orbitals. The effect of the conjugate part can be viewed as a modification of the bound-free dipole integral, essentially projecting out the occupied frozen orbital contributions in the continuum orbital. An explicit study of the relative importance of these contributions was made for the case of C 1*s* ionization. Here the conjugate contributions were seen to enhance quite substantially the "direct" cross section at low photoelectron energy. Towards higher energy their influence becomes small, as the bound-free overlap integrals tend to vanish rapidly.

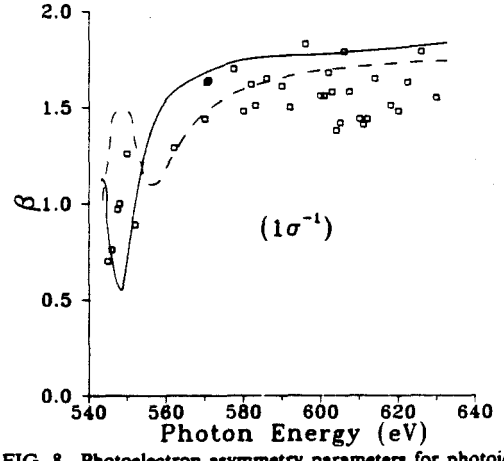

FIG. 8. Photoelectron asymmetry parameters for photoionization leading to the $1\sigma^{-1}$ (O $1s^{-1}$) state of CO^+. ——, present results (length) in the FCHF approximation; – – – present results (length) in the RCHF approximation; □, experimental results of Ref. 6.

To better understand the potential and the limitation of the RCHF approximation we have analyzed its results by means of perturbation theory. With respect to energies, i.e., resonance positions or term values (below the 1*s* threshold) the RCHF description is complete through first order but only partially recovers the correct second-order contributions. As expected, the RCHF comprises, apart from exchange terms, contributions associated with ionic relaxation. In particular, the screening of the 1*s* hole by the reorganization of the valence electrons is correctly described in second order. It is this effect that leads to considerably larger resonance energies than calculated using the unscreened 1*s*-hole potential of the FCHF model. The analysis in second order reveals also the main deficiency of the RCHF approximation: the neglect of target polarization, i.e., effects associated with the response of the ion to the presence of the photoelectron. The polarization correction makes the ion-electron potential more attractive and leads to a lowering of resonance positions. The discrepancies found between the RCHF results and experimental results have to be attributed mainly to this source. The analysis by perturbation theory has also been applied to the *N*-electron transition moment. Apart from contributions vanishing in the CVS approximation, here a consistent first-order treatment is achieved at the RCHF level.

The picture emerging from this study shows that, recognizing its limitations, the RCHF approximation establishes a good approach to the theoretical description of *K*-shell ionization, and is, indeed, superior to the FCHF model which ignores the important relaxation effects. A very efficient computational scheme, combining our methods for solving the single-particle scattering equations with the new formulation of the transition moment, is now available for further such studies.

ACKNOWLEDGMENTS

This material is based upon research supported by the National Science Foundation under Grant No. CHE85-21391. One of us (J.S.) wishes to express his gratitude for the hospitality given during his stay at Caltech's Laboratory of Chemical Physics. He also acknowledges funding by the German Federal Ministry for Research and Technology under the Contract No. 05 352AX-3. The authors

acknowledge use of the resources of the San Diego Supercomputer Center which is supported by the National Science Foundation.

APPENDIX: OVERLAP AND TRANSITION MATRIX ELEMENTS FOR FROZEN AND RELAXED STATES

In the following we consider two distinct sets $\{|\phi_i\rangle\}$ and $\{|\psi_i\rangle\}$ of orbitals, e.g., the sets of frozen and relaxed HF orbitals discussed in Sec. II. The associated operators in second-quantized notation are denoted by a_i and c_i, respectively. The Slater determinants of the first N orbitals,

$$|\Phi_0^N\rangle = |\phi_1 \cdots \phi_N| \,, \tag{A1}$$

$$|\bar{\Phi}_0^N\rangle = |\psi_1 \cdots \psi_N| \,, \tag{A2}$$

within each set are referred to as the frozen and relaxed ground states, respectively. Further definitions needed are the relaxed-frozen overlap matrix $\underline{S}$,

$$S_{ij} = \langle \psi_i | \phi_j \rangle, \quad i,j \le N \tag{A3}$$

and the matrix $\underline{d}$ of dipole integrals

$$d_{ij} = \langle \psi_i | \hat{d} | \phi_j \rangle, \quad i,j \le N \,. \tag{A4}$$

Both matrices are $N \times N$ matrices defined for the sets of occupied orbitals $1, \ldots, N$. In a more compact (matrix) notation we may write

$$\underline{S} = (\boldsymbol{\psi}^\dagger, \boldsymbol{\phi}) \,,$$

$$\underline{d} = (\boldsymbol{\psi}^\dagger, \hat{d}\boldsymbol{\phi}) \,,$$

where $\boldsymbol{\phi} = (|\phi_1\rangle, \ldots, |\phi_N\rangle)$ and $\boldsymbol{\psi} = (|\psi_1\rangle, \ldots, |\psi_N\rangle)$ denote rows of the first N frozen and relaxed orbitals, respectively. The biorthogonalization procedure for the two sets $\boldsymbol{\phi}$ and $\boldsymbol{\psi}$ of mutually nonorthogonal functions consists of determining the unitary transformations

$$\bar{\boldsymbol{\phi}} = \boldsymbol{\phi}\, \underline{U} \,, \tag{A5a}$$

$$\bar{\boldsymbol{\psi}} = \boldsymbol{\psi}\, \underline{V} \tag{A5b}$$

within each of these sets, fulfilling the condition that the overlap matrix for the transformed orbitals be diagonal ($\underline{\Delta}$):

$$(\bar{\boldsymbol{\psi}}^\dagger, \bar{\boldsymbol{\phi}}) = \underline{V}^\dagger (\boldsymbol{\psi}^\dagger, \boldsymbol{\phi}) \underline{U} = \underline{V}^\dagger \underline{S}\, \underline{U} = \underline{\Delta} \,. \tag{A6}$$

As in (A1) and (A2) one may define Slater determinants $|\bar{\Phi}_0^N\rangle$ and $|\bar{\Phi}_0^N\rangle$ for the sets of biorthogonalized orbitals $\bar{\boldsymbol{\phi}}$ and $\bar{\boldsymbol{\psi}}$. Since $\underline{U}$ and $\underline{V}$ are unitary matrices the relations

$$|\bar{\Phi}_0^N\rangle = \det(\underline{U}) |\Phi_0^N\rangle \,, \tag{A7a}$$

$$|\bar{\bar{\Phi}}_0^N\rangle = \det(\underline{V}) |\bar{\Phi}_0^N\rangle \tag{A7b}$$

hold, where

$$|\det(\underline{U})| = |\det(\underline{V})| = 1 \,.$$

Using these relations and Eq. (A6) one readily arrives at the well-known result

$$\langle \bar{\Phi}_0^N | \Phi_0^N \rangle = \det(\underline{S}) \tag{A8}$$

for the relaxed-frozen ground-state overlap, which, of course, can also be obtained directly. Next we consider the $(N-1)$-electron overlap integral of the relaxed and frozen single-hole states $c_q |\bar{\Phi}_0^N\rangle$ and $a_p |\Phi_0^N\rangle$, respectively. Using the biorthogonalized orbitals we may write

$$\langle \bar{\Phi}_0^N | c_q^\dagger a_p | \Phi_0^N \rangle = \sum_{r,s} V_{qr}^* U_{ps} \langle \bar{\bar{\Phi}}_0^N | \bar{c}_r^\dagger \bar{a}_s | \bar{\Phi}_0^N \rangle \det(\underline{U}\, \underline{V}^*)^{-1} \,. \tag{A9}$$

Here the operators $\bar{c}_r$ and $\bar{a}_s$ are defined with respect to the biorthogonalized orbitals with transformation relations reading

$$a_p = \sum_{s=1}^{N} U_{ps} \bar{a}_s \,, \tag{A10a}$$

$$c_q = \sum_{r=1}^{N} V_{qr} \bar{c}_r \,. \tag{A10b}$$

Now the matrix element on the right-hand side of Eq. (A9) is readily evaluated, yielding

$$\langle \bar{\bar{\Phi}}_0^N | \bar{c}_r^\dagger \bar{a}_s | \bar{\Phi}_0^N \rangle = \delta_{rs} \frac{\langle \bar{\bar{\Phi}}_0^N | \bar{\Phi}_0^N \rangle}{\langle \bar{\psi}_r | \bar{\phi}_r \rangle} \,. \tag{A11}$$

Inserting this result in Eq. (A9) we obtain

$$\langle \bar{\Phi}_0^N | c_q^\dagger a_p | \Phi_0^N \rangle = \sum_r V_{qr}^* U_{pr} (\langle \bar{\psi}_r | \bar{\phi}_r \rangle)^{-1} \langle \bar{\Phi}_0^N | \Phi_0^N \rangle \,. \tag{A12}$$

Comparison of the expression on the right-hand side with the relation

$$\underline{S}^{-1} = \underline{U}\, \underline{\Delta}^{-1} \underline{V}^\dagger \,, \tag{A13}$$

which follows from Eq. (A6), leads to the final result

$$\langle \bar{\Phi}_0^N | c_q^\dagger a_p | \Phi_0^N \rangle = (\underline{S}^{-1})_{pq} \langle \bar{\Phi}_0^N | \Phi_0^N \rangle \,. \tag{A14}$$

The important feature of this result is that all "biorthogonalized" quantities have dropped out and the final expression requires only the simple overlap matrix $\underline{S}$. Proceeding in the same way we may evaluate the transition moment for the single-hole states:

$$\begin{aligned}
\langle \bar{\Phi}_0^N | c_q^\dagger \hat{D} a_p | \Phi_0^N \rangle &= \sum_{r,s} V_{qr}^* U_{ps} \langle \bar{\bar{\Phi}}_0^N | \bar{c}_r^\dagger \hat{D} \bar{a}_s | \bar{\Phi}_0^N \rangle \det(\underline{U}\, \underline{V}^*)^{-1} \\
&= \left[\sum_{\substack{r,s \\ r \neq s}} V_{qr}^* U_{ps} \frac{-\langle \bar{\psi}_s | \hat{d} | \bar{\phi}_r \rangle}{\langle \bar{\psi}_s | \bar{\phi}_s \rangle \langle \bar{\psi}_r | \bar{\phi}_r \rangle} + \sum_r V_{qr}^* U_{pr} \left[\sum_{i \neq r} \frac{\langle \bar{\psi}_i | \hat{d} | \bar{\phi}_i \rangle}{\langle \bar{\psi}_i | \bar{\phi}_i \rangle \langle \bar{\psi}_r | \bar{\phi}_r \rangle} \right] \right] \langle \bar{\Phi}_0^N | \Phi_0^N \rangle \\
&= \left[\sum_{r,s} V_{qr}^* U_{ps} \frac{-\langle \bar{\psi}_s | \hat{d} | \bar{\phi}_r \rangle}{\langle \bar{\psi}_s | \bar{\phi}_s \rangle \langle \bar{\psi}_r | \bar{\phi}_r \rangle} + \sum_r V_{qr}^* U_{pr} \frac{1}{\langle \bar{\psi}_r | \bar{\phi}_r \rangle} \left[\sum_i \frac{\langle \bar{\psi}_i | \hat{d} | \bar{\phi}_i \rangle}{\langle \bar{\psi}_i | \bar{\phi}_i \rangle} \right] \right] \langle \bar{\Phi}_0^N | \Phi_0^N \rangle \\
&= [-(\underline{S}^{-1} \underline{d}\, \underline{S}^{-1})_{pq} + (\underline{S}^{-1})_{pq} \mathrm{Tr}(\underline{d}\, \underline{S}^{-1})] \langle \bar{\Phi}_0^N | \Phi_0^N \rangle \,.
\end{aligned} \tag{A15}$$

Here $\underline{d}$ is the matrix of relaxed-frozen dipole integrals defined by Eq. (A4). For the following quantities we give only the results.

(i) Overlap relaxed single excitation-frozen ground state

$$\langle \overline{\Phi}_0^N | c_l^\dagger c_j | \Phi_0^N \rangle = \sum_{r=1}^{N} \langle \psi_j | \phi_r \rangle (\underline{S}^{-1})_{rl} \langle \overline{\Phi}_0^N | \Phi_0^N \rangle \ . \tag{A16}$$

(ii) Transition moment relaxed single excitation-frozen ground state

$$\langle \overline{\Phi}_0^N | c_l^\dagger c_j \hat{D} | \Phi_0^N \rangle = \left[\sum_r \langle \psi_j | d | \phi_r \rangle (\underline{S}^{-1})_{rl} + \sum \langle \psi_j | \phi_r \rangle (-\underline{S}^{-1} \underline{d} \underline{S}^{-1} + \mathrm{Tr}(\underline{d} \underline{S}^{-1}) \underline{S}^{-1})_{rl} \right] \langle \overline{\Phi}_0^N | \Phi_0^N \rangle \ . \tag{A17}$$

(iii) Overlap relaxed $2h$-$1p$ satellite-frozen single-hole state $\langle \overline{\Phi}_0^N | c_l^\dagger c_h^\dagger c_j a_r | \Phi_0^N \rangle$ [see Eq. (27)].

(iv) Transition moment relaxed $2h$-$1p$ satellite-frozen single-hole state $\langle \overline{\Phi}_0^N | c_l^\dagger c_h^\dagger c_j \hat{D} a_r | \Phi_0^N \rangle$ [see Eq. (28)].

---

*Permanent address: Physikalisch-Chemisches Institut, Universität Heidelberg, D-6900 Heidelberg, Federal Republic of Germany.

[1]K. Siegbahn, C. Nordling, C. Johansson, J. Hedman, P. F. Heden, K. Hamrin, U. Gelius, T. Bergmark, L. O. Werme, R. Manne, and Y. Baer, *ESCA Applied to Free Molecules* (North-Holland, Amsterdam, 1971).

[2]H. Siegbahn and L. Karlsson, in *Handbuch der Physik*, edited by W. Mehlhorn (Springer, Berlin, 1982), Vol. 31.

[3]U. Gelius, J. Electron Spectrosc. Relat. Phenomn. **5**, 985 (1974).

[4]V. McKoy, T. A. Carlson, and R. R. Lucchese, J. Phys. Chem. **88**, 3188 (1984).

[5]P. H. Kobrin, S. Southworth, C. M. Truesdale, D. W. Lindle, U. Becker, and D. A. Shirley, Phys. Rev. A **29**, 194 (1984).

[6]C. M. Truesdale, S. H. Southworth, P. H. Kobrin, U. Becker, D. W. Lindle, H. G. Kerkhoff, and D. A. Shirley, Phys. Rev. Lett. **50**, 1265 (1983); C. M. Truesdale, D. W. Lindle, P. H. Kobrin, U. Becker, H. G. Kerkhoff, P. A. Heimann, T. A. Ferrett, and D. A. Shirley, Phys. **80**, 2319 (1984).

[7]D. W. Lindle, C. M. Truesdale, P. H. Kobrin, T. A. Ferrett, P. A. Heimann, U. Becker, H. G. Kerkhoff, and D. A. Shirley, J. Chem. Phys. **81**, 5375 (1984).

[8]See, e.g., C. E. Brion, S. Daniel, R. Sodlei, and A. P. Hitchcock, in *X-Ray and Atomic Inner-Shell Physics*, edited by B. Craseman (AIP, New York, 1982), and references therein.

[9]A. S. Vinogradov, B. Shlarbaum, and T. M. Zimkina, Opt. Spectrosc. (USSR) **36**, 383 (1974).

[10]A. Bianconi, H. Petersen, F. C. Brown, and R. Z. Bachrach, Phys. Rev. A **17**, 1907 (1978).

[11]D. M. Barrus, R. L. Blake, A. J. Burek, K. C. Chambers, and A. L. Pregenzer, Phys. Rev. A **20**, 1045 (1979).

[12]A. Reimer, J. Schirmer, J. Feldhaus, A. M. Bradhsaw, U. Becker, H. G. Kerkhoff, B. Langer, D. Szostak, R. Wehlitz, and W. Braun, Phys. Rev. Lett. **57**, 1707 (1986).

[13]D. Dill and J. L. Dehmer, J. Chem. Phys. **61**, 691 (1974).

[14]P. W. Langhoff, in *Electron-Molecule and Photon-Molecule Collisions*, edited by T. Rescigno, V. McKoy, and B. Schneider (Plenum, New York, 1979).

[15]R. R. Lucchese, K. Takatsuka, and V. McKoy, Physics Rep. **131**, 147 (1986).

[16]J. L. Dehmer and D. Dill, J. Chem. Phys. **65**, 5327 (1976).

[17]T. N. Rescigno and P. W. Langhoff, Chem. Phys. Lett. **51**, 65 (1977).

[18]N. Padial, G. Csanak, V. McKoy, and P. W. Langhoff, J. Chem. Phys. **69**, 92992 (1978).

[19]R. R. Lucchese and V. McKoy, Phys. Rev. A **26**, 1406 (1982).

[20]D. L. Lynch and V. McKoy, Phys. Rev. A **30**, 1561 (1984).

[21]R. L. Martin and D. A. Shirley, J. Chem. Phys. **64**, 3685 (1976).

[22]J. Berkowitz, J. L. Dehmer, Y. K. Kim, and J. P. Descleaux, J. Chem. Phys. **61**, 2556 (1974).

[23]T. Åberg, Phys. Rev. **156**, 35 (1967).

[24]A. F. Starace, in Ref. 2.

[25]T. Ishihara, J. Mizuno, and T. Watanabe, Phys. Rev. A **22**, 1552 (1980).

[26]J. Schirmer, M. Braunstein, and V. McKoy, J. Chem. Phys. (to be published).

[27]R. Arneberg, J. Müller, and R. Manne, Chem. Phys. **64**, 249 (1982).

[28]I. Cacelli, V. Carravetta, and R. Moccia, J. Phys. B **16**, 1895 (1983).

[29]W. von Niessen, J. Schirmer, and L. S. Cederbaum, Comput. Phys. Rep. **1**, 59 (1984).

[30]L. S. Cederbaum, W. Domcke, and J. Schirmer, Phys. Rev. A **82**, 206 (1980).

[31]For example, see B. H. Bransden, *Atomic Collision Theory* (Benjamin, New York, 1970).

[32]W. J. Hunt and W. Goddard, Chem. Phys. Lett. **3**, 414 (1969).

[33]J. Schirmer, Phys. Rev. A **26**, 2395 (1982).

[34]J. Schirmer, O. Walter, and L. S. Cederbaum, Phys. Rev. A **28**, 1237 (1983).

[35]See, for example, A. L. Fetter and J. D. Walecka, *Quantum Theory of Many-Particle Systems* (McGraw-Hill, New York, 1971).

[36]*Gaussian Basis Sets for Molecular Calculations*, edited by S. Huzinaga (Elsevier, Amsterdam, 1984).

[37]R. B. Lucchese and V. McKoy, Phys. Rev. A **21**, 112 (1980).

[38]A. R. Edmonds, *Angular Momentum in Quantum Mechanics* (Princeton University, Princeton, 1960).

[39]R. B. Kay, Ph. E. Van der Leeuw, and M. J. Van der Wiel, J. Phys. B **10**, 2513 (1977).

[40]G. Angonoa, O. Walter, and J. Schirmer, J. Chem. Phys. **87**, 6789 (1987).

[41]J. L. Dehmer and D. Dill, Argonne National Laboratory Report No. ANL-77-65, 1977 (unpublished), p. 65.

[42]D. Dill, S. Wallace, J. Siegel, and J. L. Dehmer, Phys. Rev. Lett. **42**, 411 (1978).

[43]F. A. Grimm, Chem. Phys. **53**, 71 (1980).